

ABSTRACT

The objective of this study is to explore concepts for control of turbulent boundary layers leading to skin-friction reduction using the direct numerical simulation technique. This report is divided into three parts where three different control methods are investigated: an active control by sensing and perturbing structures near the wall, a feedback control procedure guided by control theory, and a passive control by longitudinal riblets.

In PART I significant drag reduction is achieved when the surface boundary condition is modified to suppress the dynamically significant coherent structures present in the wall region. The wall-normal or spanwise velocity at the wall was set to be 180° out of phase with the corresponding velocity component near the wall. The drag reduction is accompanied with significant reduction in the intensity of the wall-layer structures and reductions in the magnitude of Reynolds shear stress throughout the flow. The apparent outward shift of the controlled data indicates a displaced virtual origin of the boundary layer and a thickened sublayer. Time sequences of the flow fields show that there are two essential drag reduction mechanisms. Firstly, within a short time after the control is applied, drag is reduced mainly by deterring the sweep motion without modifying the primary streamwise vortices above the wall. Consequently, the high skin-friction regions on the wall are lifted to the interior of the channel ($y^+ \approx 5$) by the control schemes. Secondly, the active control changes the evolution of the wall vorticity layer by stabilizing and preventing lifting of the spanwise vorticity near the wall, which may have led to the suppression of a source of new streamwise vortices above the wall.

In PART II mathematical methods of control theory are applied to the problem of control of fluid flow with the long range objective of developing effective methods for the control of turbulent flows. The procedure of how to cast the problem of controlling turbulence into a problem in optimal control theory is presented using model problems through the formalism and language of control theory. Then a sub-optimal control and feedback procedure for general stationary and time-dependent problems are presented using methods of calculus of variations through the adjoint state and gradient algorithms. This suboptimal feedback control procedure is applied to the stochastic Burgers equation. Two types of controls are investigated: distributed and boundary controls. The control inputs are the momentum forcing

for the distributed control and the boundary velocity for the boundary control. Costs to be minimized are defined as the sum of the mean square velocity gradient inside the domain for the distributed control or the square velocity gradient at the wall for the boundary control; and in both cases a term was added to account for the implementation cost. Several cases of both controls have been numerically simulated to investigate the performances of the control algorithm. Most cases considered show significant reductions of the costs. A version of the feedback procedure which is more effective for practical implementation has been considered and implemented, and the application of this algorithm also shows significant reductions of the costs.

In PART III direct numerical simulation is performed to analyze turbulent flow over longitudinal riblets, and to educe the mechanism of drag reduction by riblets. The computed drags on the riblet surfaces are in good agreement with the existing experimental data. The virtual origin of the wall is defined such that the maximum turbulent kinetic energy production occurs at $y^+ \approx 13$. As the ridge angle of the riblets increases, the virtual origin moves closer to the riblet tip. The mean-velocity profiles based on this virtual origin show upward and downward shifts in the log-law for drag-decreasing and drag-increasing cases, respectively. Turbulence statistics above the riblets are computed and compared with those above the flat plate. Differences in the mean-velocity profile and turbulence quantities are found to be limited to the inner region of the boundary layer. Velocity and vorticity fluctuations as well as the Reynolds shear stresses above the riblets are reduced in drag-reducing configurations. Quadrant analysis indicates that the riblets intensify the positive Reynolds-shear-stress producing events in drag-increasing configurations, while they mitigate these events in drag-reducing configurations. The Reynolds shear stresses from the first and third quadrant events are nearly unchanged by the riblets. From examination of the instantaneous flow fields, a drag reduction mechanism by riblets is proposed: riblets with small spacings reduce viscous drag by restricting the location of the streamwise vortices above the wetted surface such that only a limited area of the riblets is exposed to their induced downwash of high speed fluid. Only the tip region is exposed to high wall-shear rates in drag-reducing configurations, whereas, in drag-increasing configurations, both the middle and tip regions are exposed to them.

ACKNOWLEDGEMENTS

The authors would like to acknowledge the financial supports from the Air Force Office of Scientific Research under Grant No. AFOSR-89-0411 with Dr. James McMichael as the technical monitor. The use of the computer facilities at NASA-Ames research center is also greatly appreciated.

PART II of this report was conducted in cooperation with Professor Roger Temam. The computer program used in PART III was developed in cooperation with Professor Paolo Orlandi. Their contributions are greatly appreciated. We are also grateful for useful discussions with Professor William C. Reynolds and Mr. Tom Bewley.

TABLE OF CONTENTS

	Page
Abstract	iv
Acknowledgement	vi
Table of Contents	vii
List of Tables/Figures	xi
Nomenclature	xvii
 Preface	 1

PART I

Active Turbulence Control in Wall-Bounded Flows

Chapter

1. Introduction	4
2. Active Control Experiments	7
2.1 Control with the Normal Velocity (v -Control)	7
2.2 Control with the Spanwise Velocity (w -Control)	10
2.3 Combined Control (v - and w -Control)	10
2.4 Control with the Streamwise Velocity (u -Control)	10
2.5 Control with the Sensors at the Wall	11
2.6 Active Control Based on Optimal Control Theory	12
3. Turbulence Statistics of Manipulated Channel Flows	27
3.1 Mean Properties	27
3.2 Turbulence Intensities	29
3.3 Reynolds Shear Stress and Quadrant Analysis	30
3.4 Vorticity	31
3.5 Two-Point Correlation Functions and Spectra	32
3.6 Pressure-Strain Correlation Tensor	34
3.7 Skewness and Flatness Factors	35
4. Turbulence Structure of Manipulated Channel Flows and Drag Reduction Mechanisms	66

4.1 Turbulence Structure of Manipulated Channel Flows.....	66
4.2 Drag Reduction Mechanisms of Active Controls.....	67
4.2.1 Minimal Channel Flow.....	68
4.2.2 An Isolated Vortex Interacting with a Wall.....	70
5. Conclusions and Discussions	90

PART II

Feedback Control for Unsteady Flow and Its Application to the Stochastic Burgers Equation

Chapter

1. Introduction	94
2. Introduction to Control Theory: Some Model Problems in Flow Control	99
2.1 Stationary Channel Flow	99
2.2 Time-Dependent Channel Flow.....	101
3. Suboptimal Control and Feedback Procedures.....	104
3.1 Stationary Problem	104
3.1.1 Suboptimal Feedback Laws	106
3.2 Time-Dependent Problem	110
4. Application to the Stochastic Burgers Equation	114
4.1 The Burgers Equation with Random Forcing	114
4.2 Feedback Control Procedures.....	116
4.2.1 Distributed Control (Formulation)	116
4.2.2 Boundary Control (Formulation).....	117
4.2.3 Numerical Algorithm	118
4.3 Results of Numerical Simulation.....	118
4.3.1 Numerical Results for Distributed Control	120
4.3.2 Numerical Results for Boundary Control	121
4.4 Remarks on the Feedback Laws	123
4.5 Further Remarks on Implementation Issues	124
4.5.1 Remarks on the Time-Discretization Method	124
4.5.2 Practical Implementation of the Control Algorithm.....	125
5. Conclusions and Discussions	148

PART III

Direct Numerical Simulation of Turbulent Flow over Riblets

Chapter

1. Introduction	151
2. Computational Domain and Grid Spacing	154
3. Numerical Methods	159
4. Drag Measurement, Mean-Velocity Profile and the Virtual Origin	163
4.1 Drag Measurement	163
4.2 Mean-Velocity Profile and Origin of the Wall	165
5. Turbulence Statistics	177
5.1 Turbulence Intensities	177
5.2 Reynolds Shear Stress	179
5.3 Vorticity	180
5.4 Quadrant Analysis	180
5.5 Higher-Order Statistics	183
6. Drag Reduction Mechanism	208
7. Summary	212

APPENDIX

A. Optimal Control of Wall-Bounded Turbulent Flows	215
B. Distributed Control of the Burgers Equation	223
C. Boundary Control of the Burgers Equation	226
D. Dependence of the Control Algorithm on the Time-Discretization Method ..	230
E. A Fully Implicit Method for the Unsteady Incompressible Navier-Stokes Equations in Generalized Coordinate Systems	232
E.1 Numerical Method	233
E.2 Application to Turbulent Plane Channel Flow	241
E.2.1 Effect of the <i>CFL</i> Number on Turbulence Statistics	242
E.2.2 Suitability of a Second-Order Central-Difference Scheme for a Direct Numerical Simulation of Turbulent Channel Flow ..	243
E.3 Computational Details for Turbulent Flow over Riblets	244

F. Turbulence Statistics above the Riblets with $\alpha = 45^\circ$ for Cases $s^+ \approx 40$ and $s^+ \approx 20$	253
References.....	265

DTIC QUALITY INSPECTED 5

Accession For	
NTIS	<input checked="" type="checkbox"/> GRA&I
DTIC TAB	<input type="checkbox"/>
Unannounced	<input type="checkbox"/>
Justification	
By _____	
Distribution/	
Availability Codes	
Dist	Avail and/or Special
A-1	

LIST OF TABLES AND FIGURES

PART I

Active Turbulence Control in Wall-Bounded Flows

Table	Page
-------	------

- | | |
|---|----|
| 1 Mean flow variables of the manipulated and unmanipulated channel flows..... | 29 |
|---|----|

Figure	Page
--------	------

- | | |
|---|-------|
| 1 (a) Three dimensional view of detection planes; (b) schematic diagram of out-of-phase v -control..... | 14,15 |
| 2 Time history of the pressure gradient required to drive a fixed mass flow rate in the case of v -control..... | 16 |
| 3 Time history of the pressure gradient required to drive a fixed mass flow rate at the sensor location $y_d^+ \approx 10$ exceeded a threshold value. | 17 |
| 4 Schematic diagram of out-of-phase w -control. | 18 |
| 5 Time history of the pressure gradient required to drive a fixed mass flow rate in the case of w -control..... | 19 |
| 6 Schematic diagram of combined control. | 20 |
| 7 Time history of the pressure gradient required to drive a fixed mass flow rate in the case of combined control..... | 21 |
| 8 Time history of the pressure gradient required to drive a fixed mass flow rate in the case of u -control..... | 22 |
| 9 Joint probability density of the wall pressure fluctuations and the normal velocity.. | 23 |
| 10 Joint probability density of the fluctuating wall-shear rate and the normal velocity at $y^+ \approx 10$ | 24 |
| 11 Joint probability density of g_w and the normal velocity at $y^+ \approx 10$ | 25 |
| 12 Time history of the pressure gradient required to drive a fixed mass flow rate with sensors on the wall..... | 26 |
| 13 Mean-velocity profiles..... | 36 |
| 14 Near-wall behavior of the mean velocity. | 37 |

15	Root-mean-square velocity fluctuations.	38,39
16	Production and dissipation of the turbulence kinetic energy.	40
17	Root-mean-square pressure fluctuations.	41
18	Reynolds shear stress and total shear stress.	42
19	Correlation coefficient of u' and v'	43
20	Reynolds shear stress from each quadrant.	44,45
21	Root-mean-square vorticity fluctuations.	46,47
22	Root-mean-square values of the streamwise vorticity component.	48
23	Root-mean-square values of the normal vorticity component.	49
24	Root-mean-square values of the spanwise vorticity component.	50
25	One-dimensional spectra of wall shear-rate fluctuations.	51
26	One-dimensional power spectra of wall pressure fluctuations.	52
27	One-dimensional energy spectra.	53,54
28	Two-point correlations of the velocity fluctuations.	55,56,57
29	Two-point correlations. (a) Wall shear-rate fluctuations; (b) wall pressure fluctuations.	58,59
30	Diagonal elements of the pressure-strain correlation tensor.	60,61
31	Skewness and flatness factors of the velocity fluctuations.	62,63
32	Skewness and flatness factors of the Reynolds shear stress.	64
33	Probability density distribution. (a) Wall shear-rate fluctuations; (b) wall pressure fluctuations.	65
34	Contours of streamwise velocity fluctuations in an (x, z) plane.	72,73,74
35	Contours of control-input velocities at the wall.	75
36	Variation of mean spanwise streak spacing with distance from wall estimated from the two-point correlations, $R_{uu}(r_z^+)$	76
37	Contours of streamwise vorticity fluctuations in a cross-flow plane.	77
38	Contours of spanwise vorticity fluctuations in a cross-flow plane.	78
39	Time history of the horizontally averaged wall-shear rate at the lower wall for minimal channel flow.	79

40	Time sequence of the evolution of the wall vorticity layer for minimal channel flow.....	80,81,82
41	Velocity vector (v, w) and contours of the spanwise vorticity in a (y, z) plane.	83,84,85
42	Schematic diagram of a drag reduction mechanism by active controls in a cross-flow plane.....	86
43	Time sequence of the evolution of a vortex dipole.....	87,88,89

PART II

Feedback Control for Unsteady Flow and Its Application to the Stochastic Burgers Equation

Table	Page
1 Variation of the cost with respect to the iteration k for case (ii').	126

Figure	Page
1 Instantaneous velocity profiles.	127,128
2 Mean-velocity profiles.....	129
3 Velocity profiles with no control and $Re = 1500$, $\Delta t_r = 0.01$	130
4 Variation of the cost and its convergence with respect to the parameter of descent ρ_0 for case (ii).	131
5 Time history of flow parameters for case (ii). (a) Cost; (b) energy; (c) wall velocity gradient; (d) momentum forcings.	132,133
6 Time history of flow parameters for case (iii). (a) Cost; (b) energy; (c) wall velocity gradient; (d) momentum forcings.	134,135
7 Temporal evolution of flow parameters and velocity profiles with and without random forcing and control.	136,137
8 Convergence of the sensitivity of the cost function at $t = 0.001$ for case (ii) and $\theta_1(u) = u$	138
9 Time history of flow parameters, and velocity profile for case (ii'). (a) Cost; (b) energy; (c) wall velocity gradient; (d) velocity profile at $t = 2$	139,140
10 Time history of the cost. (a) Case (iii'); (b) case (iv').	141

11	Phase diagram of control velocity and velocity gradient at the wall for the time interval $0 < t < 2$. (a) Case (ii'); (b) case (iii').	142
12	Variation of the cost and sensitivity with respect to time-discretization methods for case (ii').	143
13	Time history of the cost for various iterations k for case (ii').	144
14	Time history of the wall velocity gradient for various iterations k for case (ii').	145
15	Time history of the cost and wall velocity gradient with $k = 1$ for case (iv').	146
16	Time history of the cost and wall velocity gradient with $k = 1$ for case (ii').	147

PART III

Direct Numerical Simulation of Turbulent Flow over Riblets

Table	Page
1 Parameters for the simulations of turbulent flows over riblets.	155
2 Drag variation for each riblet configuration.	164
3 Wall-shear velocity and location of the virtual origin for each riblet configuration.	167

Figure	Page
1 (a) Three-dimensional view of computational domain; (b) cross-sectional view of riblet configuration.....	156,157
2 Computational mesh near riblets in the case of $s^+ \approx 20$ and $\alpha = 45^\circ$	158
3 Coordinate transformation.....	162
4 Time history of wall-shear rates at both flat and riblet walls in the case of $s^+ \approx 20$ and $\alpha = 60^\circ$	170
5 Mean-velocity profiles for cases with $\alpha = 60^\circ$	171,172
6 (a) Wall-shear rates and (b) contribution to the drag at several spanwise positions on riblet surfaces.....	173,174
7 Mean-velocity profiles in the case of $s^+ \approx 20$ and $\alpha = 60^\circ$	175
8 Variation of mean-velocity profiles with the location of the virtual origin for cases with $\alpha = 60^\circ$	176

9	Root-mean-square velocity fluctuations in global coordinates.	185,186,187
10	Contours of root-mean-square velocity fluctuations in the (y, z) plane for cases with $\alpha = 60^\circ$	188,189
11	Root-mean-square velocity fluctuations in wall coordinates.	190
12	Reynolds shear stress for cases with $\alpha = 60^\circ$	191,192
13	Total shear stress for cases with $\alpha = 60^\circ$	193
14	Root-mean-square vorticity fluctuations in global coordinates.	194,195,196
15	Root-mean-square vorticity fluctuations in wall coordinates.	197
16	Turbulent kinetic energy for cases with $\alpha = 60^\circ$	198
17	Turbulent energy production for cases with $\alpha = 60^\circ$	199
18	Reynolds shear stress from each quadrant normalized by the mean centerline velocity for cases with $\alpha = 60^\circ$	200,201
19	Reynolds shear stress from each quadrant normalized by the absolute value of the local mean Reynolds shear stress for cases with $\alpha = 60^\circ$	202,203
20	Skewness factors.	204,205
21	Flatness factors.	206,207
22	Instantaneous flows over the riblets with $\alpha = 60^\circ$	210
23	Schematic diagram of drag increase and reduction mechanisms by riblets.	211

APPENDIX

Figure	Page
E.1 Convergence behavior of the Newton-iterative method for different <i>CFL</i> numbers in turbulent plane channel flow.	245
E.2 Variation of root-mean-square velocity fluctuations with respect to the <i>CFL</i> number.	246
E.3 Variation of the Reynolds shear stress with respect to the <i>CFL</i> number.	247
E.4 Variation of root-mean-square vorticity fluctuations with respect to the <i>CFL</i> number.	248
E.5 Variation of root-mean-square velocity fluctuations by doubling the number of grid points.	249

E.6	Variation of the Reynolds shear stress by doubling the number of grid points.	250
E.7	Variation of root-mean-square vorticity fluctuations by doubling the number of grid points.	251
E.8	Convergence behavior of the Newton-iterative method for different <i>CFL</i> numbers in turbulent flow over riblets.	252
F.1	Mean-velocity profiles for cases with $\alpha = 45^\circ$	255
F.2	Variation of mean-velocity profiles with the location of the virtual origin for cases with $\alpha = 45^\circ$	256
F.3	Root-mean-square velocity fluctuations in global coordinates for cases with $\alpha = 45^\circ$	257,258,259
F.4	Root-mean-square velocity fluctuations in wall coordinates for cases with $\alpha = 45^\circ$	260
F.5	Reynolds shear stress for cases with $\alpha = 45^\circ$	261
F.6	Root-mean-square vorticity fluctuations for cases with $\alpha = 45^\circ$	262,263,264

NOMENCLATURE

Roman Symbols

A	Stokes operator, see equation (2.2) in PART II
A_f, A_r	Wetted surface areas of the flat plate and the plate with riblets
C	General linear or nonlinear operator, see equation (2.3) in PART II
C_f	Skin-friction coefficient
c_k^j	Metric quantity, see equation (E.6)
D	Drag, see equation (2.9) in PART II
D^i	Divergence operator, see equation (E.4)
D_f, D_r	Drags of the flat plate and of the riblet surface, see equation (4.1) in PART III
\bar{D}_r	Time- and plane-averaged drag of the riblet surface, see equation (4.2) in PART III
$\mathcal{D}J/\mathcal{D}\phi$	Sensitivity of the cost function with respect to the control input, see equation (3.7) in PART II
$-dP/dx$	Mean pressure gradient
E	Energy inside domain, $\int \frac{1}{2}u^2 dx$ in PART II also Scalar function, see equation (2.5) in PART II
E_{uu}, E_{vv}, E_{ww}	One-dimensional energy spectra
e	α_0, α_1
F	Flatness factor also Operator, see equation (2.5) in PART II also Parameter of the surface roughness, see equation (4.6) in PART III
F^i	Function, see equation (E.15)
f	Control input forcing, see equation (4.4) in PART II
G	G^1, G^2, G^3
G^i	Gradient operator, see equations (E.5) and (E.6)
g_w	Surface detection criterion, $\partial/\partial z(\partial w/\partial y) _w$

h	Height of the riblet
h^+	Height of the riblet in wall units
J, \tilde{J}	Cost function also Jacobian of the coordinate transformation
k	Turbulent kinetic energy
k_x, k_z	Streamwise and spanwise wavenumbers
L	Length of the computational domain in PART II
L^i	$L^i = L_1^i + L_2^i$
L_1^i, L_2^i	Diffusion terms without and with cross derivatives respectively
L_x, L_z	Streamwise and spanwise computational periods
l, m	Parameters for feedback control, see equation (2.3) in PART II
l_b, m_b	Parameters for boundary control, see equation (4.9) in PART II
l_d, m_d	Parameters for distributed control, see equation (4.6) in PART II
M	Mass flux
M_{ij}	Operator, see equations (E.18) and (E.19)
N^i	Convection term
N_{x_i}	Number of the grid points, N_x, N_y, N_z in x, y, z directions respectively
P_k	Production of turbulent kinetic energy
p	Pressure
p_l, q_i	Solutions of the linearized Navier-Stokes equations, see equation (A.7)
\tilde{p}_l, \tilde{q}_i	Solutions of the linearized adjoint Navier-Stokes equations, see equation (A.10)
Q	Volume flux
Q_{ij}	Operator, see equations (E.18) and (E.19)
q	q^1, q^2, q^3
q^i	Volume flux across the faces of the numerical cells
R	Two-point correlations also Inertial and boundary terms of the Navier-Stokes equations, see equation (2.2) in PART II
R^i	Right hand side of equation (E.14)
R_{uu}, R_{vv}, R_{ww}	Two-point correlations
Re	Reynolds number

Re_c	Reynolds number based on the mean centerline velocity, $U_c\delta/\nu$
Re_l	Reynolds number based on the laminar centerline velocity, $U_l\delta/\nu$
Re_m	Reynolds number based on the bulk mean velocity, $U_m\delta/\nu$
Re_Γ	Reynolds number based on the circulation of the vortex, Γ/ν
Re_τ	Reynolds number based on the wall-shear velocity, $u_\tau\delta/\nu$
r_x^+, r_z^+	Streamwise and spanwise separations of two-point correlation
S	Skewness factor
s	Spacing of the riblet
s^+	Spacing of the riblet in wall units
T	Time constant
t	Time
U_c	Mean centerline velocity
U_l	Laminar centerline velocity
U_m	Bulk mean velocity
u	u_1, u_2, u_3
u, v, w	Streamwise, normal (to the wall), and spanwise velocity components
\bar{u}_i	Mean velocity averaged over x and z (PART I) also Mean velocity averaged over x, t , and the same spanwise locations over different riblets (PART III)
u'_i	Velocity fluctuations, $u'_i = u_i - \bar{u}_i$
u^+	u/u_τ
u_i	u, v, w
u_τ	Wall-shear velocity, $(\tau_w/\rho)^{\frac{1}{2}}$
u_{τ_f}	Wall-shear velocity at the flat plate
u_{τ_m}	Wall-shear velocity at the manipulated channel wall
u_{τ_u}	Wall-shear velocity at the unmanipulated channel wall
$u_{\tau_r}^*$	Wall-shear velocity at the virtual origin of the riblet, see equation (4.3) in PART III
v_{th}	Threshold value of v for v -control
x, y, z	Streamwise, normal (to the wall), and spanwise coordinates
x_i	x_1, x_2, x_3
y_d	Distance of the detection point measured from the wall
y_o	Location of the virtual origin of the riblet, see equation (4.4)

in PART III

y^+	yu_τ/ν
y_m^+	Location of the maximum turbulent kinetic energy production
y_s^+	Viscous sublayer thickness in wall units

Greek Symbols

α	Ridge angle of the riblet
α^{jk}	Metric quantity, see equation (E.6)
α_i	Coefficients of suboptimal feedback laws, see equation (3.9) in PART II
β	Parameter of the virtual origin location, see table 3 in PART III
Γ	Circulation of the vortex
γ	Observation, Cu
γ_d	Desired value of observation
γ_k^j	Metric quantity, see equation (E.6)
Δt	Computational time step
Δt_r	Time scale of the random forcing
Δx_i	Computational grid spacing
δ	Channel half-width, boundary layer thickness
δ^*	Displacement thickness
δ_{ij}	Kronecker delta
ϵ_k	Dissipation of the turbulence kinetic energy
ζ	Solutions of the linearized adjoint Navier-Stokes equations, see equation (3.6) in PART II
η	Solutions of the linearized Navier-Stokes equations, see equation (3.5) in PART II
η^i	Generalized coordinates, η^1, η^2, η^3
θ	Momentum thickness
θ_i	Shape function, see equation (2.7) in PART II
λ, λ'	Constant values, see equation (4.11) in PART II
λ^+	Mean streak spacing in wall units

μ	Viscosity
ν	Kinematic viscosity
ρ	Density also Parameter of descent in PART II
ρ_0, ρ_1	Parameters of descent for boundary control in PART II
σ	Root-mean-square value of the random forcing
τ_w	Wall-shear stress
ϕ	Control input velocity at the wall also Power spectrum also Scalar, see equation (E.9)
$\hat{\phi}$	Arbitrary test function in PART II
ϕ_{ij}	Pressure-strain correlation tensor
χ	Random forcing
ψ	Control input velocity at the boundary, see equation (4.7) in PART II
ω_i	$\omega_x, \omega_y, \omega_z$
$\omega_x, \omega_y, \omega_z$	Streamwise, normal, and spanwise vorticity components

Other Symbols

$()^k$	Iteration index of the gradient algorithm, see equation (3.2) in PART II
$()^r$	Iteration index for the Newton-iterative method in appendix E
$\hat{()}$	Intermediate step in fractional step method in appendix E
$\overline{()}$	Average over x and z (PART I) also Average over x, t , and the same spanwise locations over different riblets (PART III) also Optimal pair of the control (appendix A)
$()'$	Deviation from its mean value
$()^+$	Non-dimensional quantity scaled by the wall variables
$()^*$	Adjoint operator in PART II also Integration over the wetted surface, see equation (4.1)

in PART III

$()_m$	Value at the manipulated channel
$()_u$	Value at the unmanipulated channel
$()_w$	Value at the wall
$\langle \rangle_x$	Average over x (PART II)

Abbreviations

<i>CFL</i>	Courant-Friedrichs-Lewy number
<i>rms</i>	Root mean square

PREFACE

The problem of controlling turbulent flows is one of the most challenging problems in fluid dynamics. Despite several studies of boundary layer control in the 1950s, no successful practical applications resulted, and efforts on this topic subsided. The revival of interest in controlling turbulent flows in recent years may be attributed to several factors. The accumulated knowledge of coherent structures in turbulent flows points to new methods of controlling turbulence. Rising fuel costs provided economical impetus for development of more efficient and longer range aircraft. Finally, the substantial advance in computer hardware has made it feasible to test active control strategies through direct numerical simulations and has also led to the development of miniature sensors, micro-processors and actuators for the implementation of control strategies.

Control experiments have enjoyed considerable success in mixing layers where the near-field hydrodynamic mechanisms are well understood. However, the origin and dynamics of coherent structures in turbulent boundary layers are still not completely known; therefore, turbulence control experiments have been largely empirical and largely based on the qualitative observations of coherent structures.

Many efforts have been directed towards manipulation of turbulent boundary layers by passive devices both externally (with thin flat plates or airfoil section devices placed in the outer region of the boundary layer) and internally (with streamwise grooves submerged in the inner region of the boundary layer) for the purpose of reducing viscous drag. Such devices play a passive role in the sense that there is no feedback loop to sense and then manipulate flow structures. The experimental data are sufficiently consistent to anticipate potential of such devices for turbulent drag reduction, even though the detailed mechanisms are not clearly understood. Most notably, the use of grooved surfaces (riblets) has found some practical applications.

As compared to a passive control strategy, application of active control to turbulent flows is much more difficult, because the control strategy would involve a timely response through a feedback loop as flow structures are modified. Proper implementation of active control in a fully developed turbulent flow which is highly

unsteady, three-dimensional and stochastic would require construction and implementation of many miniature actuators and sensors. Most existing active control strategies have been applied to transitional flows.

When the physics of a problem is well-known, such as the existence of organized patterns, one may attempt to devise a scheme to manipulate these patterns, or at least impede their formation by preassigned kinematic modifications. However, when the physics of a phenomenon is not known or is very complicated, it is tempting to appeal to the more systematic but less intuitive methods of control theory. Application of control theory to fluid mechanics problems has not yet been considered mainly because of its complexity. With the advance of super computers and the ability for direct numerical simulation of turbulence, however, the capability now exists to test the viability of using control theory in turbulent flows.

This study consists of three parts. In PART I, we investigate several active control strategies to explore concepts for manipulation of turbulent boundary layers using direct numerical simulation. Dynamically significant coherent structures are modified by applying either normal or spanwise velocity at the wall to achieve skin-friction reduction. In PART II, we develop suboptimal control and feedback procedures for unsteady flow using feedback control theory. The feedback control procedures are then tested with the stochastic Burgers equation. In PART III, we present simulations of turbulent flows over riblets to investigate the resulting turbulence modifications and drag reduction mechanisms.

PART I

Active Turbulence Control in Wall-Bounded Flows

CHAPTER 1

INTRODUCTION

The potential benefits of managing and controlling turbulent flows that occur in various engineering applications are known to be significant. Organized structures in turbulent flows play an important role in turbulent transport (Cantwell 1981 and Robinson 1991). Therefore, attempts to control turbulent flows for engineering applications have focused on the manipulation of the coherent structures. Most turbulence control strategies have been developed for free-shear flows where the hydrodynamic stability mechanism in the near field is basically understood (Ho & Huang 1982). Turbulence control strategies to date for wall-bounded turbulent flows have focused on passive approaches. For example, flow devices such as riblets or LEBUs (Large-Eddy-Break-Up devices) may be placed in the boundary layer in an attempt to suppress the formation or interaction of organized flow structures. Such devices play a passive role in the sense that there exists no feedback loop to sense and then manipulate flow structures. The present study is aimed at the active control of dynamically significant coherent structures to achieve skin-friction reduction. The control strategy will respond instantly through a feedback loop as flow structures are modified.

The most widely observed coherent structures in the wall layer are streaks: elongated regions of low- and high-speed fluid alternating in the spanwise direction. From flow visualization data, Kline *et al.* (1967) pointed out that the production of turbulence in boundary layers is largely due to the bursting event which consists of the lift-up, oscillation, and violent breakup of the streaks. The sweep event (Corino & Brodkey 1969), which is described as the inrush of high-speed fluid towards the wall, is also believed to be a major contributor to turbulence production. Some of these event-oriented descriptions of important phenomena in turbulent boundary layers are beginning to change, largely from examination of direct numerical simulation databases. For example, the bursting event may not be anything more than a consequence of the convection of a single streamwise vortex past a fluid marker (Kim & Moin 1986). The passage of the vortex lifts the marker, and as the marker wraps around the vortex, it appears as oscillation in a side view.

In this chapter, we use the terms *sweep* and *ejection* at a *point* to simply denote the flow direction towards or away from the wall respectively.

Contour plots of instantaneous turbulent velocity and pressure fluctuations show that only the streamwise velocity component is significantly elongated in the streamwise direction. The pressure patterns are round, and the normal (to the wall) velocity component is highly intermittent (Moin 1987). Therefore, intense regions of turbulence production are also highly intermittent. One of the most striking features of turbulent boundary layers are the strong shear layers protruding from the wall into the flow. Jiménez *et al.* (1988) note that the high density of these shear layers, at least at low Reynolds numbers, has previously been overlooked. Virtually every snap-shot of the flow in the form of a contour plot of the spanwise component of vorticity, ω_z , contains these shear layers. Moreover, their shape is very similar to those observed in transitional channel flow (Jiménez 1987). The shear layers are associated with high turbulence production and have long life times, travelling in a straight path downstream (Johansson, Alfredsson & Kim 1987). In addition, both experimental and numerical data indicate that the shear layers have high amplitude pressure signatures at the wall (Johansson, Her & Haritonidis 1987 and Alfredsson *et al.* 1988), which is of particular interest for their detection in an active control experiment.

Direct numerical simulations have emerged as a powerful tool in turbulence structure research. Owing to the availability of all the flow variables at many spatial locations and the ability to readily alter flow boundary conditions, numerical simulations also provide a unique laboratory for testing and designing turbulence control concepts. Although some of the concepts may not turn out to be feasible for implementation, simulations can provide data on what may be possible to achieve just from fluid dynamical considerations. The primary role of simulations in the field of flow control will be to guide experiments for complex flows. Computer simulations have been used for active stabilization of laminar boundary layers (Metcalfe *et al.* 1986). Early work on control of fully developed turbulent flows via numerical simulations has been limited to passive control (Kuhn *et al.* 1984).

In this study, we use the direct numerical simulation technique to explore concepts for manipulation of turbulent channel flow with the ultimate goal of drag reduction. The numerical technique used in this study is identical to that of Kim, Moin & Moser (1987), to which the reader is referred for a detailed description.

However, in this study, we calculated the time advancement for the convective terms according to a third-order Runge-Kutta method instead of the original Adams-Bashforth method. The boundary condition for the wall velocity components is modified according to the particular control strategy.

The base flow is a fully developed channel flow. Fully developed turbulent channel flow is homogeneous in the streamwise and spanwise directions, and periodic boundary conditions are used in these directions. Preliminary experiments were performed using $32 \times 65 \times 32$ spectral modes (streamwise, normal to the wall, and spanwise, respectively) at $Re_c = 1800$ based on the centerline velocity of the unmanipulated channel and the channel half-width. Starting with the same initial field, several different boundary conditions were tried to achieve an optimal result. The final computation uses $128 \times 129 \times 128$ spectral modes at $Re_c = 3300$, from which most of results presented in PART I are obtained. This particular Reynolds number was chosen for comparison with the results for the unmanipulated channel (Kim *et al.* 1987). For the Reynolds numbers considered here, the streamwise and spanwise computational periods (L_x and L_z) are chosen to be $4\pi\delta$ and $4\pi/3\delta$, respectively, where δ is the channel half-width.

In this study, x, y , and z denote the streamwise, normal (to the wall), and spanwise directions, respectively. The velocities are u, v , and w in the x, y , and z directions, respectively, and are used interchangeably with the subscripted variables u_1, u_2 , and u_3 . The subscript w indicates the value at the wall, and the superscript $+$ indicates a non-dimensional quantity scaled by the wall variables: for example, $y^+ = yu_\tau/\nu$, where ν is the kinematic viscosity and $u_\tau = (\tau_w/\rho)^{1/2}$ is the wall-shear velocity.

In chapter 2, several numerical experiments for active control of turbulent channel flow are described. Turbulence statistics of the manipulated channel flows are given in chapter 3. Modified turbulent structures and mechanisms of drag reduction by active manipulation at the wall are presented in chapter 4, followed by conclusions and a general discussion in chapter 5.

CHAPTER 2

ACTIVE CONTROL EXPERIMENTS

Several different control strategies were investigated for the purpose of drag reduction: controls with the normal, spanwise and streamwise velocities, control with selective normal velocity, and control with the sensors at the wall. All numerical experiments were conducted in a fully developed channel flow. Unmanipulated channel flow provided a base for comparison. In the control experiments, all conditions were kept the same as in the unmanipulated simulation except for the boundary conditions through which control strategies were implemented. The skin-friction reduction was measured in terms of the change in the mean pressure gradient necessary to drive the flow with a fixed mass flow rate. Most of the computations were carried out with a coarse grid ($32 \times 65 \times 32$) at $Re_c = 1800$. The use of this coarse grid allowed the exploration of many different strategies for optimum control which would otherwise have required excessive computer resources. To validate the coarse-grid computations, some calculations were performed with a fine grid ($128 \times 129 \times 128$), yielding essentially the same results for low order statistics.

Based on the knowledge that most of the Reynolds stress producing events are associated with streamwise vortices, we explored several strategies with the aim of reducing the strength of the streamwise vortices. A summary of results obtained using different control strategies is presented in the following sections.

2.1 Control with the normal velocity (*v*-control)

The aim of this study was to examine if we can reduce the wall skin friction by suppressing the sweep and ejection events. We applied blowing or suction on the channel walls exactly opposite to the normal component of the velocity at a prescribed y location (see figure 1). At each instant the boundary condition for $v(x, z)$ at the wall was prescribed to be $-v(x, z)$ at y_d , where $y_d(> 0)$ is the distance of the detection point measured from the wall. Thus, when fluid moving toward the wall (sweep) was detected at y_d , an equally strong blowing velocity was imposed at the wall to "cancel" the sweep event. Similarly, when fluid moving away from the wall (ejection) was detected at y_d , an equally strong suction was applied.

The initial condition for the calculations was an instantaneous velocity field from the fully developed channel flow. The mass flux through the channel remained constant since the equation of continuity implies $\int_{L_x} \int_{L_z} v(x, y, z) dx dz = 0$ for any y . Thus, any skin-friction reduction would be manifested in changes in the mean pressure gradient necessary to drive the flow with a fixed mass flow rate. Several computations were performed with the coarse mesh ($32 \times 65 \times 32$) for several different y_d to examine the effect of the location of detection. Using the same initial velocity field, the calculations were continued with the new boundary conditions, until a new statistically steady state was obtained or until it became apparent that the drag would increase substantially.

Figure 2 shows the time histories of the pressure gradients that were required to drive a fixed mass flow rate for an unmanipulated fully developed channel flow and for manipulated channel flows. Substantial skin-friction reduction was obtained ($\approx 25\%$ on each wall) with $y_d^+ \approx 10$. For other y_d^+ locations, either the drag was substantially increased ($y_d^+ \approx 26$) or the reduction was small ($y_d^+ \approx 5$). Note that for the Reynolds number considered, $Re_c = 1800$, the maximum turbulent drag reduction possible is 63% (74% for $Re_c = 3300$), which would correspond to the flow becoming laminar.

The efficiency of the process was measured by estimating the ratio of the power saved ($(-dP/dx|_u + dP/dx|_m) U_m$) to the ideal power input ($p_w v + \rho v^3/2$), where $-dP/dx|_u$ and $-dP/dx|_m$ are mean pressure gradients for the unmanipulated and manipulated channels, respectively, and U_m is the bulk mean velocity. For the case of 25% reduction, the ratio was about 30, indicating that the required ideal power input was negligible. This estimate did not take into account, for example, the valve losses that would be present in practical applications. Finally, it should be pointed out that in-phase control, i.e. $v(x, z)$ at the wall was prescribed to be $v(x, z)$ at y_d , led to a significant drag increase.

We also performed selective control experiments to affect only the strong events. The out-of-phase boundary condition was applied at the surface only when the normal velocity at the sensor location y_d exceeded a threshold value, v_{th} . In comparison to the 25% reduction for $v_{th} = 0$, 20% and 15% reductions were obtained with $v_{th} = v_{rms}$ and $v_{th} = 2v_{rms}$, respectively (figure 3), where v_{rms} is the root-mean-square value of the normal velocity at $y = y_d$. Only 25% and 5%, respectively,

of the total surface area were controlled, indicating that most of the reduction was indeed due to the suppression of the stronger events.

It is known that uniform blowing decreases the skin friction and increases the strength of the fluctuating quantities, but uniform suction has nearly the opposite effect. To investigate which part of the control process, i.e., blowing or suction, is more effective in achieving the skin-friction reduction, several combinations of blowing/suction strategies were investigated. In the active control simulations, blowing reduces the strength of the fluctuating quantities as well as the skin friction. The amount of the skin-friction reduction by active blowing is larger than that by uniform blowing when the mean value of active blowing is the same as the magnitude of uniform blowing. Active suction increases the skin friction less than uniform suction does, but significantly stabilizes the flow.

Other numerical experiments, such as control of a selective bandwidth of the streamwise and spanwise wave lengths, control with sensor locations at a fixed y^+ instead of y , control applied to only a portion of the surface area, and control on only one channel wall, were conducted. The most significant result among selective controls based on wave lengths was that up to 10% drag reduction was obtained by applying the control to only one streamwise Fourier coefficient corresponding to the largest wave length ($k_x = 0.5$) and all the spanwise waves. Control with sensor locations at a fixed y^+ gave the same skin-friction reduction as control with a sensor location at a fixed y . In the case of fixed y^+ control, the distance of the sensors from the wall moves in the normal direction, because the control changes the value of the mean wall-shear velocity. Control was also applied to only a portion of the surface area. Half and quarter stripped walls were exposed to a control input velocity. Skin-friction reduction was proportional to the surface area being controlled. In order to investigate whether the control at one wall affects the skin-friction at the other wall, control was applied to only one wall. The skin-friction reduction on the manipulated wall was identical to that obtained on one wall when control was applied at both walls, and the value of the skin-friction on the unmanipulated wall was the same as that of the natural channel flow.

2.2 Control with the spanwise velocity (w -control)

Noting that streamwise vortices lead to strong spanwise velocity as well as normal velocity, the out-of-phase boundary condition was applied to the spanwise velocity at the surface (figure 4). Several sensor locations ranging from $y_d^+ = 5$ to 25 were tested, and the best result was obtained with $y_d^+ = 10$ yielding about 30% drag reduction (figure 5), slightly better than the optimum v -control. With $y_d^+ > 20$ the drag was increased. In-phase control of the spanwise velocity gave a significant increase of drag.

2.3 Combined control (v - and w -control)

The out-of-phase boundary condition was applied to both v and w at the surface, which corresponds to blowing and suction with different angles to the wall (figure 6). This combined control yielded 30% reduction (figure 7) which is nearly the same as in the w -control. In some cases, depending upon the initial field, the combined control was so effective that the flow became laminar. The laminarization is probably due to the low Reynolds number of the simulation (below the critical value) and probably would not occur at high Reynolds numbers.

2.4 Control with the streamwise velocity (u -control)

Since the skin friction is directly related to the streamwise velocity near the wall, we could affect the drag by modifying the streamwise velocity near the wall through a " u -control" scheme. The out-of-phase u -control with $y_d^+ = 10$ actually resulted in an increase, while the in-phase control (that is, the velocity at the surface has the same sign as that at the sensor location) gave about 10% reduction (figure 8). This is an expected result since the in-phase control reduces $\partial u' / \partial y$ at the wall while the out-of-phase control increases the streamwise velocity gradient at the wall. However, it is rather surprising that we can not do better than 10% reduction with u -control while up to 30% drag reduction was achieved with transverse velocity controls.

2.5 Control with the sensors at the wall

Although the control algorithms described above were successful in reducing the drag, they are not feasible for practical implementation. Among other things, it is not practical to place sensors within the flow field. We, therefore, investigated the possibility of using flow variables at the wall for detection of structures above the wall.

Probability density functions were used to examine the relationship between the wall variables and the flow above the wall. Three different wall variables – wall pressure, streamwise wall-velocity gradient $\partial u / \partial y|_w$, and a quantity derived from the Taylor series expansion of the normal velocity component about the wall – were examined to determine to what extent one can reproduce the v -control experiment by placing sensors only *at* the wall.

The joint probability density functions of the wall pressure and the normal velocity at different y -locations did not reveal any particular correlations (figure 9), indicating that wall pressure alone is not an adequate detector of the flow toward the wall or away from it. One may wonder whether the downstream wall pressure is more appropriate to detect the normal velocity above the wall because the representative flow pattern around high pressure fluctuations at the wall is that of upstream inrush of high speed fluid impinging on the wall followed by the ejection of low speed fluid downstream (Moin, Kim & Choi 1989). However, the joint probability density function of the wall pressure and the upstream normal velocity showed only a little improvement in the correlation.

The joint probability density function of $v(y^+ \approx 10)$ and $\partial u / \partial y|_w$ is shown in figure 10. The streamwise velocity derivative at the wall appears to be a better detector of the events at $y^+ \approx 10$ than the pressure; in particular, high amplitude positive values of $\partial u / \partial y|_w$ are likely to be associated with sweeps. Negative values of $\partial u / \partial y|_w$, however, do not provide adequate discrimination between sweeps and ejections.

The leading term in the Taylor series expansion of v near the wall is

$$v(y) = \frac{y^2}{2} \frac{\partial^2 v}{\partial y^2} \Big|_w + \dots$$

From the continuity equation, one can deduce the equivalent relationship

$$v(y) = -\frac{y^2}{2} \left[\frac{\partial}{\partial x} \frac{\partial u}{\partial y} \Big|_w + \frac{\partial}{\partial z} \frac{\partial w}{\partial y} \Big|_w \right] + \dots \quad (2.1)$$

Our numerical tests have shown that the correlation of the first term in the bracket with $v(y^+ \approx 10)$ is negligible. The joint probability density of v at $y^+ \approx 10$ and $g_w = \frac{\partial}{\partial z} \frac{\partial w}{\partial y} \Big|_w$ (figure 11) indicates a high correlation between the two variables, suggesting that g_w could be a good candidate for the surface detection criterion.

A v -control experiment based on g_w yielded only about 6% reduction of drag (figure 12). For the w -control experiments, we used $\frac{\partial w}{\partial y} \Big|_w$ as the detection criterion, because it is a first leading order term in the Taylor series expansion of the spanwise velocity component about the wall, and obtained essentially the same result. These results were rather disappointing considering that passive control of turbulence with surface riblets can yield about the same drag reduction.

2.6 Active control based on optimal control theory

The control algorithms described above were successful in reducing the drag. However, the control strategy used does not have a rigorous theoretical foundation. In this section we investigate control of turbulent boundary layers by placing sensors at the wall using *optimal control theory*.

Abergel & Temam (1990) addressed the problem of minimizing turbulence fluctuations from the point of view of optimal control theory. Following their procedures, we obtain a first-order optimality condition for the specific cost function $J(\phi)$,

$$J(\phi) = \int_0^T \int_x \int_z \frac{1}{4} \left[\left(\frac{\partial u}{\partial y} \right)_w^2 + \left(\frac{\partial w}{\partial y} \right)_w^2 \right] dz dx dt + \frac{\alpha}{2} \int_0^T \int_x \int_z \phi^2 dz dx dt, \quad (2.2)$$

where T is the control time, α is an arbitrary constant, and ϕ is the input normal velocity at the wall. The subscript w indicates the value at the wall. The quantity inside the bracket is the square magnitude of the instantaneous shear rates at the

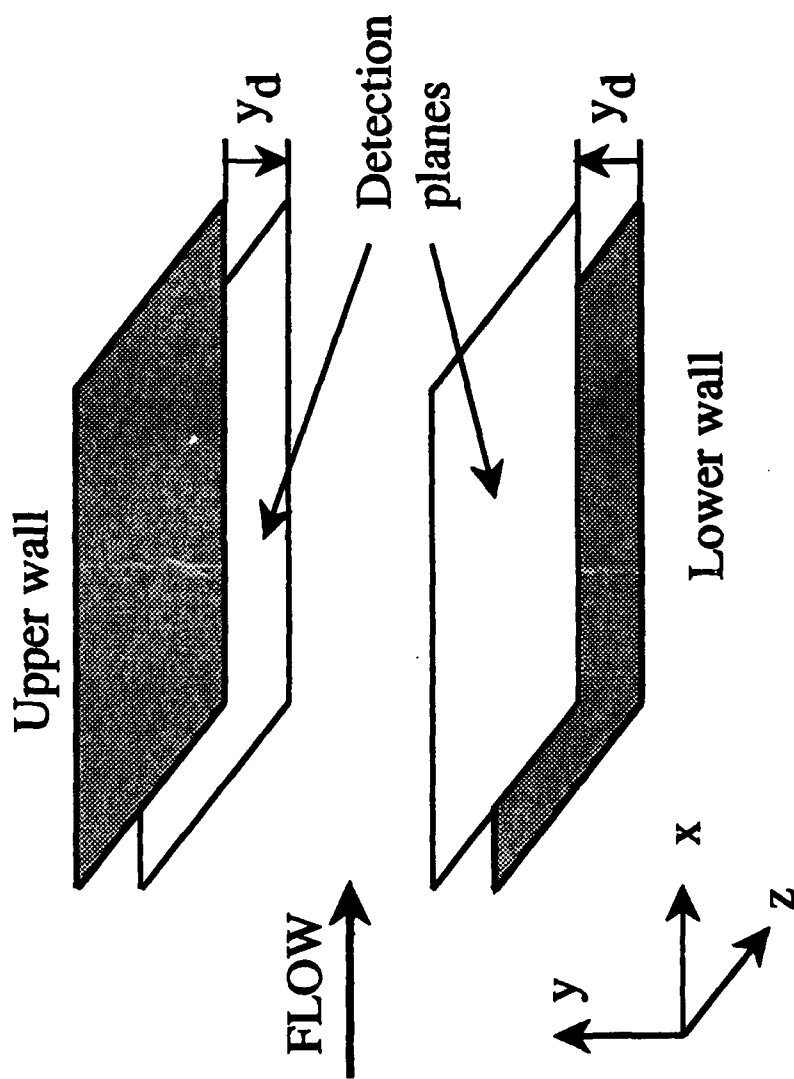
wall. Note that this quantity does not exactly represent the drag at the wall. More cost functions including the square of the drag are discussed in appendix A.

The first-order optimality condition minimizing J gives the relation (see appendix A),

$$\bar{\phi} = \frac{1}{2\alpha} \left[\frac{\partial}{\partial x} \frac{\partial \bar{u}}{\partial y} \Big|_w + \frac{\partial}{\partial z} \frac{\partial \bar{w}}{\partial y} \Big|_w \right] + \frac{Re}{\alpha} \bar{p}'_l \Big|_w, \quad (2.3)$$

where overbar indicates the optimal pair ($\bar{u}_i, \bar{v}_w = \bar{\phi}$), and \bar{p}'_l is the fluctuating part of linearized adjoint pressure.

The first term of the control input velocity ϕ is exactly the same as in section 2.5 (equation (2.1)), which was obtained from the Taylor series expansion of the normal velocity component about the wall. A control experiment based on this function (the first term of equation (2.3)) yielded about 6% drag reduction. The inclusion of the linearized adjoint wall pressure (the second term of equation (2.3)) into the control input velocity should give a higher drag reduction. However, the application of this optimal control algorithm to unsteady three dimensional Navier-Stokes equations is not practical due to the great complexity of the algorithm; one has to *iteratively* solve the linearized adjoint Navier-Stokes equations as well as the Navier-Stokes equations (Abergel & Temam 1990). The detailed procedure for obtaining equation (2.3) is described in appendix A.



(a)

FIGURE 1. For caption see the following page.

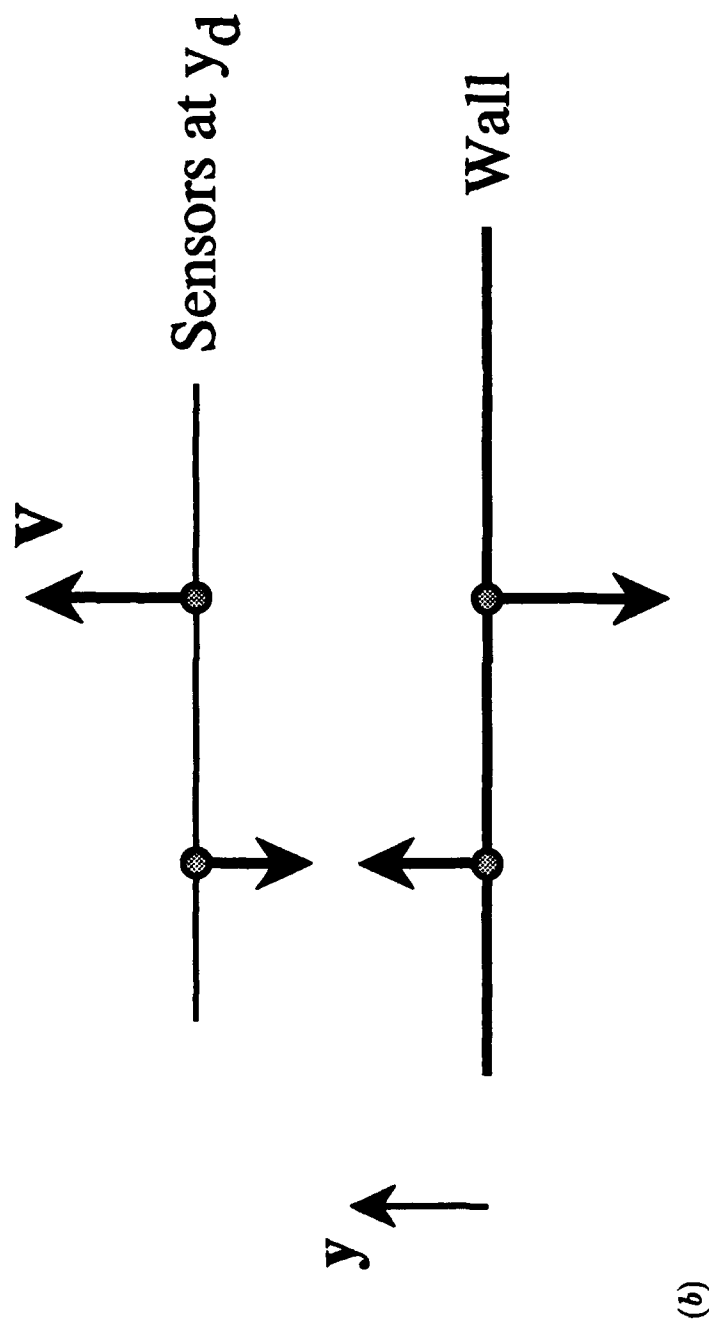


FIGURE 1. (a) Three dimensional view of detection planes; (b) schematic diagram of out-of-phase v -control.

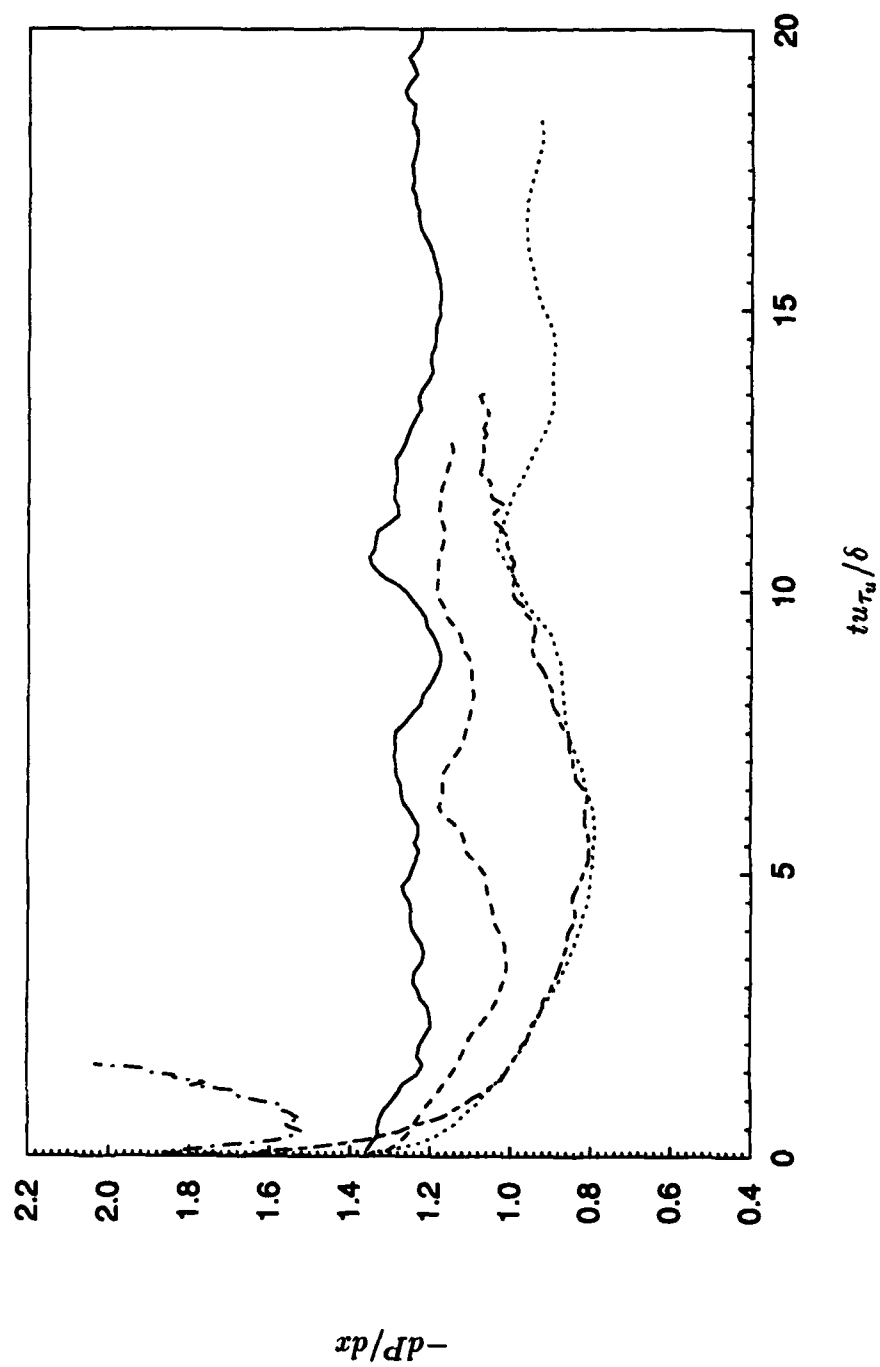


FIGURE 2. Time history of the pressure gradient required to drive a fixed mass flow rate in the case of v -control: —, unmanipulated channel; ----, manipulated channel with sensors at $y_d^+ \approx 10$; , $y_d^+ \approx 20$; -.-.-, $y_d^+ \approx 26$.

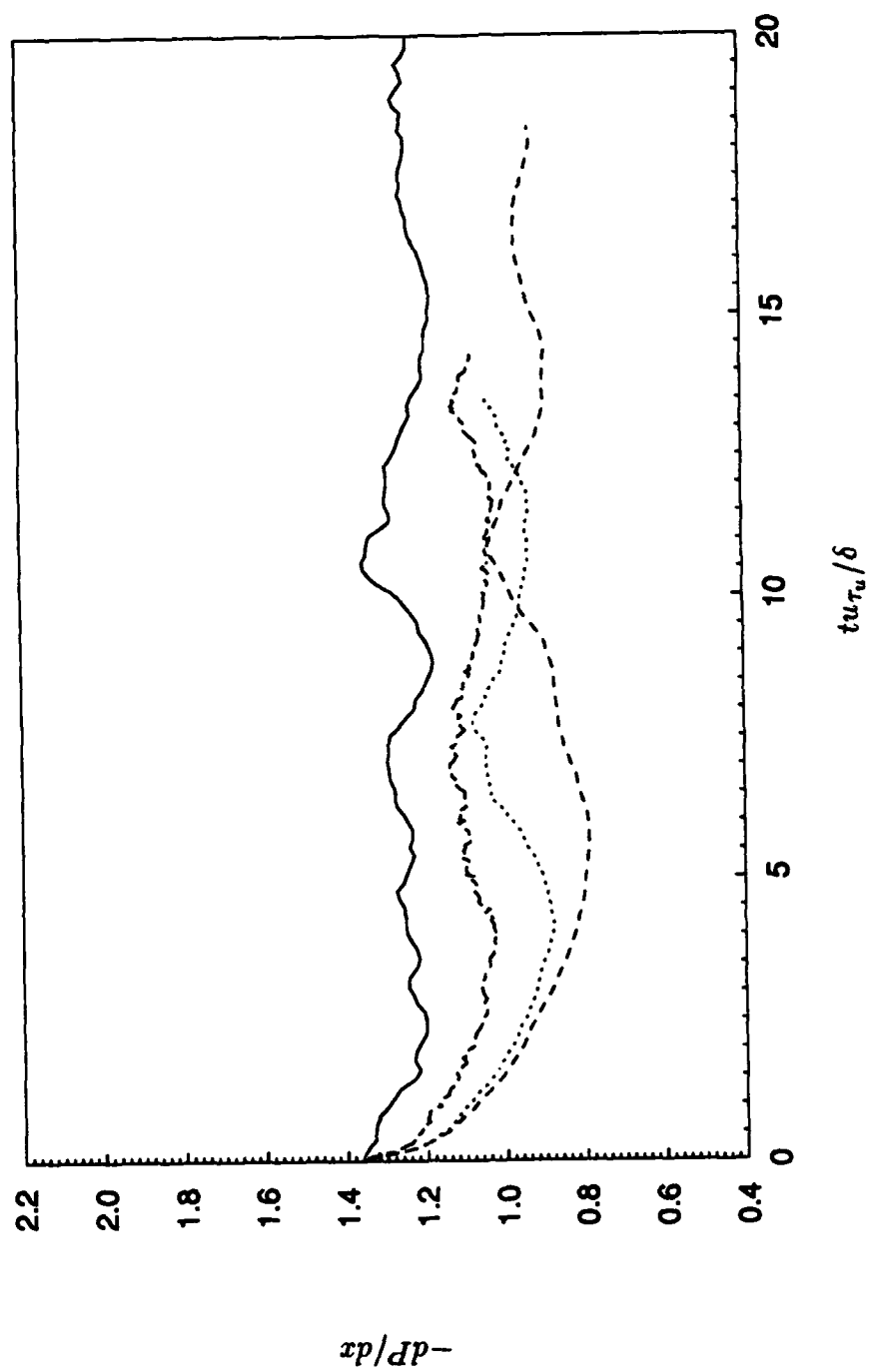


FIGURE 3. Time history of the pressure gradient required to drive a fixed mass flow rate: —, unmanipulated channel; ----, manipulated channel at the sensor location $y_d^+ \approx 10$ exceeded a threshold value $v_{th} = 0$; , $v_{th} = v_{rms}$; - · - · , $v_{th} = 2v_{rms}$.

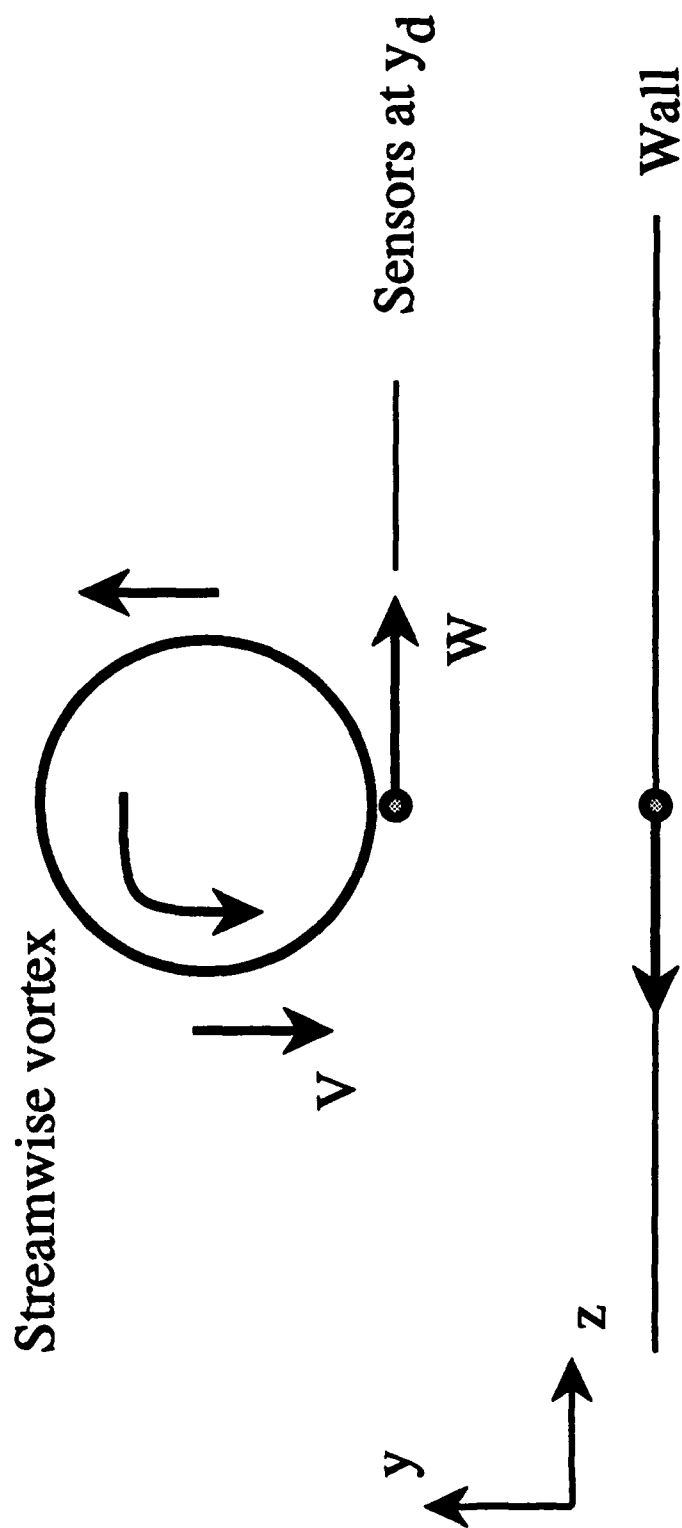


FIGURE 4. Schematic diagram of out-of-phase w -control.

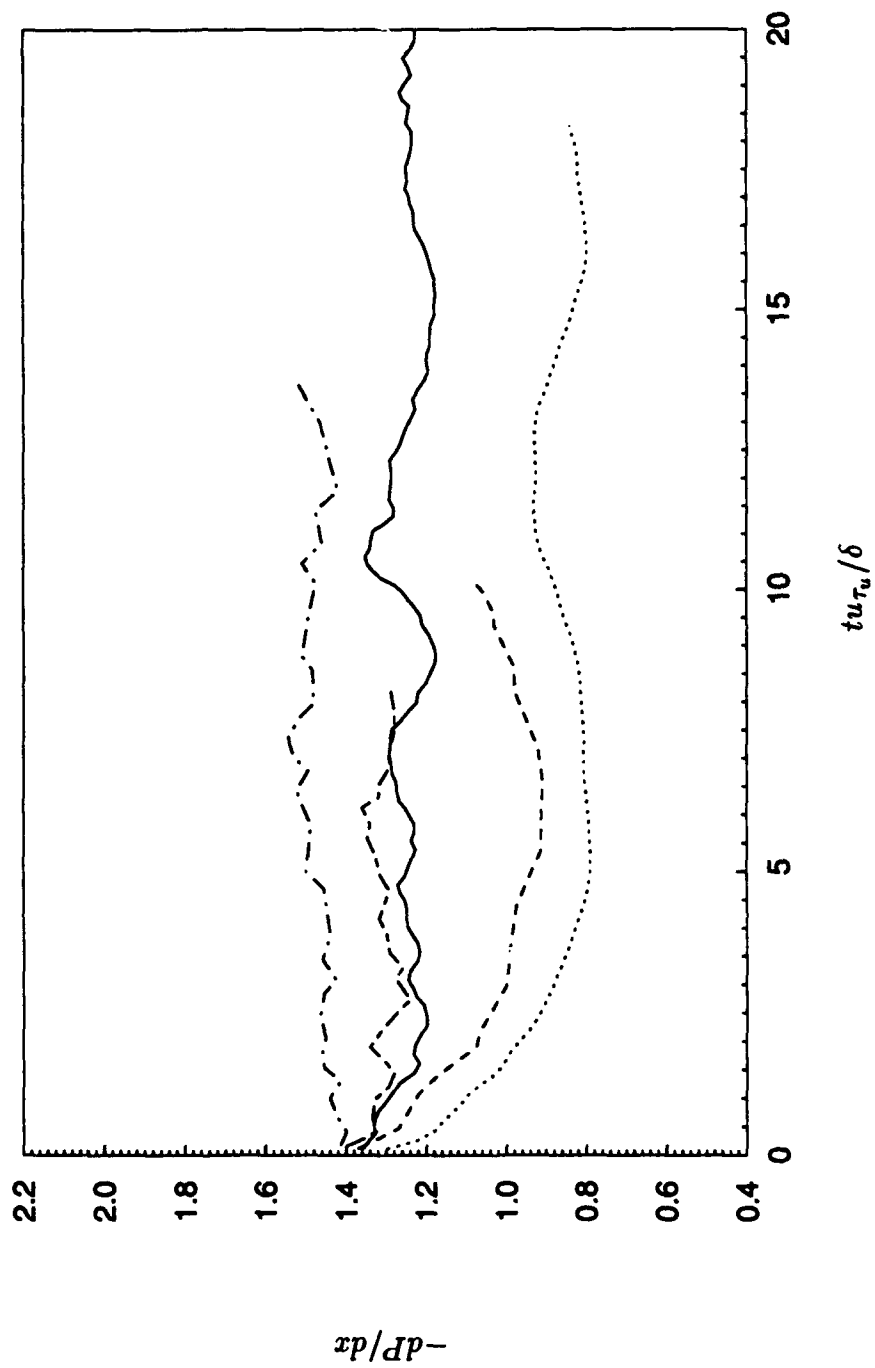


FIGURE 5. Time history of the pressure gradient required to drive a fixed mass flow rate in the case of w -control:
 —, unmanipulated channel; ---, manipulated channel with sensors at $y_d^+ \approx 5$; , $y_d^+ \approx 10$; ----, $y_d^+ \approx 20$;
 ----, $y_d^+ \approx 26$.

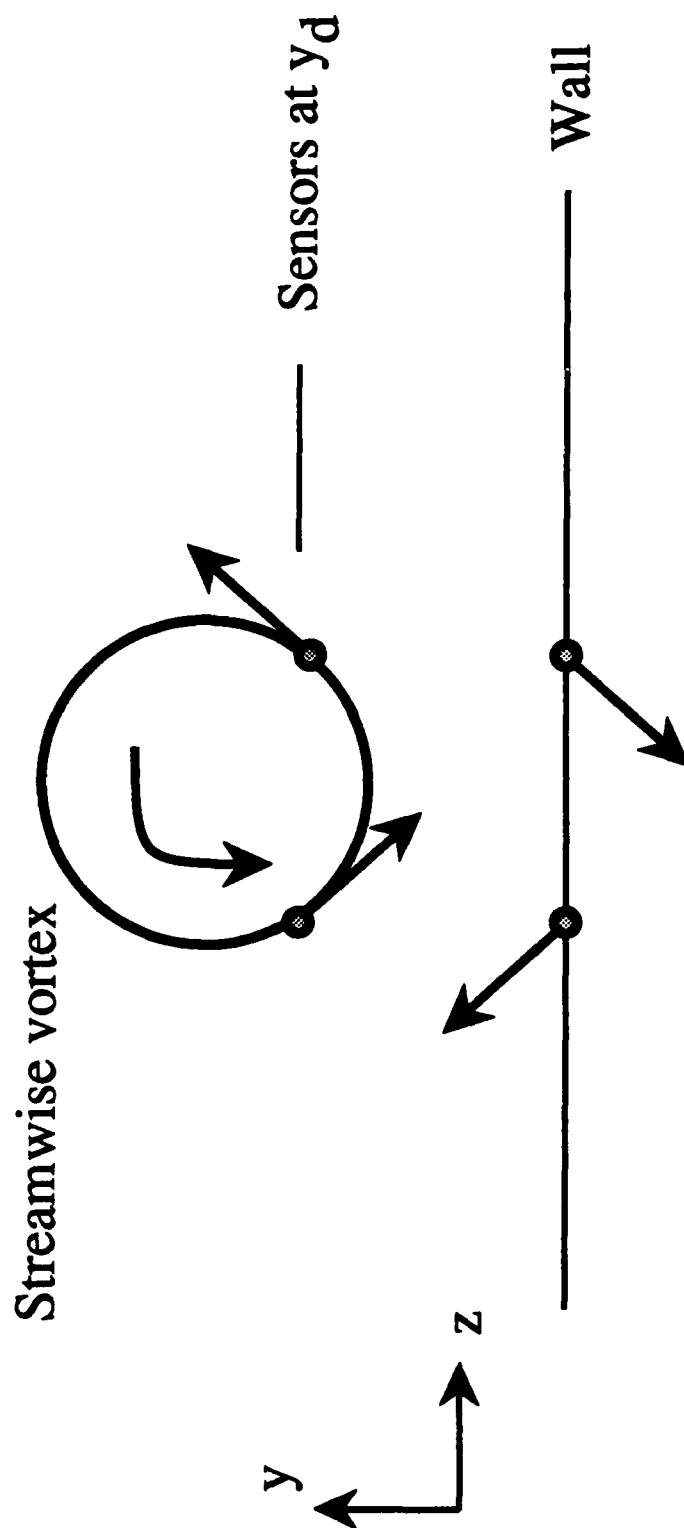


FIGURE 6. Schematic diagram of combined control.

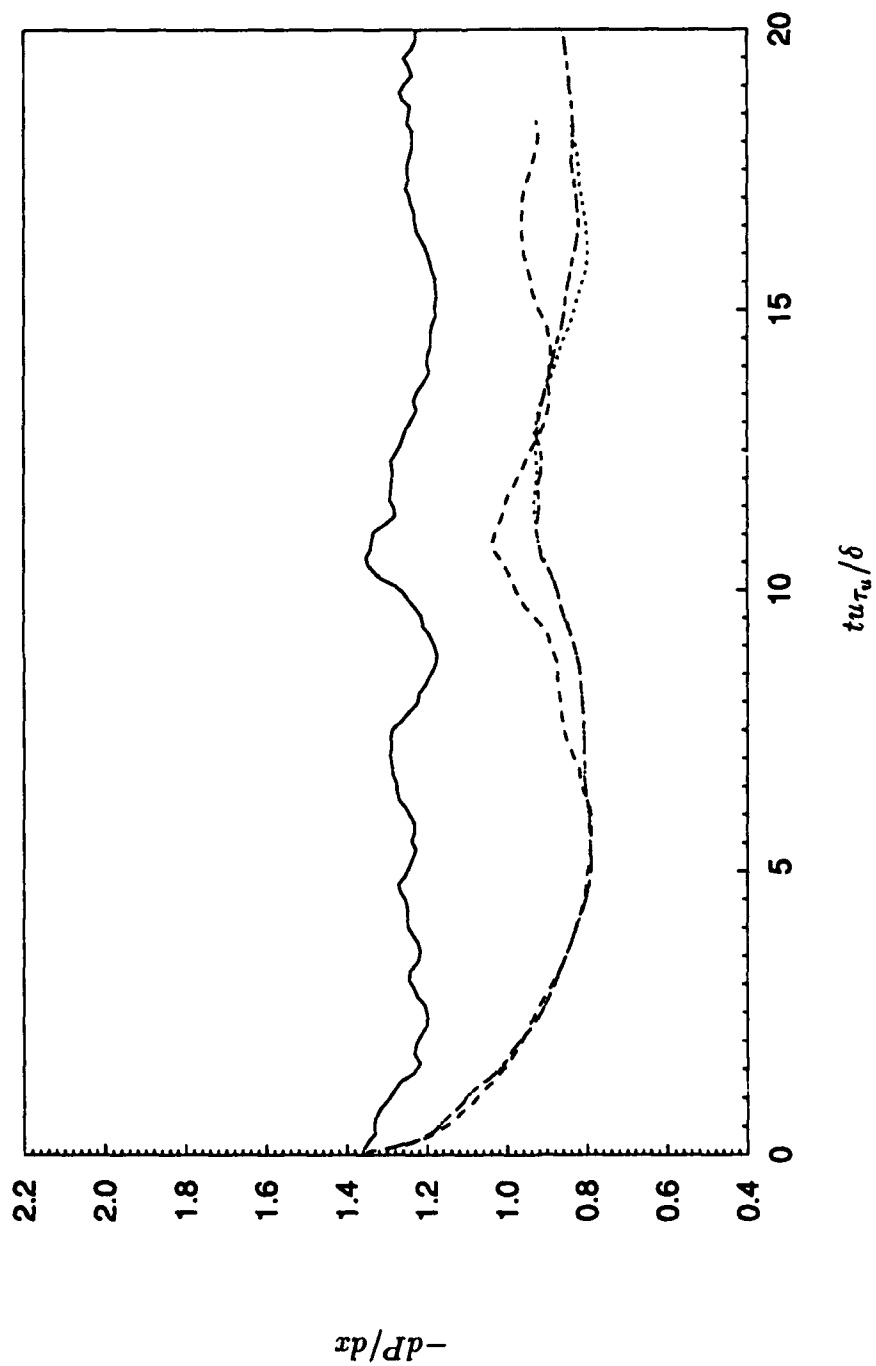


FIGURE 7. Time history of the pressure gradient required to drive a fixed mass flow rate: —, unmanipulated channel; ---, manipulated channel at the sensor location $y_d^+ \approx 10$ in the case of v -control; ·····, w -control; -·-·-, combined control.

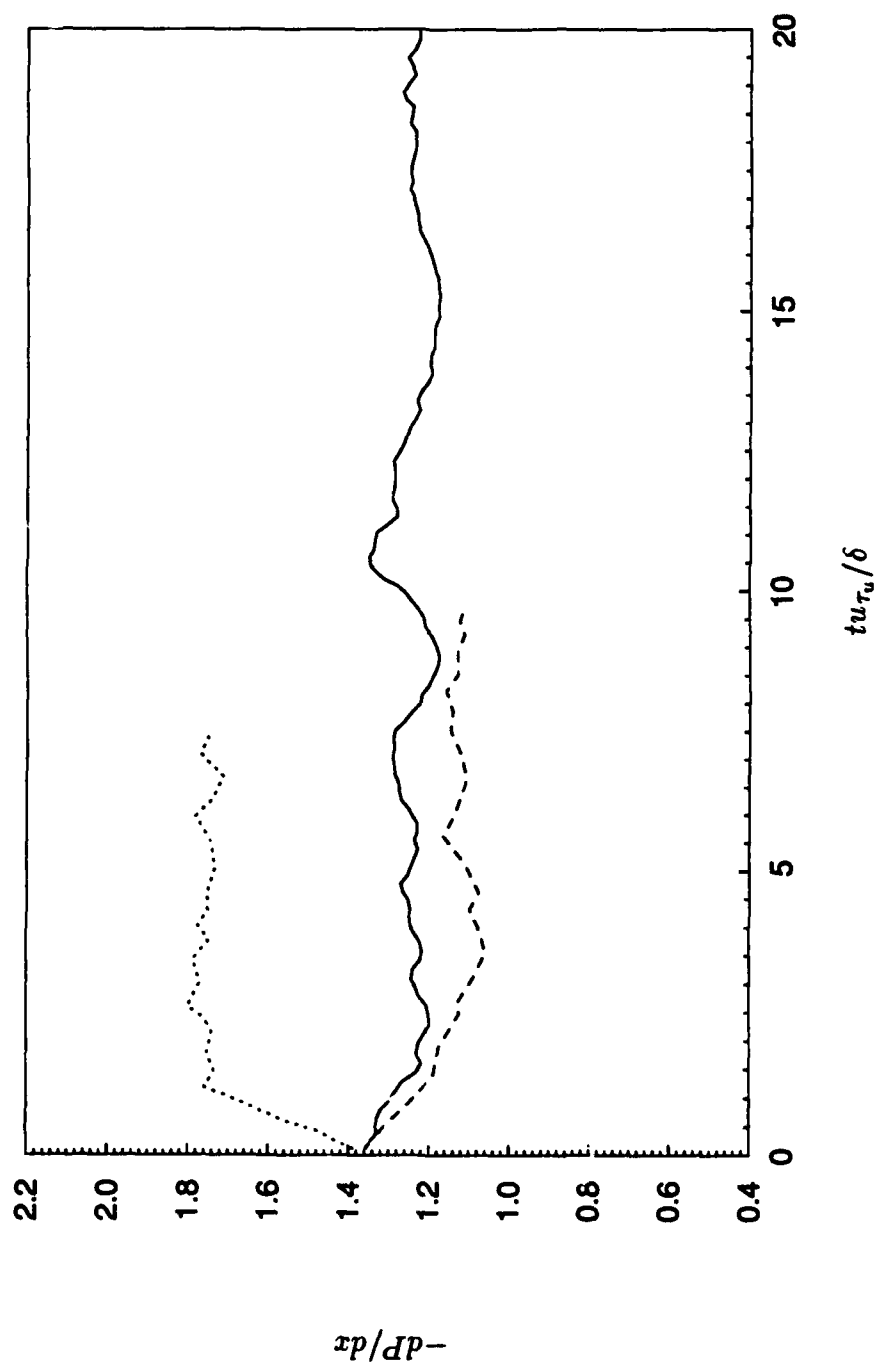


FIGURE 8. Time history of the pressure gradient required to drive a fixed mass flow rate in the case of u -control: —, unmanipulated channel; ---, in-phase with u' at the sensor location $y_d^+ \approx 10$; , 180° out-of-phase.

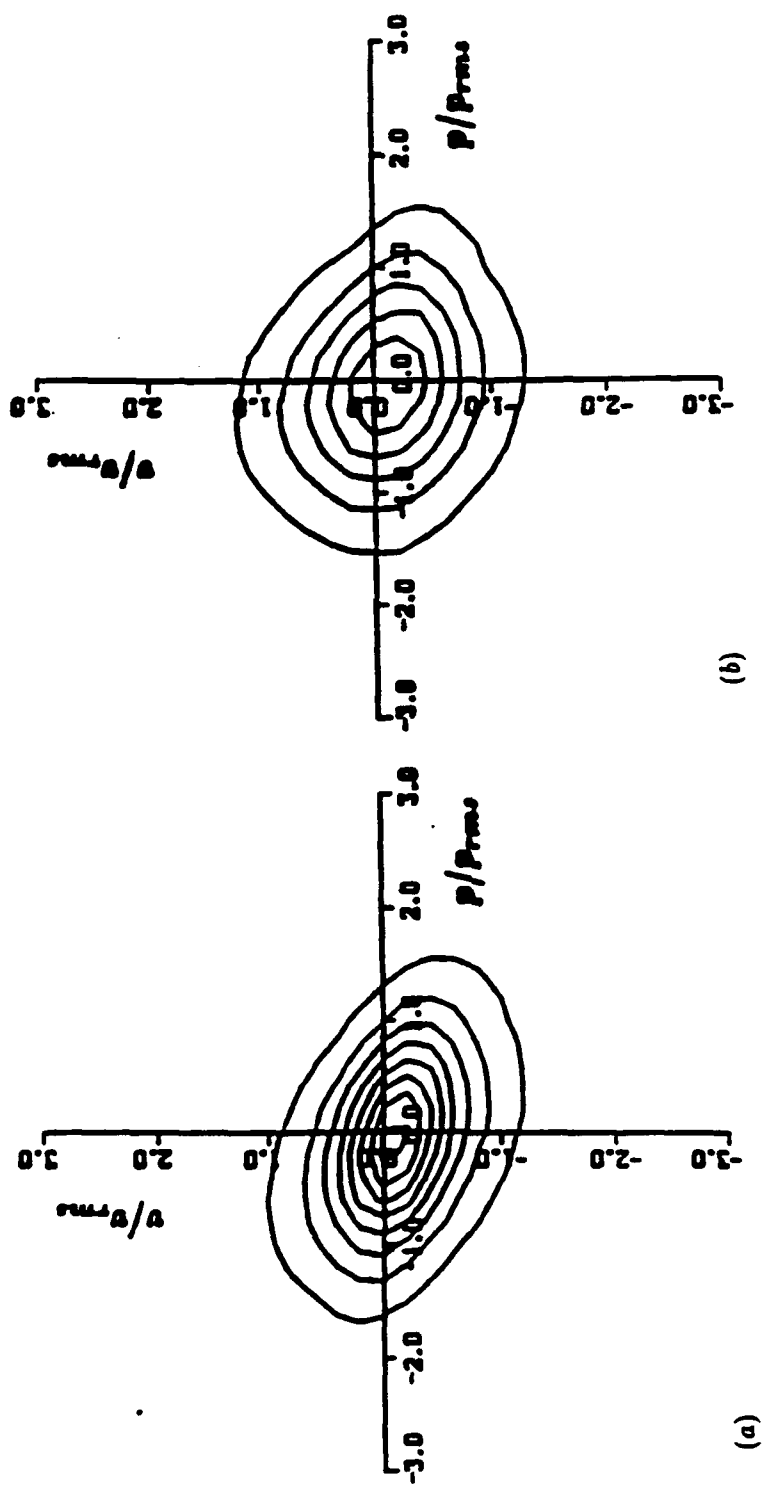


FIGURE 9. Joint probability density of the wall pressure fluctuations and the normal velocity at (a) $y^+ = 0.2$; (b) $y^+ \approx 10$. The value of the outer contour in each plot is 0.05, and the increment is 0.05.

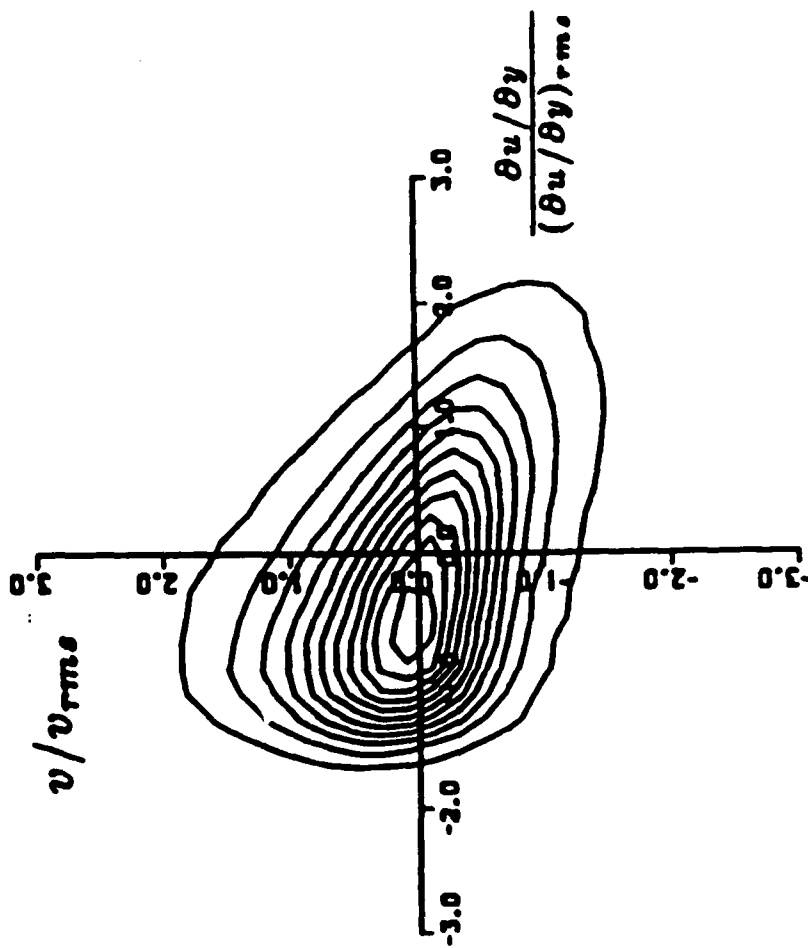


FIGURE 10. Joint probability density of the fluctuating wall-shear rate and the normal velocity at $y^+ \approx 10$. The contour levels are from 0.025 to 0.275 by increments of 0.025.

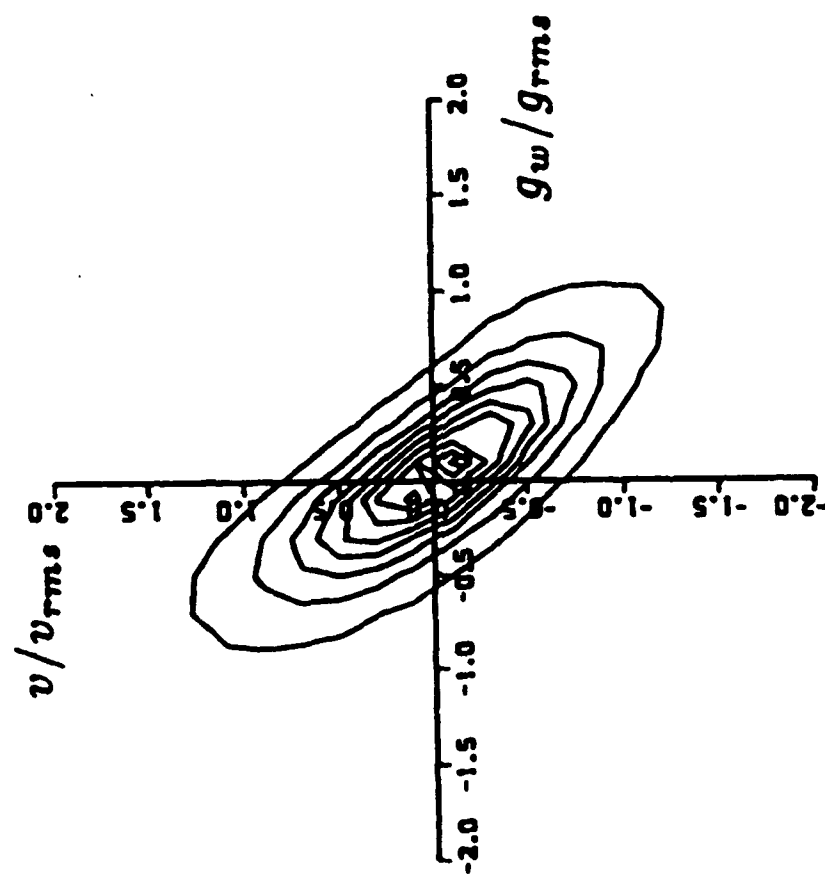


FIGURE 11. Joint probability density of g_w and the normal velocity at $y^+ \approx 10$. The contour levels are from 0.125 to 0.875 by increments of 0.125.

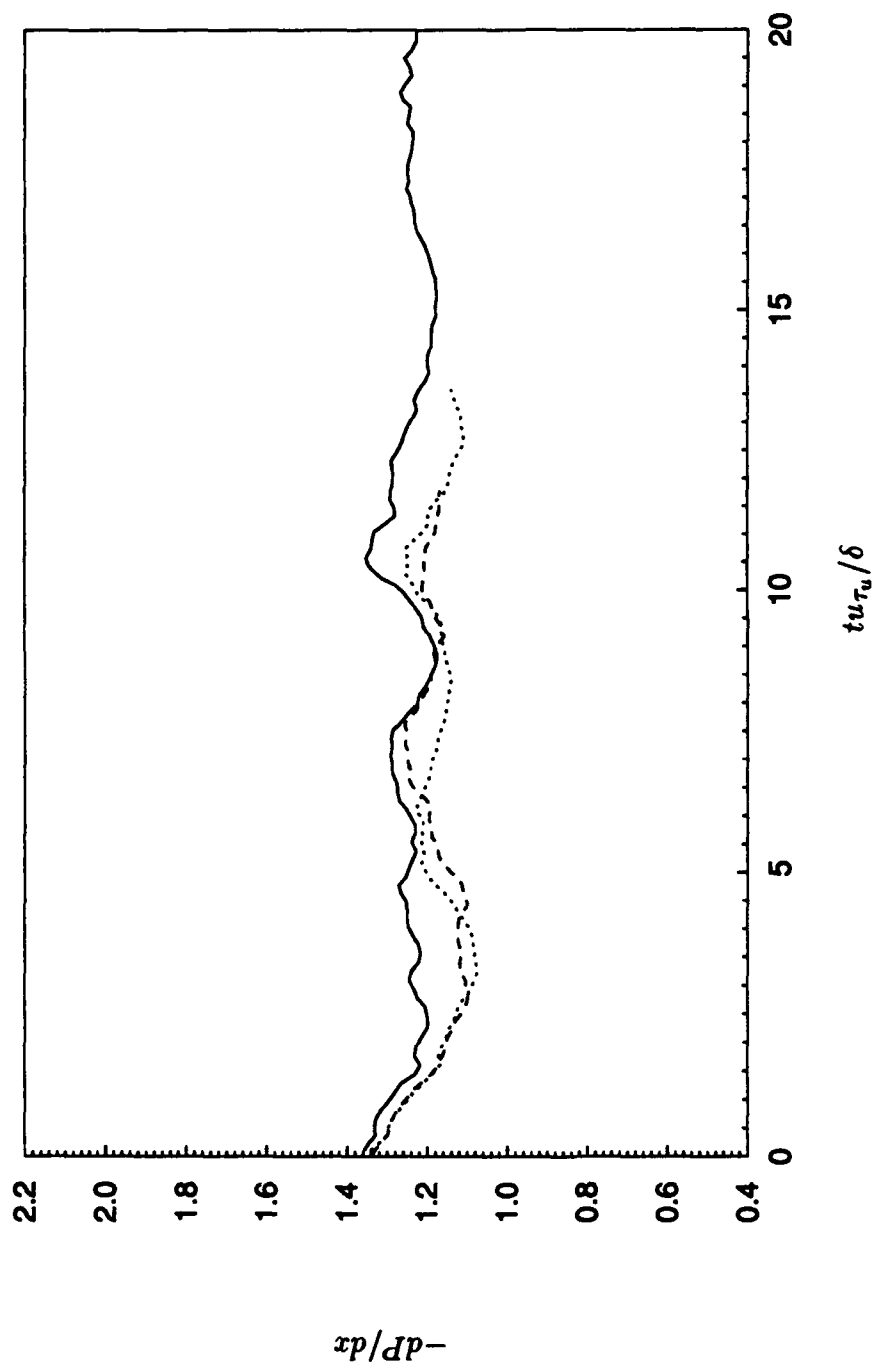


FIGURE 12. Time history of the pressure gradient required to drive a fixed mass flow rate: —, unmanipulated channel; ----, v -control with sensing g at the wall; ·····, w -control with sensing $\partial w / \partial y$ at the wall.

CHAPTER 3

TURBULENCE STATISTICS OF MANIPULATED CHANNEL FLOWS

Some key features of the flow fields obtained using v - and w -control schemes were studied to examine differences between manipulated and unmanipulated channel flows. Using the optimum y_d^+ location found with the coarse mesh, we performed computations for detailed analysis of the modified flow fields for the case of $y_d^+ \approx 10$, using $128 \times 129 \times 128$ spectral modes for $Re_c = 3300$ based on the centerline velocity of the unmanipulated channel and the channel half-width.

The statistically steady states of the manipulated channel flows were identified by the linear profile of total shear stress, $-\overline{u'v'} + (1/Re_c)\partial\bar{u}/\partial y$, and by a quasi-periodic behavior of the horizontally averaged wall-shear rate. Statistics reported here were averaged only over planes parallel to the wall. Therefore, some statistical fluctuations are expected to be present.

The statistics of the manipulated channel flows were compared to those of the unmanipulated channel flow (Kim *et al.* 1987). All velocity and length scales are normalized by either the unmanipulated wall-shear velocity u_{τ_u} , or the local wall-shear velocity u_τ , and the channel half-width δ , where u_τ is u_{τ_u} for the unmanipulated channel and u_{τ_m} for the manipulated channel. The wall coordinate y^+ was obtained using local wall-shear velocity u_τ unless otherwise indicated. The Reynolds number based on the local wall-shear velocity u_τ and channel half-width δ is about 155 for the manipulated channel flows, and 180 for the unmanipulated channel flow. The Reynolds number based on the bulk mean velocity and the channel width is constant ($Re_m \approx 5600$) regardless of the control because the mass flow rate is kept constant through the computations. In this study, an overbar indicates an average over x and z , and a prime indicates perturbation from this average.

3.1 Mean properties

The mean-velocity profile normalized by the local wall-shear velocity is shown in figure 13 for both unmanipulated and manipulated channels. The slope of the log-law in the manipulated channel remains about the same as that in the unmanipulated channel. However, the intercept of the log-law with $u^+ = y^+$ was increased

from $y^+ \approx 10$ in the unmanipulated channel to $y^+ \approx 15$. This upward shift in the log-law has previously been observed in drag-reduced flows such as large-eddy breakup devices (Bandyopadhyay 1986 and Nguyen *et al.* 1987), riblets (Hooshmand *et al.* 1983, Choi 1989, and PART III of the present study), and polymers (Lumley 1973 and Virk 1975).

The shift in the log-law may be considered the result of the increase of the viscous sublayer thickness. From the Taylor series expansion,

$$\bar{u}(y) = \frac{\partial \bar{u}}{\partial y}|_w y + \frac{1}{2} \frac{\partial^2 \bar{u}}{\partial y^2}|_w y^2 + O(y^3). \quad (3.1)$$

Using the streamwise momentum equation and $\partial u/\partial x = \partial u/\partial z = 0$ at the wall, equation (3.1) can be recast in terms of wall variables as follows

$$u^+ = y^+ - \frac{1}{2Re_\tau} \left(\frac{\delta}{u_\tau^2} \right) \left[-\frac{1}{\rho} \frac{dP}{dx} - \overline{v_w \frac{\partial u'}{\partial y}}|_w \right] y^{+2} + O(y^{+3}). \quad (3.2)$$

where $u^+ = \bar{u}/u_\tau$, $y^+ = u_\tau y/\nu$, $Re_\tau = u_\tau \delta/\nu$, and $-dP/dx(> 0)$ is the mean pressure gradient. In the case of the unmanipulated channel flow ($v_w = 0$), the departure from the law of the wall ($u^+ = y^+$) is mainly due to the mean pressure gradient. As shown in figure 10, the correlation between v_w ($= -v$ at $y^+ \approx 10$) and $\partial u/\partial y|_w$ is relatively weak; therefore, the magnitude of $\overline{v_w \partial u'/\partial y}|_w$ is much smaller than that of the mean pressure gradient in the case of v -control. In the case of w -control ($v_w = 0$), $\overline{v_w \partial u'/\partial y}|_w = 0$. Thus, again the departure from the law of the wall is mainly due to the mean pressure gradient. The reduction of the coefficient of y^{+2} term is accompanied by the drag (or mean pressure gradient) reduction as a result of the control. Figure 14 shows the limiting behaviors of the mean velocities. The viscous sublayer thickness y_s^+ , in which the law of the wall, $u^+/y^+ \approx 1$, is satisfied, is increased by the control. For the unmanipulated channel, $y_s^+ \approx 5$; for the manipulated channels, $y_s^+ \approx 10$.

Other mean properties, such as the skin-friction coefficient, displacement thickness, and momentum thickness, are shown in table 1. Comparison of these properties with experimental data is documented in Kim *et al.* (1987) for the unmanipulated channel flow. A reduction in the skin-friction coefficient C_f in the controlled

Case	Re_m	Re_c	Re_τ	$\frac{u_\tau}{U_m}^\dagger$	$\frac{U_c}{U_m}$	C_f^\ddagger	δ^*/δ	θ/δ
no control	5600	3300	180	0.064	1.16	8.37×10^{-3}	0.135	0.083
<i>v</i> -control	5600	3300	158	0.057	1.16	6.40×10^{-3}	0.137	0.079
<i>w</i> -control	5600	3300	154	0.055	1.16	6.09×10^{-3}	0.140	0.080

† The bulk mean velocity is defined as $U_m = \frac{1}{2} \int_{-1}^1 \bar{u} d(\frac{y}{\delta})$.

‡ $C_f = \tau_w / \frac{1}{2} \rho U_m^2$.

Table 1. Mean flow variables of the manipulated and unmanipulated channel flows.

cases is evident from table 1. The displacement thickness δ^* is slightly increased, while the momentum thickness θ is slightly decreased. For the case of boundary layer flows, the momentum thickness is directly related to the skin friction at the wall, so that a decrease of the momentum thickness correlates with a reduction in skin-friction (White 1974).

3.2 Turbulence intensities

Turbulence intensities above the manipulated channel walls are shown in figure 15, and they are compared with those above the unmanipulated wall (Kim *et al.* 1987). Turbulence intensities are significantly reduced by the control throughout the channel except very near the wall. The increase of v_{rms} or w_{rms} very near the wall is due to the input control. The changes of turbulence intensities with the active control schemes are in sharp contrast to the results of Kuhn *et al.* (1984) using a compliant surface and Choi (1989) using a longitudinal riblet, in which only local modification in the near-wall region was observed. Normalization of the turbulence intensities and the distance from the wall with the local wall-shear velocity u_τ is shown in figure 15 (b). The major difference among the data sets is the apparent outward shift of the controlled data, suggesting a displaced virtual origin of the boundary layer and a thickened sublayer. The value of the outward shift of the turbulence intensities is approximately 5 wall units, which coincides with the increased viscous sublayer thickness. The structural change of turbulence near the wall will be discussed in detail in chapter 4.

The production and dissipation of the turbulent kinetic energy also show the same trend, indicating that the overall turbulence activity is weakened by the control (figure 16). The locations of the maximum production are at $y^+ \approx 12$ for the

unmanipulated channel and 17 for the manipulated channels, which also correspond to the locations of the maximum streamwise velocity fluctuation.

Figure 17 shows the profile of root-mean-square pressure. The pressure fluctuations are substantially reduced throughout the channel with both control schemes. The reduction of the surface-pressure fluctuation is especially notable since this implies that one can also reduce the structure-generated noise within the turbulent boundary layer simultaneously with the skin friction.

3.3 Reynolds shear stress and quadrant analysis

The Reynolds shear stress, $-\overline{u'v'}$, and the correlation coefficient are shown in figures 18 and 19, respectively. Also shown in figure 18 (a) is the total shear stress, $-\overline{u'v'} + (1/Re_{\tau_u})\partial\bar{u}/\partial y$, where $Re_{\tau_u} = u_{\tau_u}\delta/\nu$ and u_{τ_u} is the wall-shear velocity for the unmanipulated channel flow (table 1). In the fully developed channel flow considered here, this profile should be a straight line when the flow reaches an equilibrium state. The computed result clearly indicates that this is the case. The slope of the total shear stress is reduced by the control schemes. Also, there is a significant reduction in the Reynolds shear stress throughout the channel. There is a noticeable region around $y^+ \approx 5$ in which Reynolds shear stress is nearly zero. Figure 19 illustrates that in the v -control a significant positive correlation between u' and v' occurs very near the wall, and either negative (v -control) or zero (w -control) correlation occurs near $y^+ \approx 5$. The highly positive correlation very near the wall in the v -control is owing to the absence of first- and third- quadrant events (figure 20).

The quadrant analysis of the Reynolds shear stress provides detailed information on the contribution to the total turbulence production from various events occurring in the flow (Kim *et al.* 1987). The second quadrant ($u' < 0$ and $v' > 0$; ejection) and fourth quadrant ($u' > 0$ and $v' < 0$; sweep) events contribute to the positive Reynolds shear stress (positive production), and the first quadrant ($u' > 0$ and $v' > 0$) and third quadrant ($u' < 0$ and $v' < 0$) events contribute to the negative Reynolds shear stress (negative production).

The contribution to the Reynolds shear stress from each quadrant normalized by the wall-shear velocity or the local mean Reynolds shear stress is shown in figure 20. Sums of the values at each position y from the four quadrants in figures 20 (a)

and (b) are equal to the local mean Reynolds shear stress and one, respectively. In the case of unmanipulated channel, the ejection event is dominant away from the wall, and the sweep event is dominant in the wall region; at $y^+ \approx 12$, these contributions are about the same. In the manipulated channels, the Reynolds shear stress from the sweep and ejection events are significantly reduced by both controls (figure 20 (a)). The fractional contribution from each quadrant event shows that there is no noticeable difference above $y^+ \approx 20$ except for an outward shift of the data; at $y^+ \approx 17$ the contributions from the ejection and sweep events are about the same (figure 20 (b)). That is, the active control schemes do not alter the structure of the outer-wall turbulence, but simply attenuate the strength of the turbulence. The fourth quadrant events are most dominant near the wall regardless of the control. A sharp increase in the normalized Reynolds shear stress from each quadrant near $y^+ \approx 5$ and the centerline in figure 20 (b) is owing to the negligible mean Reynolds shear stress at those locations. In the case of v -control, the first- and third- quadrant events are negligible below $y^+ \approx 1$, whereas they are still significant in the case of w -control.

3.4 Vorticity

Vorticity fluctuations are shown in figure 21. All three vorticity fluctuations are substantially reduced throughout the channel with both control schemes. The vorticity fluctuations in wall coordinates are shown in figure 21 (b). The major difference among the data sets is the apparent outward shift of the controlled data, as was discussed in section 3.2. w -control increases the streamwise vorticity fluctuation at the wall while v -control reduces the root-mean-square value as compared with the unmanipulated channel case.

Each component of the vorticity consists of two terms, i.e.

$$\omega_x = \frac{\partial w}{\partial y} - \frac{\partial v}{\partial z}, \quad \omega_y = \frac{\partial u}{\partial z} - \frac{\partial w}{\partial x}, \quad \omega'_z = \frac{\partial v}{\partial x} - \frac{\partial u}{\partial y}.$$

The root-mean-square value of each term of the streamwise, normal and spanwise components is shown in figures 22 - 24, respectively. Regardless of the control schemes, near the wall, ω_x , ω_y and ω'_z are mostly dominated by $\partial w/\partial y$, $\partial u/\partial z$

and $\partial u'/\partial y$, respectively. The contribution of the normal velocity gradient to the magnitude of the streamwise and spanwise vorticities is negligible near the wall.

Since the streamwise vorticity fluctuations are dominated by $\partial w/\partial y$, we experimented with a control scheme which altered the wall spanwise velocity in order to make $\omega_x = \partial w/\partial y = 0$ at the wall. This boundary condition is equivalent to using an in-phase control of the spanwise velocity, matching the sensor location at the grid point nearest to the wall. A significant increase of the skin friction was obtained, and the vorticity fluctuations as well as the velocity fluctuations were increased substantially.

Despite the comparable drag reduction by both control schemes, w -control increases the streamwise vorticity fluctuation at the wall, while v -control reduces the root-mean-square value compared to the unmanipulated channel case (figure 21 (a)). Furthermore, the skin friction is significantly increased with the boundary condition $\omega_x|_w = 0$. Therefore, one may conclude that the secondary streamwise vorticity at the wall does not contribute to the dynamics of near-wall turbulence and may be nothing but the kinematical result of the presence of the primary streamwise vortex due to the no-slip boundary condition. However, this is a rather puzzling deduction because Jiménez & Moin (1991) have demonstrated significant interactions between the primary and secondary vortices. Our control schemes seem to reduce or alter the interaction between the primary vortex and secondary streamwise vorticity at the wall (chapter 4).

3.5 Two-point correlation functions and spectra

Figure 25 shows the one-dimensional spectra of the wall-shear rate fluctuations, $\partial u'/\partial y$, for both control cases. Differences in the spectra of v - and w -control cases are noticeable. In the case of v -control, the power is significantly reduced at the small streamwise wavenumbers, whereas there is little reduction in the moderate and large streamwise wavenumber region. In the case of w -control, however, the power is reduced at all the streamwise wavenumbers. In the small spanwise wavenumber region, the spectra show the reduction for both control schemes. Note that the power reduction at the smallest spanwise wavenumber by the v -control scheme is larger than that by the w -control scheme, as opposed to that for the smallest streamwise wavenumber. In the case of v -control, there is a noticeable

increase in power at the large spanwise wavenumbers, indicating that the characteristic eddy size becomes smaller in the lateral direction. This change does not occur in the w -control; the power is significantly reduced at all the spanwise wavenumbers.

Wall pressure spectra are shown in figure 26. Power is reduced at all wavenumbers except for a negligible increase at large spanwise wavenumbers and a small increase in smallest streamwise wavenumber (v -control) which could be due to an inadequate statistical sample.

Figure 27 shows the energy spectra in the manipulated and unmanipulated channels. At $y^+ \approx 0.2$, the energy spectrum of the streamwise velocity shows the same behavior as discussed for the wall-shear rate. The significant increase of energy in the normal and spanwise velocities at this location is a result of input wall-velocity. However, the energy of each velocity component is reduced at all wavenumbers above $y^+ \approx 5$ (figure 27 (b)).

Two-point correlations of the velocity are shown in figure 28 for both control cases, and are compared with those of the uncontrolled channel flow. The spanwise two-point correlations clearly indicate that the velocity fields are modified in different ways. In the unmanipulated channel, local minimum locations of spanwise two-point correlations of the streamwise and spanwise velocities are nearly identical ($r_z^+|_{min} \approx 50$) below $y^+ \approx 10$, while $r_z^+|_{min} \approx 25$ for the normal velocity component (Kim *et al.* 1987). In both controlled flows, below $y^+ \approx 5$, the streamwise microscale, which is defined by the curvature of the streamwise two-point correlation of u' at $r_x^+ = 0$, is significantly reduced, as compared to that in the uncontrolled flow, indicating that the streaky structure has been annihilated in that region in the manipulated channels. In the case of v -control, the two-point correlation of the streamwise velocity at $y^+ \approx 0.2$ is similar to that of the normal velocity at that location; the structure of the streamwise velocity very near the wall is clearly affected by the action of blowing and suction. Near $y^+ \approx 5$, the qualitative behavior of two-point correlation of u' in the manipulated channels becomes similar to that in the unmanipulated channel.

Two-point correlations of the wall-shear rate and wall pressure are shown in figure 29. The streamwise integral scale of the wall shear-rate fluctuation is significantly reduced by the controls. The two-point correlation of the wall pressure,

however, is changed very little by the control schemes, indicating that the scales of turbulence structure above the viscous sublayer, which strongly influence the wall-pressure fluctuations (Kim 1989), have not been affected much by the control action, even though the strength of the turbulence structure has been reduced significantly throughout the channel (figures 15 and 17).

3.6 Pressure-strain correlation tensor

The profiles of the diagonal elements of the pressure-strain correlation tensor

$$\phi_{ij} = p' \left(\frac{\partial u'_i}{\partial x_j} + \frac{\partial u'_j}{\partial x_i} \right)$$

are shown in figure 30. These terms govern the exchange of energy among the three components of turbulent kinetic energy (Hinze 1975). The negative sign for $\phi_{\kappa\kappa}$ (no summation) indicates loss, or transfer of energy from $\overline{u'^2_\kappa}$ to other components, whereas a positive sign denotes energy gain. In the case of the unmanipulated channel, except in the vicinity of the wall, the streamwise velocity fluctuations transfer energy to the cross-stream velocity components. However, very near the wall, there is a large transfer of energy from the normal component of turbulence intensity to the streamwise and spanwise velocity components. This phenomenon is referred as the *splatting* or impingement effect (Moin & Kim 1982).

In the manipulated channels, the pressure-strain correlations are changed, especially very near the wall ($y^+ < 5$). As a consequence of supplying the control velocity at the wall, we can anticipate that energy is transferred from the input wall-velocity component to other velocity components very near the wall. That is, energy from the normal component is transferred to the streamwise and spanwise components in the v -control, while energy from the spanwise component is transferred to the streamwise and normal components in the w -control. The shape of the pressure-strain terms is little changed except for an apparent thickening of the layer. However, the rate of energy transfer from the normal velocity component to the spanwise component is reduced, indicating that the splatting is considerably weakened by both controls.

3.7 Skewness and flatness factors

The skewness and flatness factors of u' and p' are shown in figure 31. The skewness and flatness factors of all quantities are significantly different from the those for a Gaussian distribution (0 and 3, respectively). The skewness and flatness of the pressure are little changed near the wall. The skewness of u' in the controlled channel is changed only near the wall: with v -control, the streamwise velocity is highly positively-skewed in the vicinity of the wall with abrupt reduction near $y^+ \approx 5$ and follows that of the unmanipulated channel flow further from the wall. However, with w -control, the skewness of u' is only gradually reduced near $y^+ \approx 5$.

The skewness of the normal velocity in the manipulated channels is rather drastically changed. In both control cases, the skewnesses of u' and v' are positive in the region $3 < y^+ < 12$. However, the skewnesses of u' and v' in the unmanipulated channel are positive and negative in this region, respectively. Considering that the Reynolds shear-stress-producing events for $y^+ < 12$ are from the fourth quadrant (sweep) events in the unmanipulated channel, the control schemes apparently prevent the strong sweep events in this region. The skewness factor of the Reynolds shear stress is shown in figure 32. Once again, the effect of controls on the flow structure is limited to the near wall region.

The flatness of u' is significantly increased very near the wall for both controls, while the flatness of v' is considerably reduced. The flatness of v' near $y^+ \approx 5$ shows that the intermittency of the normal velocity in this region is significantly reduced owing to the control. The flatness factors of the Reynolds shear stress in the controlled channels show a highly intermittent character near the wall, which is also seen in the unmanipulated channel.

Figure 33 shows the probability density functions of the wall-shear rate and wall-pressure fluctuations. There is little change in wall pressure data, while the wall-shear rate shows a significant change owing to the controls. The probability density functions of the wall-shear rate show significant reductions in the positive tail and amplifications in the negative tail with both controls.

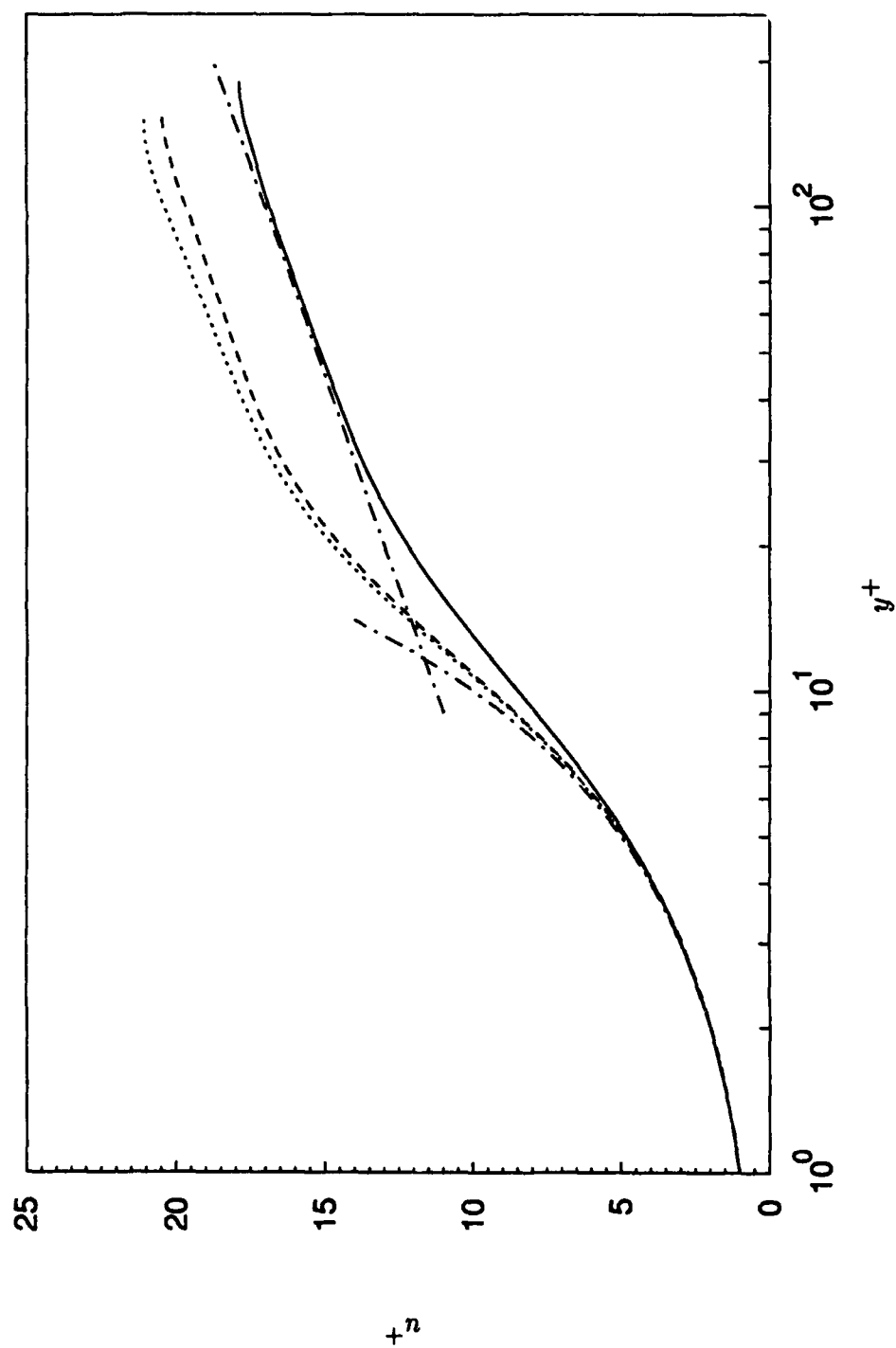


FIGURE 13. Mean-velocity profiles: —, no control; ---, v^+ -control; , w^+ -control; —·—·—, law of the wall ($u^+ = y^+$ and $u^+ = 2.5 \ln y^+ + 5.5$).

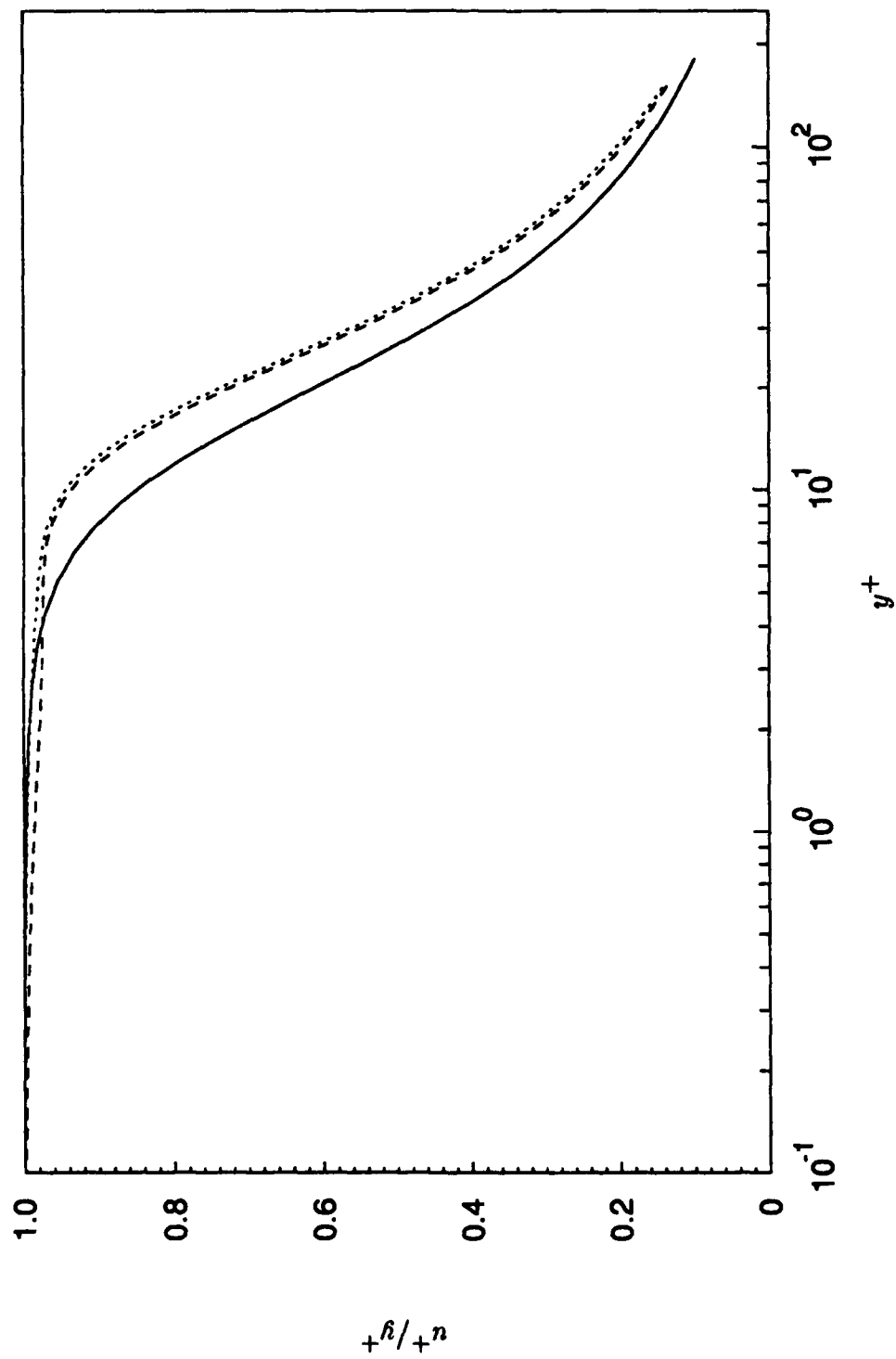


FIGURE 14. Near-wall behavior of the mean velocity: —, no control; ---, v -control; , w -control.

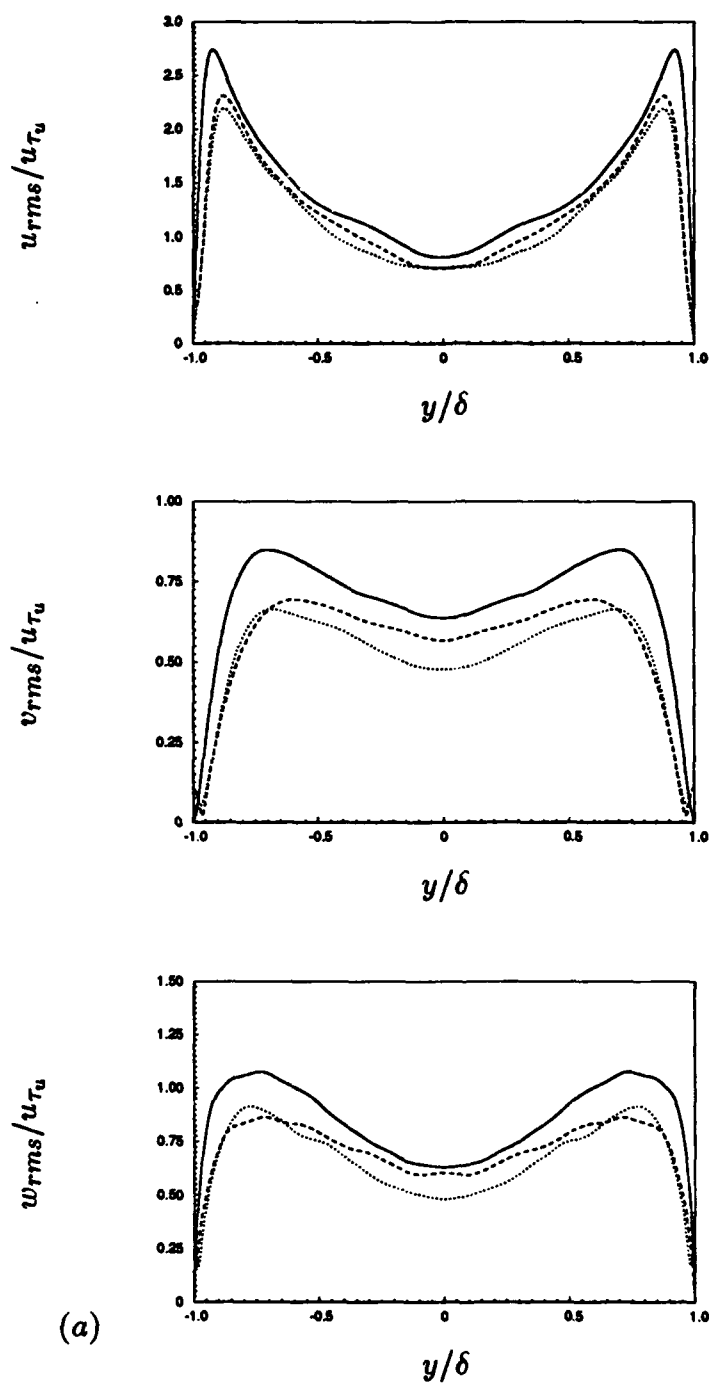


FIGURE 15. For caption see the following page.

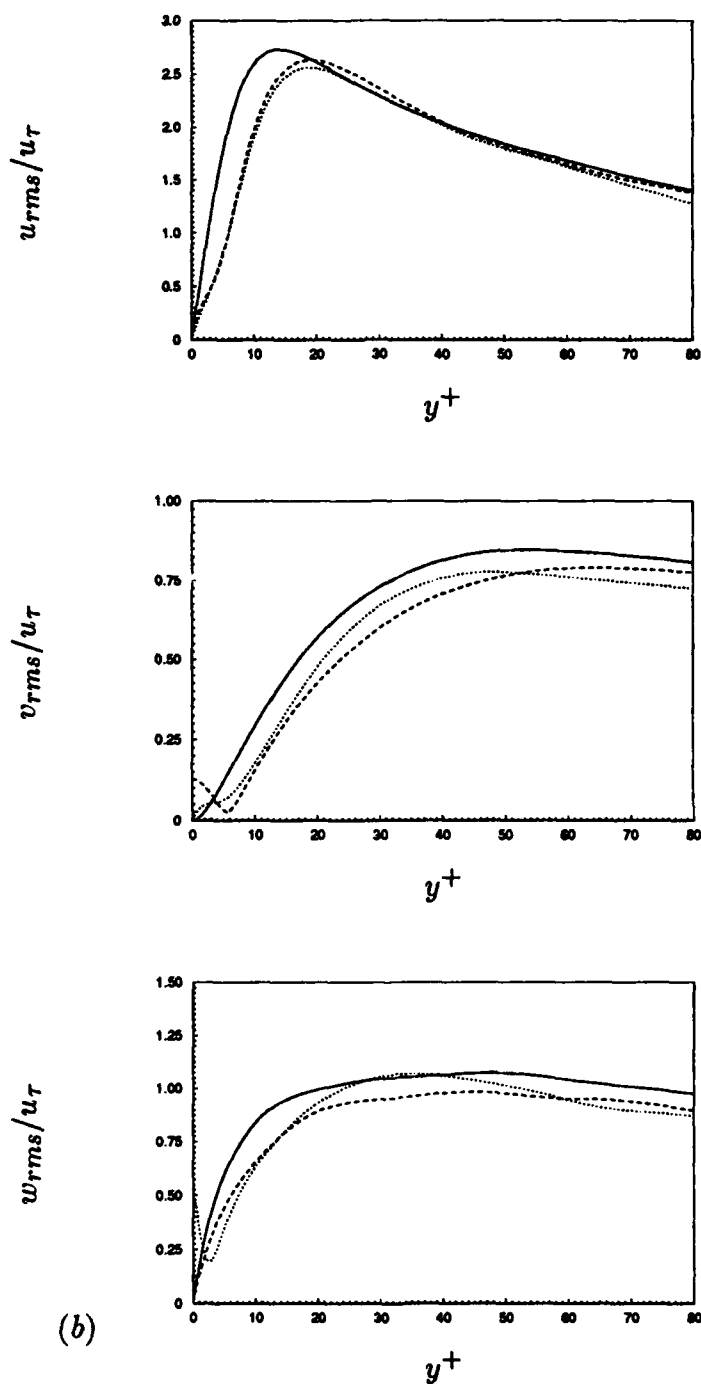


FIGURE 15. Root-mean-square velocity fluctuations normalized by the wall-shear velocity: —, no control; ----, v -control; ·····, w -control. (a) In global coordinates; (b) in wall coordinates. Note that in wall coordinates, u_τ is u_{τ_u} for the unmanipulated wall and u_{τ_m} for the manipulated wall, and $y^+ = yu_\tau/\nu$.

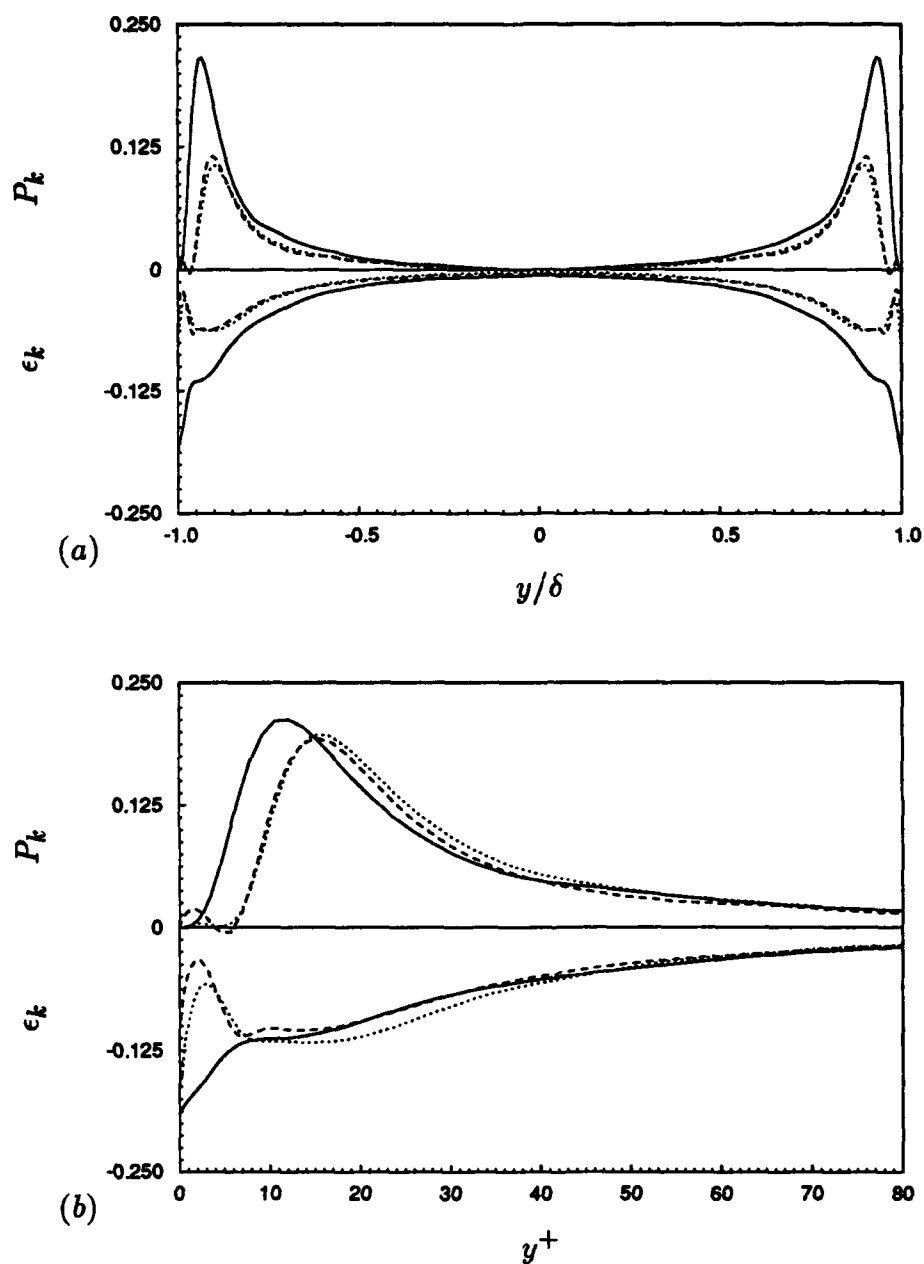


FIGURE 16. Production (P_k) and dissipation (ϵ_k) of the turbulence kinetic energy: —, no control; ---, v -control;, w -control. (a) In global coordinates; (b) in wall coordinates. In wall coordinates, values are non-dimensionalized by the local wall-shear velocity.

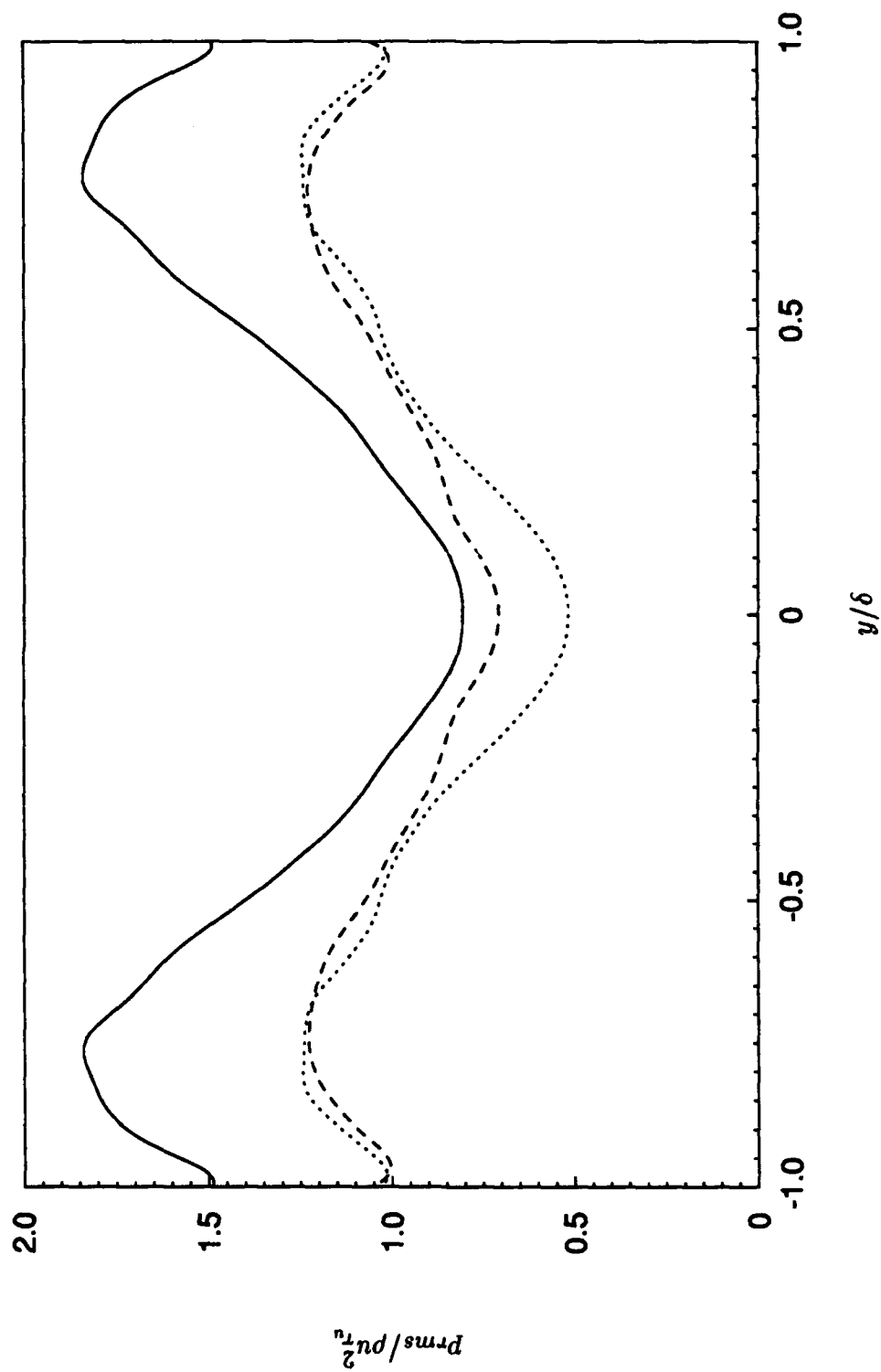


FIGURE 17. Root-mean-square pressure fluctuations normalized by the wall-shear velocity, u_{τ_w} : —, no control; ----, v-control; , w-control.

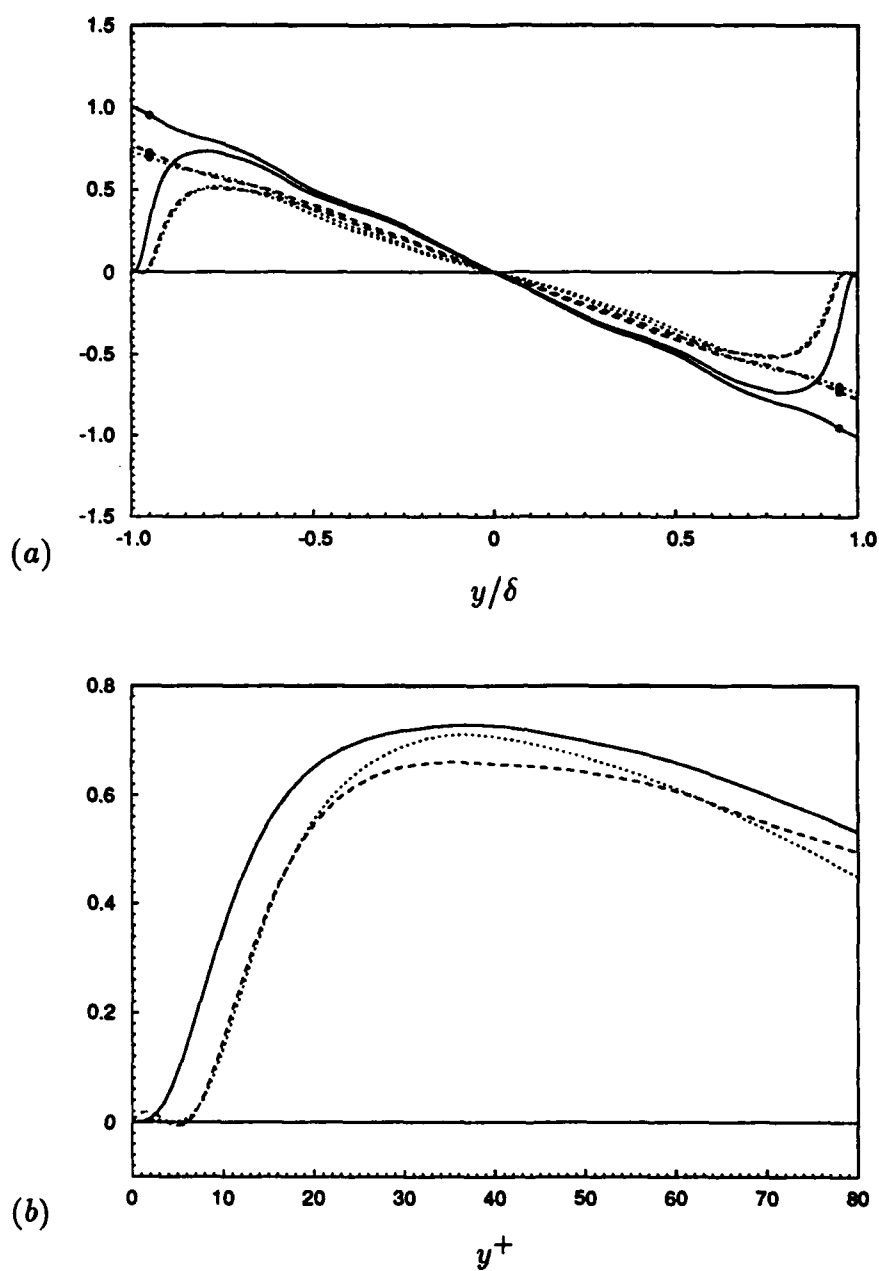


FIGURE 18. Reynolds shear stress (lines) and total shear stress (lines with \bullet) normalized by the wall-shear velocity: —, no control; ---, v -control; , w -control. (a) In global coordinates; (b) in wall coordinates. In wall coordinates, values are non-dimensionalized by the local wall-shear velocity.

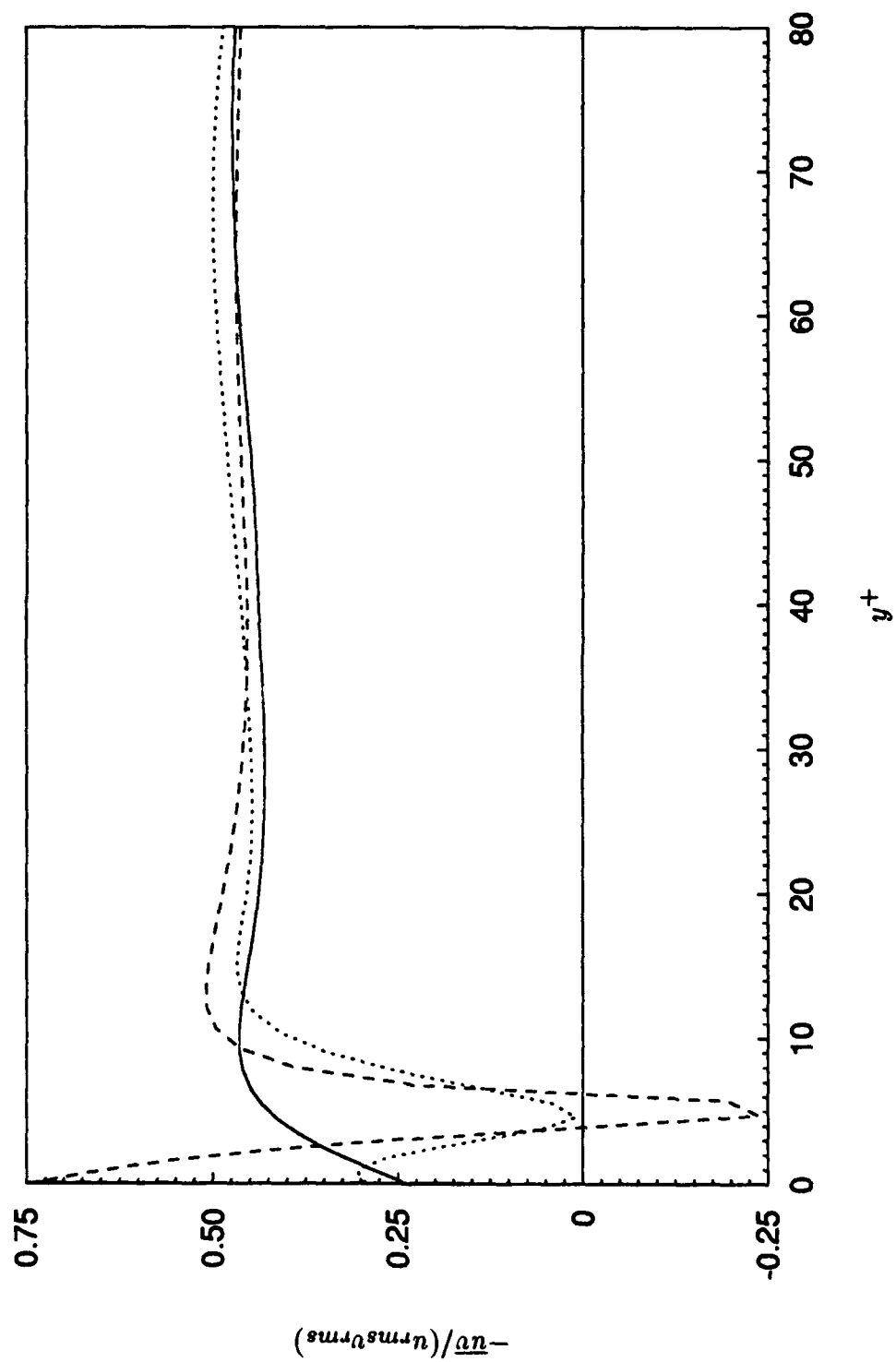


FIGURE 19. Correlation coefficient of u' and v' in local coordinates: —, no control; ---, v -control; , w -control.

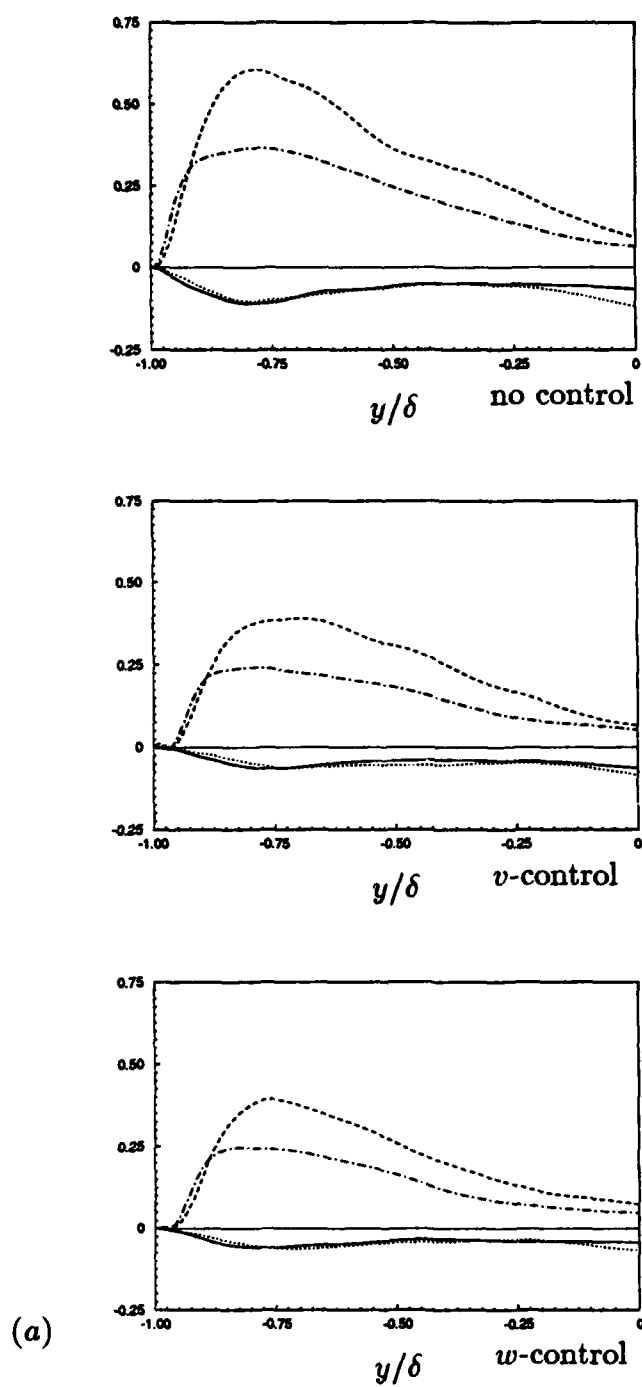


FIGURE 20. For caption see the following page.

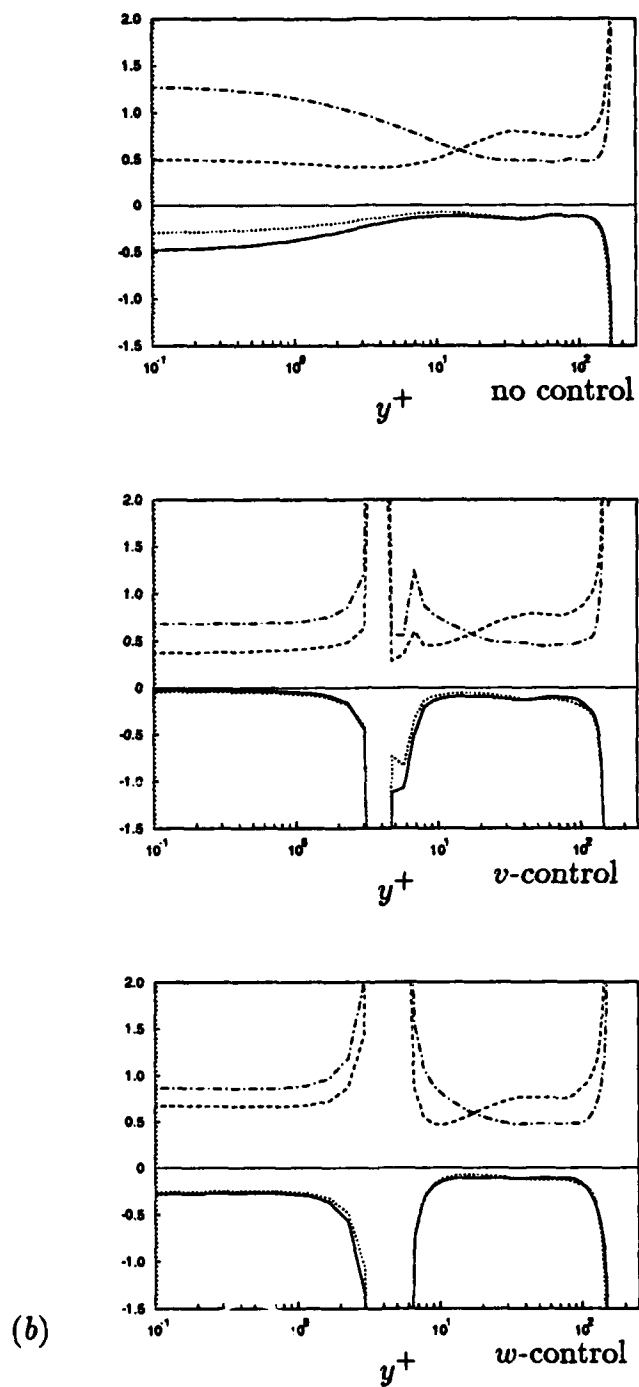


FIGURE 20. Reynolds shear stress from each quadrant normalized by (a) the wall-shear velocity u_{τ_w} ; (b) the local mean Reynolds shear stress $|\overline{uv}|$: —, first; ----, second; , third; — · —, fourth quadrant.

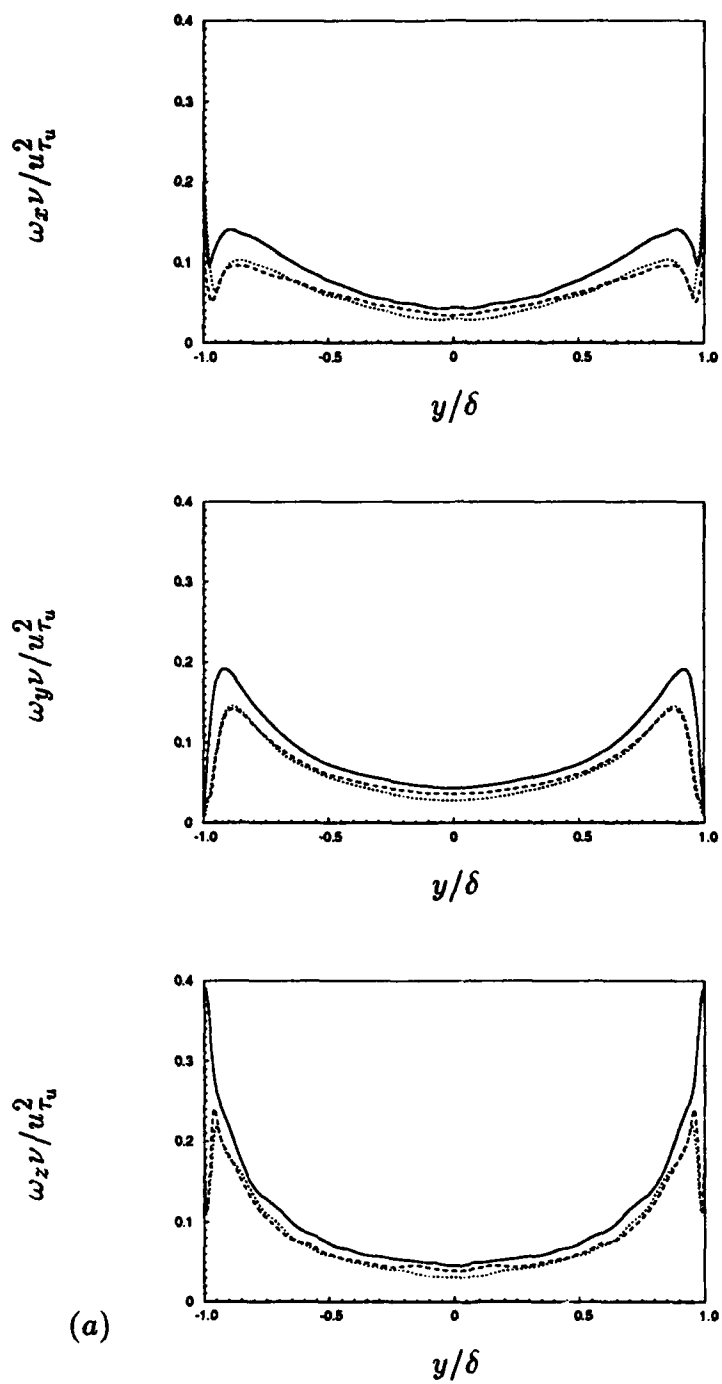


FIGURE 21. For caption see the following page.

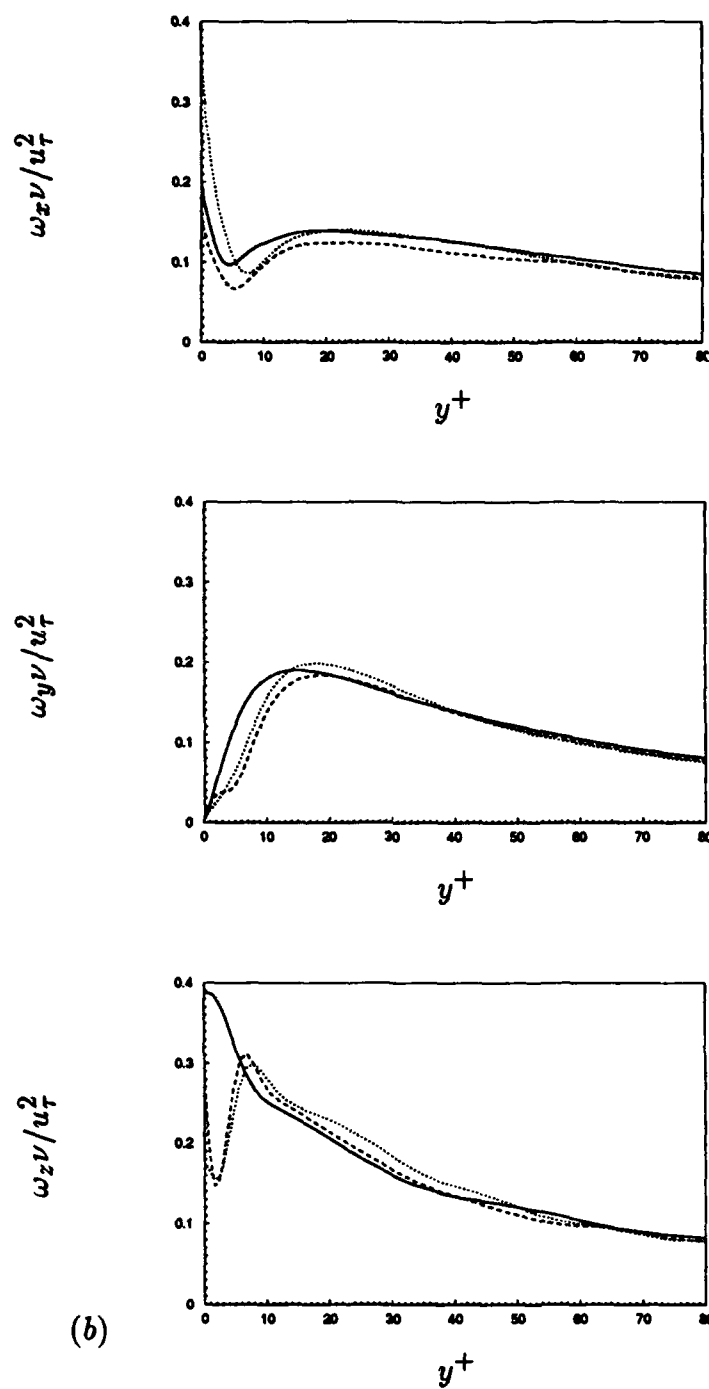


FIGURE 21. Root-mean-square vorticity fluctuations normalized by the wall-shear velocity: —, no control; ----, v -control; ·····, w -control. (a) In global coordinates; (b) in wall coordinates. In wall coordinates, values are non-dimensionalized by the local wall-shear velocity.

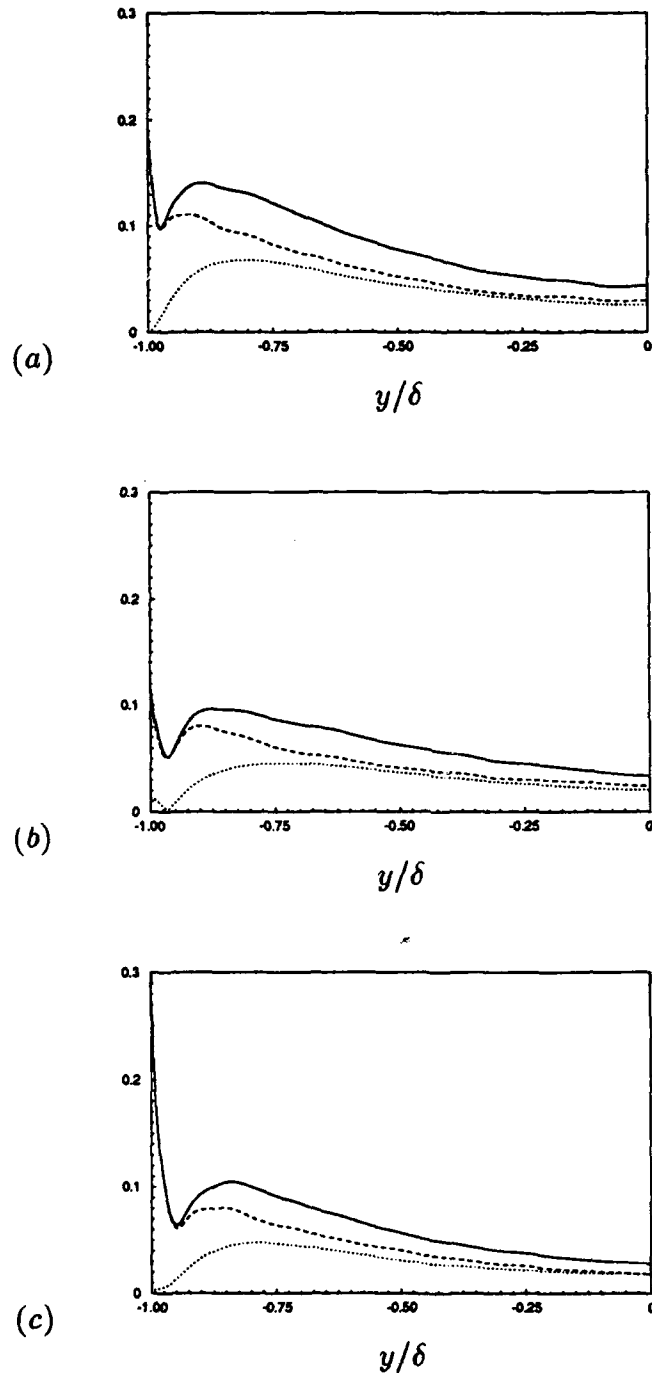


FIGURE 22. Root-mean-square values of the streamwise vorticity component normalized by the wall-shear velocity: —, $\omega_x \nu / u_{\tau_u}^2$; ----, $(\partial w / \partial y) \nu / u_{\tau_u}^2$; ·····, $(\partial v / \partial z) \nu / u_{\tau_u}^2$. (a) No control; (b) v -control; (c) w -control.

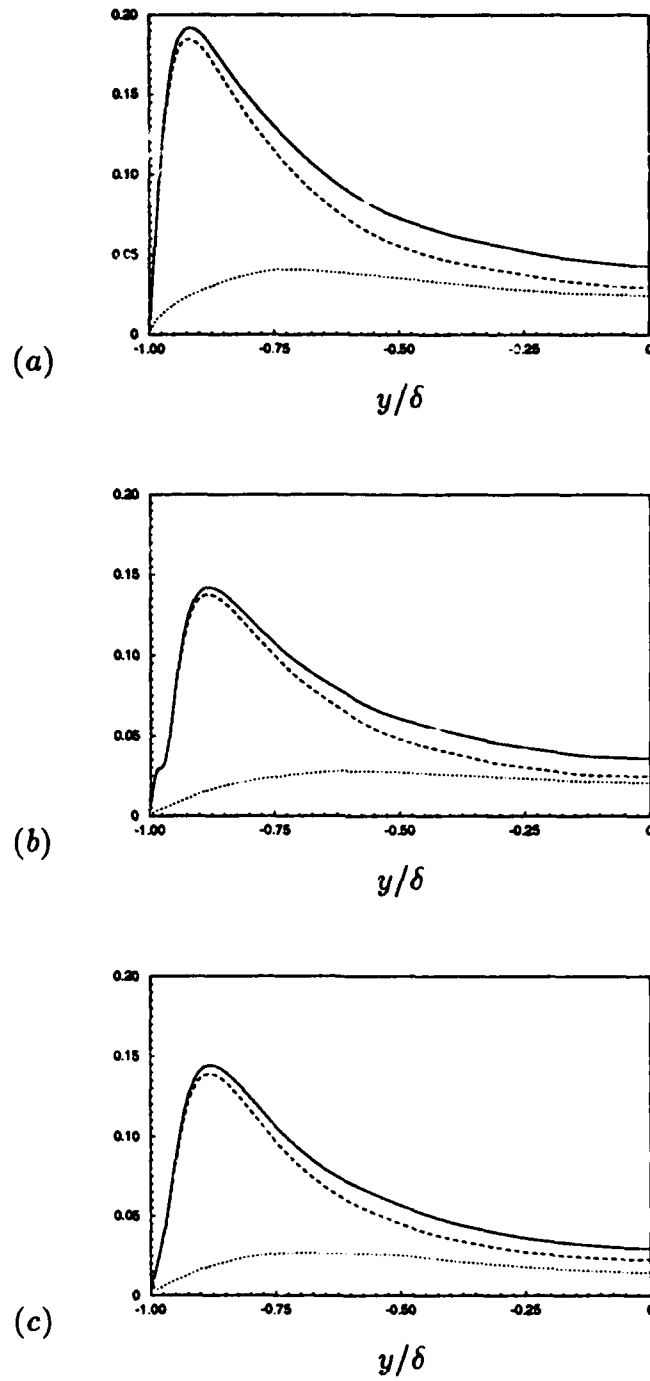


FIGURE 23. Root-mean-square values of the normal vorticity component normalized by the wall-shear velocity: —, $\omega_y \nu / u_{\tau_u}^2$; ----, $(\partial u / \partial z) \nu / u_{\tau_u}^2$; , $(\partial w / \partial x) \nu / u_{\tau_u}^2$. (a) No control; (b) v -control; (c) w -control.

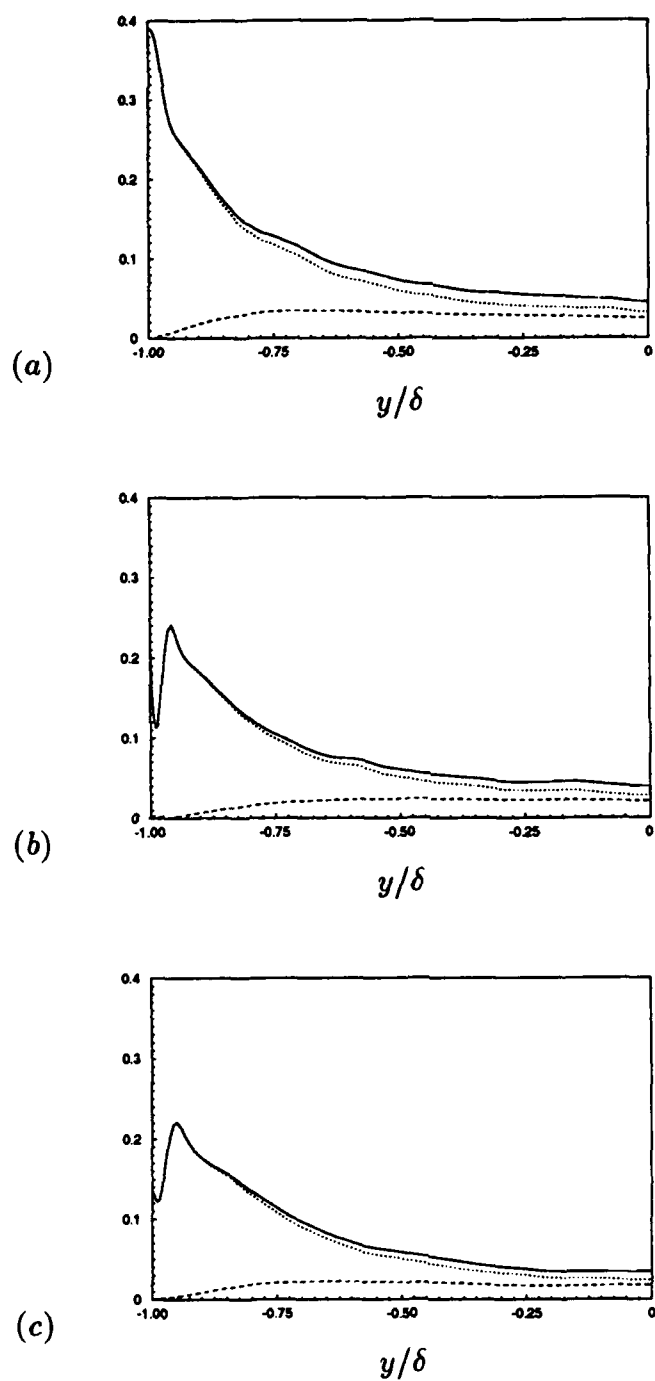
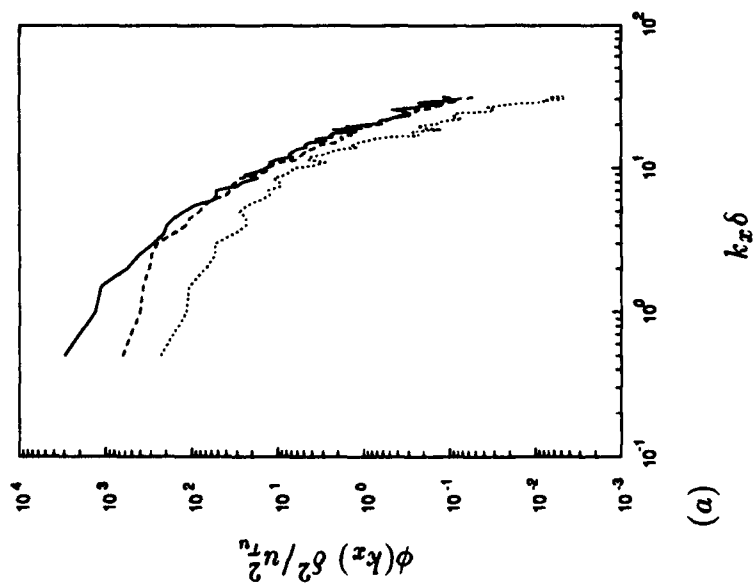
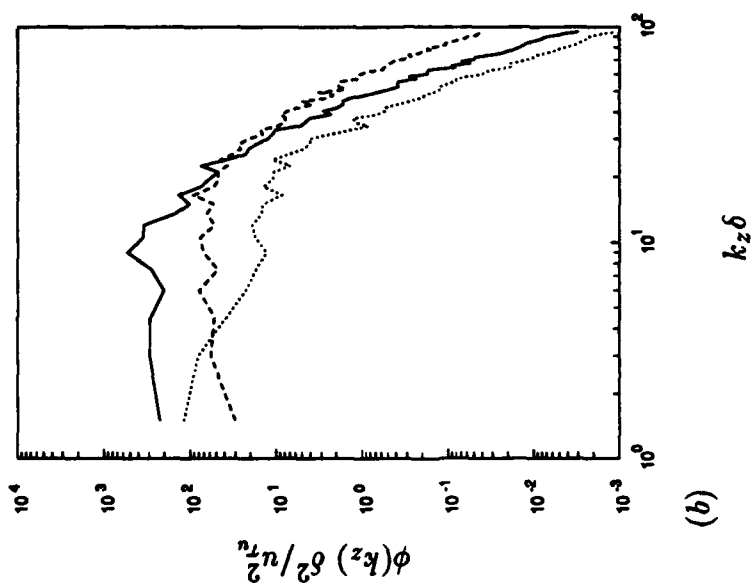


FIGURE 24. Root-mean-square values of the spanwise vorticity component normalized by the wall-shear velocity: — , $\omega'_z \nu / u_{\tau_u}^2$; ---- , $(\partial v / \partial x) \nu / u_{\tau_u}^2$; , $(\partial u' / \partial y) \nu / u_{\tau_u}^2$. (a) No control; (b) v -control; (c) w -control.

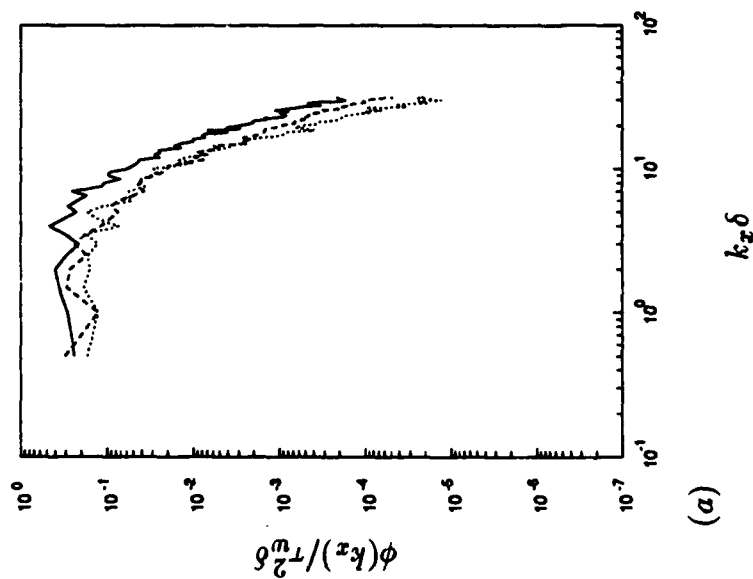


(a)

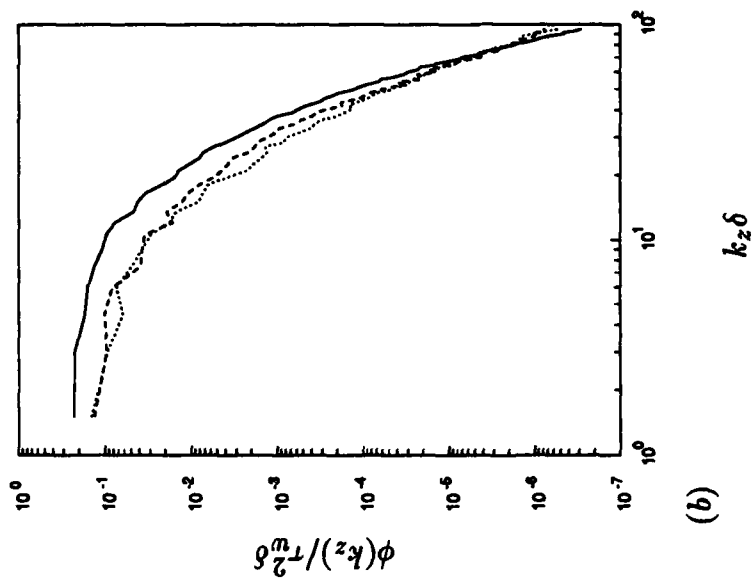


(b)

FIGURE 25. One-dimensional spectra of wall shear-rate fluctuations: —, no control; ----, v-control; , w-control. (a) In the streamwise direction; (b) in the spanwise direction.



(a)



(b)

FIGURE 26. One-dimensional power spectra of wall pressure fluctuations: —, no control; ---, w-control; ·····, v-control; - · - ·, w-v-control. (a) In the streamwise direction; (b) in the spanwise direction.

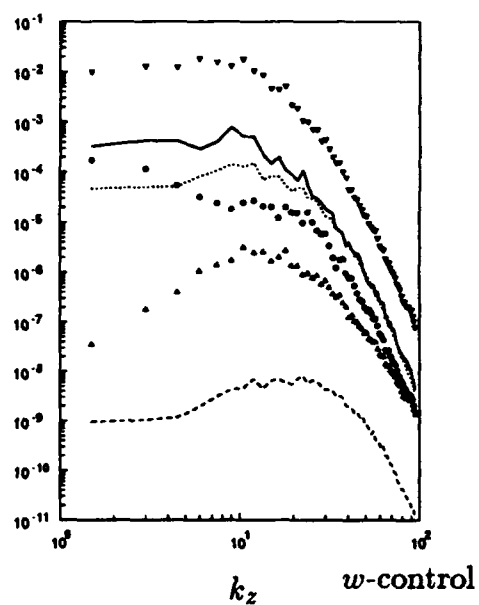
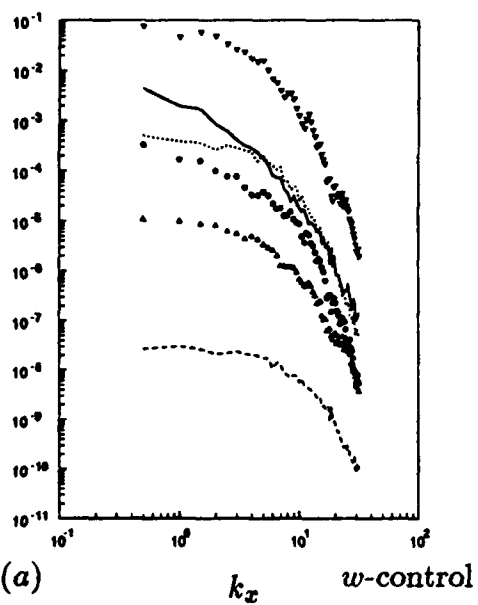
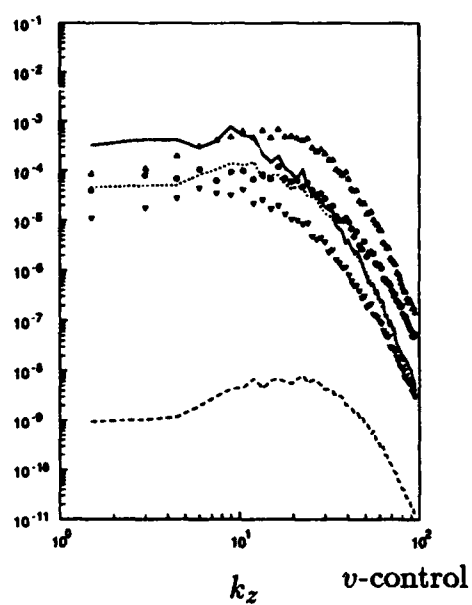
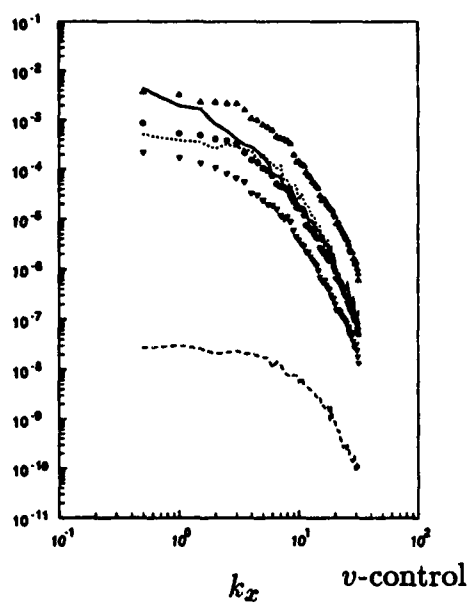


FIGURE 27. For caption see the following page.

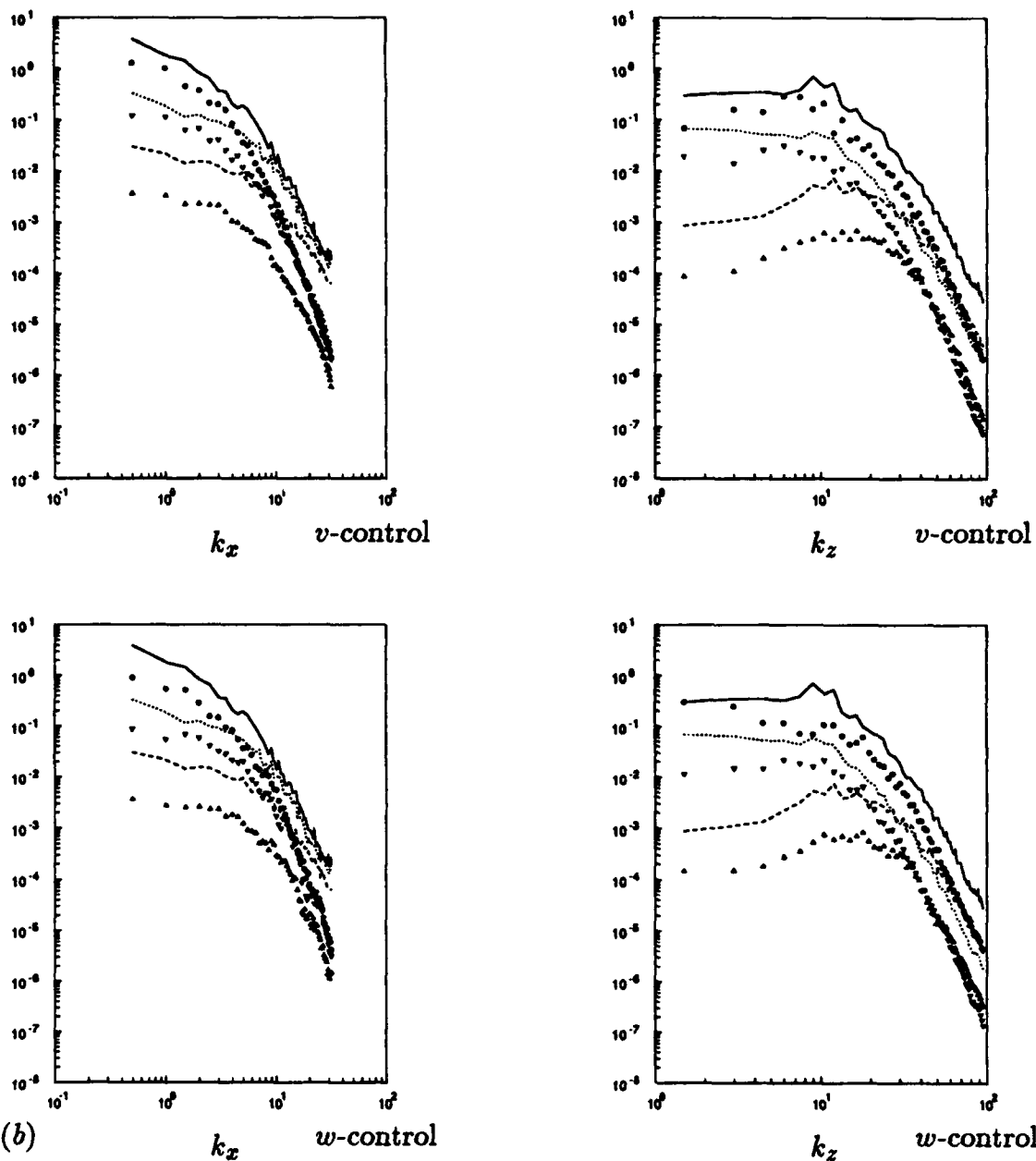


FIGURE 27. One-dimensional energy spectra: For the unmanipulated wall, — , E_{uu} ; ---- , E_{vv} ; , E_{ww} ; for the manipulated walls, \circ , E_{uu} ; Δ , E_{vv} ; ∇ , E_{ww} . (a) At $y^+ \approx 0.2$; (b) at $y^+ \approx 10$.

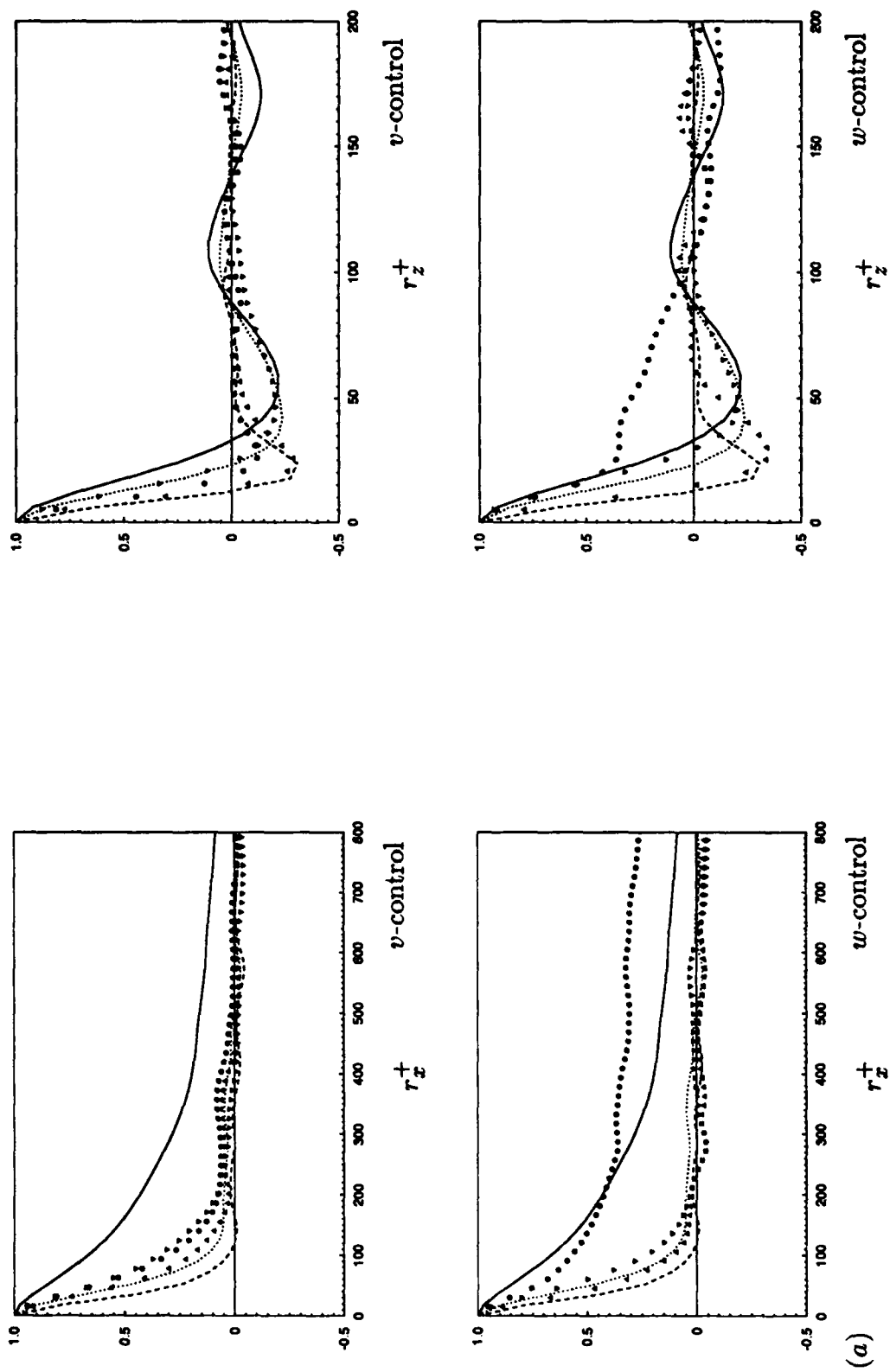


FIGURE 28. For caption see the following page.

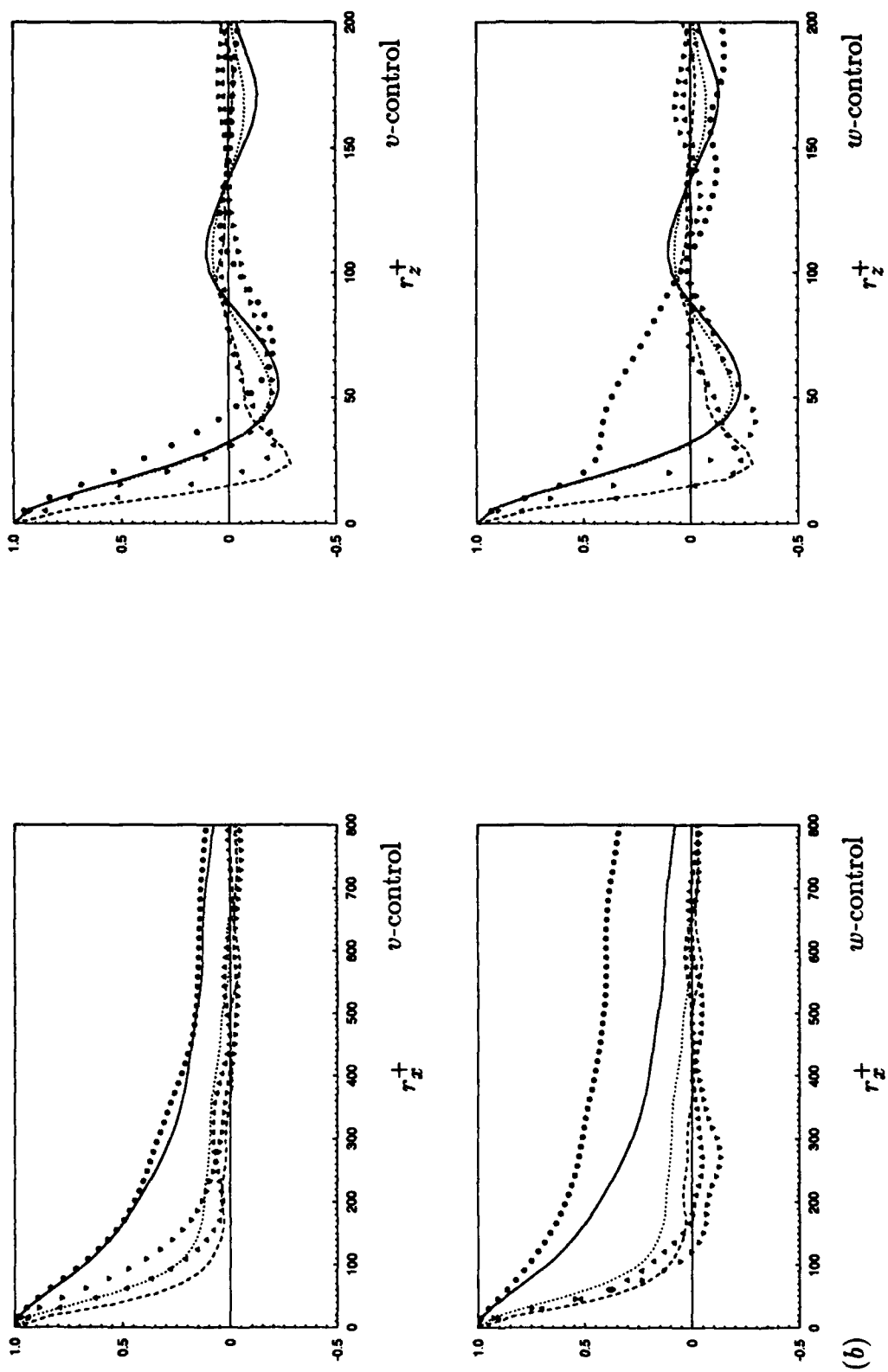


FIGURE 28. For caption see the following page.

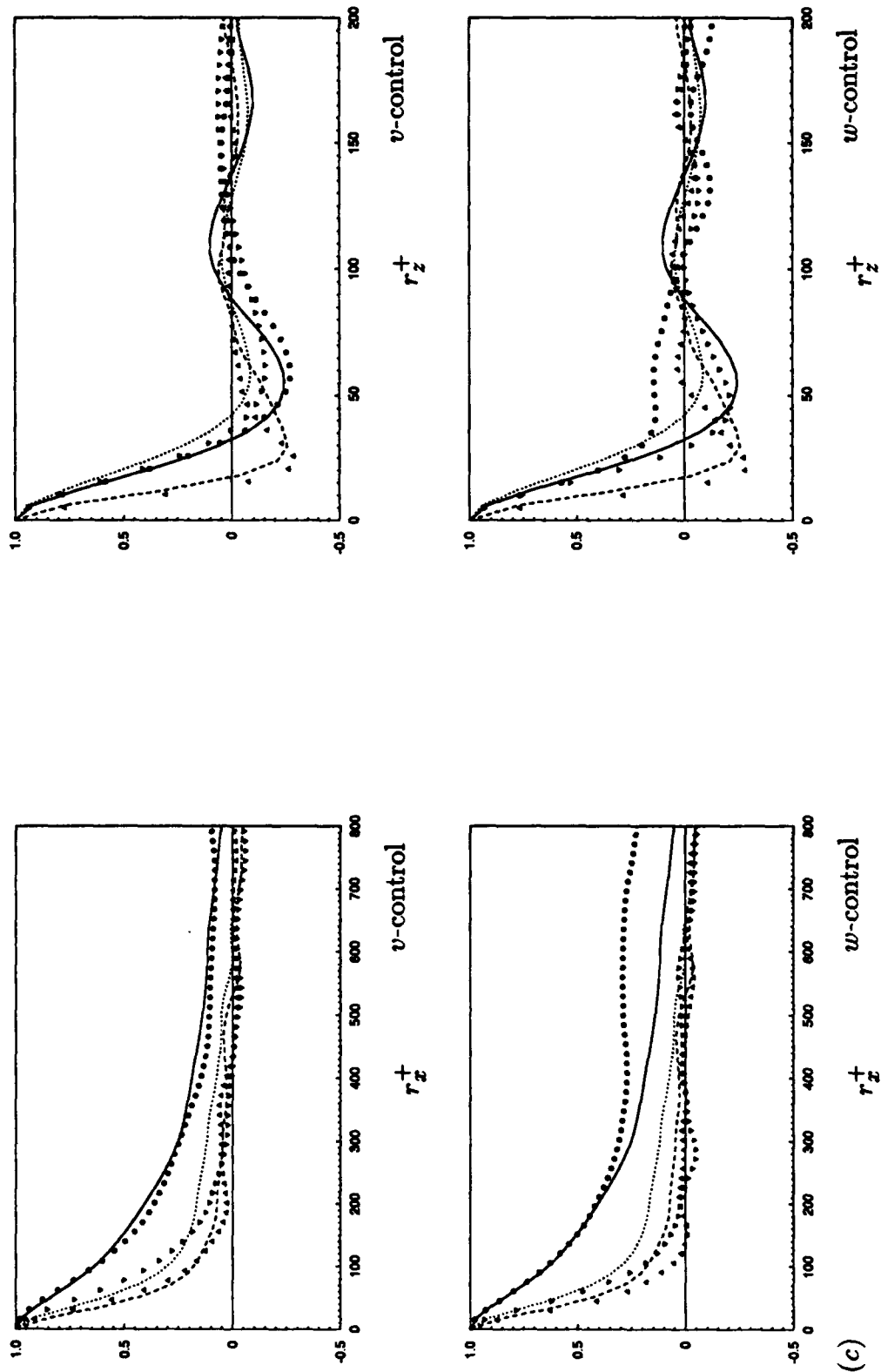


FIGURE 28. Two-point correlations: For the unmanipulated wall, —, R_{uu} ; ---, R_{vv} ; , R_{ww} ; - · - · - , R_{vw} ; for the manipulated walls, o , R_{uu} ; Δ , R_{vv} ; ∇ , R_{ww} . (a) At $y^+ \approx 0.2$; (b) at $y^+ \approx 5$; (c) at $y^+ \approx 10$.

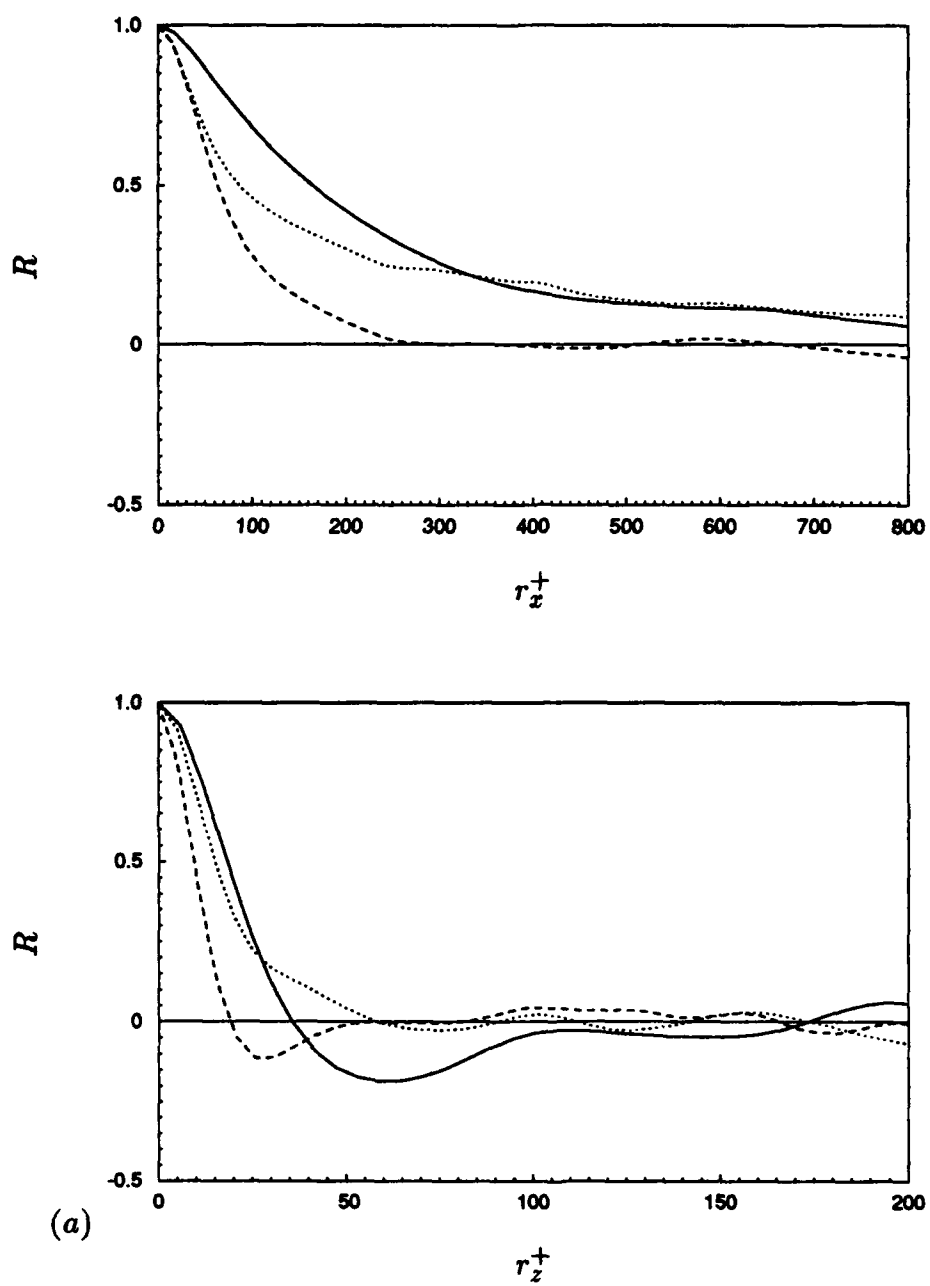


FIGURE 29. For caption see the following page.

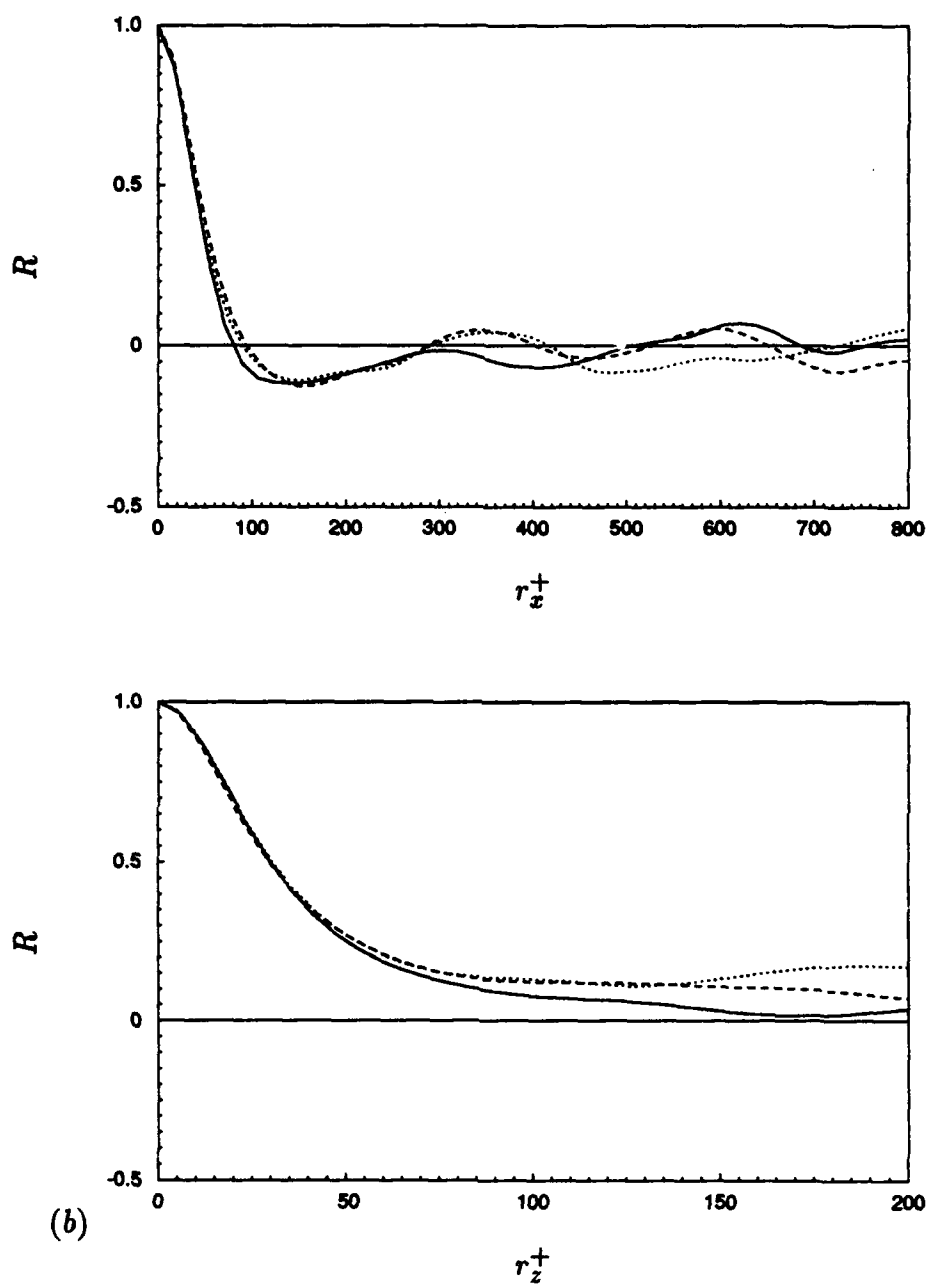


FIGURE 29. Two-point correlations: —, no control; ----, v -control; ·····, w -control. (a) Wall shear-rate fluctuations; (b) wall pressure fluctuations.

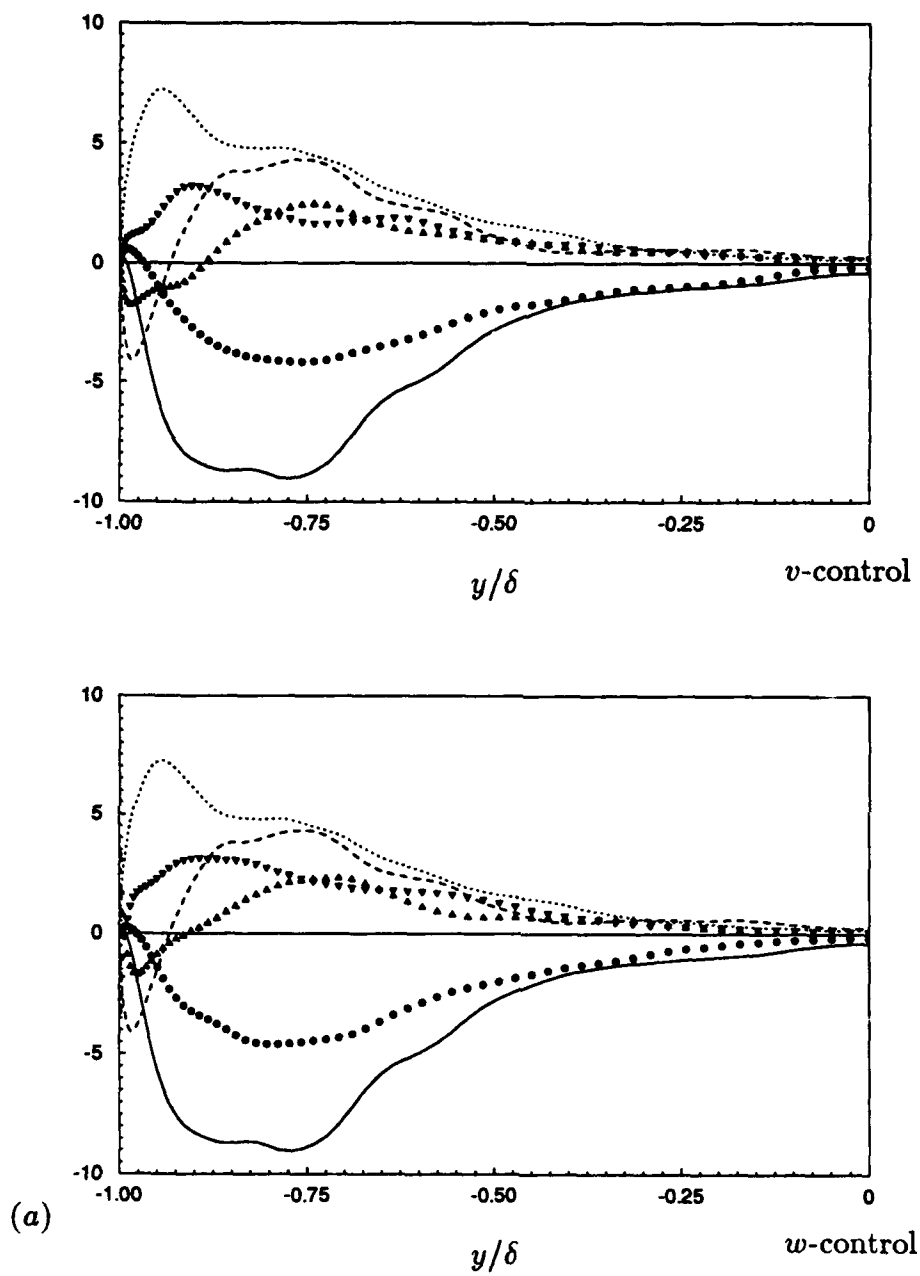


FIGURE 30. For caption see the following page.

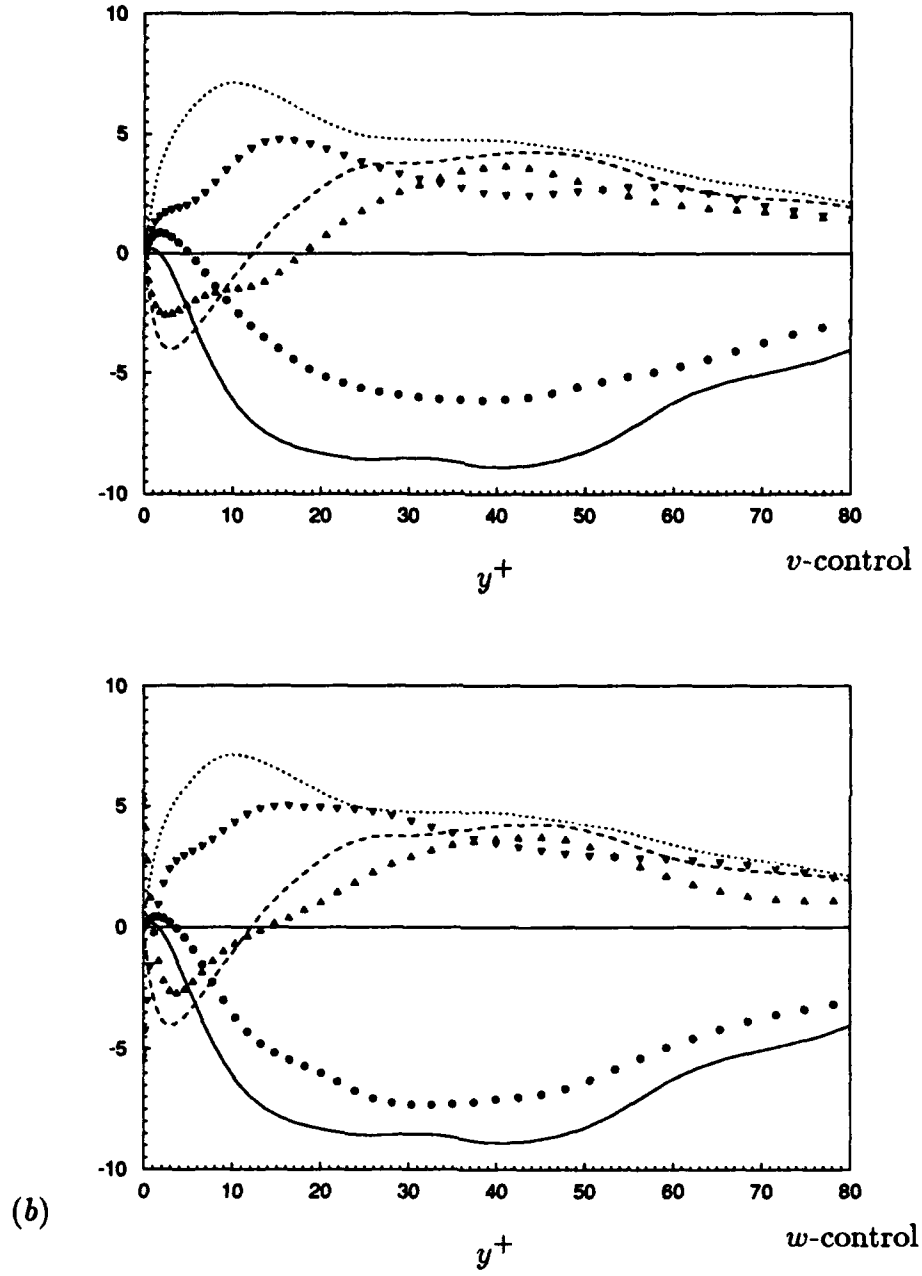


FIGURE 30. Diagonal elements of the pressure-strain correlation tensor: For the unmanipulated wall, —, ϕ_{11} ; ---, ϕ_{22} ; ·····, ϕ_{33} ; for the manipulated walls, o, ϕ_{11} ; Δ , ϕ_{22} ; ∇ , ϕ_{33} . (a) In global coordinates; (b) in wall coordinates.

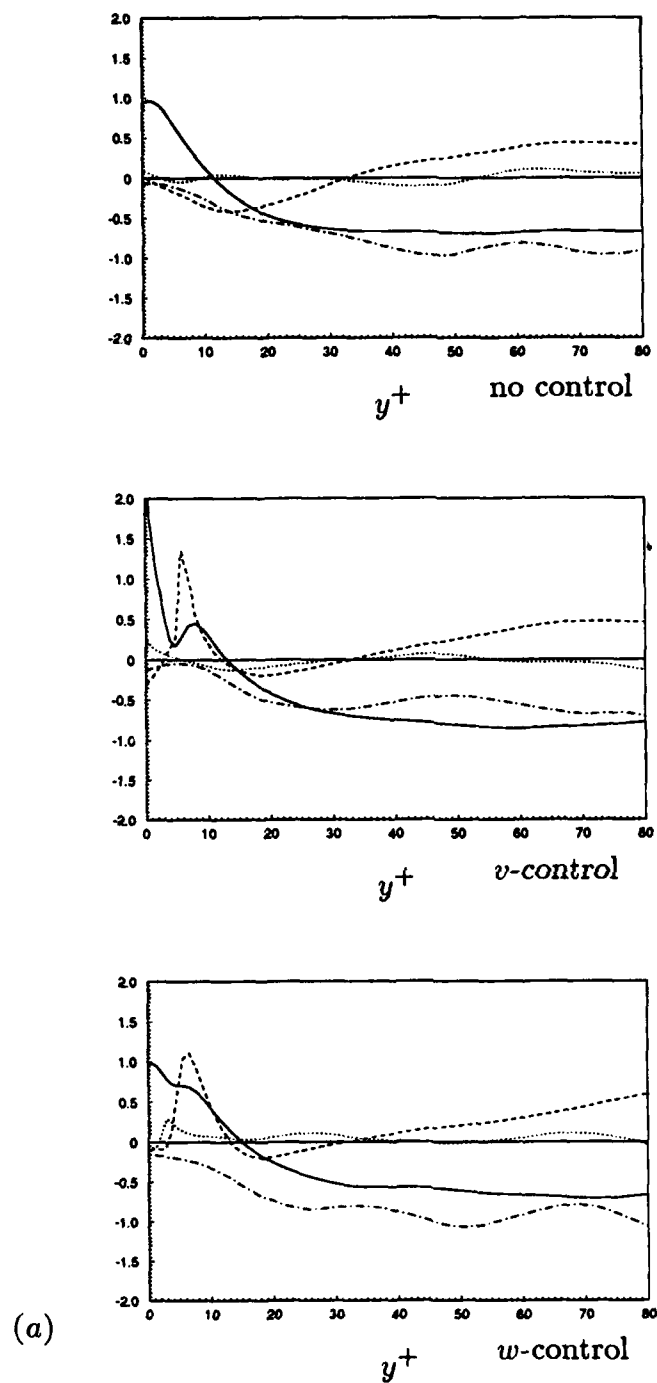


FIGURE 31. For caption see the following page.

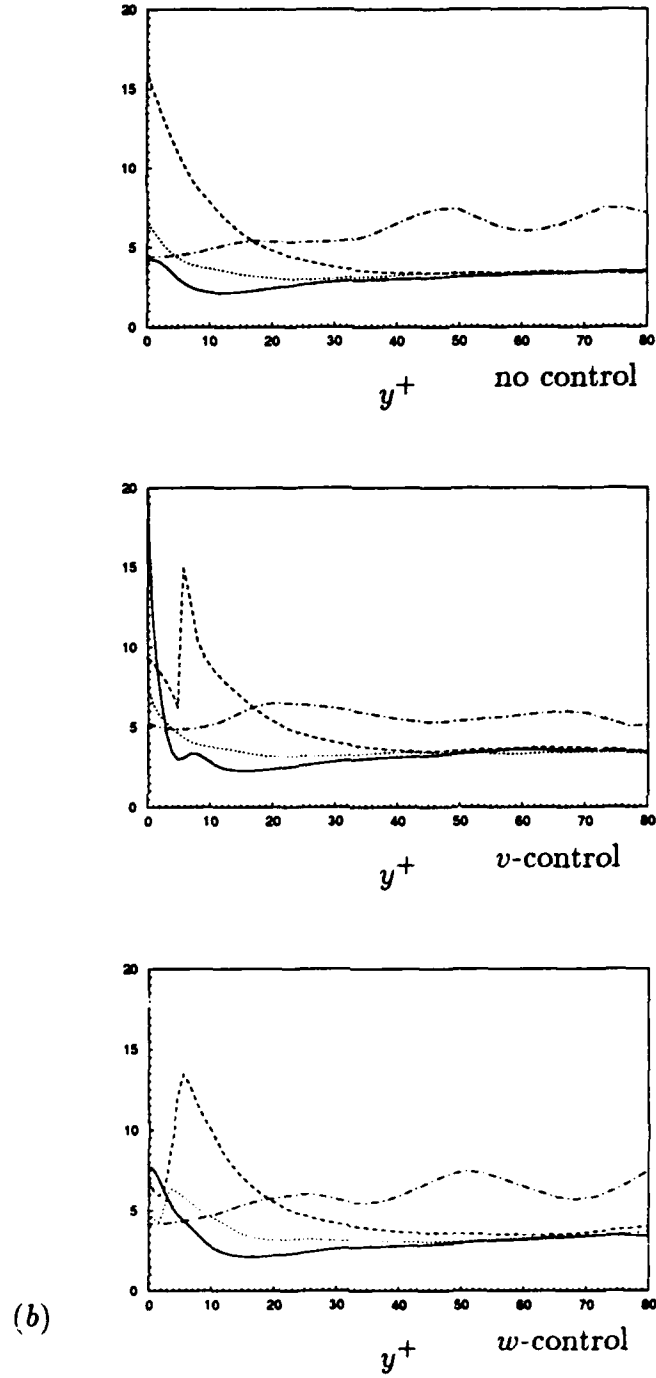


FIGURE 31. Skewness and flatness factors in local coordinates. (a) Skewness, — , $S(u')$; ---- , $S(v')$; , $S(w')$; — — , $S(p')$; (b) flatness, — , $F(u')$; ---- , $F(v')$; , $F(w')$; — — , $F(p')$.

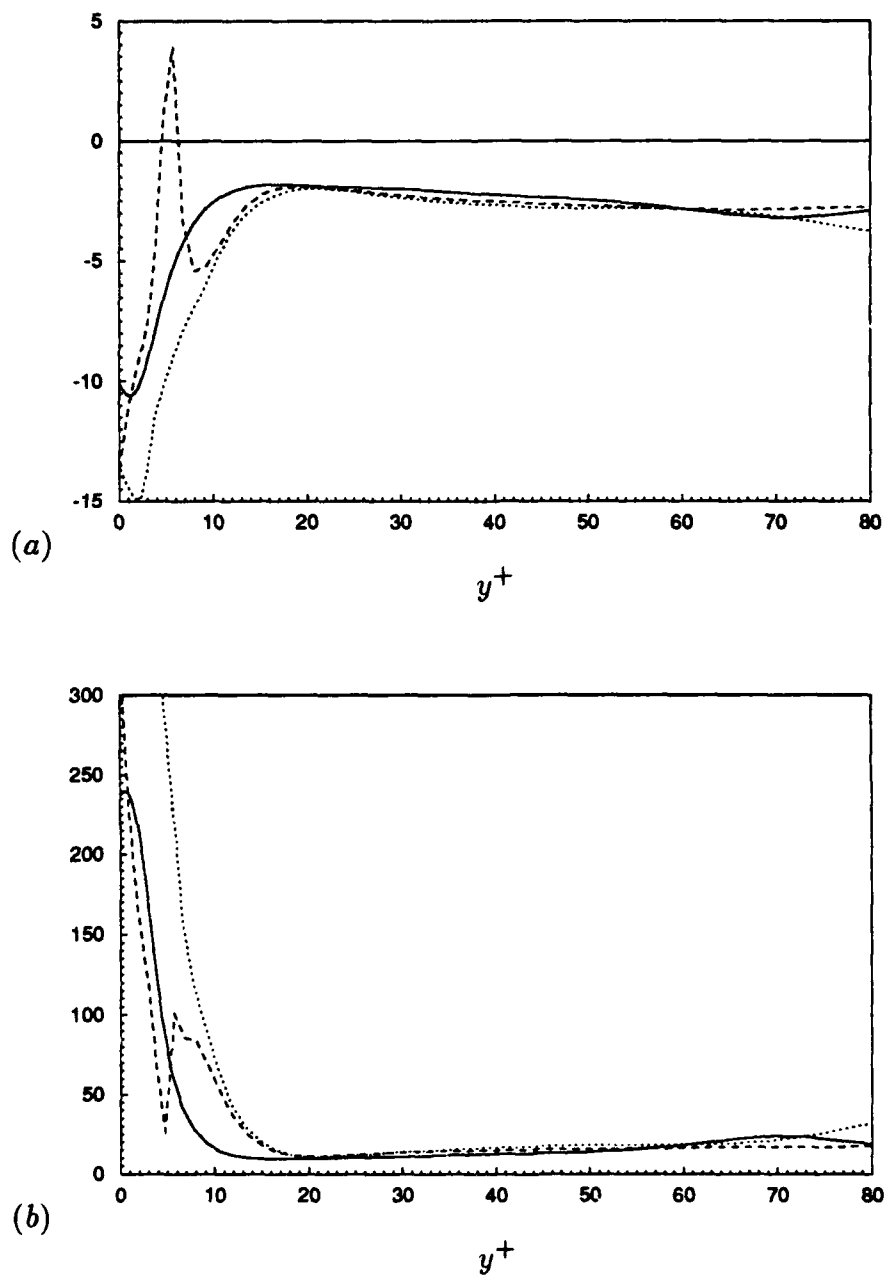


FIGURE 32. Skewness and flatness factors of the Reynolds shear stress: —, no control; ----, v -control; ·····, w -control. (a) $S(u'v')$; (b) $F(u'v')$.

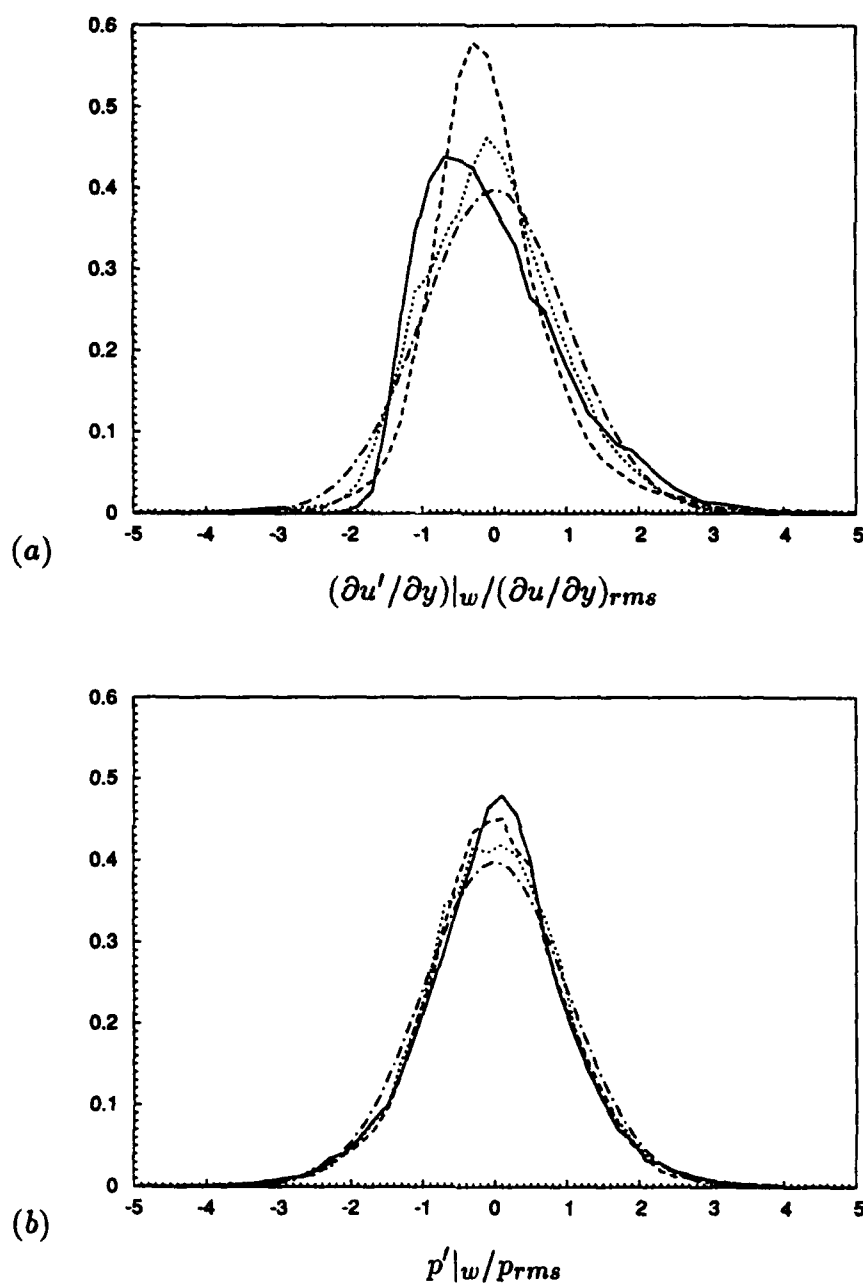


FIGURE 33. Probability density distribution: — , no control; ---- , v -control; , w -control; — — , Gaussian distribution. (a) Wall shear-rate fluctuations; (b) wall pressure fluctuations.

CHAPTER 4

TURBULENCE STRUCTURE OF MANIPULATED CHANNEL FLOWS AND DRAG REDUCTION MECHANISMS

As mentioned in chapter 3, the turbulence statistics in the manipulated channels are substantially different from those in the unmanipulated channel. A relatively small amount of either blowing and suction or spanwise velocity at the surface appreciably changes turbulence statistics throughout the channel. Differences between two-point correlations and spectra of the v - and w -controlled channels reveal that, despite comparable drag reductions, the structures are manipulated in different fashions. Also, the control strategies presented in chapter 3 are not capable of eliminating all of the essential features of turbulent structures, but they are able to weaken most structures substantially, thus yielding a 25% drag reduction. Assuming that the best resulting velocity field is laminar, the maximum possible drag reduction at $Re_c = 3300$ is 74%. In this chapter, we focus on turbulence structures in the manipulated channels by examining instantaneous flow fields and study drag reduction mechanisms caused by active controls.

4.1 Turbulence structure of manipulated channel flows

Contour plots of the streamwise velocity of both manipulated channel flows in the wall region are shown in figure 34, and are compared with those of the unmanipulated channel flow. There is no streaky structure below $y^+ \approx 5$ in the manipulated channels, and at $y^+ = 5$ and 10 the mean streak spacing appears to be larger than in the unmanipulated channel. Also, the active control schemes significantly reduce the magnitude of the streamwise velocity in the wall region. Examples of the input control velocities at the wall, i.e. the normal velocity for v -control and the spanwise velocity for w -control, are shown in figure 35. In the case of v -control, the contours of the streamwise velocity near the wall are quite similar to those of the wall-normal velocity. This observation was confirmed statistically with two-point correlations in section 3.5 (figure 28).

The mean streak spacing can be obtained from the two-point correlation of the streamwise velocity. The mean spacing between streaks is roughly twice of the separation distance at which the correlation of the streamwise velocity is negative and reaches a minimum. Figure 36 shows the mean streak spacings of the manipulated and unmanipulated channel flows. Due to the lack of streaky structures very near the wall in the manipulated channels, streak spacings are not shown for that region. For $y^+ < 10$, the mean streak spacing is clearly increased in the manipulated channels, and it has nearly the same value above $y^+ \approx 10$ as in the unmanipulated channel. Note that we have used the local wall-shear velocity u_τ when the mean streak spacing is calculated in wall units. Hence the physical dimension of the mean streak spacing in the manipulated channels is actually larger than that in the unmanipulated channel even above $y^+ \approx 10$.

Contours of instantaneous streamwise vorticity in a (y, z) plane in the manipulated and unmanipulated channels are shown in figure 37. The reduction in the intensity of the streamwise vorticity near the wall is apparent. Figure 38 shows the contours of instantaneous spanwise vorticity in a (y, z) plane. The intensity is, again, significantly reduced. The high skin-friction regions near the unmanipulated wall do not appear near the manipulated walls. Instead, the high skin-friction regions are shifted slightly to the interior ($y^+ \approx 5$) of the manipulated channel by action of the controls. This is one important drag reduction mechanism and will be described in detail in the following section.

4.2 Drag reduction mechanisms of active controls

In this section, we focus on investigating the dynamics and underlying mechanisms that lead to the reduction in drag and the strength of the large-scale structures. We employ two approaches as outlined below.

In general, it is rather difficult to study the dynamics associated with a turbulent flow. The main reasons for this difficulty are twofold. First, at any given instant, the flow is crowded with several structures at broad scales and associated complex interactions. Second, the computational cost required to follow the temporal evolution of a given structure over a long period is prohibitive. The approach in the present study is based on the work of Jiménez & Moin (1991), which demonstrated that the essential dynamics associated with the streamwise vortical

structures present in the wall region can be reproduced in what they referred to as the “minimal channel” flow. In their study, they isolated one or two streamwise vortices by choosing a periodic computational domain such that it could only accommodate these minimal set of structures. It is a relatively easy task then to follow the evolution of a single vortical structure in this manner. Of course, some interactions between different structures are absent in the minimal channel flow (Jiménez & Moin 1991). However, since the near-wall turbulence statistics were reproduced accurately, Jiménez & Moin implied that such interactions may not be essential to turbulence dynamics in the wall region. Computed flow fields in the minimal channel with both v - and w -control strategies implemented are analyzed below to investigate the dynamics associated with a streamwise vortex.

In the second approach, we examine an even simpler model problem. To gain further insight on how the surface boundary condition interacts with a streamwise vortex, we performed numerical simulations of an isolated vortex dipole interacting with a wall, with and without control manipulations. In the absence of background turbulence, one can study the dynamics of the vortex interaction with the wall in a straightforward manner.

4.2.1 Minimal channel flow

The database of Jiménez & Moin (1991) is used as the base flow for control. The Reynolds number based on the laminar centerline velocity U_l and channel half-width δ is 2000. The computational box for this particular Reynolds number is $\pi\delta$, 2δ and 0.35δ in x , y and z directions, respectively. At this particular Reynolds number, the flow is turbulent at only one wall. Jiménez & Moin (1991) chose this Reynolds number in order to study the structure of the vorticity field because flow features are “cleaner” at low Reynolds numbers, but similar features are also observed at higher Reynolds numbers where both walls are turbulent.

Figure 39 (a) shows the time history of the horizontally averaged wall-shear rate from $U_l t / \delta = 0$ to 120. In this period, there are two *intermittency* cycles according to Jiménez & Moin (1991). In the intermittency cycle, all of the characteristic turbulent intensities as well as the wall-shear rate vary strongly. The velocity fields at $U_l t / \delta = 0$ and 23.125 were used as initial flows to apply both control schemes. The latter flow field was chosen during the turbulence activation period.

For convenience, we call SEQ1 the evolution of the flow fields with an initial flow of $U_1 t / \delta = 0$ and SEQ2 the evolution of the flow fields with an initial flow of $U_1 t / \delta = 23.125$. The modified wall-shear rates owing to the controls are shown in figure 39 (b). The wall-shear rates are significantly reduced in both SEQ1 and SEQ2. Intensities of the velocity and vorticity fluctuations are also considerably reduced. The controlled flow fields (SEQ1 and SEQ2) were stored in time increments of $U_1 t / \delta = 5$ ($u_\tau^2 t / \nu \approx 24$) and visually analyzed and compared to the corresponding unmanipulated sequences.

Regions of high skin friction are closely related to the location and strength of streamwise vortices near the wall. The sweep motion due to strong streamwise vortices creates high skin-friction regions on the wall. Most of the vorticity in the wall region is spanwise owing to mean shear. Further from the wall where the large streamwise vortices are located ($y^+ = 15 - 40$), this is no longer true, and the three vorticity components have comparable magnitudes. Therefore, possible origins of the strong streamwise vortices are the tilting of the ω_z vortex lines by spanwise variation of the streamwise velocity ($\omega_z \partial u / \partial z$) and tilting of the normal vorticity by the prevailing shear ($\omega_y \partial u / \partial y$).

Time sequences of the evolution of the wall-vorticity layer in the manipulated and unmanipulated channels (SEQ1) are shown in figure 40. Each frame in the time sequence shows an instantaneous view of the position of the sheet as it approaches the active peak in the intermittency cycle shown in figure 39. The surface is marked by individual transverse vortex traces initiated at $y^+ \approx 7.5$ in a relatively undisturbed part of the layer. In the unmanipulated channel, the lifting of the layer away from the wall over the low-velocity streak is evident, as is the waviness of the streak itself. The lifting process is mainly due to a strong streamwise vortex above the wall (Jiménez & Moin 1991). A short time after applying control, the lifting of the vortex line essentially disappears. The vortex lines modified by the active control schemes are mainly composed of the spanwise vorticity near the wall, and the absence of tilting and lifting of the spanwise vorticity prevents new formation of the streamwise vorticity above the wall. Vortex traces initiated at $y^+ \approx 5$ and 10 followed the same trend.

The time history of the skin friction on the manipulated walls shows that the skin friction decreases as soon as the control is applied to the flow even though

the primary streamwise vortex above the wall is not immediately affected. Therefore, there must be another drag reduction mechanism besides the reduction of the strength of the streamwise vortex above the wall. In order to investigate this effect more clearly, we applied both controls at $U_t t / \delta = 23.125$, when the skin friction is increasing very rapidly on the unmanipulated wall (figure 39). An abrupt decrease of the wall-shear rate was found with both control schemes.

Figure 41 shows cross-flow velocity vectors (v, w) and contours of the spanwise vorticity in a (y, z) plane at $U_t t / \delta = 30$, when there is a significant reduction of the skin friction in the manipulated cases (SEQ2). The figure shows that turbulent structures remain essentially unchanged except very near the wall. The high skin-friction regions on the wall are lifted to the interior of the channel ($y^+ \approx 5$) by the control schemes. The sweep motion due to strong streamwise vortices is directly deterred by active controls. A schematic diagram of the drag reduction mechanism is shown in figure 42. Note that, in the case of w -control, a wall-normal velocity is induced very near the wall by the spanwise velocity distribution at the wall; from the continuity equation at the wall, $\partial v / \partial y = -\partial w / \partial z \neq 0$, leading to higher values of v near the wall.

4.2.2 An isolated vortex interacting with a wall

Although the minimal flow unit is useful to trace turbulent structures in time, the flow in the minimal channel is still too complicated to easily isolate the effect of the control schemes on the primary streamwise vortex above the wall. To gain further insight on how the control affects the dynamics of the streamwise vortices, a two-dimensional vortex pair interacting with a wall with and without boundary manipulation was simulated. Of course, the results described below represent a highly idealized situation, because there is no mechanism of stretching or tilting of vortices in this flow. The strength of the primary vortex pair in this simulation continuously decreases owing to viscous diffusion.

The Reynolds number of the initial vortex dipole is $Re_\Gamma = \Gamma / \nu = 1800$, where Γ is the circulation of the vortex, and ν is the kinematic viscosity. The size of the computational box is chosen to be $2\pi\delta$ and 2δ in z and y directions, respectively, where δ is the channel half-width. The computations are performed using 128×65 spectral modes (spanwise and normal to the wall). The vortex dipole is initially

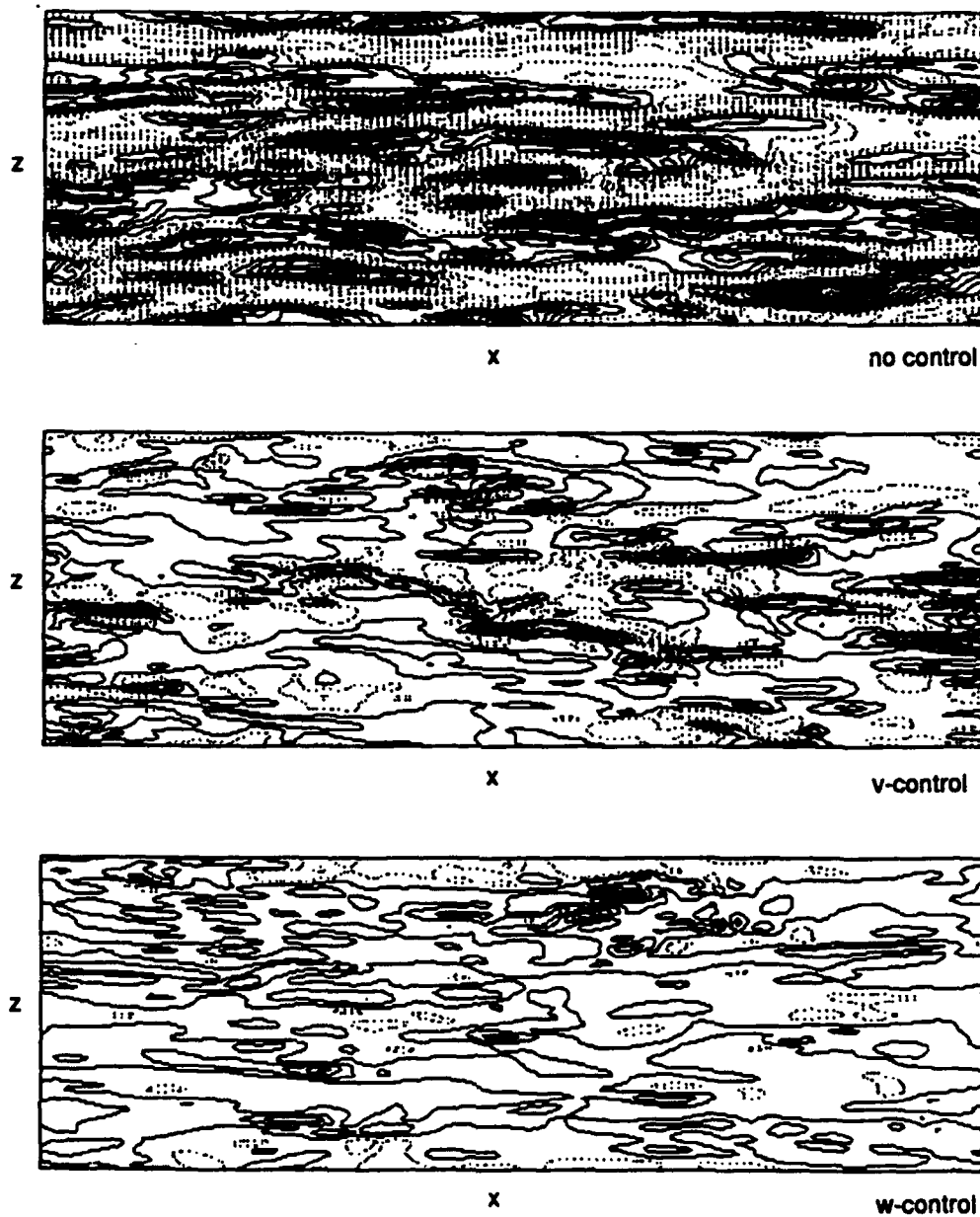
located at the center of the channel. Due to the self-induced motion of the vortex dipole, it approaches to the lower channel wall ($y = -\delta$). The sensor location for the control was chosen to be $y = -0.83\delta$. Two other sensor locations ($y = -0.94\delta$ and -0.67δ) gave similar results.

Figure 43 shows the time sequences of the vorticity in the manipulated and unmanipulated channels. In the unmanipulated channel, the vortex behavior is similar to Orlandi's results (1990). A vortex near a no-slip wall induces secondary vorticity of opposite sign at the wall and carries it up to generate a new free vortex (figure 43 (a)). The lifted secondary vortices inhibit the separation of the primary vortices. In the v -control scheme shown in figure 43 (b), the vortices separate. Here, the lifting of the secondary vorticity at the wall is clearly prohibited, and the y -location of the center of the primary vortex is nearly constant owing to the absence of the lifted secondary vortices. From the sequence of the v -controlled flow, it may be suggested that the v -control scheme changes the interaction between the primary vortex and the secondary vorticity by preventing the lifting process.

On the other hand, the vortex motion in the w -controlled channel is quite similar to that in the unmanipulated channel (figure 43 (c)). There is clear lifting of the secondary vorticity. However, the difference is that stronger secondary vorticities are created at the wall by the w -control scheme. Hence, the primary vortex is lifted further into the interior of the channel by this lifted stronger secondary vortices, so that the sweep effect near the wall is reduced. The vortex rebounding time (Orlandi 1990) is also increased by the stronger secondary vortices.

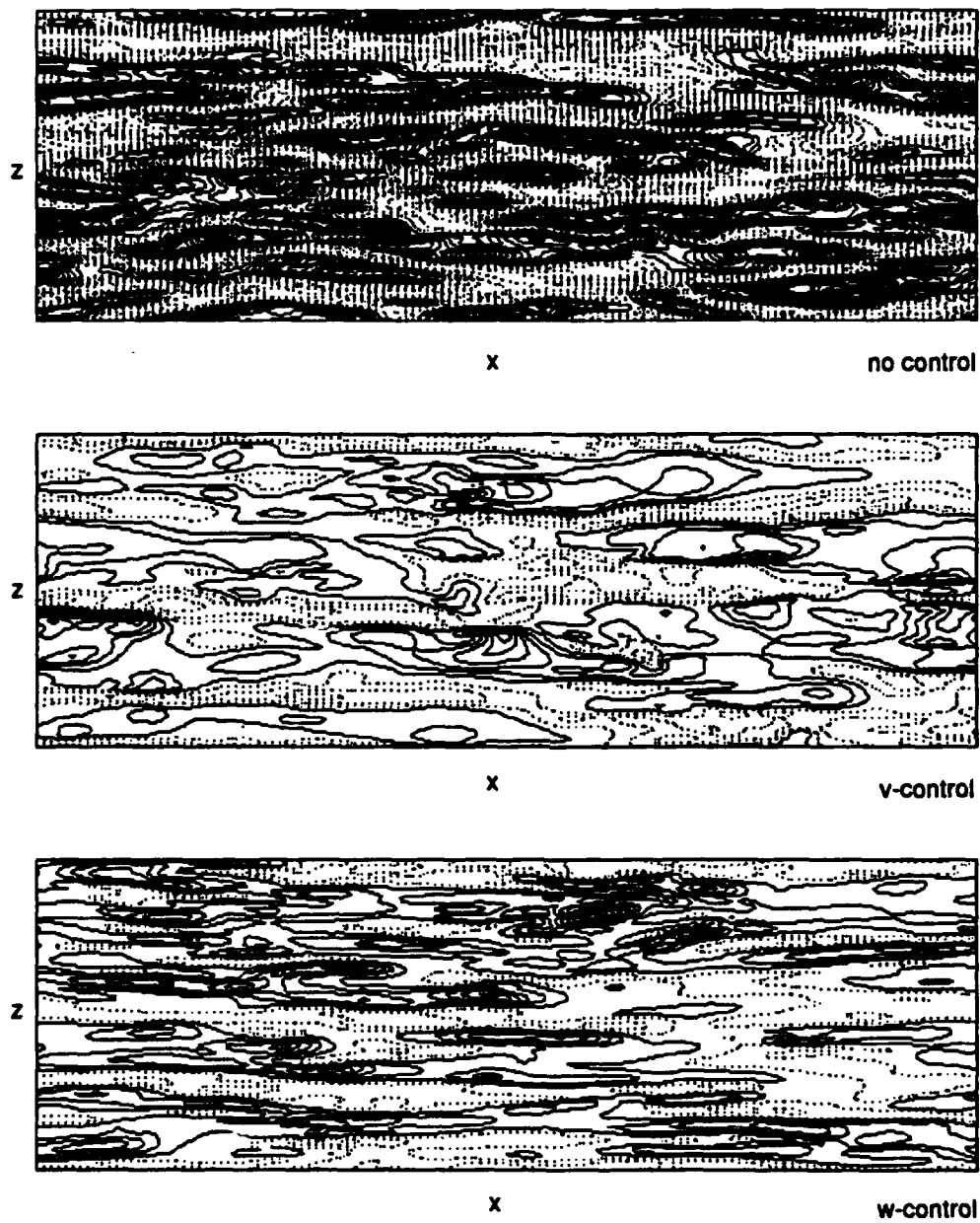
The maximum value of the vorticity and the circulation of the primary vortices are not changed by the control actions, indicating that the active control schemes applied do not reduce the strength of the primary vortices, but change their relative locations and interactions with the wall.

In order to investigate the effect of the streamwise vortex dipole on the mean skin friction on the wall, we performed two-dimensional numerical simulations in which a parabolic streamwise velocity was superimposed on the streamwise vortex dipole. Skin-friction reduction was found using both control schemes.



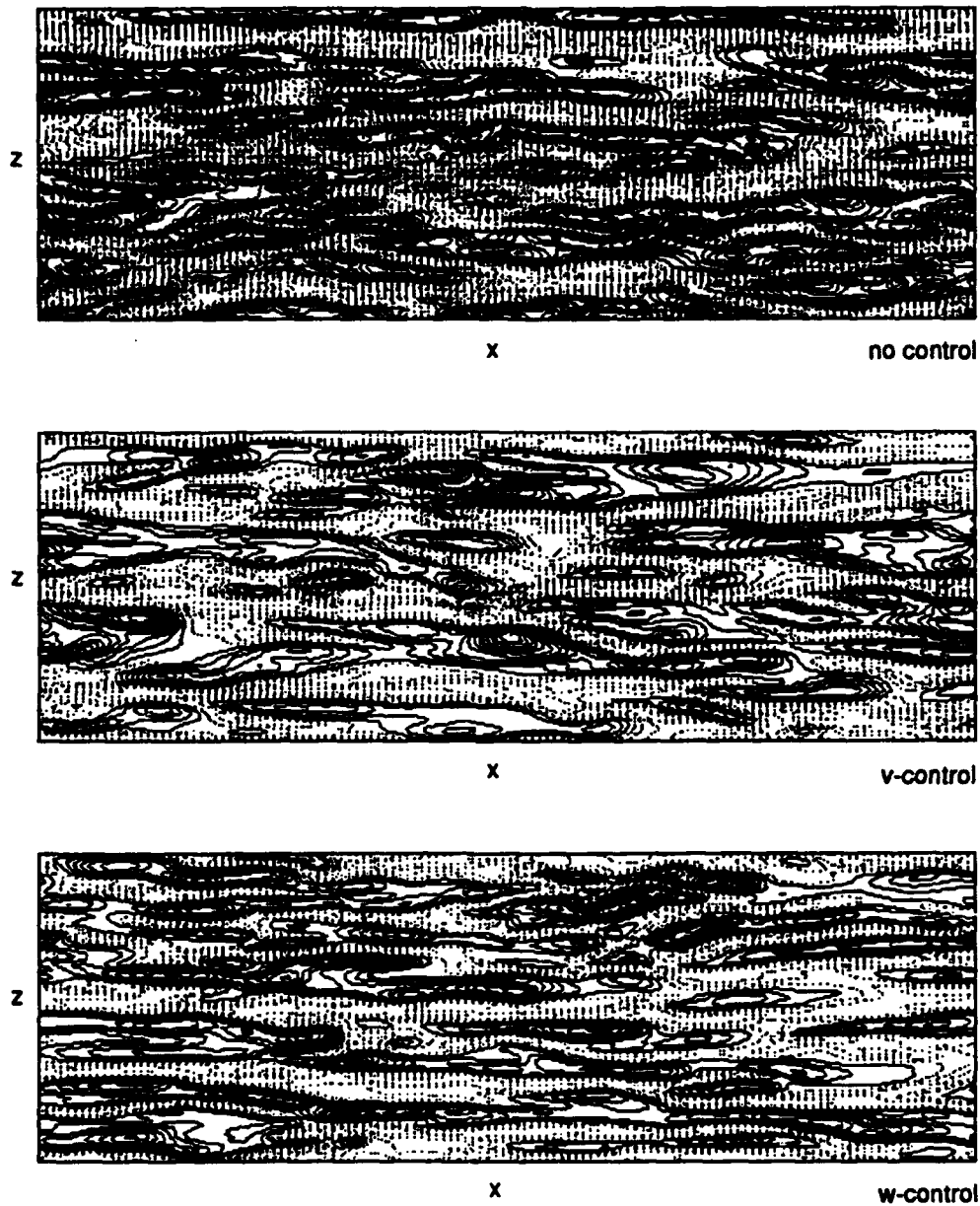
(a)

FIGURE 34. For caption see the following page.



(b)

FIGURE 34. For caption see the following page.



(c)

FIGURE 34. Contours of streamwise velocity fluctuations in an (x, z) plane. (a) At $y^+ \approx 1$; (b) at $y^+ \approx 5$; (c) at $y^+ \approx 10$. The contour levels normalized by u_{τ_w} range (a) from -0.8 to 3 by increments of 0.2 ; (b) from -2.8 to 7 by increments of 0.4 ; (c) from -5 to 7 by increments of 0.5 . Negative contours are dotted.

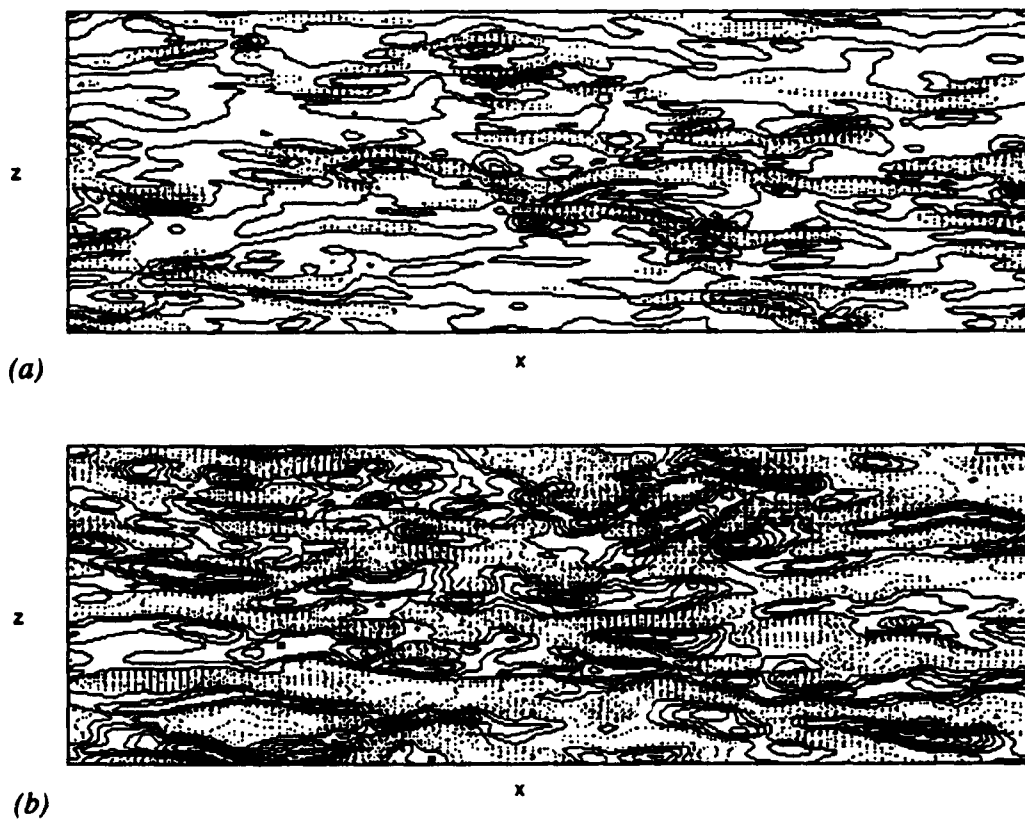


FIGURE 35. Contours of control-input velocities at the wall. (a) Normal velocity fluctuations (v -control); (b) spanwise velocity fluctuations (w -control). The contour levels normalized by u_{τ_w} range (a) from -1 to 1 by increments of 0.1; (b) from -2 to 2 by increments of 0.2. Negative contours are dotted.

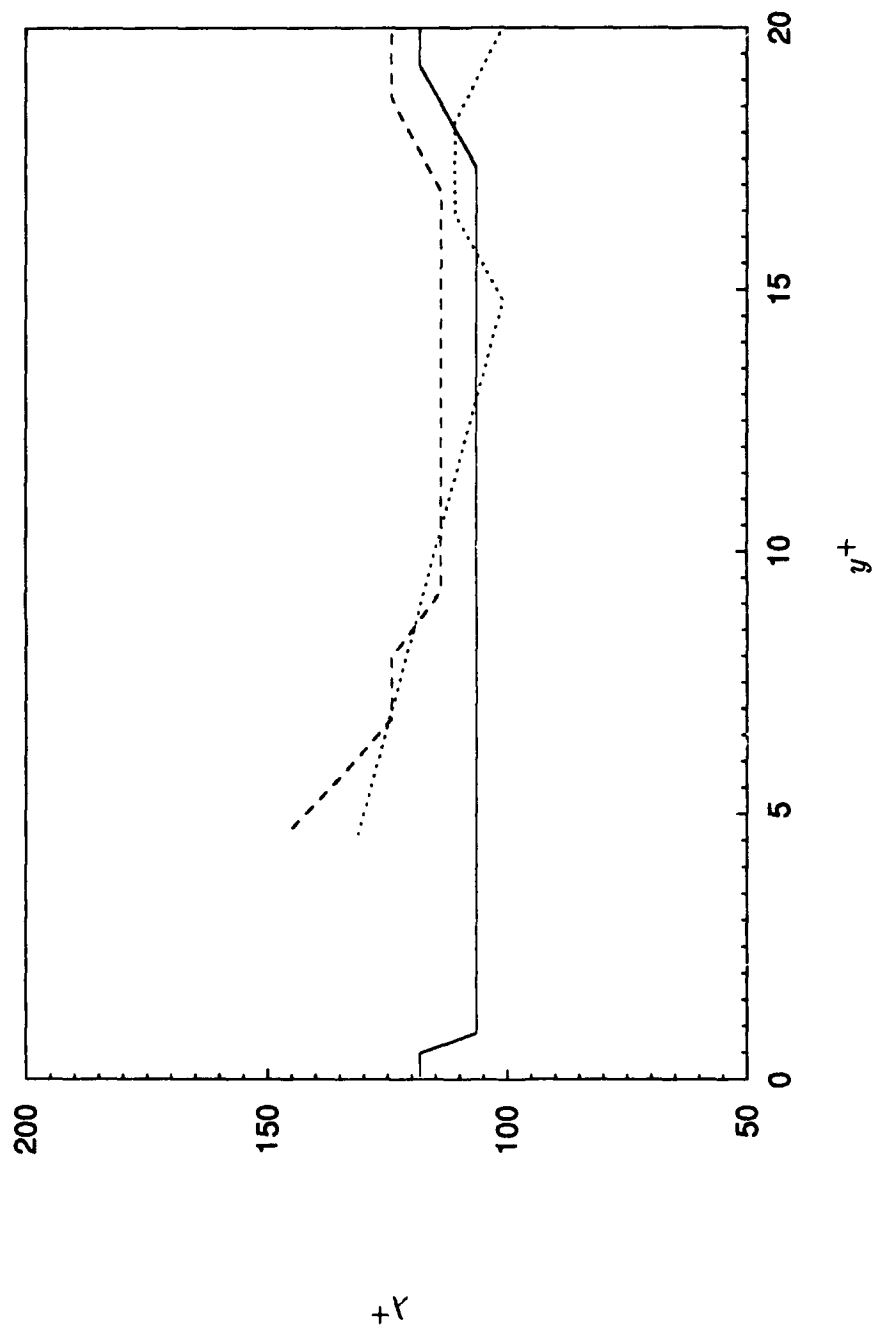


FIGURE 36. Variation of mean spanwise streak spacing with distance from wall estimated from the two-point correlations, $R_{uu}(r_z^+)$. —, No control; ---, v -control; ·····, w -control. Values are non-dimensionalized by the local wall-shear velocity.

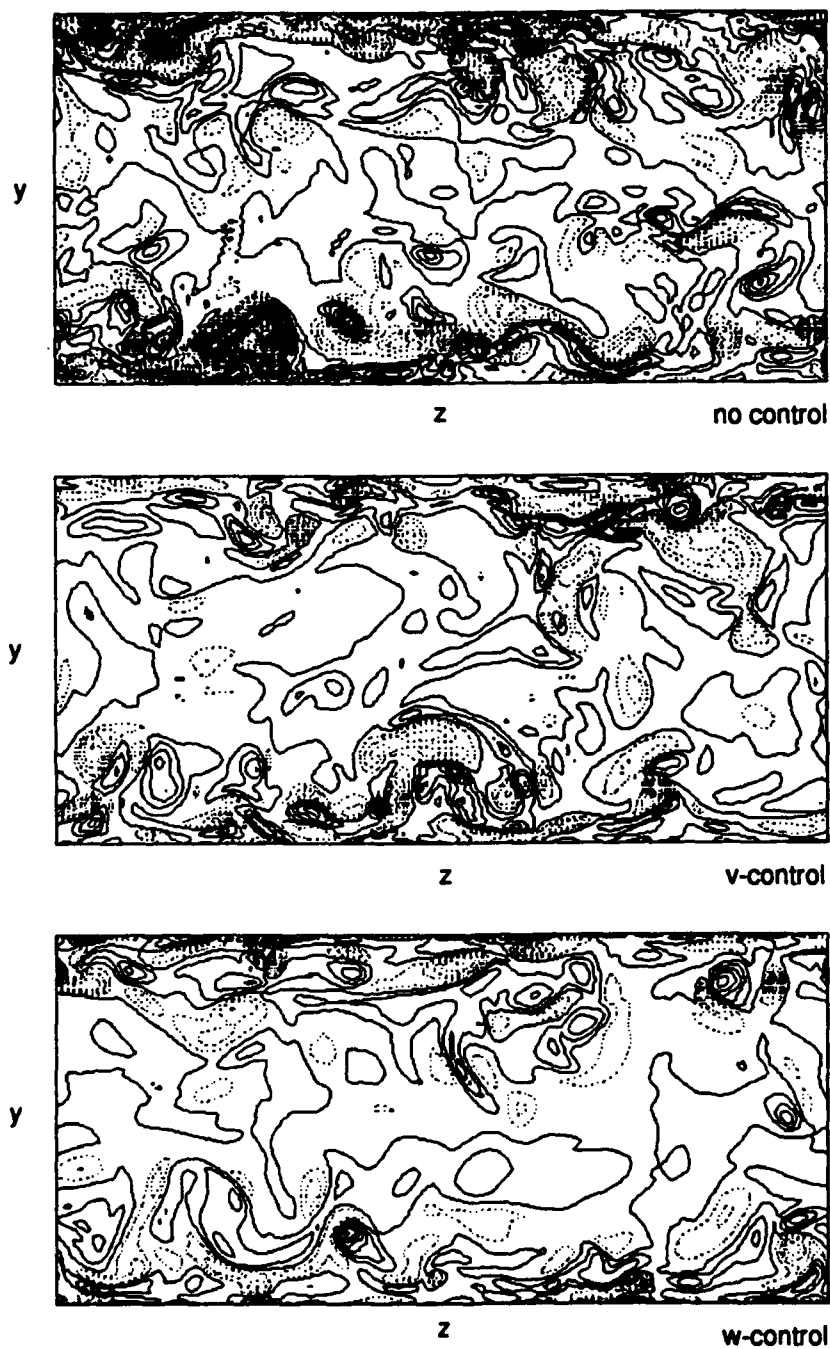


FIGURE 37. Contours of streamwise vorticity fluctuations in a cross-flow plane. The contour levels range from $\omega_x \delta / u_{\tau u} = -120$ to 120 by increments of 10. Negative contours are dotted. The plot domain extends from the lower wall to the upper wall in y .

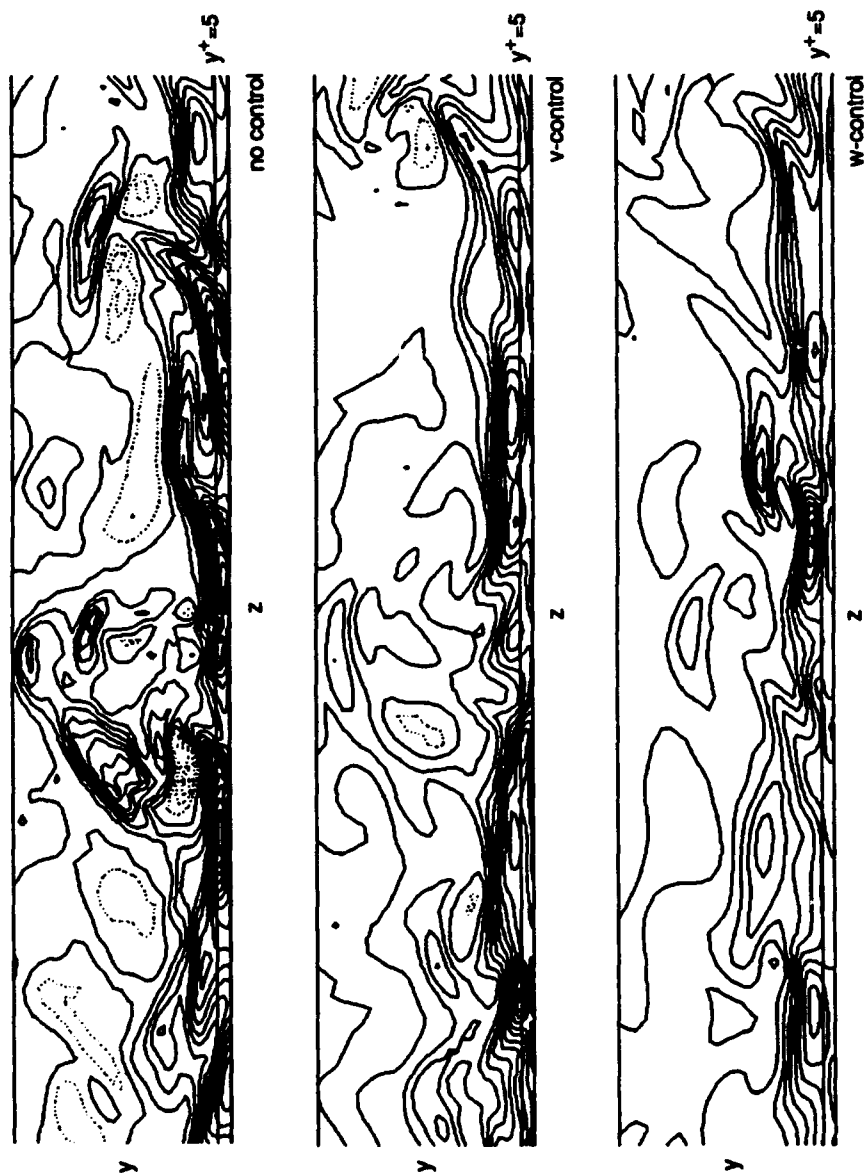


FIGURE 38. Contours of spanwise vorticity fluctuations in a cross plane. The contour levels range from $\omega_z \delta / u_{\tau_0} = -340$ to 100 by increments of 20. Positive contours are dotted. The plot domain extends from $y/\delta = -1$ (lower wall) to $y/\delta = 0.5$.

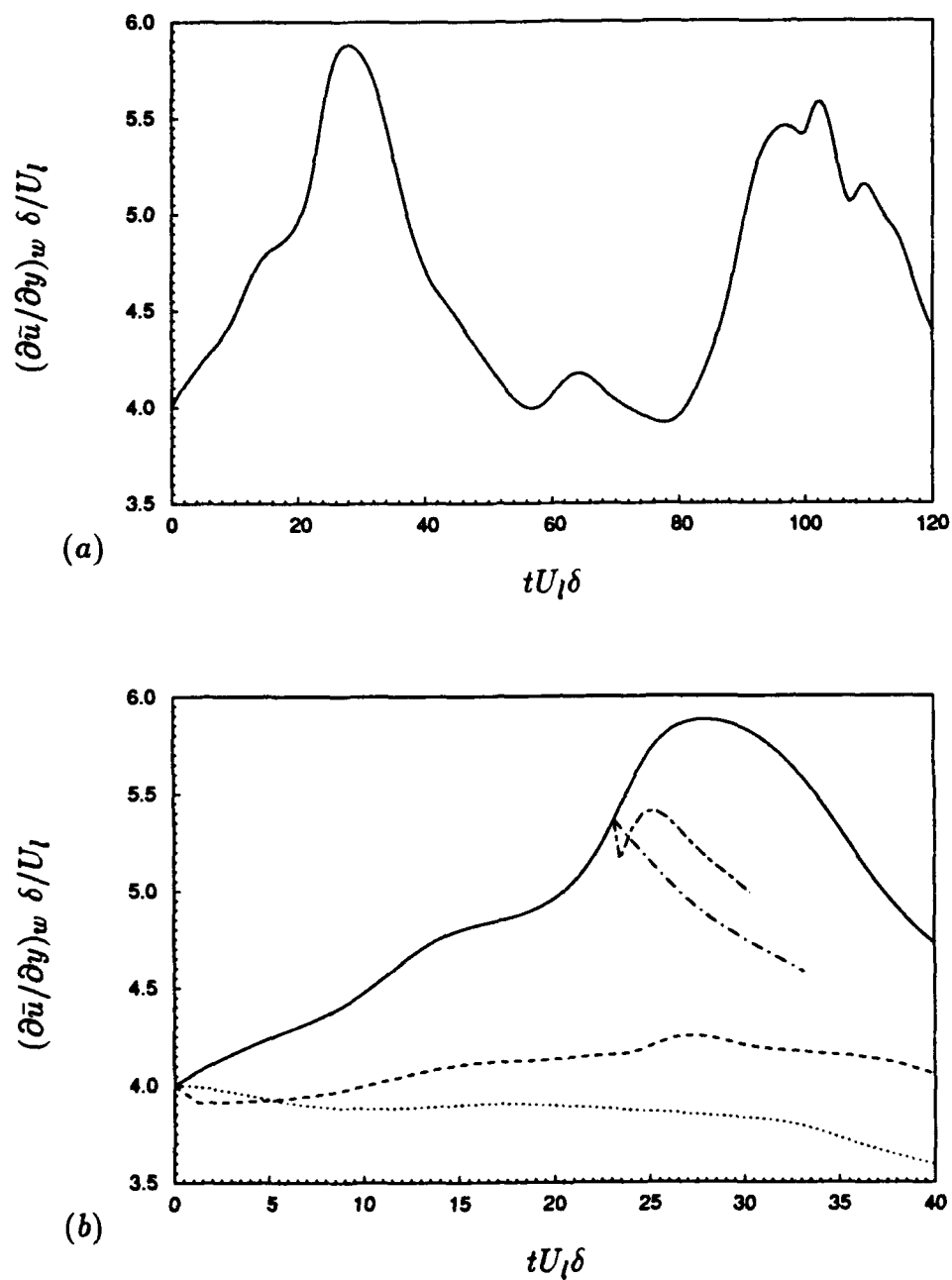


FIGURE 39. Time history of the horizontally averaged wall-shear rate at the lower wall for minimal channel flow: (a) —, no control; (b) —, no control; ----, v -control (SEQ1); ·····, w -control (SEQ1); ---, v -control (SEQ2); —·—, w -control (SEQ2). $(\partial \bar{u} / \partial y)_w \delta / U_l = 2$ corresponds to fully developed laminar channel flow.

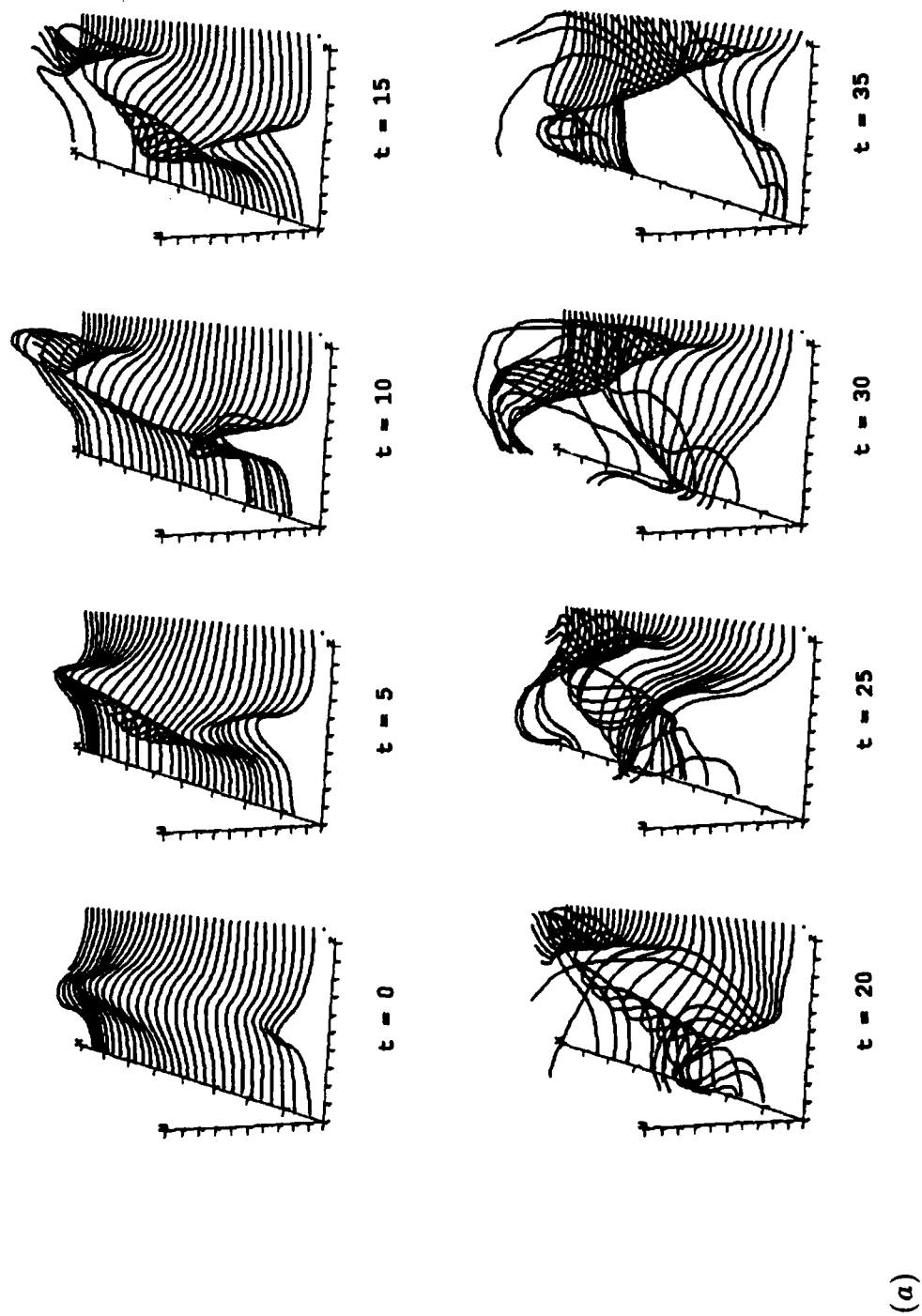
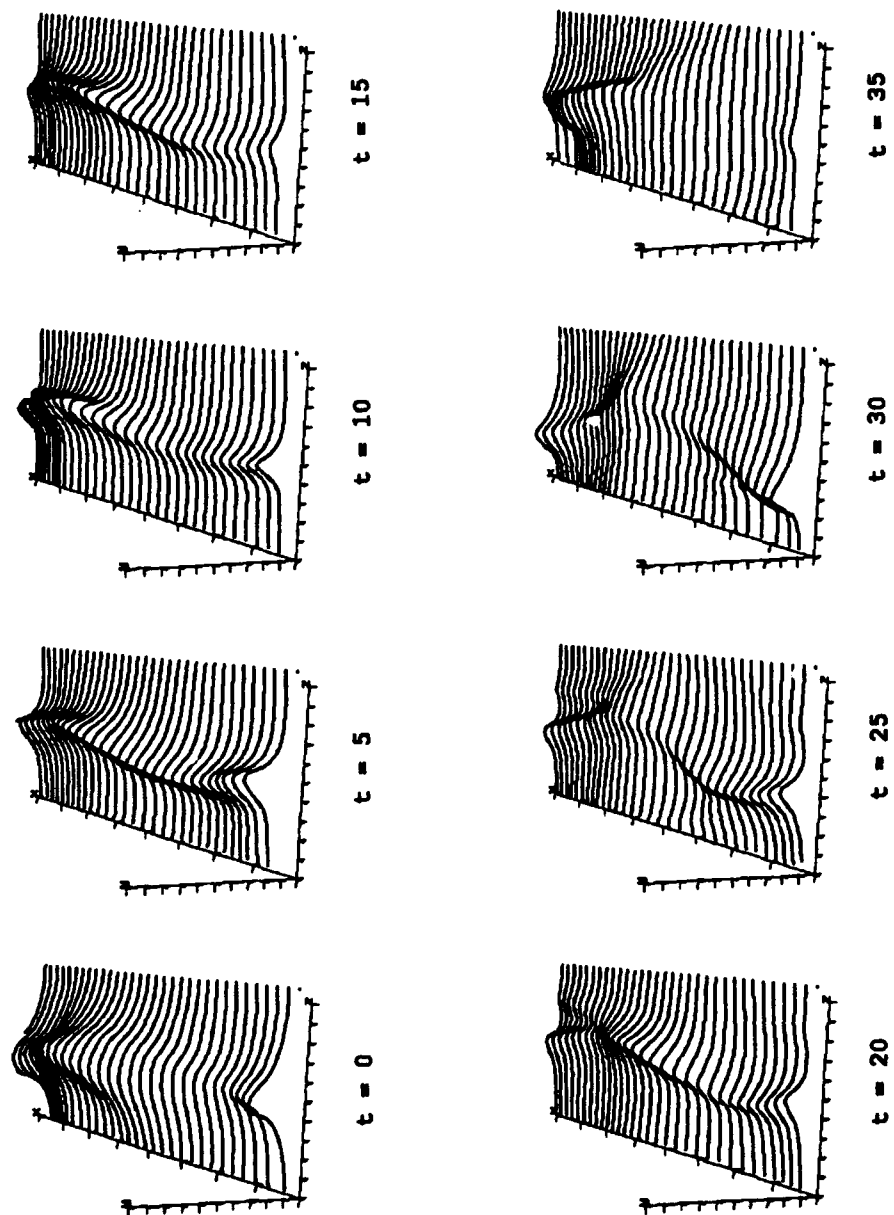


FIGURE 40. For caption see the following page.



(b)

FIGURE 40. For caption see the following page.

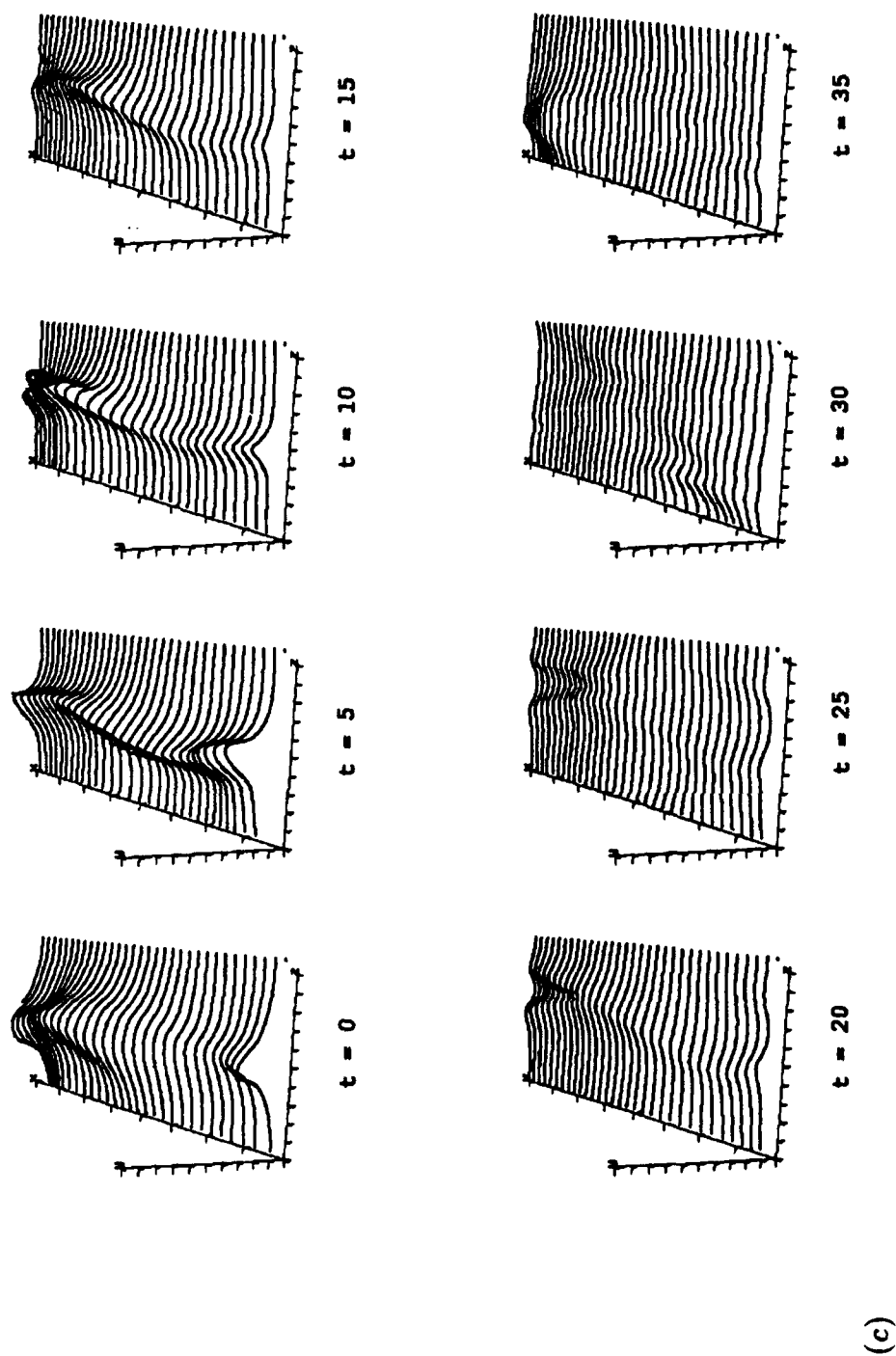
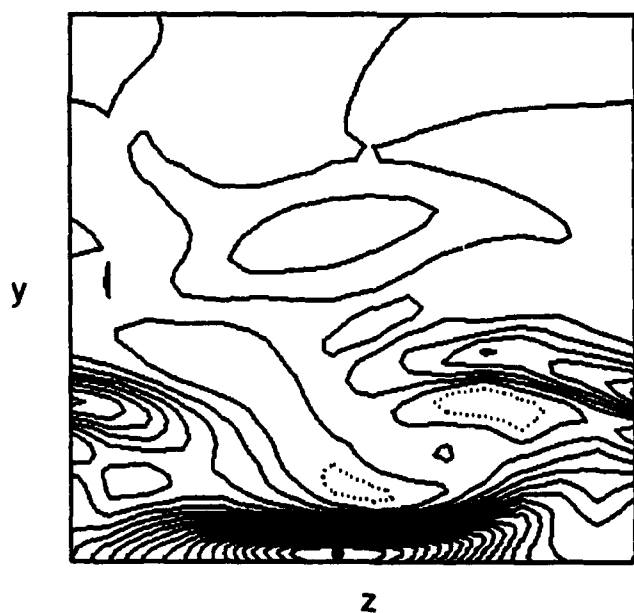
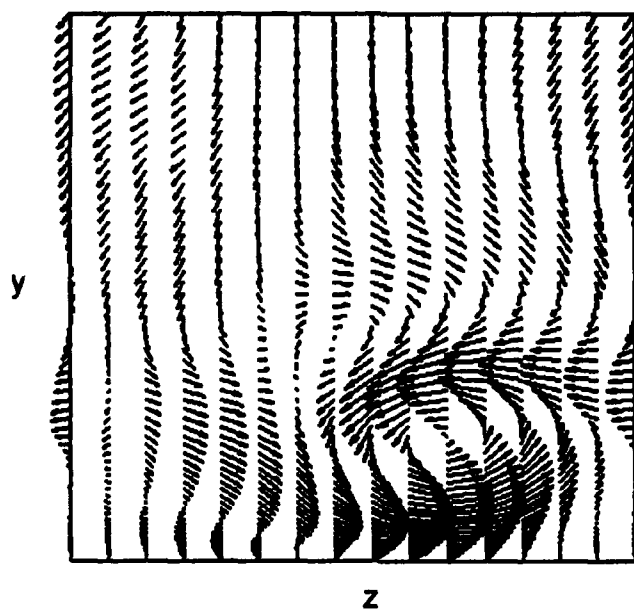
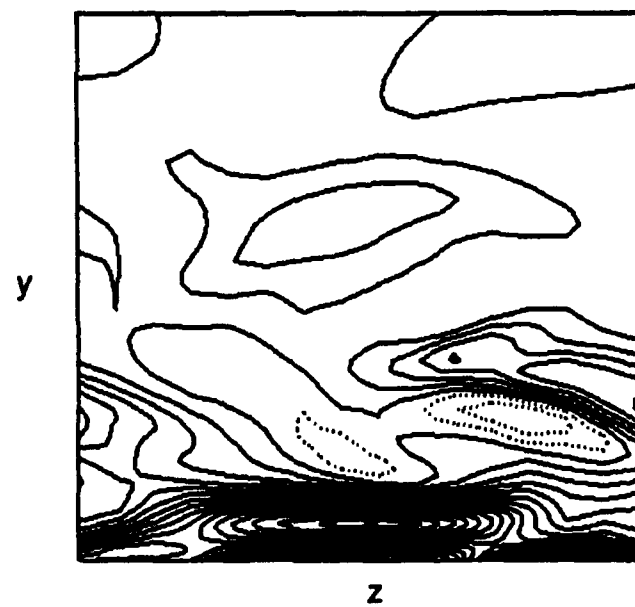
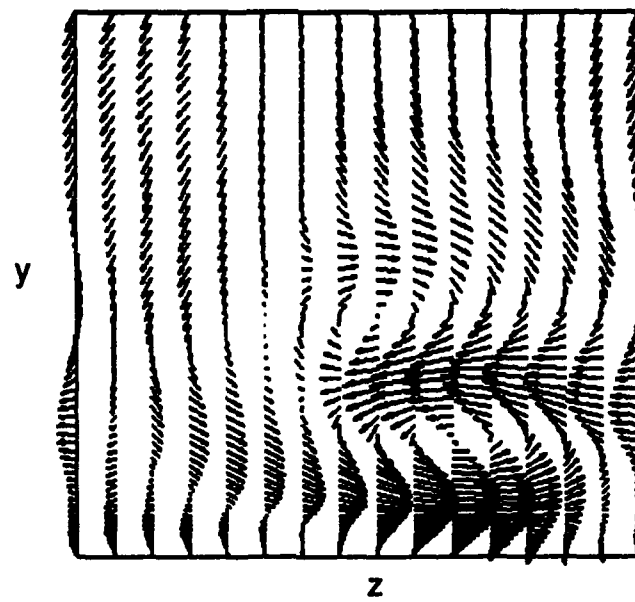


FIGURE 40. Time sequence of the evolution of the wall vorticity layer for minimal channel flow: (a) no control; (b) v -control; (c) w -control. Flow is into the page. Vortex surface is initiated from the right edge of the computational domain at $y^+ \approx 7.5$. Full computational box ($L_x = \pi\delta$ and $L_z = 0.35\pi\delta$) is shown.



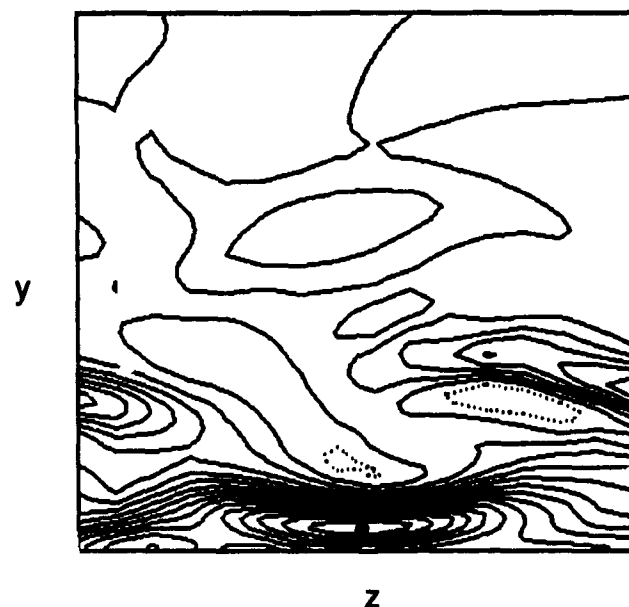
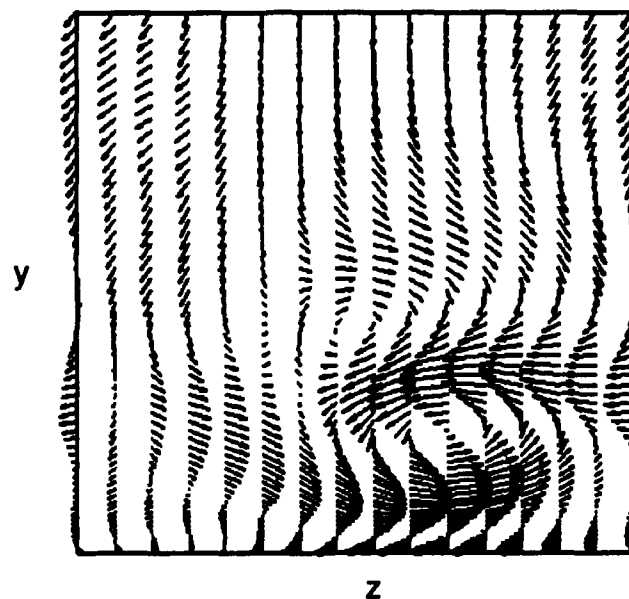
(a)

FIGURE 41. For caption see the following page.



(b)

FIGURE 41. For caption see the following page.



(c)

FIGURE 41. Velocity vector (v, w) and contours of the spanwise vorticity in a (y, z) plane: (a) no control; (b) v -control; (c) w -control. The contour levels range from $\omega_z \delta / U_l = -10$ to 2 by increments of 0.5. Positive contours are dotted. • denotes the location of the maximum spanwise vorticity. The plot domain extends from the lower wall to the centerline.

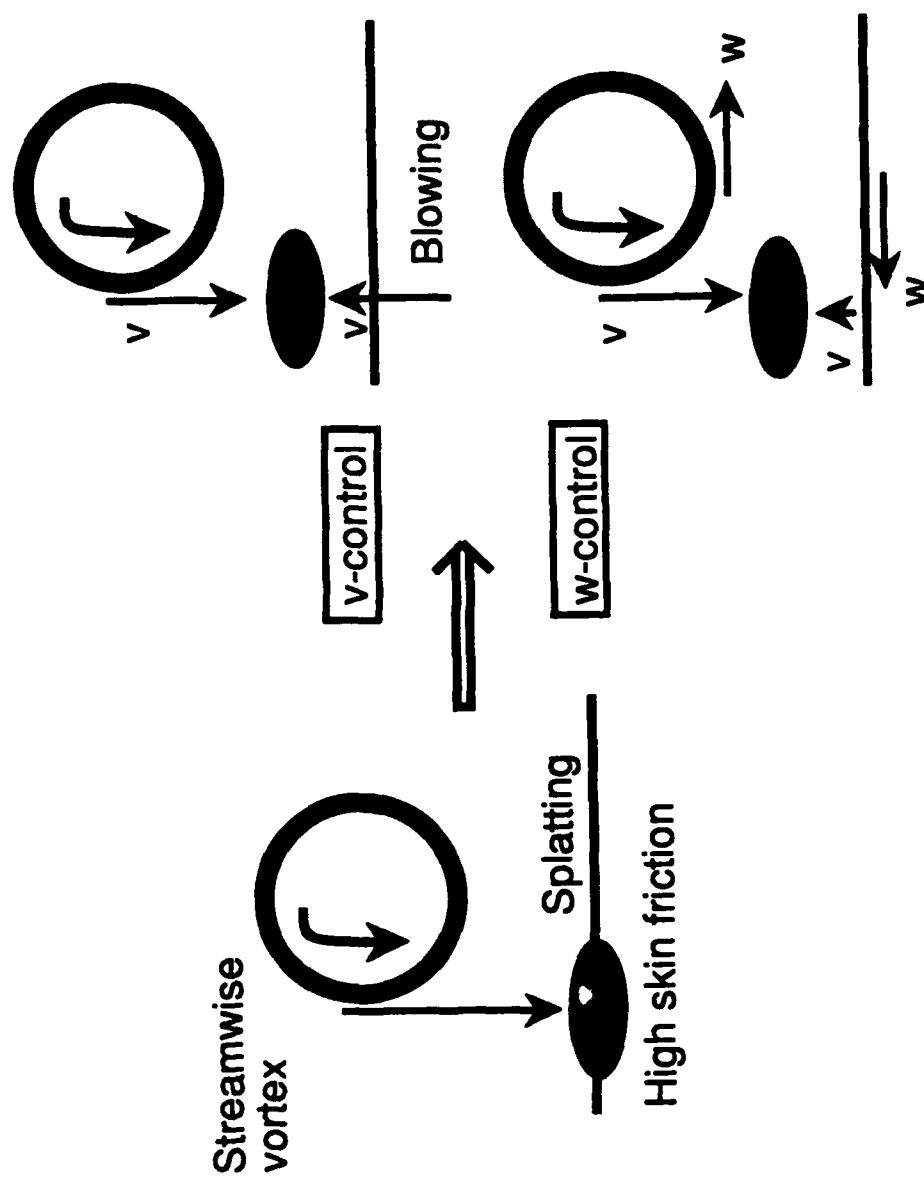
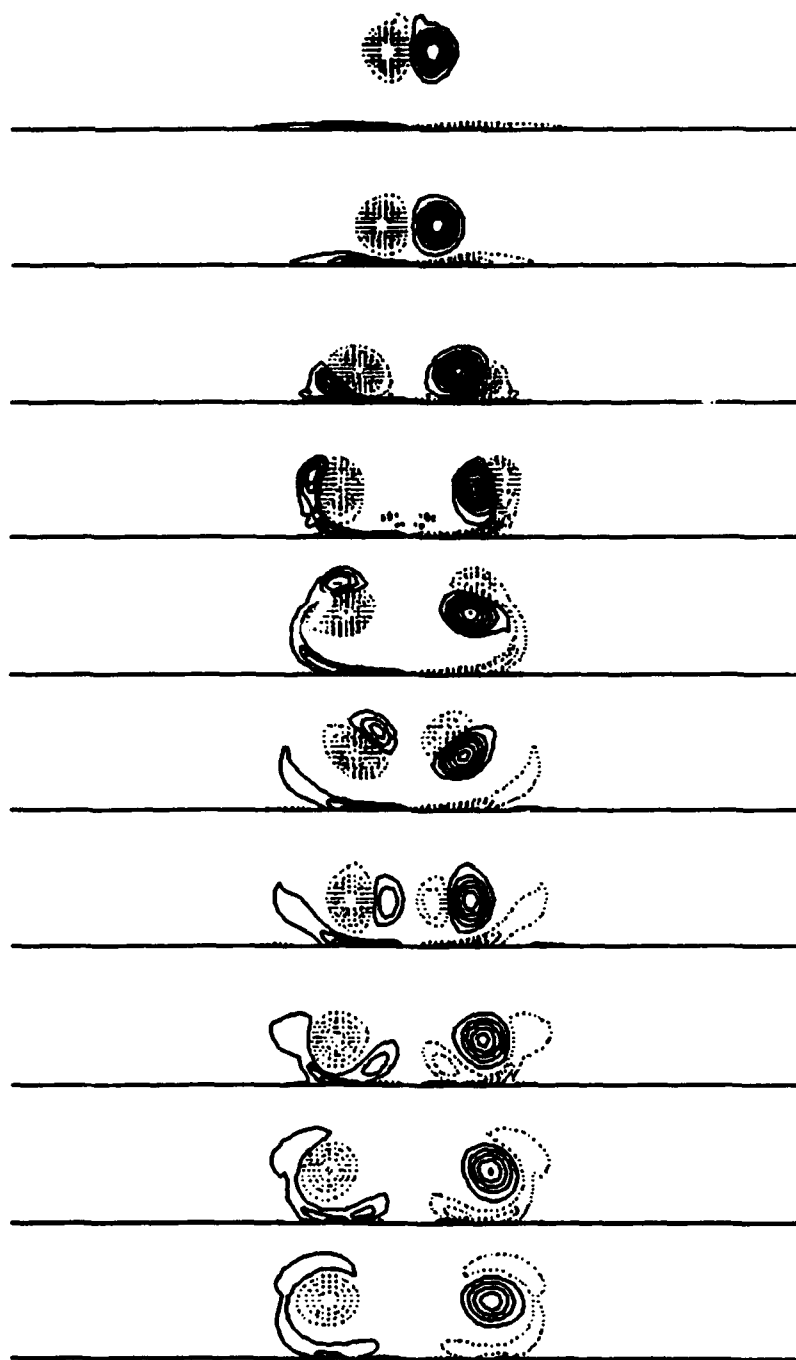
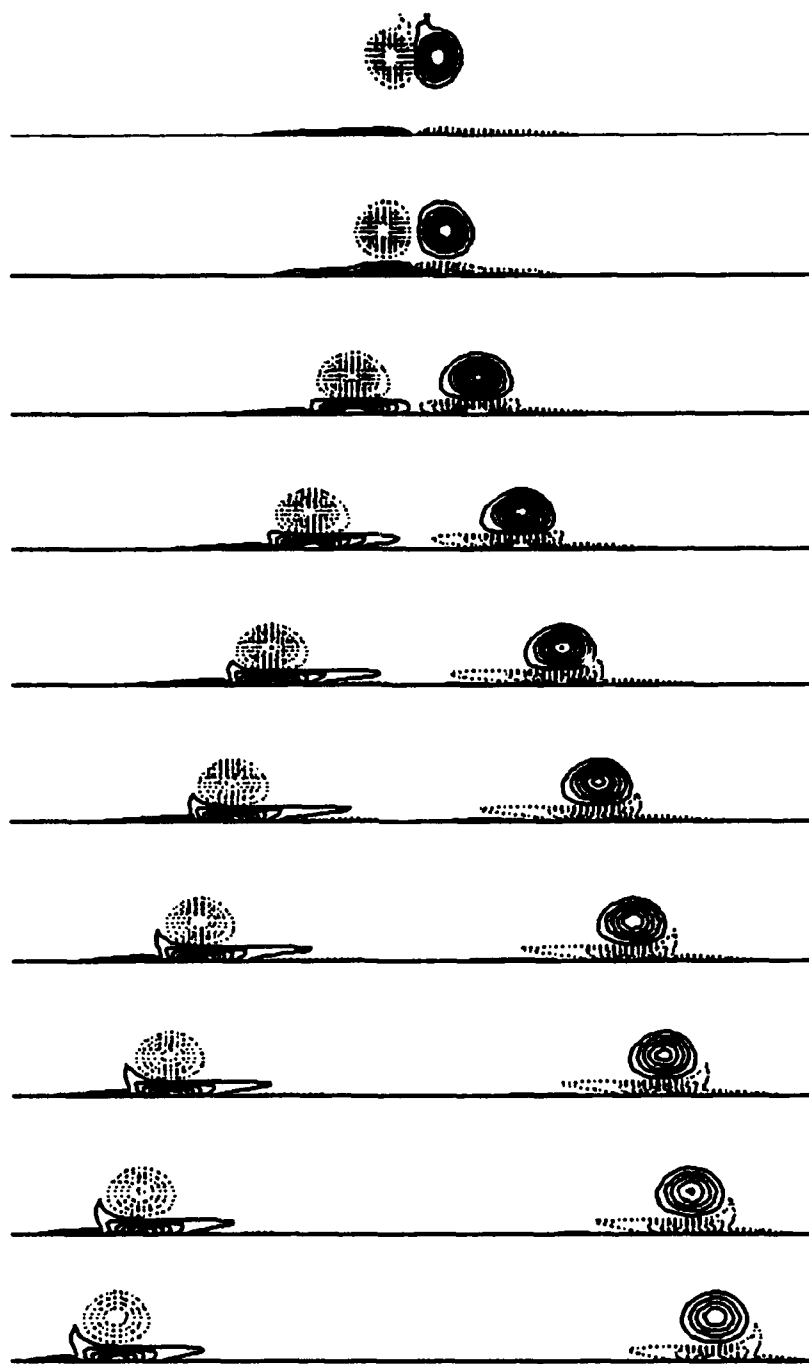


FIGURE 42. Schematic diagram of a drag reduction mechanism by active controls in a cross-flow plane.



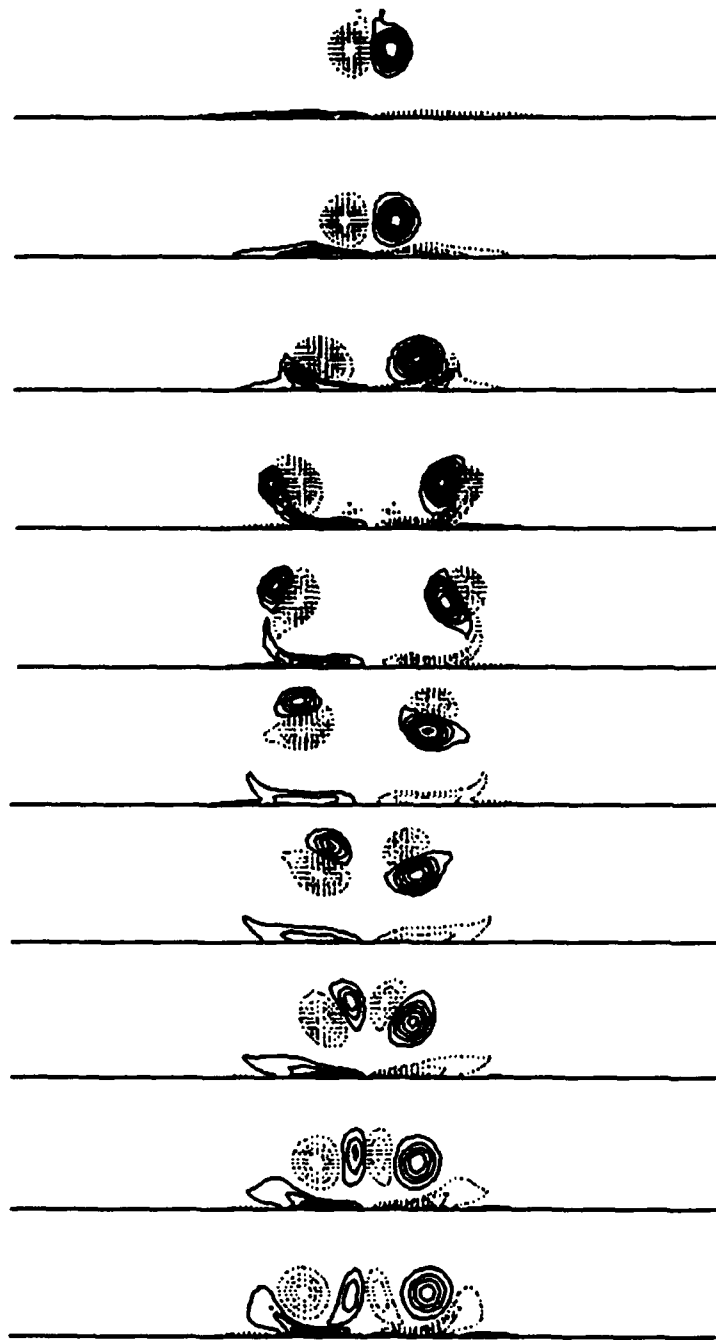
(a)

FIGURE 43. For caption see the following page.



(b)

FIGURE 43. For caption see the following page.



(c)

FIGURE 43. Time sequence of the evolution of a vortex dipole from $\Gamma t/\delta^2 = 1$ to 10 with increments of 1: (a) no control; (b) v -control; (c) w -control. The flow fields from $\Gamma t/\delta^2 = 0$ to 1 are identical regardless of boundary manipulations. Time increases from top to bottom. The contour levels of the vorticity ($\omega_x \delta^2/\Gamma$) range from -15 to 15 by increments of 2. Negative contours are dotted.

CHAPTER 5

CONCLUSIONS AND DISCUSSIONS

Active control strategies were investigated for the purpose of drag reduction using direct numerical simulation of turbulent channel flow. These included controls with the normal, spanwise and streamwise velocities, control with selective normal velocity, and control with the sensors at the wall. The skin-friction reduction was measured in terms of the change in the mean pressure gradient necessary to drive the flow with a fixed mass flow rate. The algorithm was based on the input velocity at the wall being proportional to the instantaneous velocity at a location near the wall. For instance, in the case of the normal-velocity control, the blowing or suction velocity at the wall was exactly opposite to the normal component of the velocity at a prescribed y -location, y_d . The optimum location for matching the velocity was $y_d^+ \approx 10$. Approximately 20 – 30% reduction in the skin friction was achieved by controlling either the normal or the spanwise velocity at the wall.

In selective control experiments which affected only the strong events, the input control velocity was applied at the surface only when the normal velocity at the sensor location y_d exceeded a threshold value, v_{th} . In comparison to the 25% reduction for $v_{th} = 0$, 20% and 15% reductions were obtained with $v_{th} = v_{rms}$ and $v_{th} = 2v_{rms}$, respectively, where v_{rms} is the root-mean-square value of the normal velocity at $y = y_d$. Only 25% and 5%, respectively, of the total surface area were controlled, indicating that most of the drag reduction was indeed due to the suppression of the stronger events.

Control of turbulent boundary layers by placing sensors only at the wall was investigated for practical implementation. It was found that $g_w = \partial/\partial z (\partial w/\partial y)|_w$, which is a leading term in the Taylor series expansion of v near the wall, was the best surface detection criterion. A control based on this variable yielded about 6% drag reduction. Application of optimal control theory to turbulent channel flow resulted in an expression for the optimal input velocity which contained g_w as well as the linearized adjoint wall pressure fluctuations. However, the implementation of this control algorithm was impractical.

The statistics of the manipulated channel flows were compared to those of the unmanipulated channel flow. The mean velocity as well as turbulent intensities were altered by the boundary modification. An upward shift in the log law and an increase of the viscous sublayer thickness were obtained in the manipulated channels, which had been observed previously in other drag-reduced flows. The major difference among the data sets was the apparent outward shift of the controlled data, suggesting a displaced virtual origin of the boundary layer and a thickened sublayer. The value of the outward shift of flow variables was approximately 5 wall units, which coincided with the increased viscous sublayer thickness.

Velocity, pressure, and vorticity fluctuations as well as the Reynolds shear stress were significantly reduced throughout the channel. This change of turbulence intensity with the active control schemes was in sharp contrast to the result of using a compliant surface or longitudinal riblets, in which only local modifications in the near-wall region were observed. Instantaneous flow fields showed that streaky structures below $y^+ \approx 5$ were clearly diminished by the active control, and the spacing of the streaky structure above $y^+ \approx 5$ was increased in the manipulated channels.

Drag reduction mechanisms were studied with two different approaches: a minimal channel flow and an isolated vortex pair interacting with a wall. Time sequences of the flow fields in the minimal channel showed that there were two essential drag reduction mechanisms. Firstly, within a short time after control is applied, drag is reduced mainly by deterring the sweep motion without modifying the primary streamwise vortices above the wall. Consequently, the high skin-friction regions on the wall are lifted to the interior of the channel ($y^+ \approx 5$) by the control schemes. Secondly, the active control changed the evolution of the wall vorticity layer by stabilizing and preventing lifting of the spanwise vorticity near the wall. The absence of this lifting process suppresses a possible source of new streamwise vortices above the wall.

In order to isolate the effect of the control schemes on the dynamics of a primary streamwise vortex above the wall, a two-dimensional vortex dipole interacting with a wall was simulated with and without boundary manipulation. The effects of the normal and spanwise velocities at the wall on the primary streamwise vortex pair were significantly different. The control scheme with the normal velocity altered the mutual interaction between the primary vortex pair and the secondary vorticity

by preventing the lifting of the secondary vorticity. On the other hand, the vortex motion with the spanwise-velocity control was quite similar to that in the unmanipulated channel. There was clear lifting of the secondary vorticity. However, the stronger secondary vorticity created by the spanwise-velocity control changed the location of the primary vortex pair as well as the flow time scale.

PART II

Feedback Control for Unsteady Flow and Its Application to the Stochastic Burgers Equation

CHAPTER 1

INTRODUCTION

Many strategies of controlling turbulent flows have been investigated to achieve different goals such as drag reduction and heat and mass transfer augmentation. There are, in general, many ways of reducing the skin-friction by *passive* means: riblets, large eddy break-up (LEBU) devices, compliant walls, polymer addition, etc (for a succinct summary of this subject, see Bushnell & McGinley 1989). Among them, surface mounted longitudinal grooves in turbulent boundary layers are most successful in reducing net drag, in spite of a substantial increase in the surface area (see e.g. Bechert & Bartenwerfer 1989, Walsh 1983 and PART III of the present study).

In PART I of the present study, we used the direct numerical simulation technique to explore concepts for *active control* of turbulent channel flow with the goal of drag reduction using selective blowing and suction at the wall. The drag reduction (about 20%) was accompanied by significant reductions in the intensity of the wall-layer structures and reductions in the magnitude of Reynolds stresses throughout the flow. Experimental efforts using active (or feedback) control devices to control turbulence are described in Bushnell & McGinley (1989).

When certain aspects of the physics of a problem are well-known, such as the existence of organized patterns, one can devise a scheme to manipulate these patterns, or at least impede or amplify their formation by preassigned kinematic modifications. However, when the physics of a phenomenon is not known or is very complicated, it is tempting to appeal to the more systematic but less intuitive methods of *control theory*. This is the objective of this work: to provide a framework for systematic control of turbulent flows.

The issue of minimizing turbulence in an evolutionary Navier-Stokes flow was addressed from the point of view of *optimal control* by Abergel and Temam (1990). They derived theoretical results for various physical situations. However, the application of their optimal control algorithm to the unsteady three-dimensional Navier-Stokes equations is not practical due to the great complexity of the algorithm.

In fact the problem of controlling turbulent flows using control theory is considerably difficult. We encounter here two major difficulties which have been addressed by two different segments of the scientific community: the control of nonlinear systems studied mostly in the control community, and the problems related to the resolution of two or three dimensional flows, in the presence of turbulence and complicated geometries, studied by the fluid mechanics community.

While the control of linear systems is fairly well understood, the control of nonlinear systems remains the subject of active research at this time, even in finite and small dimensions. For such applications as the control of flight or the control of industrial processes, the objective has been to improve the control processes based on a simplified linear description of the process. The basic theoretical as well as practical issue is the determination of efficient nonlinear feedback controllers. However, as is well known in the fluid mechanics community, nonlinearity leads to complex and often chaotic behaviors and linearization of the governing equations produces approximations that are only valid for a limited time.

Nonlinear control theory has been studied by Lions (1971), in his early work on distributed systems, i.e. in infinite dimension; he addresses the question of existence of an optimal control and the derivation of necessary conditions. Nonlinear control theory has been addressed more recently by numerous authors from the point of view of H^∞ theory; see, among others, Foias & Tannenbaum (1989) and for the infinite dimensional case Barbu (1992). Feedbacks of nonlinear distributed systems are addressed for instance by Banach & Baumann (1990), Byrnes & Gilliam (1991), and Kang *et al.* (1991) for the Burgers equation.

The control of fluid flow itself is a rapidly developing subject which has been already addressed by several authors. Beside the work mentioned at the beginning of this introduction, emanating mostly from the fluid mechanics community, more theoretically oriented work can be found in Gunzburger *et al.* (1991, 1992), Sritharan *et al.* (1991) and Abergel & Temam (1990, 1992); see also the references above for the Burgers equation and the book edited by Sritharan (1992) and the proceedings of the IMA Conference edited by Gunzburger (1992).

Let us summarize for the more mathematically oriented reader the theoretical and numerical work done on control of flows. Gunzberger *et al.* consider various optimal control problems (open loop) in fluid mechanics and study mathematical and

numerical problems such as the existence of optimal controls, necessary optimality conditions of the first order, the discretization of these problems by finite elements, convergence and error estimates for the discrete problems. Sritharan and coauthors consider also mathematical and numerical problems for control of flows. For open loop problems they provide the open loop control using an appropriate version of the Maximum Principle of Pontryagin. They study theoretical questions concerning closed loop problems in relation with the Hamilton-Jacobi-Bellman equation. This approach provides in principle the feedback law corresponding to the optimal control but necessitates the solution of hyperbolic equations in infinite (or large) dimensions. In the articles mentioned above concerning the optimal control of the Burgers equation, the authors introduce a feedback law for a related linear problem. The solution of the Burgers equation supplemented with this feedback forcing is then studied; it is shown that damping is enhanced and this is numerically confirmed for solutions of these equations which display a discontinuity (shock). Finally the work of Abergel & Temam (1990, 1992) already referred to, concerns theoretical and numerical problems for the control of turbulence: for several physically relevant situations the problem is set as an optimal control problem, existence of optimal control is proved; necessary conditions of optimality are derived; gradient type algorithms are described which necessitate the classic techniques of control theory (in particular adjoint state and adjoint equations) for their effective implementation.

The work that we present here departs from the previous works. Instead of searching for an *optimal control*, we address the more practical problem of trying to reduce the cost function through a procedure which could be efficiently implemented, i.e. we favor effectiveness over optimality. The determination of the cost function is a part of the modelling of the control problem. As it is explained later, the cost is a weighted sum of the cost generated by the flow that we want to reduce (e.g. the drag force), and the cost of the work necessary to implement the control. From the point of view of control theory the method that we present here is a suboptimal procedure based on the determination, *at each instant of time*, of the best control among an *a priori* chosen class of feedback controls. For cases in which off-line optimal designs can be constructed, the implementation of real time feedback controllers usually requires much more computational power than off-line optimal designs. However, it is quite difficult to implement a simple off-line optimal controller for unsteady flows, particularly for turbulent flows. The optimal control

procedures suggested by Abergel & Temam (1990) require the iterative solution of the Navier-Stokes equations and their adjoint on the *global time period*; such computations are out of reach at this time (see also appendix A). Accordingly, the implementation of off-line and on-line optimal controllers for unsteady flows, especially for turbulent flows, is very difficult. Hence, as compared to optimal control, our suboptimal feedback procedure does not require excessive computer resources because it only requires information at each instant of time. At this stage, we do not have any theoretical justification of our method from the point of view of control theory, except the good numerical results.

As a first step towards the solution of the much more difficult problem of controlling the Navier-Stokes equations, we consider here the control of systems governed by the Burgers equation. The Burgers equation has been studied extensively both theoretically and numerically. The Burgers equation describes the formulation and decay of weak waves in a compressible fluid as well as being a one-dimensional model of the Navier-Stokes equations. Chambers *et al.* (1988) showed that the statistics of the solutions of the Burgers equation subject to random forcing qualitatively resemble those of the velocity fluctuations normal to the wall in the direct numerical simulation of channel flow by Kim *et al.* (1987).

The objective of this study is to develop a feedback control method of minimizing a cost function, and to apply that method to the Burgers equation as a first step towards application to fluid mechanics problems. The extension of the feedback control algorithm to the Navier-Stokes equations will necessitate more delicate developments and more extensive computer resources and will be addressed in the future. Chapter 2 is partly expository and directed to fluid mechanicians not familiar with control theory. It shows how to cast the problem of controlling turbulence in a channel flow into a problem in optimal control theory, and introduces the formalism and language of control theory. Chapter 3 describes our feedback control algorithm for general stationary and time-dependent problems. Also, chapter 3 presents the method for the purpose of suboptimal feedback laws when an analytical representation of feedback laws, i.e. an explicit functional dependence between the quantity being measured by a sensor and the quantity being controlled by an actuator, is difficult. Then in chapter 4 we apply this method to the distributed and boundary controls of the stochastic Burgers equation. The results of numerous

computations with or without control are presented and discussed. A computational issue together with practical (or physical) implementation of the present control algorithm is also addressed in chapter 4. Our method depends partly on the time-discretization method for the state equation, namely the Burgers equation. Hence we study in this chapter the effect of the time-discretization method on the control algorithms and present the results of the practical control algorithm. Conclusions and discussions are given in chapter 5. Appendices B, C and D contain some technical details on the implementation of the control algorithms.

CHAPTER 2

INTRODUCTION TO CONTROL THEORY: SOME MODEL PROBLEMS IN FLOW CONTROL

Keeping in mind that turbulent flows are time dependent, we will distinguish between stationary and time-dependent flows and start with the case of stationary flows.

2.1 Stationary channel flow

Consider a stationary channel flow, where x is the streamwise direction, z is the spanwise direction, and the walls are at $y = \pm 1$. The mass flux is prescribed and is equal to M . Periodicity of velocities and pressure is assumed in the z direction, and periodicity of velocities with an unknown drop of pressure is assumed in the x direction. Let $u = (u_1, u_2, u_3)$ denote the velocity vector of the fluid, and assume that the flow is controlled through blowing and suction at the wall, i.e. through the wall-normal velocity at the wall

$$\phi = u_2|_w, \quad (2.1)$$

where $\int \int \phi \, dx_1 dx_3 = 0$ is imposed so that the mass flux M is constant. It can be shown that the stationary Navier-Stokes equations reduce to a functional equation for u (see e.g. Temam 1984, 1991) involving ϕ :

$$\nu Au + R(u, \phi) = 0. \quad (2.2)$$

Here $\nu > 0$ is the kinematic viscosity, A is the so-called Stokes operator, and R corresponds to the inertial and boundary terms and is a function of u and ϕ ; R actually depends on M although the dependence is not made explicit here.

A typical optimal control problem for equation (2.2) is the following: find the best ϕ such that some observation $\gamma = Cu$ achieves some desired value γ_d or is at least as close as possible to γ_d , where C is a general linear or nonlinear operator which may involve integrals of u and/or derivatives of u . In the language of control theory:

u is the *state* of the system and equation (2.2) is the *state equation*;

ϕ is the *control*;

γ is the *observation*.

The *cost function* could be, for instance, the function $J = J(\phi)$ [†]

$$J(\phi) = \frac{l}{2} \|\phi\|^2 + \frac{m}{2} \|Cu - \gamma_d\|^2. \quad (2.3)$$

Here $\frac{m}{2} \|Cu - \gamma_d\|^2$ ($m > 0$, $\|Cu - \gamma_d\| = L_2$ norm of $Cu - \gamma_d$) accounts for the *cost* of γ being different from γ_d ; $\frac{l}{2} \|\phi\|^2$ ($l \geq 0$, $\|\phi\| = L_2$ norm of ϕ) is the cost of implementing the control itself; l/m is small or zero for cheap controls and large for expensive controls. For example, high blowing and suction flow rates are reflected in high values of $\frac{l}{2} \|\phi\|^2$. High values of l/m may also be used to empirically account for indirect costs such as expensive equipments for realizing fast actuator response. Values of l and m in the cost function are dimensional quantities and are usually prescribed from a parametric study. Keep in mind, however, that equation (2.2) is an idealized problem which, due to the absence of turbulence, would only make sense physically for very viscous fluids.

The mathematical formulation of the problem is the following:

Find ϕ which minimizes J subject to equation (2.2), i.e. in the notations used in the optimization theory, [‡]

$$\text{Inf}_{\phi} J(\phi). \quad (2.4)$$

The control ϕ can be unrestricted or restricted to some admissible set of controls \mathcal{U}_{ad} due to physical and technological limitations.

[†] u is a function of ϕ through (2.2), $u = u(\phi)$. Hence the second term of J is also a function of ϕ . Note that u is the traditional notation for the control in control theory, and it is also commonly use u for the velocity in fluid mechanics. We use the latter convention here.

[‡] In optimization theory $\text{Inf}_{\phi} J(\phi)$ denotes indifferently the problem of minimizing $J(\phi)$ in the class of ϕ 's or the actual value of the corresponding infimum.

The methods of calculus of variations indicate that a problem such as (2.4) possesses at least one solution and give us some characterizations on the best ϕ through the adjoint state and some algorithms to reach the best (optimal) control. Feedback theory involves constructing ϕ as a function of u or some observation of u . Although feedback schemes are mainly relevant to time-dependent problems, we can formulate such a scheme here.

Searching for the best feedback in a prescribed class of feedbacks, we reduce the problem to a parameter optimization one. For instance, without advocating such a choice, we could look for

$$\phi = E + Fu, \quad (2.5)$$

where E and F are a scalar function on the wall and an operator to be determined, respectively. Now problem (2.4) with equation (2.5) substituted into equation (2.2) becomes:

Find E, F which minimize $J(\phi) = \tilde{J}(E, F)$ subject to equations (2.2) and (2.5):

$$\inf_{E, F} \tilde{J}(E, F). \quad (2.6)$$

Instead of equation (2.5) more general shape functions $\theta_0(u), \dots, \theta_r(u)$ could be considered with

$$\phi = \sum_{i=0}^r \alpha_i \theta_i(u). \quad (2.7)$$

The practical importance of these shape functions is discussed in sections 3.1, 4.3 and 4.4. Note that as in equation (2.5), the θ_i 's are functionals of u and not simple pointwise functions. They may involve complex or nonlocal operations such as differentiation or integration of u . The α_i 's are determined through a control algorithm and thus are *a posteriori* functions of u .

2.2 Time-dependent channel flow

The *state equation* is the Navier-Stokes equations including the boundary condition (2.1) and other boundary conditions. We infer from the mathematical theory of the Navier-Stokes equations (see e.g. Ladyzhenskaya 1963 and Temam 1984,

1991) that these conditions and equations amount to an evolution equation of infinite dimension for the velocity field $u = u(x, t)$. It reads (compare to equation (2.2))

$$\frac{\partial u}{\partial t} + \nu Au + R(u, \phi) = 0. \quad (2.8)$$

Here u is the velocity vector field; again, R accounts for the inertial and boundary terms and depends on the mass flux M , although the dependence on M is not made explicit here.

The drag is essentially measured on average by $D = D(u)$:

$$D = \int \int \left[\frac{\partial u_1}{\partial x_2} \Big|_{x_2=-1} - \frac{\partial u_1}{\partial x_2} \Big|_{x_2=1} \right] dx_1 dx_3. \quad (2.9)$$

Here $x_1 = x, x_2 = y, x_3 = z$, and $x_2 = y = \pm 1$ are the walls. The choice of the cost function is at our disposal and depends on the costs that we want to reduce. If we choose to reduce a time average of the drag as expressed by equation (2.9), then a plausible cost function could be

$$J(\phi) = \frac{l}{2} \frac{1}{T} \int_0^T \int \int_w |\phi|^2 dx_1 dx_3 dt + \frac{m}{2} \frac{1}{T} \int_0^T |D|^2 dt, \quad (2.10)$$

where D is a function of ϕ through u which itself is a function of ϕ . A control problem like (2.4) can be posed:

Find $\phi = \phi(x_1, x_3, t)$ which minimizes J subject to equations (2.8) and (2.10):

$$\inf_{\phi} J(\phi). \quad (2.11)$$

The methods of control theory and calculus of variation (Lions 1971), as developed in Abergel and Temam (1990), prove the existence of an optimal control (the best ϕ) and produce an algorithm for its determination. However, in their present form, and especially for turbulent flows, these classical methods require the iterative solution of the Navier-Stokes equations and their adjoint (see chapter 3) on the whole and large interval $(0, T)$; such computations are out of reach at this time

(see appendix A). Furthermore, optimal control of unsteady flows depends on the initial distribution of velocities $u|_{t=0}$, although one would hope that the effects of initial velocities dissipate as T becomes large.

If equation (2.8) were linear, the optimal control would be given by a linear feedback law:

$$\phi = E + Fu, \quad (2.12)$$

where F is an operator that is the solution of a Riccati type equation, and E is easily determined. When equation (2.8) is nonlinear, to the best of our knowledge there is no general method for constructing the feedback law corresponding to the *optimal* control even for finite and small dimensions (as in flight control), not to mention high or infinite dimensional problems. There is also no general nonlinear estimators and the solution of a control problem could require in principle the repeated solution of the state equation with different forcing terms.

In the next chapter we describe some empirical and not yet fully mathematically justified procedures proposed to address these problems and overcome these difficulties.

CHAPTER 3

SUBOPTIMAL CONTROL AND FEEDBACK PROCEDURES

In this chapter, we present a systematic approach to the mathematical formulation of the problem of minimizing a cost function using feedback control and parameter optimization procedures. We consider first the stationary case and then the more important and more relevant case of time-dependent problems.

3.1 Stationary problem

Equations (2.2), (2.3) and (2.4) define an optimal control problem which can be satisfactorily solved by a gradient algorithm (although a conjugate gradient method would be better, we now restrict ourselves to a gradient algorithm for simplicity).

The gradient algorithm consists of computing the Fréchet derivative [†]

$$\frac{\mathcal{D}J}{\mathcal{D}\phi} \quad (3.1)$$

and using the following iterative process for the cost minimization,

$$\phi^{k+1} - \phi^k = -\rho \frac{\mathcal{D}J}{\mathcal{D}\phi}(\phi^k), \quad (3.2)$$

where ϕ^k is a member of a sequence of controls and ρ is the parameter of descent whose optimal value can be found either by a trial-and-error procedure or by relevant theoretical studies (see e.g. Luenberger 1973). By Taylor's formula and equation (3.2),

[†] When it exists, the Fréchet differential of J in the direction of $\hat{\phi}$ is defined by (Finlayson 1972)

$$\frac{\mathcal{D}J}{\mathcal{D}\phi} \hat{\phi} = \lim_{\epsilon \rightarrow 0} \frac{J(\phi + \epsilon \hat{\phi}) - J(\phi)}{\epsilon}$$

$$J(\phi^{k+1}) \approx J(\phi^k) + \frac{\mathcal{D}J}{\mathcal{D}\phi}(\phi^k) (\phi^{k+1} - \phi^k), \quad (3.3)$$

$$J(\phi^{k+1}) \approx J(\phi^k) - \rho \left| \frac{\mathcal{D}J}{\mathcal{D}\phi}(\phi^k) \right|^2$$

so that the sequence $J(\phi^k)$ is clearly decreasing. With the same methods as in Abergel and Temam (1990) relying on optimization theory, we can prove that the sequence ϕ^k will converge to an optimal control for suitable ρ 's if the initial value ϕ^0 is chosen sufficiently close to an optimal state.

The introduction of the adjoint state and adjoint state equation produces a convenient way to compute the Fréchet derivative (3.1). Let

$$\eta = \frac{\mathcal{D}u}{\mathcal{D}\phi} \hat{\phi}, \quad (3.4)$$

where the right hand side of equation (3.4) is the Fréchet differential of u with respect to ϕ applied to a test function $\hat{\phi}$ (of the same type as ϕ). Then, by Fréchet differentiation of equation (2.2), we promptly see that η is solution of equation

$$\nu A\eta + \frac{\mathcal{D}R}{\mathcal{D}u}(u, \phi)\eta + \frac{\mathcal{D}R}{\mathcal{D}\phi}(u, \phi)\hat{\phi} = 0. \quad (3.5)$$

By Fréchet differentiation of the functional J in (2.3) and using equation (3.4) we obtain

$$\frac{\mathcal{D}J}{\mathcal{D}\phi} \hat{\phi} = l < \phi, \hat{\phi} > + m < Cu(\phi) - \gamma_d, C\eta >,$$

where $< \cdot, \cdot >$ indicates the inner product. Define the adjoint state ζ through the following adjoint state equation (see e.g. Luenberger 1973)

$$\nu A^* \zeta + \left(\frac{\mathcal{D}R}{\mathcal{D}u}(u, \phi) \right)^* \zeta = C^*(Cu(\phi) - \gamma_d). \quad (3.6)$$

In equation (3.6) and hereafter asterisks, $*$, indicate adjoint operators with respect to the inner product under consideration $< \cdot, \cdot >$. Then

$$\begin{aligned}
\langle Cu(\phi) - \gamma_d, C\eta \rangle &= \langle C^*(Cu(\phi) - \gamma_d), \eta \rangle \\
&= \langle \nu A^* \zeta + \left(\frac{\mathcal{D}R}{\mathcal{D}u}(u, \phi)\right)^* \zeta, \eta \rangle \\
&= \langle \zeta, \nu A \eta + \left(\frac{\mathcal{D}R}{\mathcal{D}u}(u, \phi)\right) \eta \rangle \\
&= - \langle \zeta, \frac{\mathcal{D}R}{\mathcal{D}\phi}(u, \phi) \hat{\phi} \rangle \quad (\text{by (3.5)}) \\
&= - \langle \left(\frac{\mathcal{D}R}{\mathcal{D}\phi}(u, \phi)\right)^* \zeta, \hat{\phi} \rangle.
\end{aligned}$$

Hence, we get

$$\frac{\mathcal{D}J}{\mathcal{D}\phi} \hat{\phi} = l \langle \phi, \hat{\phi} \rangle - m \langle \left(\frac{\mathcal{D}R}{\mathcal{D}\phi}(u, \phi)\right)^* \zeta, \hat{\phi} \rangle.$$

Since $\hat{\phi}$ is an arbitrary test function, we deduce that

$$\frac{\mathcal{D}J}{\mathcal{D}\phi}(\phi^k) = l\phi^k - m \left(\frac{\mathcal{D}R}{\mathcal{D}\phi}(u^k, \phi^k)\right)^* \zeta^k \quad (3.7)$$

and we are in a position to implement the gradient algorithm (3.2). Note that the solution of the adjoint equation is used to obtain the Fréchet derivative in equation (3.2). Once ϕ^k is known, compute the adjoint state ζ^k by solving equation (3.6) with $\phi = \phi^k$ and $u = u^k$. Obtain ϕ^{k+1} from equation (3.2) using equation (3.7). Then compute u^{k+1} by solving the state equation (2.2) with $\phi = \phi^{k+1}$, and continue until convergence.

3.1.1 Suboptimal feedback laws

The feedback procedure described above results in the determination of ϕ as an implicit function of u in the entire domain: indeed, in order to update the control input ϕ , one has to solve the adjoint state equation (3.6), in which data on u may

be needed for the entire domain. However, for the practical implementation of the control algorithm such a detailed knowledge of u is not available. Of course, in some control problems, in particular in the linear case, the construction of a dynamical model of the actual system is quite possible using appropriate filters or state estimators (e.g. Kalman filters and compensators), so one may not necessarily need the knowledge of u in the entire domain. Given a limited data, such state estimators aim to provide important dynamic behaviors of the actual systems. However, it is quite difficult to find such a dynamical model in nonlinear unsteady flows, especially in turbulent flows. At the end of chapter 4, we present a method to avoid a detailed knowledge of u for the boundary control of the stochastic Burgers equation.

If the control ϕ is explicitly determined from measurable quantities, it will be much easier to construct feedback control devices. Such *feedback laws* are pursued in this subsection. Physically a feedback law amounts to a formula relating the quantity being measured by a sensor such as pressure or stresses or temperature to the quantity being controlled by an actuator such as blowing rate at the boundary.

In the previous section, we indicated how to determine ϕ which minimizes the cost. For most nonlinear control problems, ϕ has an implicit dependence on u , i.e. ϕ can not be represented as an explicit function of u . However, it may be possible, from physical intuition or experience, that feedback laws for ϕ , $\phi = \phi(u)$, can be constructed which produce a reduction of costs: For example, in the drag reduction study (PART I), the control relations such as $\phi = -u_2|_{y+\approx 10}$ and $\phi = \alpha_1 \partial/\partial x_3 (\partial u_3/\partial x_2)|_w$ give a significant reduction of drag, where ϕ is the blowing and suction at the wall, u_2 and u_3 are the normal and spanwise velocities, respectively, and α_1 is a constant. Here, we present a quite general framework which should be able to accommodate even the experimental experience gained from the physical observation of unsteady flows.

Suboptimal feedback laws can be implemented in a similar manner by looking for the best feedback

$$\phi = \phi(u), \quad (3.8)$$

in a particular class of functions corresponding to a suitable approximation of equation (3.8)

$$\phi = \alpha_0 + \alpha_1 \theta_1(u), \quad (3.9)$$

where $\theta_1(u)$ is prescribed from physical intuition or experience, and α_0 and α_1 are determined through a control algorithm and thus have an implicit dependence on u , i.e. $\alpha_0 = \alpha_0(u)$ and $\alpha_1 = \alpha_1(u)$. In fact, equation (3.9) contains two elements of equation (2.7) ($\theta_0(u) = 1$). As we already mentioned, $\theta_1(u)$ can be a simple function of u or it can be a complicated functional involving integrals or derivatives of u . For example, $\theta_1(u)$ can be the velocity derivative at the wall which can be measured directly in the physical implementation of the control algorithm and thus, $\theta_1(u)$ represents the quantity that is measured using suitable sensors in the control process. Note that, when $\theta_1 = 0$ (no input from the physical experience), the optimization problem is the initial control problem (2.4). Hence, the optimization problem with $\theta_1 = 0$ produces the optimal control but it does not provide an explicit feedback law. The feedback law in (3.9) can be obtained from control theory for linear optimal or suboptimal problems (see equation (2.12)). For nonlinear control problems, however, if the function $\theta_1(u)$ cannot be determined by control theory, it can be specified by physical intuition. The proper choice of θ_1 may produce simple expressions for α_0 and α_1 (e.g. constant values). Such a feedback will be certainly easy to implement. One of our objectives, therefore, is to inquire whether one can determine α_0 and α_1 as explicit functions of measurable quantities which can be prescribed *a priori* in practical implementations.

For a feedback of this type, set $e = \{\alpha_0, \alpha_1\}$. The cost function J is chosen to be a function \tilde{J} of α_0 and α_1 through equations (2.3) and (3.9) [†]:

$$\tilde{J}(e) = \frac{l}{2} \|e\|^2 + \frac{m}{2} \|Cu - \gamma_d\|^2, \quad (3.10)$$

where $\|e\|^2 = \|\alpha_0\|^2 + \|\alpha_1\|^2$.

The analog of the gradient algorithm (3.2) consists of constructing two sequences α_0^k, α_1^k , recursively defined by

[†] We implicitly assume that $\tilde{J}(e)$ is finite. If this is not true for all e 's in the considered class of feedbacks, we discard those for which $\tilde{J}(e)$ is infinite. Note that this difficulty does not arise in the discretized problem.

$$\begin{aligned}
\alpha_0^{k+1} - \alpha_0^k &= -\rho_0 \frac{\mathcal{D}\tilde{J}}{\mathcal{D}\alpha_0}(\alpha_0^k, \alpha_1^k), \\
\alpha_1^{k+1} - \alpha_1^k &= -\rho_1 \frac{\mathcal{D}\tilde{J}}{\mathcal{D}\alpha_1}(\alpha_0^k, \alpha_1^k).
\end{aligned}
\tag{3.11}$$

Note that the parameters of descent $\rho > 0$ are chosen differently in the two equations (3.11).

The introduction of the adjoint state and adjoint state equation again produces a convenient way to compute the Fréchet derivatives in equation (3.11). Let us define first η using the Fréchet differential in the direction of $\hat{e} = \{\hat{\alpha}_0, \hat{\alpha}_1\}$

$$\eta = \frac{\mathcal{D}u}{\mathcal{D}e} \hat{e} = \frac{\mathcal{D}u}{\mathcal{D}\phi} \frac{\mathcal{D}\phi}{\mathcal{D}e} \hat{e}, \tag{3.12}$$

where

$$\begin{aligned}
\frac{\mathcal{D}\phi}{\mathcal{D}e} \hat{e} &= \frac{\mathcal{D}\phi}{\mathcal{D}\alpha_0} \hat{\alpha}_0 + \frac{\mathcal{D}\phi}{\mathcal{D}\alpha_1} \hat{\alpha}_1 \\
&= \hat{\alpha}_0 + \hat{\alpha}_1 \theta_1 + \alpha_1 \frac{\mathcal{D}\theta_1}{\mathcal{D}u} \frac{\mathcal{D}u}{\mathcal{D}e} \hat{e} \\
&= \hat{\alpha}_0 + \hat{\alpha}_1 \theta_1 + \alpha_1 \frac{\mathcal{D}\theta_1}{\mathcal{D}u} \eta.
\end{aligned}$$

Then, by Fréchet differentiation of equation (2.2), we promptly see that η is the solution of the equation

$$\nu A \eta + \frac{\mathcal{D}R}{\mathcal{D}u} \eta + \frac{\mathcal{D}R}{\mathcal{D}\phi} (\hat{\alpha}_0 + \hat{\alpha}_1 \theta_1 + \alpha_1 \frac{\mathcal{D}\theta_1}{\mathcal{D}u} \eta) = 0,$$

or,

$$(\nu A + \frac{\mathcal{D}R}{\mathcal{D}u} + \frac{\mathcal{D}R}{\mathcal{D}\phi} \alpha_1 \frac{\mathcal{D}\theta_1}{\mathcal{D}u}) \eta + \frac{\mathcal{D}R}{\mathcal{D}\phi} (\hat{\alpha}_0 + \hat{\alpha}_1 \theta_1) = 0. \tag{3.13}$$

By Fréchet differentiation of equation (3.10) using equation (3.12) we obtain

$$\frac{\mathcal{D}\tilde{J}}{\mathcal{D}e}\hat{e} = l \langle \alpha_0, \hat{\alpha}_0 \rangle + l \langle \alpha_1, \hat{\alpha}_1 \rangle + m \langle Cu - \gamma_d, C\eta \rangle.$$

Define now the adjoint state ζ through the following adjoint state equation

$$(\nu A + \frac{\mathcal{D}R}{\mathcal{D}u} + \frac{\mathcal{D}R}{\mathcal{D}\phi}\alpha_1 \frac{\mathcal{D}\theta_1}{\mathcal{D}u})^* \zeta = C^*(Cu - \gamma_d). \quad (3.14)$$

Then by the same procedure as before we get

$$\begin{aligned} \frac{\mathcal{D}\tilde{J}}{\mathcal{D}e}\hat{e} &= l \langle \alpha_0, \hat{\alpha}_0 \rangle + l \langle \alpha_1, \hat{\alpha}_1 \rangle - m \langle \zeta, \frac{\mathcal{D}R}{\mathcal{D}\phi}(\hat{\alpha}_0 + \hat{\alpha}_1\theta_1) \rangle \\ &= \langle l\alpha_0 - m(\frac{\mathcal{D}R}{\mathcal{D}\phi})^*\zeta, \hat{\alpha}_0 \rangle + \langle l\alpha_1 - m\theta_1(\frac{\mathcal{D}R}{\mathcal{D}\phi})^*\zeta, \hat{\alpha}_1 \rangle. \end{aligned} \quad (3.15)$$

Since $\hat{\alpha}_0$ and $\hat{\alpha}_1$ are arbitrary test functions, we deduce that

$$\begin{aligned} \frac{\mathcal{D}\tilde{J}}{\mathcal{D}\alpha_0}(\alpha_0^k, \alpha_1^k) &= l\alpha_0^k - m(\frac{\mathcal{D}R}{\mathcal{D}\phi}(u^k, \phi^k))^*\zeta^k, \\ \frac{\mathcal{D}\tilde{J}}{\mathcal{D}\alpha_1}(\alpha_0^k, \alpha_1^k) &= l\alpha_1^k - m\theta_1(u^k)(\frac{\mathcal{D}R}{\mathcal{D}\phi}(u^k, \phi^k))^*\zeta^k \end{aligned} \quad (3.16)$$

and we are in a position to implement the gradient algorithm (3.11). Note that the solution of the adjoint equation is used to obtain the Fréchet derivatives in equation (3.11). Once α_0^k and α_1^k are known, compute the adjoint state ζ^k by solving equation (3.14) with $\phi = \phi^k$ and $u = u^k$. Obtain α_0^{k+1} and α_1^{k+1} from equation (3.11) using equation (3.16). Then compute u^{k+1} by solving the state equation (2.2) with ϕ^{k+1} given by equation (3.9), and continue until convergence.

3.2 Time-dependent problem

We now consider the case of time-dependent problems. The suboptimal procedure that we propose in this case consists of the following:

(1) Discretize the state equation in time.

(2) At each instant of time, the discretized equation is a stationary one to which the above procedure is applied, while the cost function is an instantaneous version of equation (2.10) (i.e. no time averaging, see equation (3.20)).

This procedure means that, at each instant of time, we are directing the flow in a direction producing the decay of the instantaneous cost function. Of course, there is no reason to believe that the controls will be optimal, or even that the cost will actually decay in the long range. However the numerical experiments conducted in the case of the stochastic Burgers equation and other model problems (not reported here) show that indeed the cost function decreases significantly without being monotonically decreasing all the time (see chapter 4 for the Burgers equation).

Consider the evolution state equation (2.8); again, this could be the original Navier-Stokes equations for channel flow. For step (1) we consider here the Crank-Nicholson method:

$$\frac{u^n - u^{n-1}}{\Delta t} + \frac{\nu}{2}(Au^n + Au^{n-1}) + \frac{1}{2}(R(u^n, \phi^n) + R(u^{n-1}, \phi^{n-1})) = 0, \quad (3.17)$$

which we rewrite as

$$Au + \mathcal{R}^n(u, \phi) = 0, \quad (3.18)$$

with $u = u^n, \phi = \phi^n$, and

$$\begin{aligned} Au &= u^n + \frac{\nu}{2}\Delta t Au^n, \\ \mathcal{R}^n(u^n, \phi^n) &= -u^{n-1} + \frac{1}{2}\Delta t(\nu Au^{n-1} + R(u^n, \phi^n) + R(u^{n-1}, \phi^{n-1})). \end{aligned} \quad (3.19)$$

At each step n , the cost function J is still given by equation (2.3)

$$J^n = J(\phi^n) = \frac{l}{2}\|\phi^n\|^2 + \frac{m}{2}\|Cu^n - \gamma_d\|^2, \quad (3.20)$$

with u^n function of $\phi^n (= u^n(\phi^n))$ through equations (3.17) - (3.19). Note that for a sufficiently small Δt there exists a unique solution u^n to equation (3.17). Hence

the difficulty of non-uniqueness of solution for equation (2.2) does not arise for equation (3.18).

The adjoint state is defined as in equations (3.4) - (3.6)

$$\eta^n = \frac{\mathcal{D}u^n}{\mathcal{D}\phi} \hat{\phi}, \quad (3.21)$$

$$\mathcal{A} \eta^n + \frac{\mathcal{D}\mathcal{R}}{\mathcal{D}u}(u^n, \phi^n) \eta^n + \frac{\mathcal{D}\mathcal{R}}{\mathcal{D}\phi}(u^n, \phi^n) \hat{\phi} = 0, \quad (3.22)$$

$$\mathcal{A}^* \zeta^n + \left(\frac{\mathcal{D}\mathcal{R}}{\mathcal{D}u}(u^n, \phi^n) \right)^* \zeta = C^*(Cu^n - \gamma_d). \quad (3.23)$$

The gradient algorithm (3.2) now reads

$$\phi^{n,k+1} - \phi^{n,k} = -\rho \frac{\mathcal{D}J}{\mathcal{D}\phi}(\phi^{n,k}), \quad (3.24)$$

where $\phi^{n,k}$ is a member of a sequence of controls at a given time step n , ρ is the parameter of descent, and k is the iteration index at each time step. By Taylor's formula, as in equation (3.3), for all n, k ,

$$J(\phi^{n,k+1}) \leq J(\phi^{n,k}),$$

and as $k \rightarrow \infty$, $\phi^{n,k}$ converges to ϕ^n which achieves the minimum of J^n . It is not necessarily true that the minimum of J^n decreases as n increases, i.e. for all n ,

$$J^n \leq J^{n-1}. \quad (3.25)$$

Using the property of adjoint operator as is done in previous section, we obtain

$$\frac{\mathcal{D}J}{\mathcal{D}\phi}(\phi^{n,k}) = l\phi^{n,k} - \frac{m}{2} \Delta t \left(\frac{\mathcal{D}\mathcal{R}}{\mathcal{D}\phi}(u^{n,k}, \phi^{n,k}) \right)^* \zeta^{n,k}, \quad (3.26)$$

and we are in a position to implement the gradient algorithm (3.24). Note that the solution of the adjoint equation is used to obtain the Fréchet derivative in equation (3.24). Once $\phi^{n,k}$ is known, compute the adjoint state $\zeta^{n,k}$ by solving equation (3.23) with $\phi^n = \phi^{n,k}$ and $u^n = u^{n,k}$. Obtain $\phi^{n,k+1}$ from equation (3.24) using

equation (3.26). Then compute $u^{n,k+1}$ by solving the state equation (3.18) with $\phi^n = \phi^{n,k+1}$, and continue until convergence.

Suboptimal feedback laws for the time-dependent problem can be implemented in a similar manner as described in section 3.1.1.

CHAPTER 4

APPLICATION TO THE STOCHASTIC BURGERS EQUATION

As a first step towards application to the problems in fluid mechanics, the feedback control procedures described in chapter 3 are applied to the Burgers equation subject to random forcing. This equation contains nonlinear convection and diffusion terms and its solution exhibits a chaotic nature; these qualities make it a natural model for the more complicated Navier-Stokes equations. We first specify the form of the Burgers equation that we consider (section 4.1). Then we show how to implement our feedback procedure for distributed and boundary control problems (section 4.2) and present and discuss the results of our numerical experiments (section 4.3). The form of the effective feedback law is discussed in section 4.4. We also discuss several implementation issues (discretization of the equation and practical implementation of the feedback procedure) in section 4.5

4.1 The Burgers equation with random forcing

Consider the randomly forced Burgers equation with no-slip boundary conditions

$$\begin{aligned} \frac{\partial \tilde{u}}{\partial \tilde{t}} + \frac{\partial}{\partial \tilde{x}} \frac{\tilde{u}^2}{2} &= \nu \frac{\partial^2 \tilde{u}}{\partial \tilde{x}^2} + \tilde{\chi}(\tilde{x}, \tilde{t}), \quad 0 < \tilde{x} < L, \\ \tilde{u}(\tilde{x} = 0) &= \tilde{u}(\tilde{x} = L) = 0, \end{aligned} \quad (4.1)$$

where \tilde{u} is the velocity, ν the kinematic viscosity, $\tilde{\chi}$ the random forcing, and L the length of the computational domain. In the absence of forcing ($\tilde{\chi} = 0$), the solutions of equation (4.1) decay to zero from any bounded initial data.

The forcing function $\tilde{\chi}$ is a white noise random process in x with zero mean (see Chambers *et al.* 1988; Bensoussan and Temam 1972, 1973). The mean-square value of the dimensional forcing, σ^2 , defines a velocity scale $U = \sqrt{\sigma L}$. The Burgers equation in nondimensional form using U and L as the typical velocity and length reads

$$\frac{\partial u}{\partial t} + \frac{\partial u^2}{\partial x} = \frac{1}{Re} \frac{\partial^2 u}{\partial x^2} + \chi(x, t), \quad 0 < x < 1, \quad (4.2)$$

$$u(x=0) = u(x=1) = 0,$$

where u, x, t and χ are dimensionless quantities, Re is the Reynolds number UL/ν , and

$$\langle \chi \rangle_x = 0, \quad \langle \chi^2 \rangle_x = 1. \quad (4.3)$$

Here $\langle \cdot \rangle_x$ denotes the average value over space. A Crank-Nicholson method in time and second-order centered differences in space are used to discretize equation (4.2). A Newton iterative method is used to solve the discretized nonlinear equation.

For the following I denotes the number of grid points, Δt the computational time step, $\Delta x = 1/(I-1)$, $u_i^n \approx u((i-1)\Delta x, n\Delta t)$, $\chi_i^n \approx \chi((i-1)\Delta x, n\Delta t)$, and $i = 2, \dots, I-1$. At each instant of time $n\Delta t$, the χ_i^n are uncorrelated random variables; χ_i^n is constant on a time interval $(p\Delta t_r, (p+1)\Delta t_r)$, where p is an integer, and, if $n\Delta t$ and $n'\Delta t$ belong to two different such intervals, all the $\chi_j^{n'}$ are independent of all the χ_i^n ($n' > n$), with $\langle \chi_i^n \rangle_x = 0$ and $\langle (\chi_i^n)^2 \rangle_x = 1$.

The solution of the Burgers equation with random forcing (equation (4.2)) depends not only on the Reynolds number Re , but also on the mean-square value $\langle \chi^2 \rangle_x$ and the time scale Δt_r of the random forcing. For all calculations presented here, $\langle \chi \rangle_x = 0$, $\langle \chi^2 \rangle_x = 1$, and $\Delta t = 0.001$, which is the largest time step which accurately predicts the small scale motion with the values of Re and Δt_r used in our calculations. A uniform computational mesh of 2048 points is used in x ($\Delta x = 1/2047$). Three different Reynolds numbers, $Re = 500, 1500, 4500$, and three different time scales, $\Delta t_r = 0.01, 0.1, 1$, are investigated. Instantaneous velocity fields for the different Reynolds numbers and different time scales Δt_r are shown in figure 1. Strong thin internal shocks can be seen for high Re and large Δt_r . Figure 2 shows the effect of the Reynolds number Re and the time scale Δt_r on the mean velocity. The magnitudes of the mean velocity and the mean velocity gradient clearly increase with increasing Re and Δt_r . Due to the convective nature of the solution of the Burgers equation, the wall layer thickness gets thinner as the Reynolds number increases (figure 2 (a), also in Chambers *et al.* 1988). The mean velocity gradient near the centerline, however, is not much changed with the

Reynolds number. On the contrary, increasing Δt_r with a fixed Reynolds number significantly increases the mean velocity gradient near the centerline as well as near the wall layer (figure 2 (b)). Wall layer thickness, however, is not affected by increasing Δt_r .

4.2 Feedback control procedures

Two types of feedback controls are investigated: distributed and boundary controls. Distributed control by body forces corresponds to the unrealistic case where volume forces are applied throughout the fluid; however it turns out to be a good introduction to more interesting and more complicated situations. It also contains all of the basic features of general control problems. For boundary control the control is the boundary velocity, which is more practical in fluid mechanics and can be implemented in real situations.

4.2.1 Distributed control (formulation)

The nondimensionalized Burgers equation with distributed control is

$$\begin{aligned} \frac{\partial u}{\partial t} + \frac{\partial}{\partial x} \frac{u^2}{2} &= \frac{1}{Re} \frac{\partial^2 u}{\partial x^2} + \chi(x, t) + f(x, t), \quad 0 < x < 1, \\ u(x, t = 0) &= u_o(x), \\ u(x = 0, t) &= 0, \quad u(x = 1, t) = 0. \end{aligned} \tag{4.4}$$

Here χ is the random forcing and u_o is the initial data, which is an instantaneous solution of the Burgers equation with random forcing χ and $f = 0$ (equation (4.2)). The control input forcing f is of the form

$$f = \alpha_0 + \alpha_1 \theta_1(u). \tag{4.5}$$

Here $\theta_1(u)$ is prescribed from physical intuition or experience (see sections 3.1.1 and 4.3), and α_0 and α_1 are determined through our control algorithm and thus have an implicit dependence on u . Note that α_0 and α_1 are not constant in time and space and they are continuously updated with the change of u .

At each instant of time, the cost function considered is

$$J^n = J(e^n) = \frac{l_d}{2} \|e^n\|^2 + \frac{m_d}{2} \int_0^1 \left(\frac{\partial u^n}{\partial x}\right)^2 dx, \quad (4.6)$$

where $\|e\|^2 = \|\alpha_0\|^2 + \|\alpha_1\|^2$. Here we want to reduce the mean square velocity gradient inside the domain at the expense of the control input. The choice of l_d and m_d (or more precisely of the ratio l_d/m_d) is an engineering problem which is not addressed here, although we do consider in our computations several values of this ratio. The detailed procedure of distributed control by body forces is described in appendix B.

4.2.2 Boundary control (formulation)

The nondimensionalized Burgers equation with boundary control is

$$\begin{aligned} \frac{\partial u}{\partial t} + \frac{\partial u^2}{\partial x} &= \frac{1}{Re} \frac{\partial^2 u}{\partial x^2} + \chi(x, t), \quad 0 < x < 1, \\ u(x, t=0) &= u_o(x), \\ u(x=0, t) &= \psi_0(t), \quad u(x=1, t) = \psi_1(t). \end{aligned} \quad (4.7)$$

Here χ is the random forcing and u_o is the initial data, which is an instantaneous solution of the Burgers equation with random forcing χ and $f = 0$ (equation (4.2)). The control input velocities at the boundary, ψ_0 and ψ_1 , are of the form,

$$\begin{aligned} \psi_0 &= \alpha_{0,0} + \alpha_{1,0} \theta_{1,0}(u), \\ \psi_1 &= \alpha_{0,1} + \alpha_{1,1} \theta_{1,1}(u), \end{aligned} \quad (4.8)$$

We denote $\alpha_0 = \{\alpha_{0,0}, \alpha_{0,1}\}$, $\alpha_1 = \{\alpha_{1,0}, \alpha_{1,1}\}$, and $\theta_1 = \{\theta_{1,0}, \theta_{1,1}\}$. Here the $\theta_1(u)$'s are prescribed from physical intuition or experience (see sections 3.1.1 and 4.3), and the α_0 's and α_1 's are determined through a control algorithm and thus have an implicit dependence on u . Note that the α_0 's and α_1 's are not constant in time and they are continuously updated with the change of u .

At each instant of time, the instantaneous cost function considered is

$$J^n = J(e^n) = \frac{l_b}{2} \|e^n\|^2 + \frac{m_b}{2} \left[\left(\frac{\partial u^n}{\partial x} \right)_{x=0}^2 + \left(\frac{\partial u^n}{\partial x} \right)_{x=1}^2 \right], \quad (4.9)$$

where $\|e\|^2 = \|\alpha_0\|^2 + \|\alpha_1\|^2$. Here we want to reduce the wall velocity gradient at the expense of the control input. The detailed procedure of boundary control by boundary velocities is described in appendix C.

4.2.3 Numerical algorithm

From the previous subsections, we can write for both control problems the numerical algorithm of minimizing the cost function J^n :

- Step 1 : Start with an initial condition u_o or a solution of the previous time step $u^{n,k-1} = u^{n-1}$. Choose initial $\alpha_0^{n,k-1}$ and $\alpha_1^{n,k-1}$.
- Step 2 : Solve the adjoint equation with $u^{n,k-1}$, and $f^{n,k-1}$ or $\psi^{n,k-1}$ to obtain $\zeta^{n,k-1}$.
- Step 3 : Update $\alpha_0^{n,k}$ and $\alpha_1^{n,k}$.
- Step 4 : Solve the discretized Burgers equation with $f^{n,k}$ or $\psi^{n,k}$ to obtain $u^{n,k}$.
- Step 5 : Iterate Steps 2-4 until $u^{n,k}$ converges.
- Step 6 : When converged, $u^n = u^{n,k}$.

4.3 Results of numerical simulation

Values of l and m in the cost function (equations (4.6) and (4.9)) are dimensional quantities and are usually prescribed from a physical setting of the actual systems (see section 2.1 and above). Also the problem can be scaled by l/m . Once l and m are given, we need to find the best ρ (the parameter of descent). We do it by trial and error instead of by theoretical procedures (see e.g. Luenberger 1973). Note that conjugate gradient methods can be used to eliminate the unnecessary trial-and-error procedure and also to get faster convergence.

As mentioned in detail in section 3.1.1, for many cases feedback laws are in general hard to obtain from a mathematical approach, and one must resort to physical intuition or experience for a better result or for a simple feedback law.

The reasons for using the formulations (4.5) and (4.8) rather than using a simple formulation ($f = f(u)$ or $\psi = \psi(u)$) are two-fold: First, the formulations (4.5) and (4.8) can accommodate experience and physical observations. Second, they can accommodate a good feedback law if we prescribe a proper $\theta_1(u)$.

We consider two cases for functions θ_1 in equations (4.5) and (4.8): $\theta_1 = 0$ and $\theta_1 \neq 0$ (Here, for simplicity we let the functions, $\theta_{1,0}$ and $\theta_{1,1}$ in equation (4.8), be equal to a same function now denoted θ_1 ; hence both ends, $x = 0$ and $x = 1$, play the same role.). We call the former *non-prescribed feedback control* because in that case the control input itself (f or ψ) does not have any information from physical experience and is determined directly from a mathematical approach. Note that non-prescribed feedback control still yields a relation between u and ϕ (f or ψ) because the α_0 's are continuously updated from our optimization procedures which need information on u (see section 4.4 on *actual feedback laws*). Since there are two different parameters ρ_0, ρ_1 in the case $\theta_1 \neq 0$, many trial-and-error iterations are needed to find the best ρ_0 and ρ_1 . Non-prescribed feedback control ($\theta_1 = 0$) is first investigated to find the best ρ_0 ; the best ρ_1 is then searched while holding $\alpha_0 = 0$. For most cases considered in the following, non-prescribed feedback control is better at finding a local minimum of the cost function in the sense that non-prescribed feedback control gives faster and more stable convergence. However, we believe that this is not always the case since it depends on the function type θ_1 and the cost J as well as on the gradient algorithm. In some other situations or with a different choice of the shape function (the class of feedback laws), the results may turn out to be better. Most of the results presented below were obtained for the non-prescribed feedback control case; some of the cases with $\theta_1 \neq 0$ are also presented.

In this section, we only discuss the results of the cases with $Re = 1500$ and $\Delta t_r = 0.01$. Cases with different Reynolds number ($Re = 4500$) and different Δt_r ($= 0.1$) have also been tested, and the results show the same trend as those with $Re = 1500$ and $\Delta t_r = 0.01$. Figure 3 shows the time-averaged mean velocity U of the no control case with $Re = 1500$ and $\Delta t_r = 0.01$ and the initial velocity u_o used in the following controls.

4.3.1 Numerical results for distributed control

Two types of shape function θ_1 (equation (4.5)) were investigated: $\theta_1 = 0$ (non-prescribed feedback control), and $\theta_1 = u$. Concerning the parameters l_d and m_d , we have chosen quite arbitrarily to study the following cases:

(i) $l_d = 1, m_d = 1$; (ii) $l_d = 1, m_d = 2047 (= 1/\Delta x)$; (iii) $l_d = 1, m_d = 4.2 \times 10^6 (= 1/\Delta x^2)$; (iv) $l_d = 0, m_d = 1$.

Results with control were compared to those with no control. A set of random values of the momentum forcing χ was stored and used for both the control and no control cases for the accurate estimation of the parameter ρ . Case (i) showed almost no change of the cost when control was applied. When the ratio of the weight parameters, m_d/l_d , is small, the input cost becomes so expensive that there is no means of reducing the total cost by addition of controls.

With non-prescribed feedback control ($\theta_1 = 0$), optimal values ρ_0 of 1, 0.001 and 10000 were found for cases (ii), (iii), and (iv), respectively. Effects of the parameter of descent ρ_0 on the cost function and its convergence are shown in figure 4. Larger cost J or divergence of the solution was obtained for ρ_0 larger than the optimal ρ_0 , and slower convergence was achieved for smaller ρ_0 . Case (ii) needed about 6 iterations to converge (figure 4 (b)). Cases (iii) and (iv) need many more iterations (about 50) to converge. From the practical point of view, however, it is not necessary to get a converged solution since a few iterations give a significant reduction of the cost function.

Figure 5 shows the time history of the cost, energy ($= \int_0^1 \frac{1}{2} u^2 dx$), wall velocity gradient, and momentum forcings (random input χ and control input f) at $x = 0.5$ for case (ii). Figure 6 shows the same for case (iii). Results of case (iv) are essentially the same as those of case (iii). It can be seen that the distributed control significantly reduces the cost as well as the energy inside the domain (see figures 6 (b) and 7 (d)).

Since one of the effects of control is to cancel or attenuate the effects of random forcing, it is interesting to investigate a case with no random forcing and no control ($\chi = f = 0$) and the same initial velocity u_0 , and compare the results to those with control. Temporal evolutions of cost and energy, and velocity profiles at $t = 2$ with no random forcing and no control ($\chi = f = 0$) are compared with control cases

(ii) and (iii) in figure 7. Energy and costs rapidly decrease and the velocity profile is smoothed when there is no random forcing. The control simply attenuates the effect of the random forcing for case (ii). Case (iii), however, shows that the control can do more than cancel the effects of random forcing.

The case $\theta_1 = u$ was tested next. By setting $\alpha_0 = 0$ in case (ii), the best ρ_1 was searched for. $\rho_1 = 2$ gave a larger cost and $\rho_1 \leq 1$ gave no change of cost as compared to the no control case. The sensitivity of the cost function with respect to the control variables is a good indicator of the effectiveness of the control variables in reducing the cost. As equation (B.7) suggests, the sensitivity is a function of not only the time step (n) but also the iteration (k). Convergence of the sensitivity with fixed n is strongly dependent on the parameter ρ , but the temporal evolution of the sensitivity at the first iteration is nearly independent of ρ . The magnitudes of the sensitivities of the cost functions for cases (ii) and (iii) were measured with the parameters $\rho_0 = \rho_1 = 1$ for case (ii), and $\rho_0 = \rho_1 = 0.001$ for case (iii). The sensitivity with respect to α_1 was at least two orders of magnitude smaller than that with respect to α_0 (figure 8).

4.3.2 Numerical results for boundary control

For simplicity, the functions $\theta_{1,0}$ and $\theta_{1,1}$ in equation (4.8) are taken to be the same so that both ends, $x = 0$ and 1 , play the same role ($\theta_{1,0} = \theta_{1,1} = \theta_1$).

Three types of such shape function θ_1 were investigated[†]: $\theta_1 = 0$ (non-prescribed feedback control), $\theta_1 = \frac{\partial u}{\partial x}$, and $\theta_1 = \frac{\partial u}{\partial x} / [1 + (\frac{\partial u}{\partial x})^2]$. Concerning the parameters l_b and m_b , we have chosen quite arbitrarily to study the following cases:

(i') $l_b = 1, m_b = 2.5 \times 10^{-7}$ ($= \Delta x^2$); (ii') $l_b = 1, m_b = 5 \times 10^{-4}$ ($= \Delta x$); (iii') $l_b = 1, m_b = 1$; (iv') $l_b = 0, m_b = 1$.

Results with control were compared to those with no control. A set of random values of the momentum forcing χ was stored and used for both the control and no control cases for the accurate estimation of the parameter ρ . All cases except

[†] Again these choices were based on physical intuition but, as explained hereafter, the results are not satisfactory. The last function was chosen to limit the magnitude of θ_1 to less than one; In this way one can expect equation (4.8) to be a more accurate truncation of the Taylor series expansion of $\psi(\theta_1)$.

(i') showed a significant reduction of the cost when control was applied. Case (i') showed no reduction of the cost since m_b was very small relative to l_b . With non-prescribed feedback control, optimal values ρ_0 of 0.001, 10^{-6} and 10^{-6} were found for cases (ii'), (iii'), and (iv'), respectively. Effects of ρ_0 on the cost function and the sensitivity are the same as those described in the distributed control subsection. Cases (ii'), (iii') and (iv') needed about 7 iterations to converge.

Figure 9 shows the time history of the cost, energy, wall velocity gradient, and velocity profile at $t = 2$ for case (ii'). Figure 10 shows the costs of cases (iii') and (iv'). Temporal evolutions of the energy, wall velocity gradient, and velocity profiles of cases (iii') and (iv') are quite similar to case (ii'). In contrast to distributed control, the energy inside the domain is changed little though the cost and $\partial u / \partial x$ at the wall are reduced significantly. The velocity profile at $t = 2$ shows that boundary control modifies the flow field only near the wall. A longer time integration up to $t = 100$ has been completed for case (iii'). Again only the wall region is modified.

One may think that a fixed non-zero wall velocity (passive control) may reduce the cost or $\partial u / \partial x$ at the wall and may even give more of a reduction than does boundary control. Several fixed non-zero wall velocities, $u(x = 0) = -u_s$, $u(x = 1) = u_s$, were tested in order to study the effect of a slip velocity at the wall, where u_s was taken from 0 to 0.1 (for the relative scale of the velocity, see figure 3). All cases considered showed a negligible reduction or a significant increase of the cost. We also used the time-averaged value of the control wall velocities obtained from the feedback control algorithm as a fixed wall velocity. The cost reduction was again negligible.

As described at the beginning of this subsection, we tested two more shape functions: $\theta_1 = \frac{\partial u}{\partial x}$ and $\theta_1 = \frac{\partial u}{\partial x} / (1 + (\frac{\partial u}{\partial x})^2)$. By setting $\alpha_0 = 0$ in case (ii'), the best ρ_1 was searched for. For the function $\theta_1 = \frac{\partial u}{\partial x}$, the simple gradient algorithm was unstable and did not converge. For the function $\theta_1 = \frac{\partial u}{\partial x} / (1 + (\frac{\partial u}{\partial x})^2)$, $\rho_1 = 0.001$ gave a reduction of the cost but converged more slowly than the non-prescribed feedback control case. Larger values of ρ_1 give either a larger cost or divergence of the solution. The sensitivity of the cost function with respect to the control variables was measured with $\rho_0 = \rho_1 = 0.001$. The sensitivity with respect to α_1 was about an order of magnitude smaller than that with respect to α_0 .

4.4 Remarks on the feedback laws

Physically a feedback law amounts to a formula relating the quantity being measured by a sensor to the quantity being controlled by an actuator. Here some comments are made on the choice of the feedback laws. As indicated before, our control is optimal among a prescribed class of feedback laws: see e.g. equations (2.5), (2.7) and (3.9) in the stationary case and similarly equations (4.5) and (4.8) in the time-dependent case. Our choices of the feedback laws, i.e. the functionals θ_i or $\theta_{i,j}$ in equations (2.7), (4.5) and (4.8), were fully arbitrary by the lack of similar results in the literature. Surprisingly the most efficient feedback laws were "the non-prescribed ones," i.e. those where the control ϕ does not explicitly depend on the state u . Hence at first sight there is no feedback, but this is not actually true since the feedback is hidden in the history of the flow. Concerning the feedback laws we would like to emphasize here the phase diagrams of the solutions using non-prescribed feedback control for cases (ii') and (iii') in figure 11. Here one of the controls (wall velocity) is plotted against one of the *observations* directly related to the cost function, namely the normal derivative $\partial u / \partial x$ at the wall. These phase diagrams can be considered as the *actual feedback laws* resulting from our method. A *linear* feedback law is achieved for case (ii'), whereas no apparent relation is found for case (iii'). For cases (iii') and (iv'), the wall velocity gradients are nearly zero irrespective of the magnitude of control wall velocities (figure 11 (b)). Therefore, a linear feedback law between wall velocity and wall velocity gradient is not found for cases (iii') and (iv'). A feedback law for case (ii') is deduced from figure 11:

$$\begin{aligned} u^n(x=0) &= 0.533 \left. \frac{\partial u}{\partial x} \right|^{n-1}(x=0), \\ u^n(x=1) &= -0.533 \left. \frac{\partial u}{\partial x} \right|^{n-1}(x=1), \end{aligned} \tag{4.10}$$

where $t = n\Delta t$. A natural and puzzling question resulting from the feedback laws in equation (4.10) was whether we could bypass our procedure and directly implement

a boundary condition of the type of equation (4.10)

$$\begin{aligned} u(x=0) &= \lambda \frac{\partial u}{\partial x}(x=0), \\ u(x=1) &= \lambda' \frac{\partial u}{\partial x}(x=1), \end{aligned} \tag{4.11}$$

with λ and λ' equal or close to ± 0.533 as in equation (4.10). We found that numerical instabilities were developing: once the wall velocity obtained from equation (4.11) is slightly deviated from the value used in actual feedback control procedures, the wall velocity gradient at the next time step is significantly increased compared to the feedback control case. Hence the actual boundary condition resulting from control algorithm is indispensable for stability.

4.5 Further remarks on implementation issues

We make here two further remarks on implementation issues: One is related to the effect of the time-discretization method and the other is related to some aspects of the gradient algorithm.

4.5.1 Remarks on the time-discretization method

It is clear that, in the time-dependent case, the time discretization of the evolution equation strongly affects equation (3.18) and therefore our whole procedure. In the most extreme case where a fully explicit scheme is used, our method can not be implemented at all. Hence we have found it important to test our method with various classical forms of time discretization. We have already presented the control procedure resulting from a fully implicit discretization of the Burgers equation using a Crank-Nicholson scheme (see equation (3.17)). We have also tested our procedure in the case of boundary control using another fully implicit method (Implicit Euler) and a semi-implicit method (Adams-Bashforth for the nonlinear term and Crank-Nicholson for the viscous term).

In the case of the boundary control using a fully implicit method, the adjoint equation (C.4) contains all the interior velocities as well as the boundary velocities

(or boundary velocity gradients). Hence, a full knowledge of the flow field would be required for the implementation of the control algorithm which is highly impractical for physical implementation. On the other hand, in the case of the boundary control using a semi-implicit method (Adams-Bashforth for the nonlinear term and Crank-Nicholson for the viscous term), one can circumvent this problem. The feedback procedure for the Burgers equation using this semi-implicit method is presented in the appendix D. The resulting adjoint equation (D.2) does not contain any velocities except the wall velocity gradients. Figure 12 shows the time history of the cost and convergence of the sensitivity for case (ii') ($l_b = 1, m_b = \Delta x$). Essentially the same result is obtained as with a fully-implicit method; the convergence behavior is only slightly changed.

4.5.2 Practical implementation of the control algorithm

From the practical point of view, sensors and actuators must be placed at the wall. In this respect, the boundary control is more realistic than the distributed control. As mentioned above, when the semi-implicit method is used, the resulting adjoint equation (D.2) does not contain any velocities except the wall velocity gradients, while all interior velocities should be measured when a fully implicit method is used. Hence, for the practical implementation of the feedback control algorithm, one has to resort to the semi-implicit method.

Also, it should be pointed out that all previous computations were carried out until the cost reached a minimum at each time step n , which required about 7 iterations at each time step. However, in practical situations, the number of iterations k should be limited to one. This is because in a physical setting $\partial u / \partial x$ at the boundary at a given instant is used to obtain the control input velocity which leads to a new velocity field at the next instant in time with the corresponding $\partial u / \partial x$ at the boundary. Physically one can not use the new data on $\partial u / \partial x$ at the boundary to go back in time and refine the input velocity.

In this subsection, we investigate the effectiveness of the control algorithm with the iteration k set equal to one, the Reynolds number, $Re = 1500$, and the computational time step, $\Delta t = 0.001$. Figures 13 and 14 show the time history of the cost and wall velocity gradient for various iterations k for case (ii') ($l_b = 1, m_b = \Delta x$). Here, the time scale of the random forcing, Δt_r , is set to be 0.01. Reductions of the

Case	No control	$k = 1$	$k = 2$	$k = 7$
$J \times 10^3$	1.098	0.4409	0.3183	0.3053
Reduction of J	—	60%	71%	72%

Table 1. Variation of the cost with respect to the iteration k for case (ii').

cost as well as the wall velocity gradient are accomplished with a few iterations. Table 1 shows the mean value of the cost and percentage reduction of the cost. The cost is significantly reduced with $k = 1$, and the reduced cost with $k = 2$ is nearly the same as that with $k = 7$, the maximum reduction of the cost. Figure 15 shows the time history of the cost and wall velocity gradient with $k = 1$ for case (iv') ($l_b = 0, m_b = 1$). Again, a cost reduction of 87% is found with only one iteration. Note that, in case (iv'), the control input cost is not included into the total cost, i.e. a cheap control.

In order to investigate the effect of the random-forcing time scale on the efficiency of the control scheme, a larger time scale, $\Delta t_r = 0.1$ was used. Time history of the cost and wall velocity gradient with $k = 1$ for case (ii') ($l_b = 1, m_b = \Delta x$) is shown in figure 16. The effect of random forcing on the wall velocity gradient is clearly seen. A cost reduction of 87% is obtained by the control, which is clearly larger than in the case of $\Delta t_r = 0.01$, where a cost reduction of 60% was obtained. The control scheme with $k = 1$ adjusts to sudden changes in the flow in a short time to create a cost reduction. Here, the random-forcing time scale is a flow time scale, and the computational time step is considered the control time scale. Clearly, it should be much easier to get a cost reduction if the flow time scale is much larger than the control time scale. The numerical experiments with two different Δt_r show that this is indeed the case.

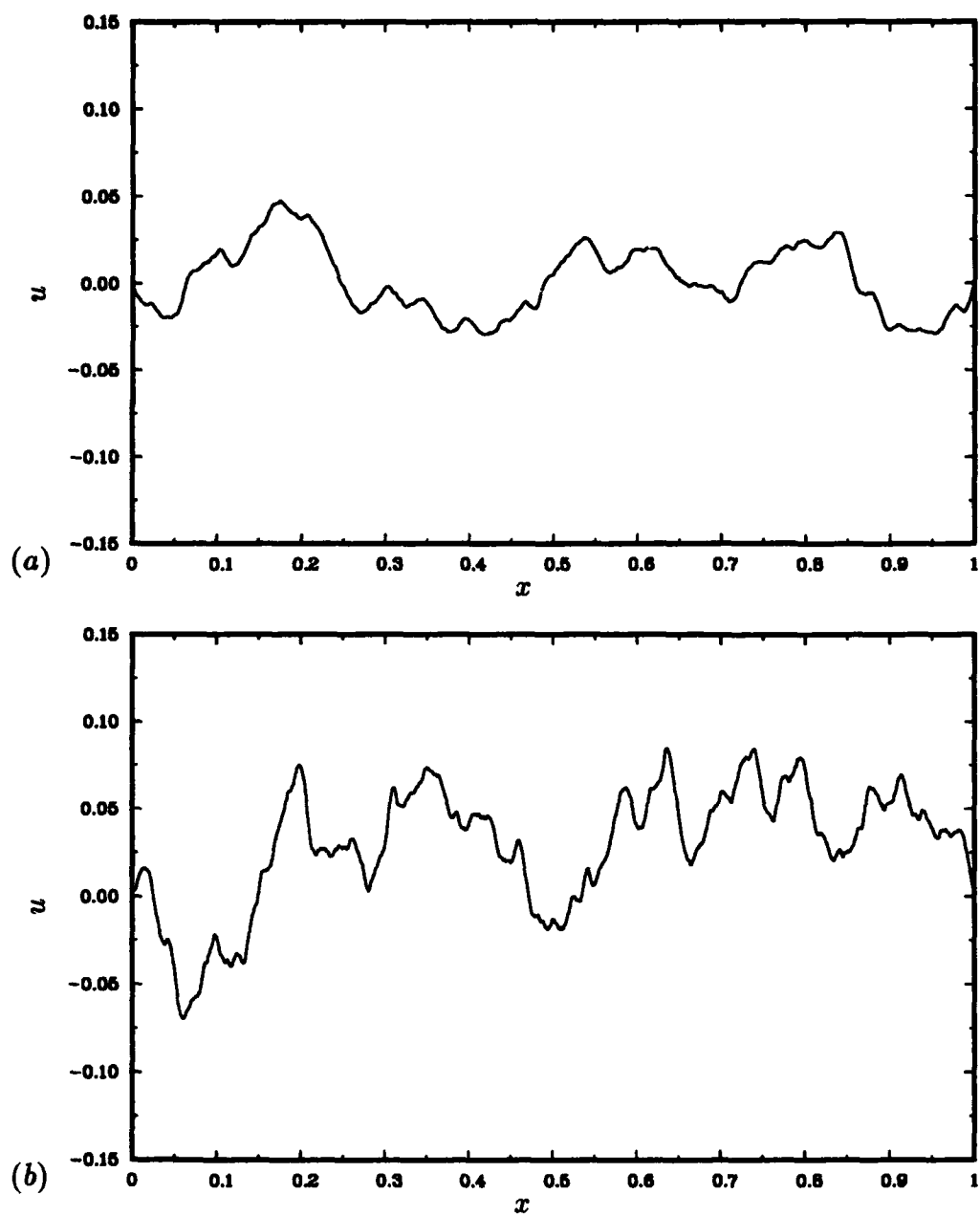


FIGURE 1. For caption see the following page.

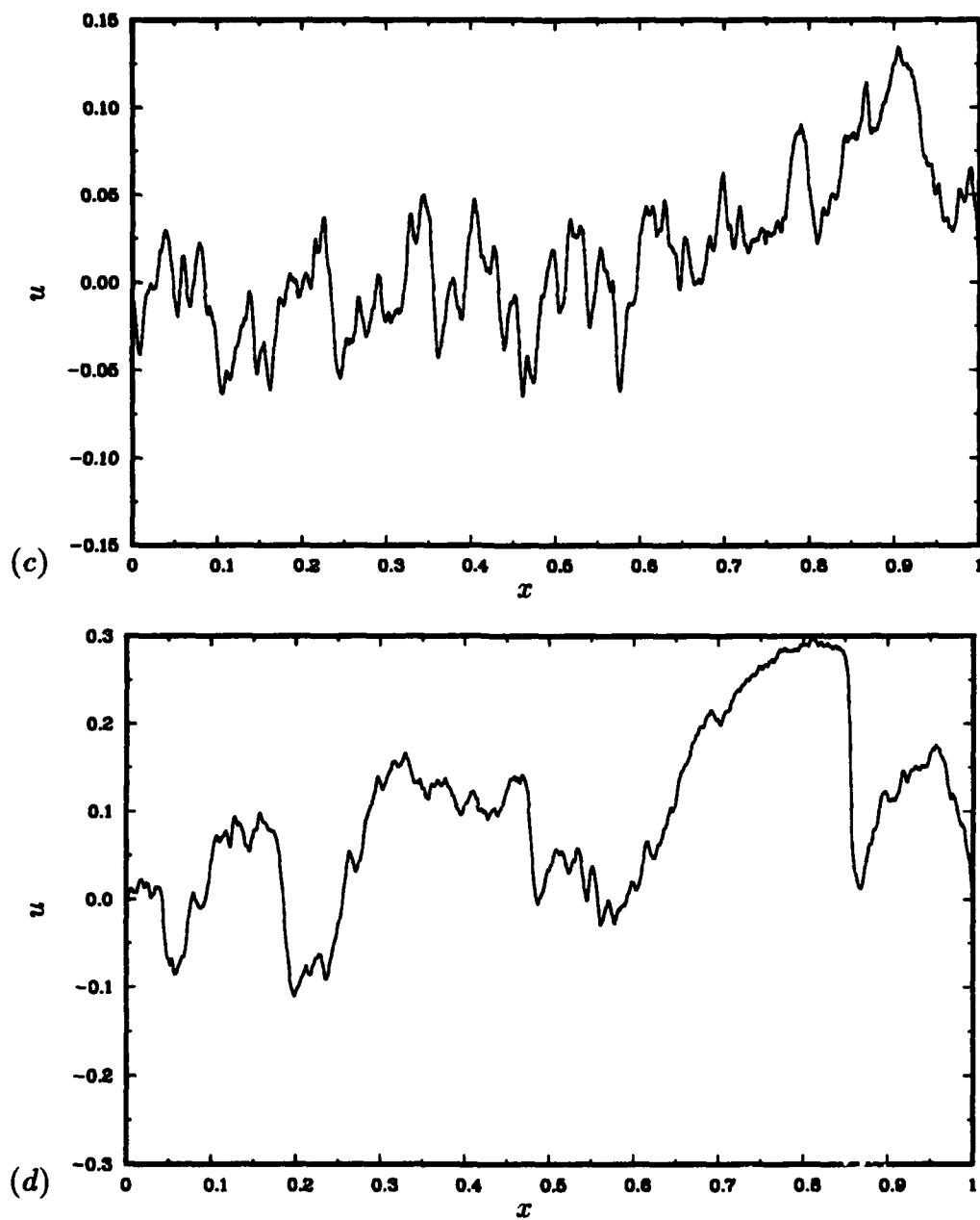


FIGURE 1. Instantaneous velocity profiles. (a) $Re = 500, \Delta t_r = 0.1$; (b) $Re = 1500, \Delta t_r = 0.1$; (c) $Re = 4500, \Delta t_r = 0.1$; (d) $Re = 4500, \Delta t_r = 1$.

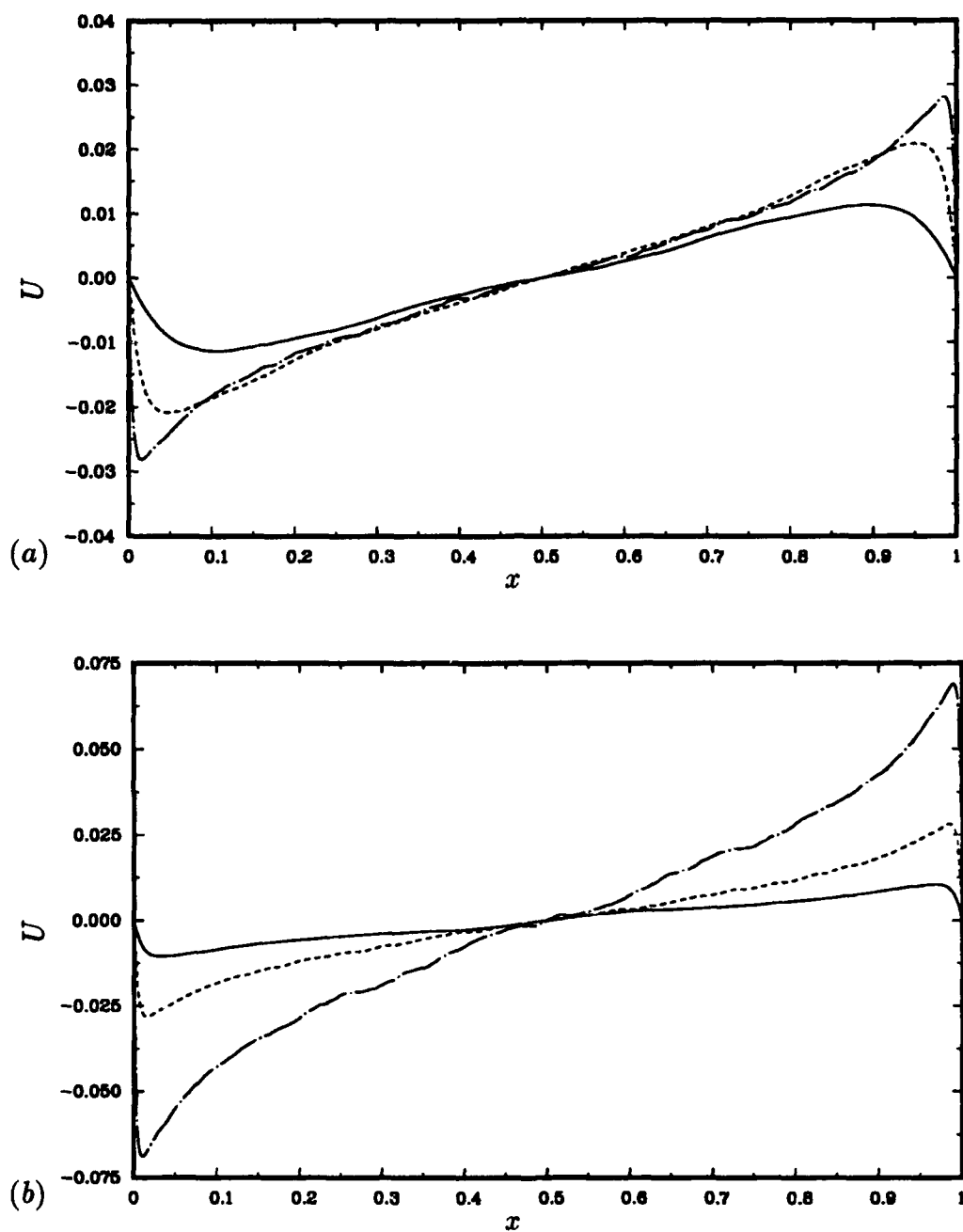


FIGURE 2. Mean-velocity profiles. (a) $\Delta t_r = 0.1$: —, $Re = 500$; ----, $Re = 1500$; -.-, $Re = 4500$; (b) $Re = 4500$: —, $\Delta t_r = 0.01$; ----, $\Delta t_r = 0.1$; -.-, $\Delta t_r = 1$.

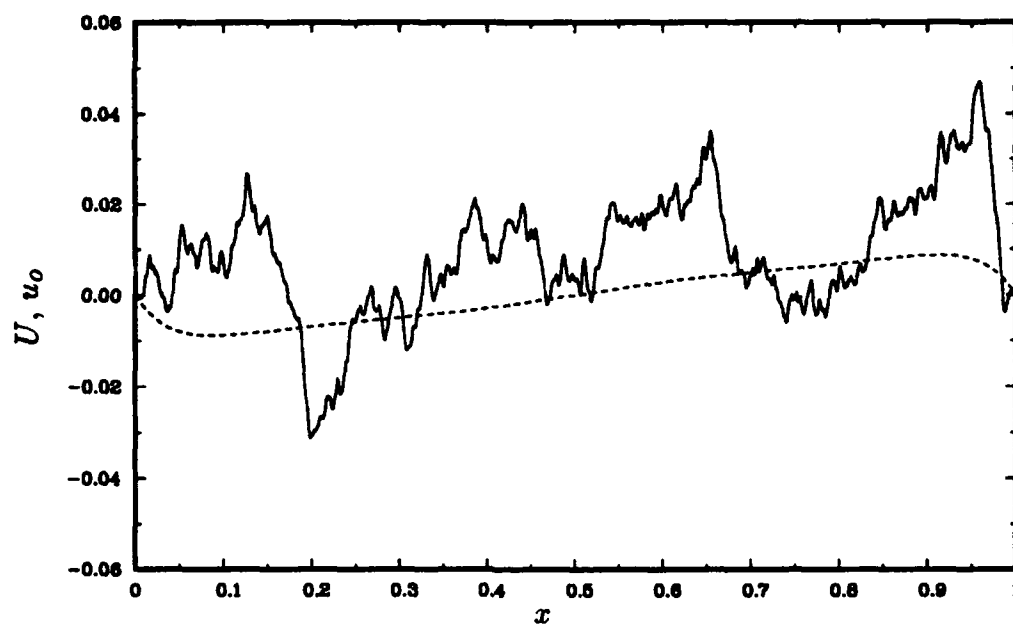


FIGURE 3. Velocity profiles: ----, time-averaged mean velocity U with no control and $Re = 1500$, $\Delta t_r = 0.01$; —, initial velocity u_0 for distributed and boundary controls.

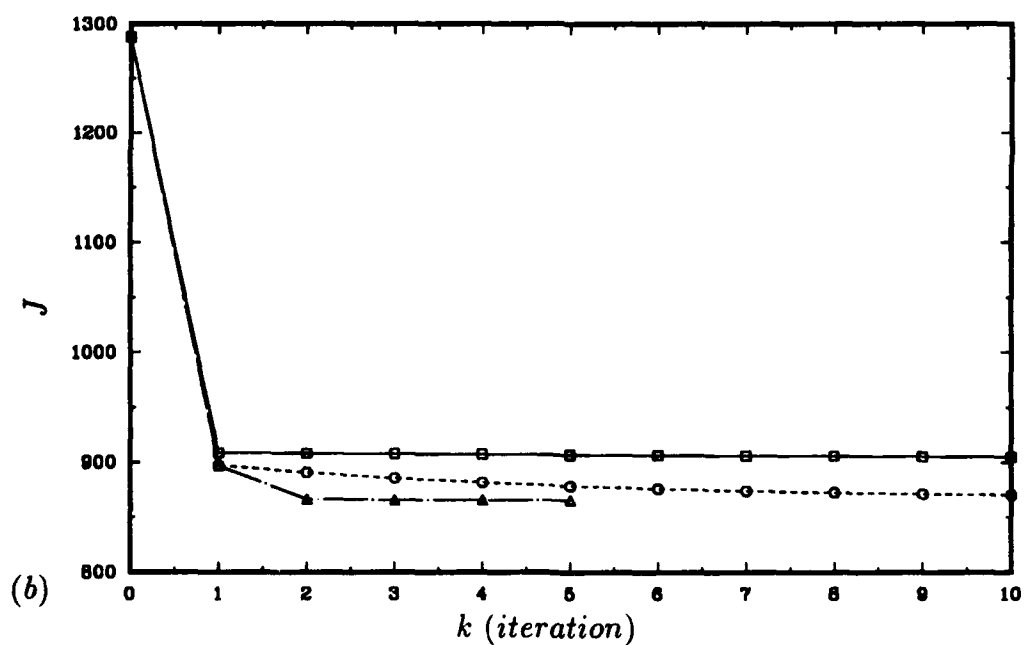
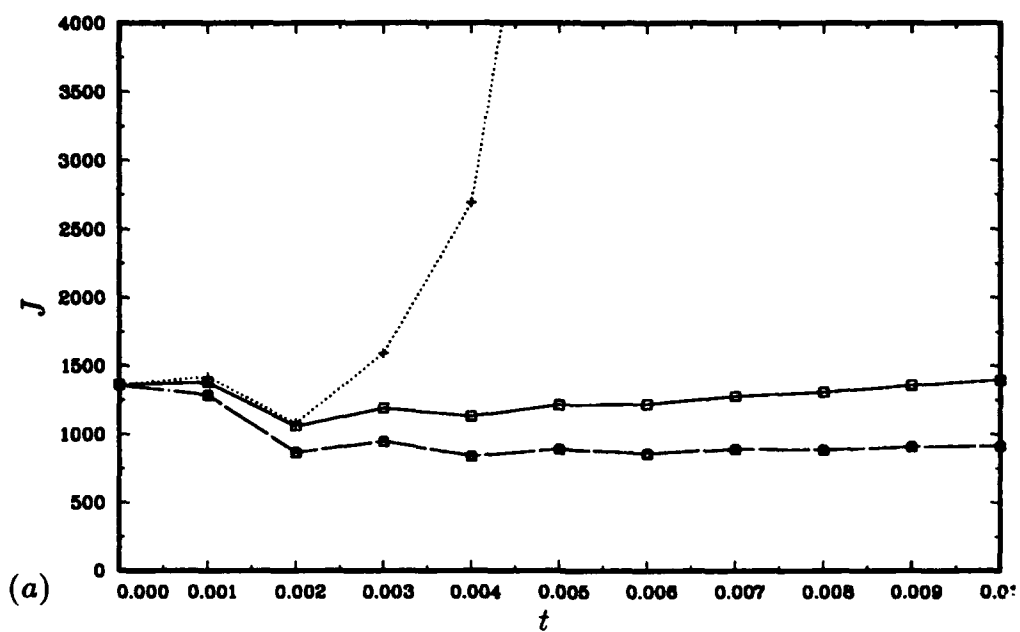


FIGURE 4. Variation of the cost and its convergence with respect to the parameter of descent ρ_0 for case (ii). (a) \square , No control; \circ , $\rho_0 = 0.1$; Δ , $\rho_0 = 1$; $+$, $\rho_0 = 1.69$; (b) at $t = 0.002$, \square , $\rho_0 = 0.01$; \circ , $\rho_0 = 0.1$; Δ , $\rho_0 = 1$.

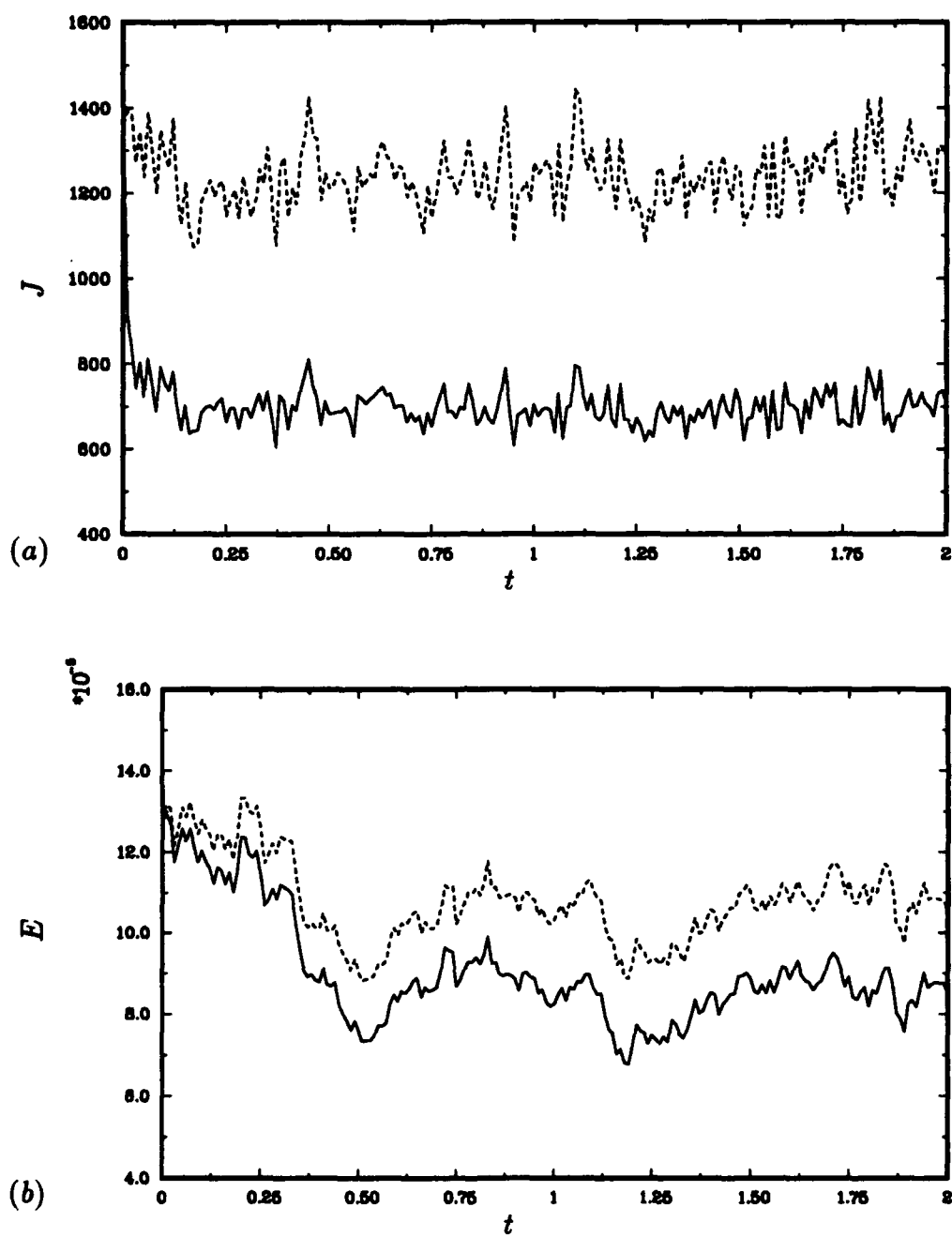


FIGURE 5. For caption see the following page.

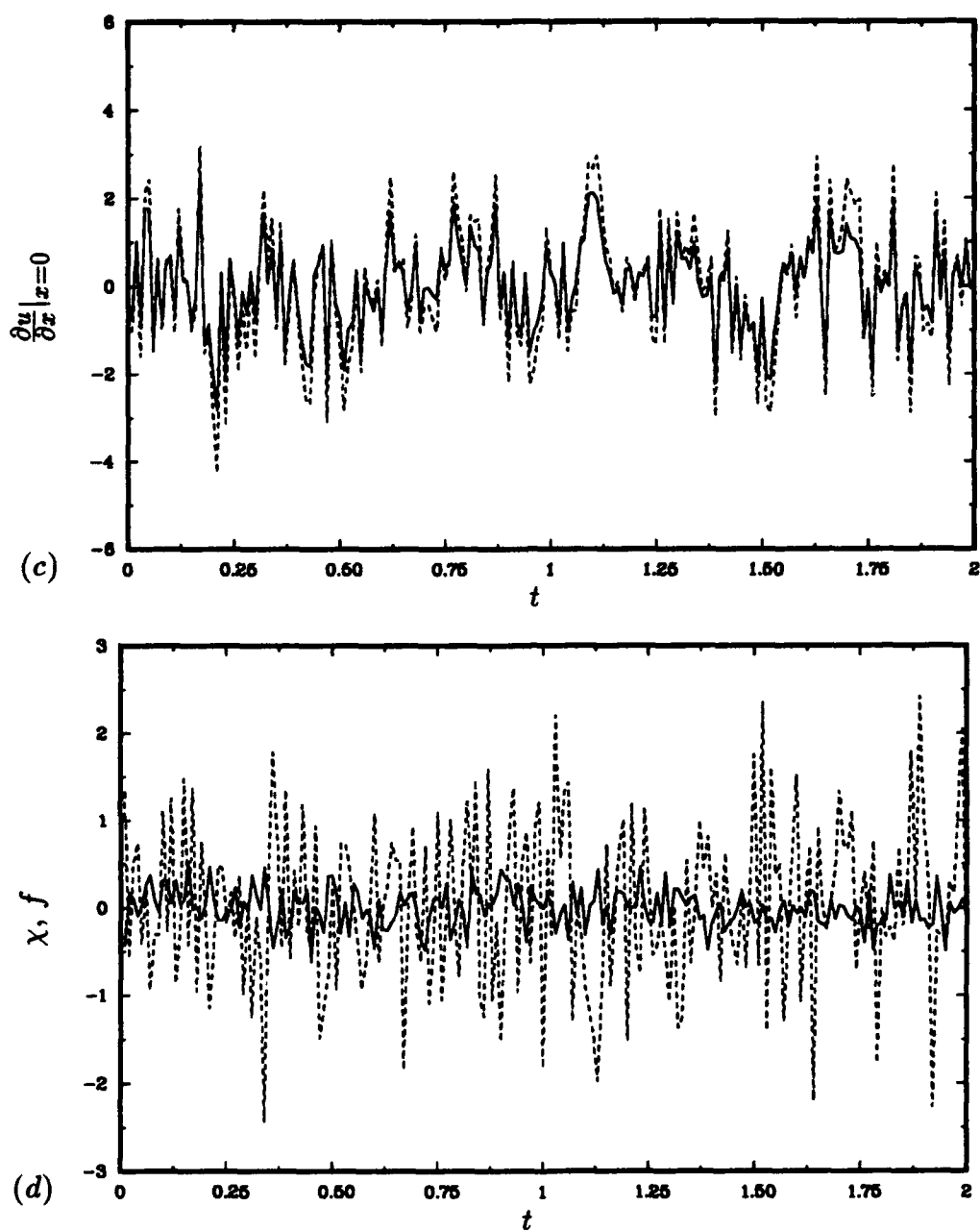


FIGURE 5. Time history of flow parameters for case (ii): — , with control; ---- , without control. (a) Cost; (b) energy inside the domain; (c) wall velocity gradient $\partial u / \partial x(x = 0)$; (d) momentum forcings at $x = 0.5$: — , control forcing f ; ---- , random forcing χ .

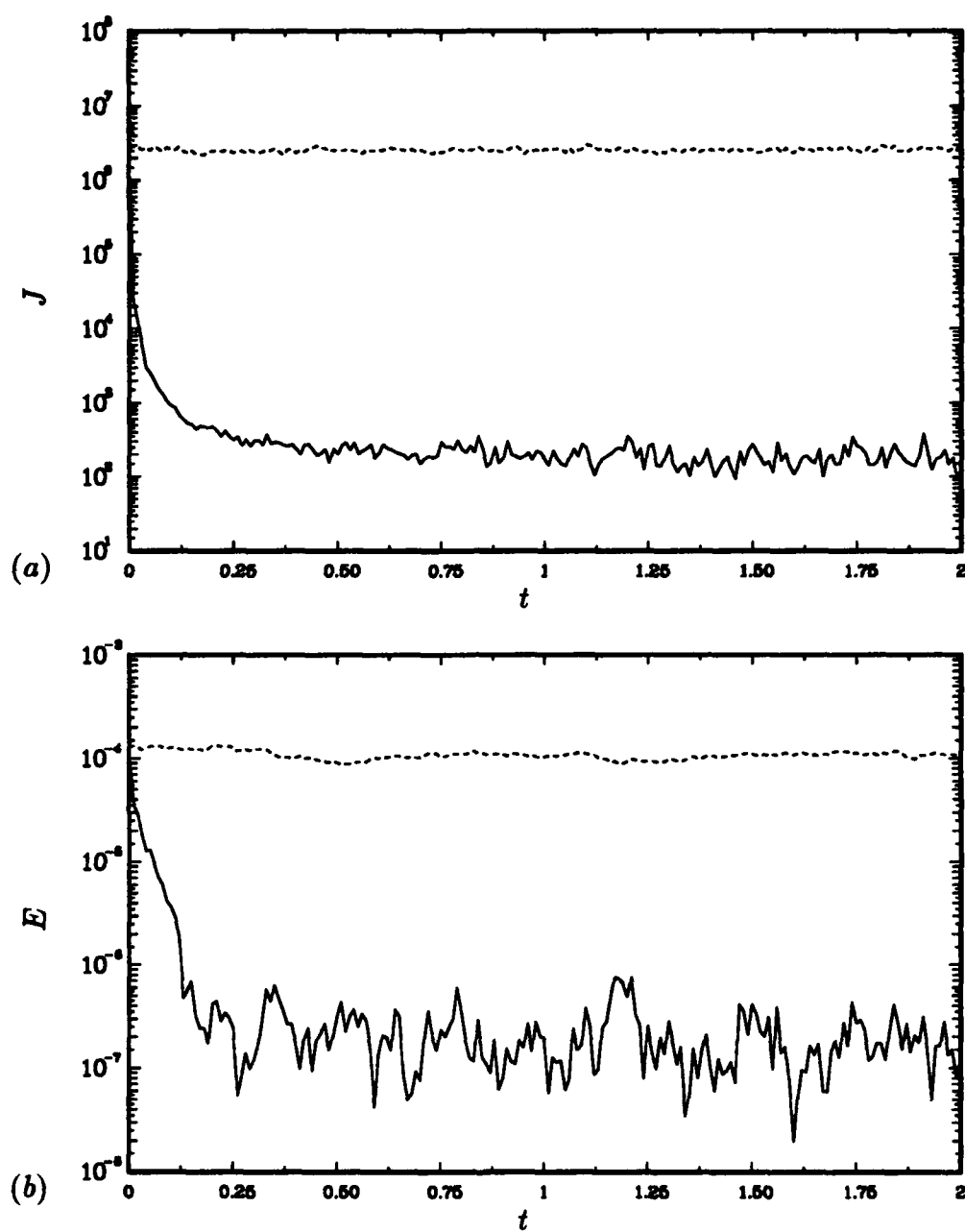


FIGURE 6. For caption see the following page.

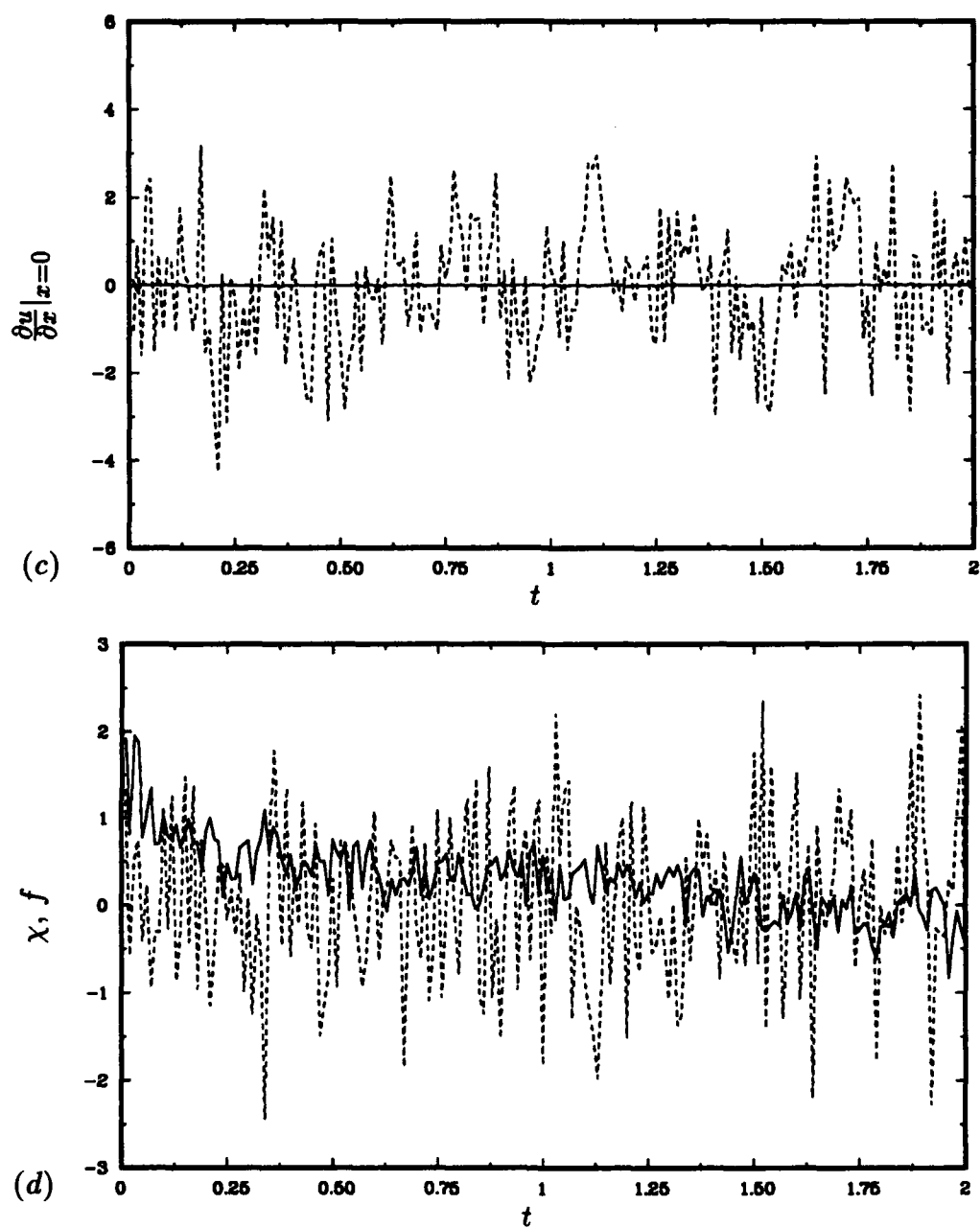


FIGURE 6. Time history of flow parameters for case (iii): — , with control; ---- , without control. (a) Cost; (b) energy inside the domain; (c) wall velocity gradient $\partial u / \partial x(x = 0)$; (d) momentum forcings at $x = 0.5$: — , control forcing f ; ---- , random forcing χ .

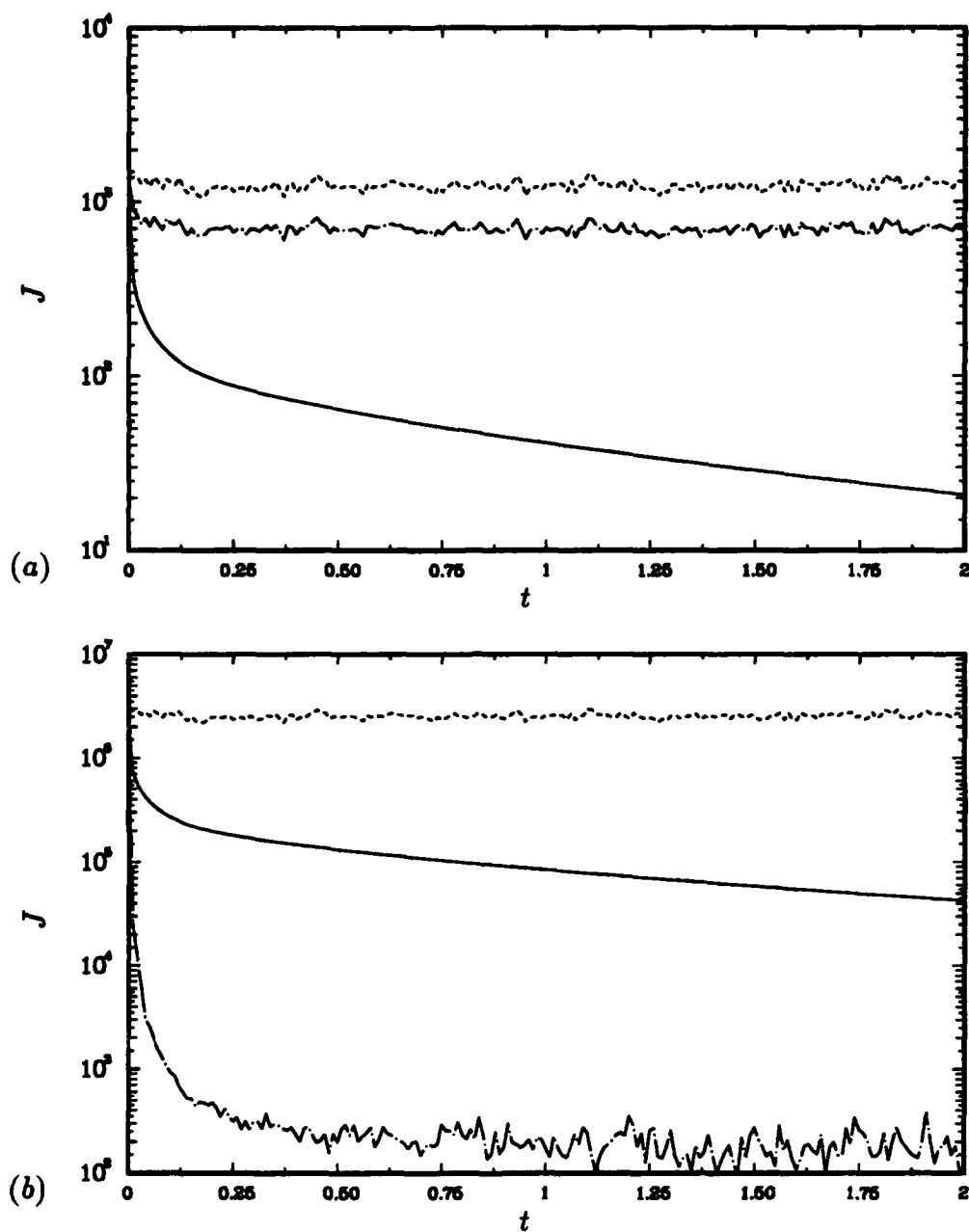


FIGURE 7. For caption see the following page.

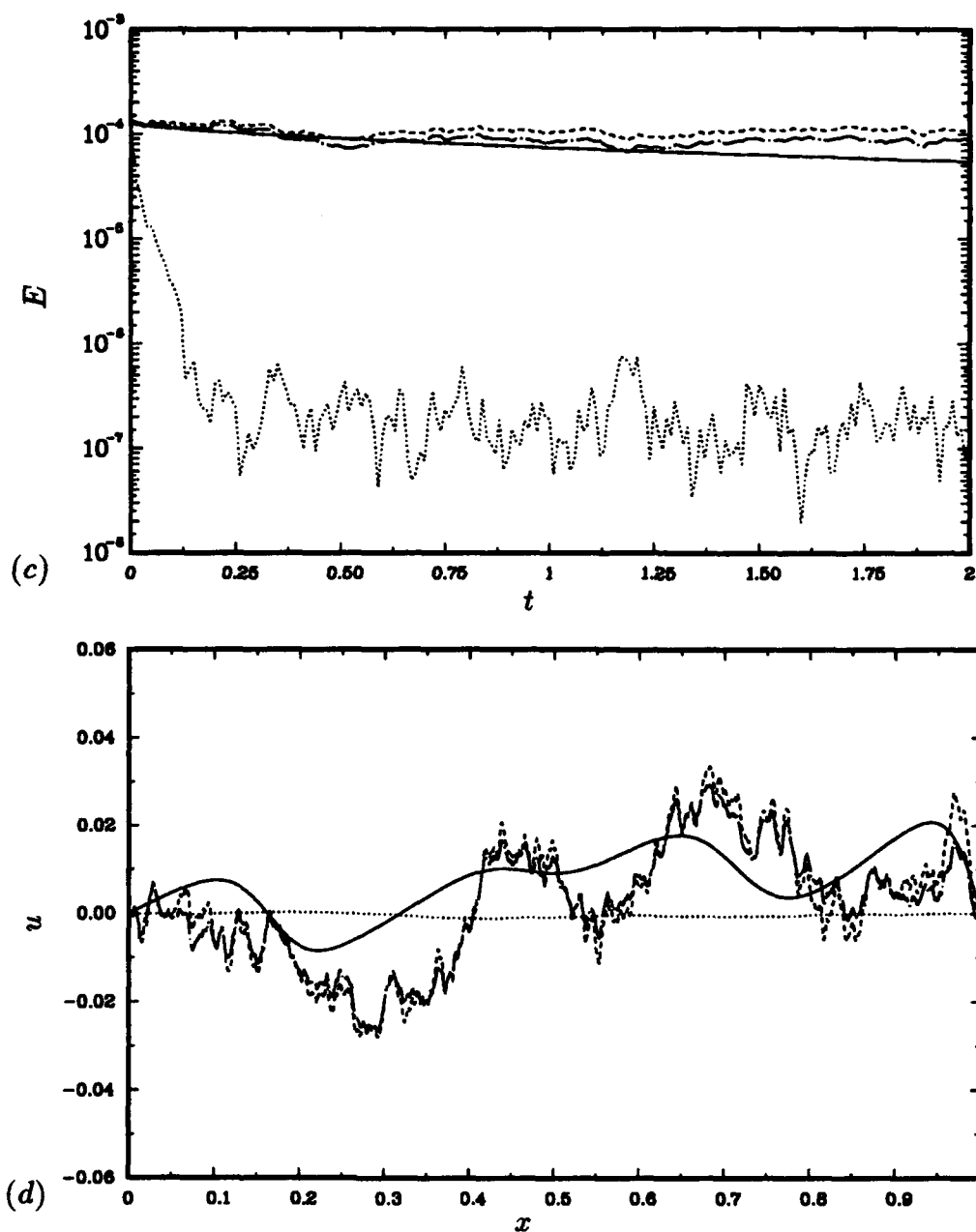


FIGURE 7. Temporal evolution of flow parameters and velocity profiles with and without random forcing and control. (a) Cost with $l_d = 1$ and $m_d = 1/\Delta x$: —, $\chi = f = 0$; ----, $f = 0$ and $\chi \neq 0$; —·—, control (case (ii)); (b) cost with $l_d = 1$ and $m_d = 1/\Delta x^2$: —, $\chi = f = 0$; ----, $f = 0$ and $\chi \neq 0$; —·—, control (case (iii)); (c) energy inside the domain: —, $\chi = f = 0$; ----, $f = 0$ and $\chi \neq 0$; —·—, control (case (ii)); ·····, control (case (iii)); (d) instantaneous velocity profiles at $t = 2$: —, $\chi = f = 0$; ----, $f = 0$ and $\chi \neq 0$; —·—, control (case (ii)); ·····, control (case (iii)).

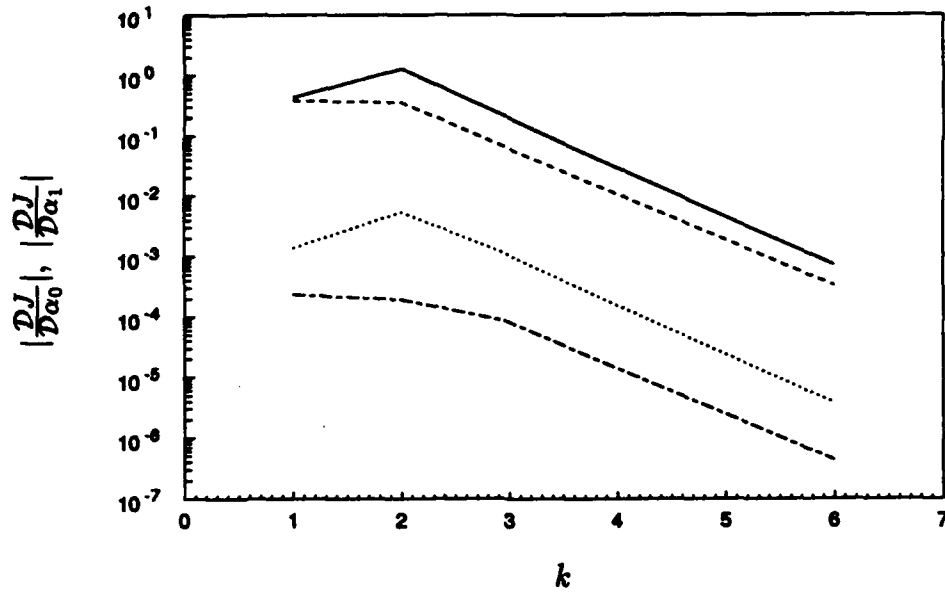


FIGURE 8. Convergence of the sensitivity of the cost function at $t = 0.001$ for case (ii) and $\theta_1(u) = u$: —, $|DJ/D\alpha_0|_{x=0.5}$; ----, $|DJ/D\alpha_0|_{x=0.01}$; ·····, $|DJ/D\alpha_1|_{x=0.5}$; ---, $|DJ/D\alpha_1|_{x=0.01}$.

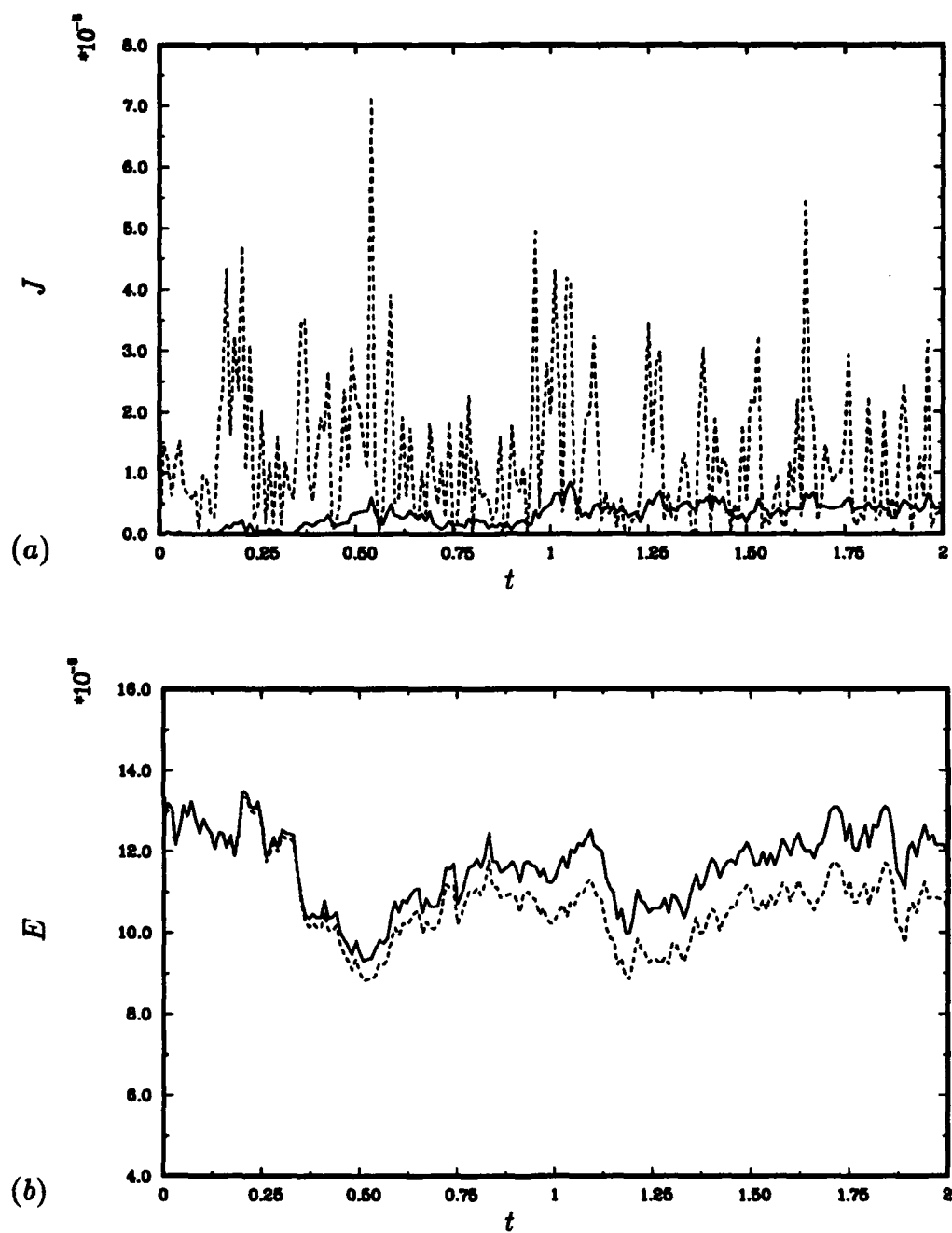


FIGURE 9. For caption see the following page.

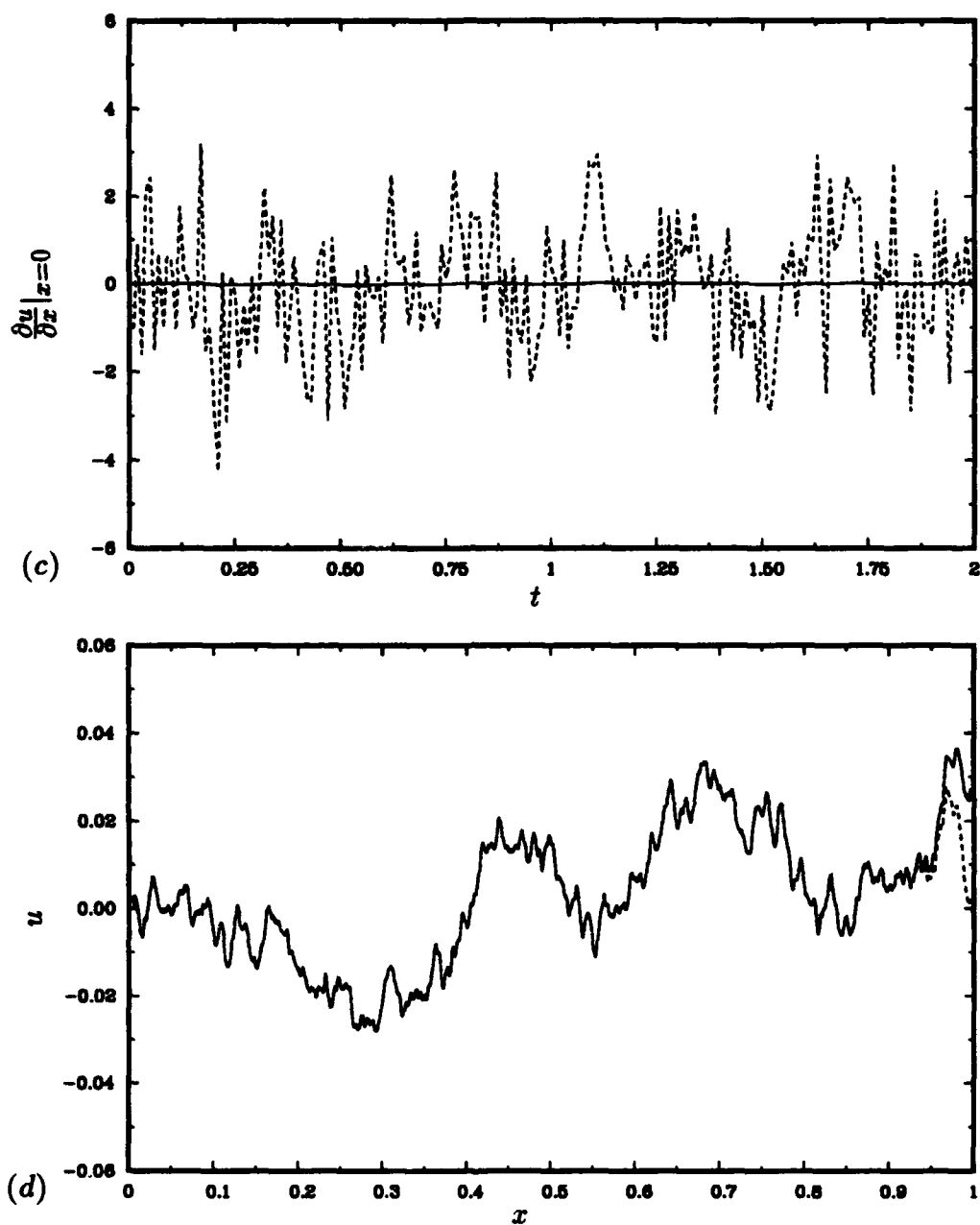


FIGURE 9. Time history of flow parameters, and velocity profile for case (ii'): —, with control; ----, without control. (a) Cost; (b) energy inside the domain; (c) wall velocity gradient $\partial u / \partial x(x = 0)$; (d) velocity profile at $t = 2$.

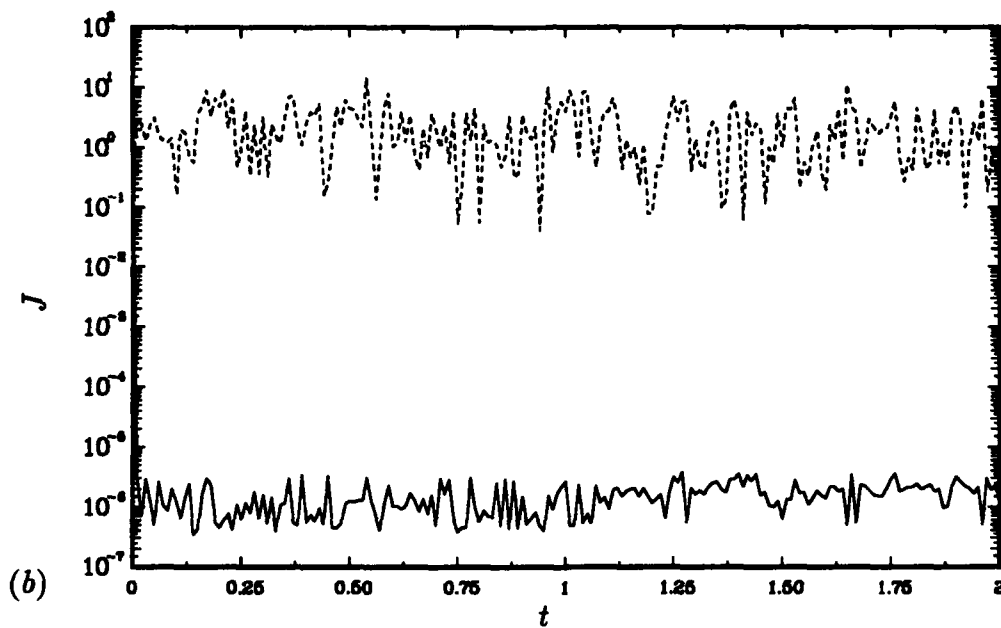
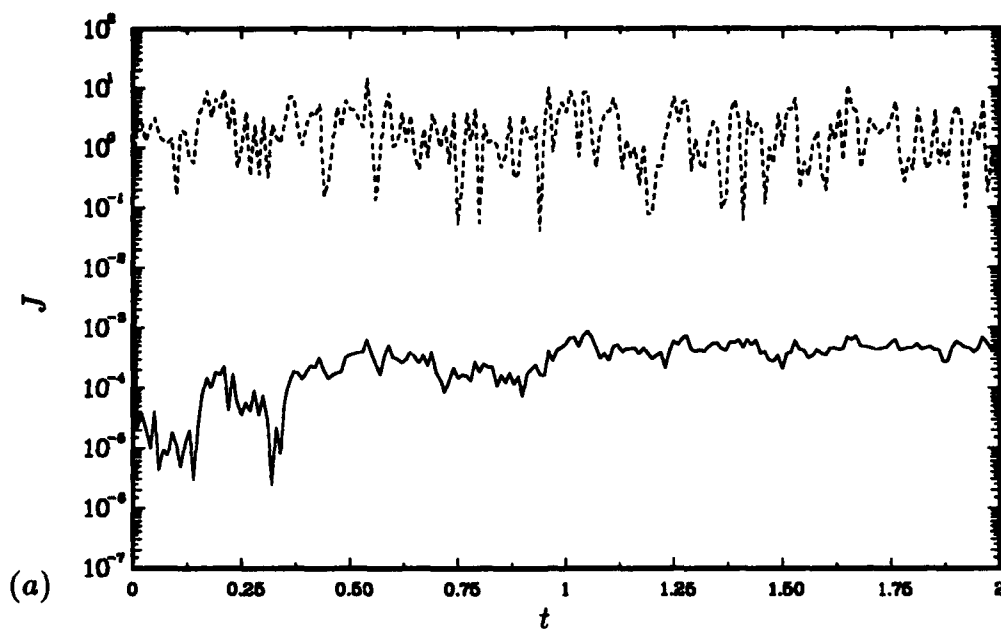


FIGURE 10. Time history of the cost: — , with control; ---- , without control.
 (a) Case (iii'); (b) case (iv').

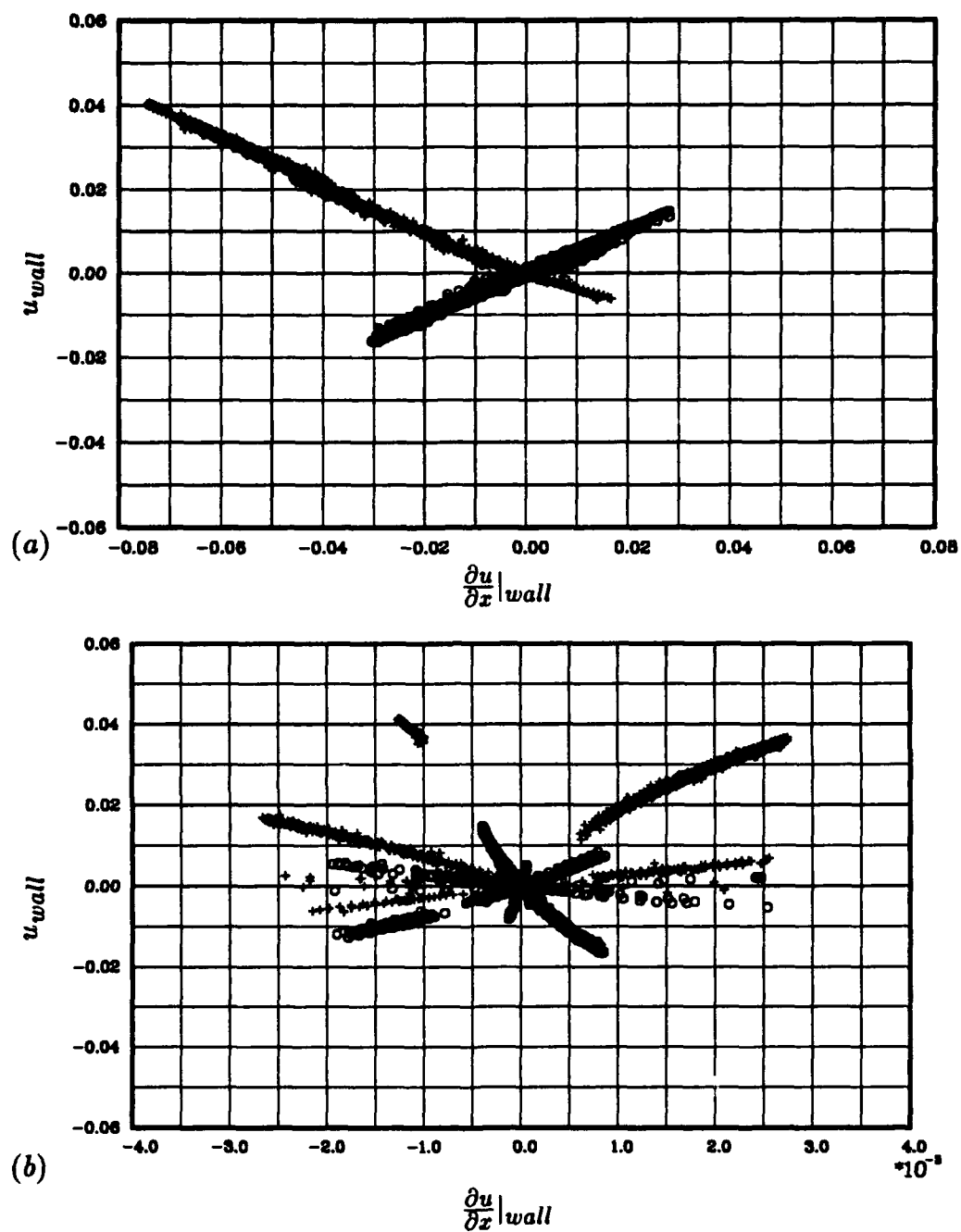


FIGURE 11. Phase diagram of control velocity and velocity gradient at the wall for the time interval $0 < t < 2$: o, at $x = 0$; +, at $x = 1$. (a) Case (ii'); (b) case (iii'). The phase diagram of case (iv') is nearly same as that of case (iii'). Note that wall velocity gradients of case (iii') are much smaller than those of case (ii').

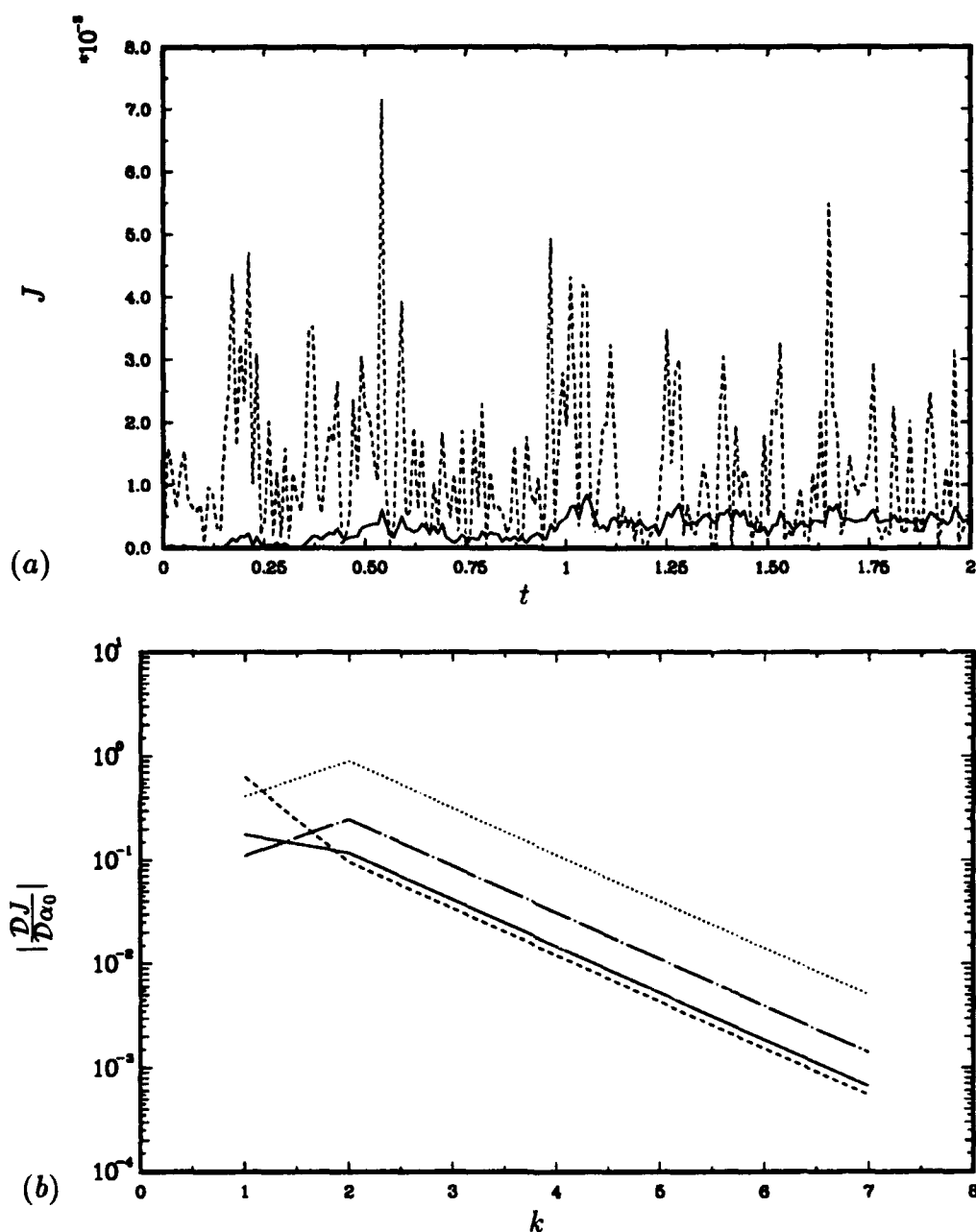


FIGURE 12. Variation of the cost and sensitivity with respect to time - discretization methods for case (ii'). (a) Time history of the cost: —, with control; ----, without control using a semi-implicit method. The result of using a fully implicit method is the same as that of using a semi-implicit method; (b) convergence of the sensitivity at $t = 0.001$: with a semi-implicit method, —, $|DJ/D\alpha_{0,0}|$; ----, $|DJ/D\alpha_{0,1}|$; with a fully implicit method, —·—, $|DJ/D\alpha_{0,0}|$; ·····, $|DJ/D\alpha_{0,1}|$.

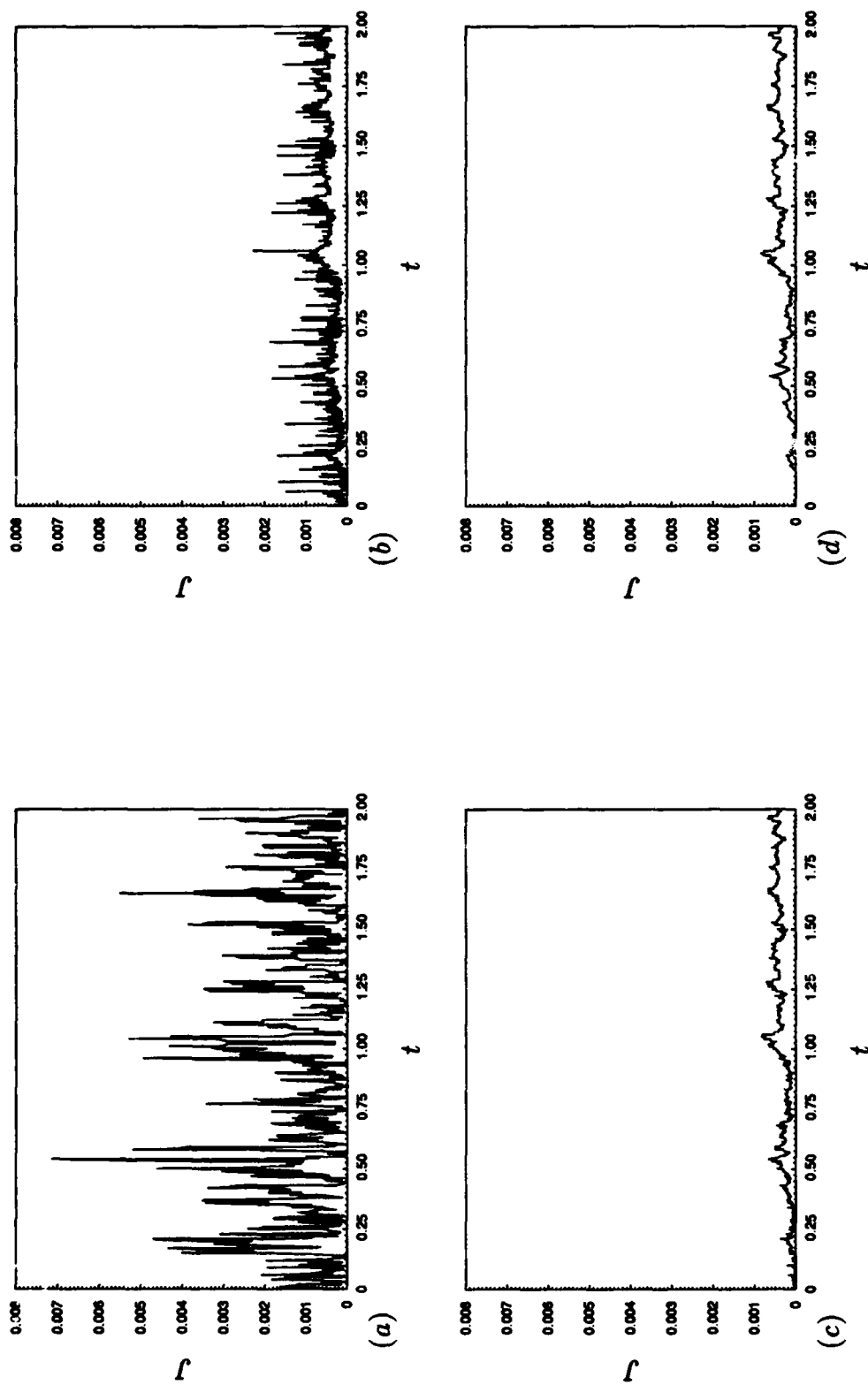


FIGURE 13. Time history of the cost for various iterations k for case (ii'): (a) without control, (b) $k = 1$; (c) $k = 2$; (d) $k = 1$ with control. $\Delta t = 0.001$, and $\rho = 0.001$ are used.

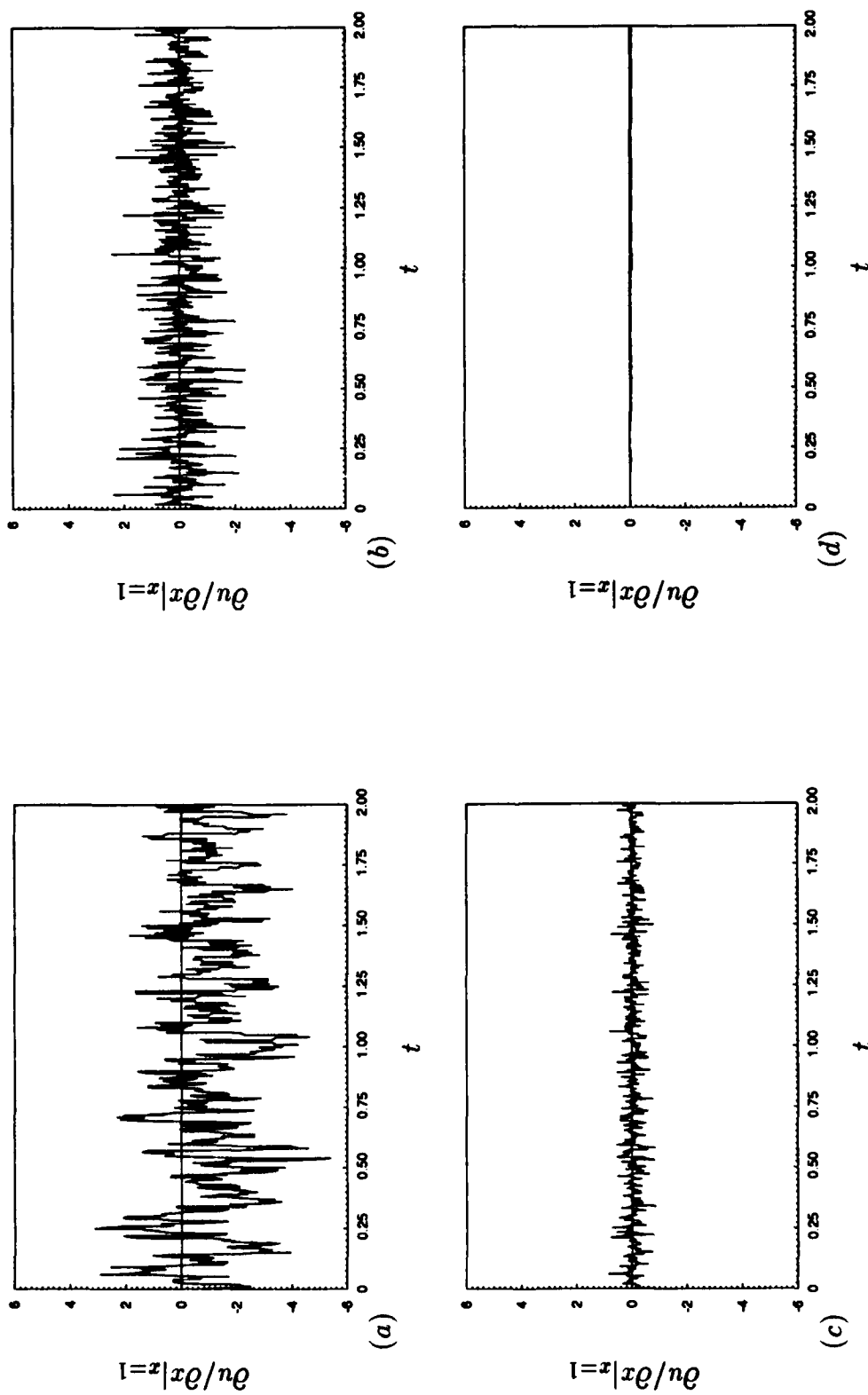


FIGURE 14. Time history of the wall velocity gradient for various iterations k for case (ii'): (a) without control; with control, (b) $k = 1$; (c) $k = 2$; (d) $k = 7$. $\Delta t_r = 0.01$, $\Delta t = 0.001$, and $\rho = 0.001$ are used.

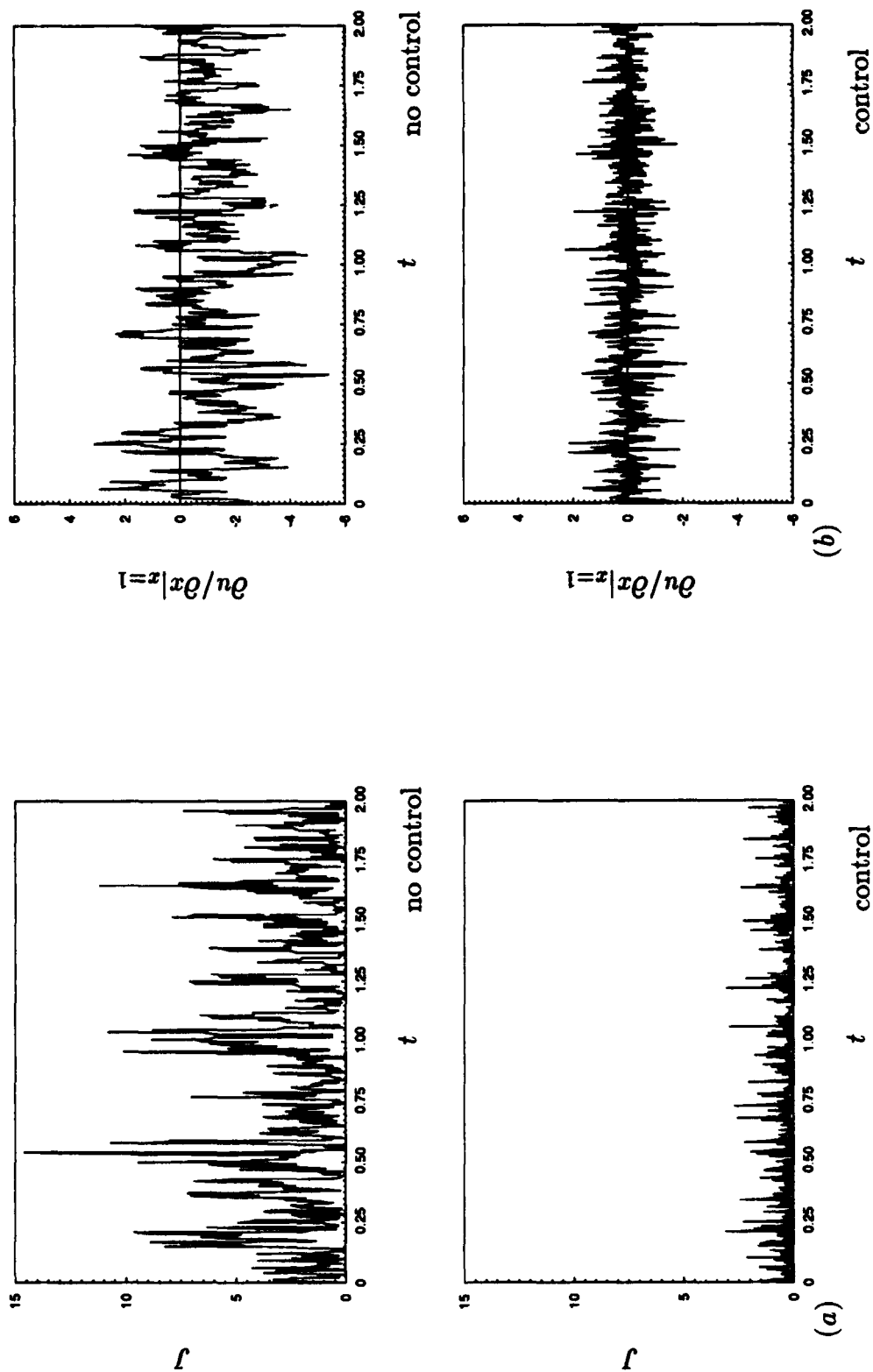


FIGURE 15. Time history of the cost and wall velocity gradient with $k = 1$ for case (iv'): (a) cost; (b) wall velocity gradient. $\Delta t_r = 0.01$, $\Delta t = 0.001$, and $\rho = 8 \times 10^{-7}$ are used. Mean values of the cost in cases with and without controls are 0.291 and 2.247, respectively.

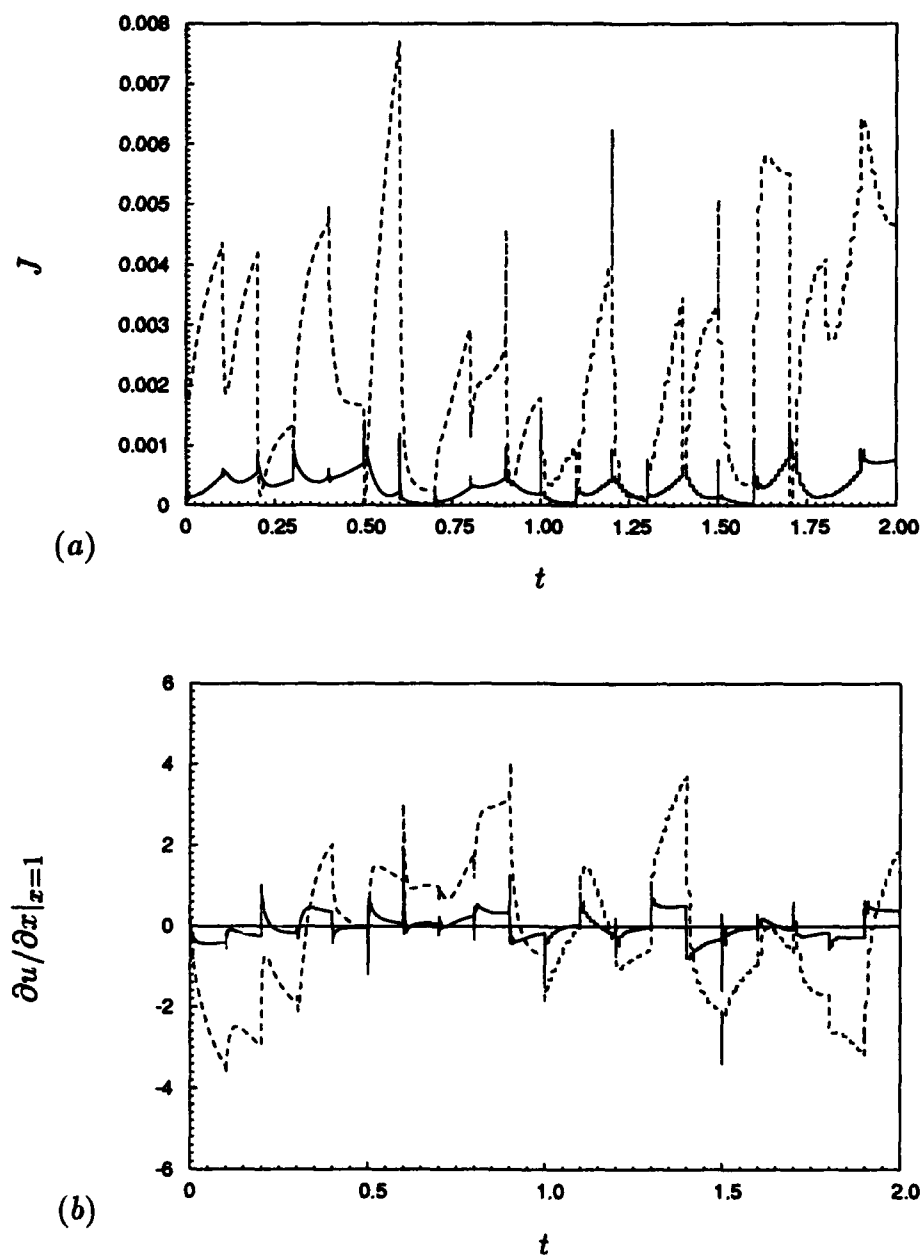


FIGURE 16. Time history of the cost and wall velocity gradient with $k = 1$ for case (ii'): —, with control; ----, without control. (a) Cost; (b) wall velocity gradient. $\Delta t_r = 0.1$, $\Delta t = 0.001$, and $\rho = 0.001$ are used. Mean values of the cost in cases with and without controls are 0.000325 and 0.00246, respectively.

CHAPTER 5

CONCLUSIONS AND DISCUSSIONS

Some avenues for the application of the mathematical methods of control theory to the problem of control of fluid flow were presented. The problem of controlling turbulence was considered and posed as a problem in optimal control theory using the methods, formalism and language of control theory. We have presented a new suboptimal control and feedback procedure, which applies to fairly general cost functions and fairly general time-dependent equations *including in particular stochastic equations*. This procedure was not strictly justified but did produce good numerical results and is fairly simple.

Feedback control procedures were applied to the stochastic Burgers equation. Two types of controls were investigated: distributed and boundary controls. Even though distributed control by body forces is rather unrealistic, it turns out to be a good introduction to more complicated situations. For boundary control, the control is the boundary velocity, which is more practical and can be implemented in real situations.

Several case studies of both types of controls have been completed to investigate the performance of the control algorithm: the reduction of cost, convergence of the gradient algorithm, dependence of the sensitivity of the cost function with respect to the control variables, effect of the parameter of descent, and choice of the form of the feedback law. Most cases considered showed a significant reduction of cost.

The role of the preassigned form of the feedback law was discussed in sections 3.1.1 and 4.4. The feedback procedures considered in the present study depend on the time-discretization method used. One would hope that the control results are insensitive to such numerical considerations. Numerical experiments show that this may indeed be the case.

The semi-implicit method seems most promising for future and more involved applications. Indeed, for boundary control using a fully implicit method the adjoint equation (equation (C.4)) contains all interior velocities as well as the boundary velocities (or boundary velocity gradients) so that the feedback control algorithm may not be practical: that is a full knowledge of the flow field would be required for

the implementation of the control algorithm when there exists no successful state estimator for the system. However using the semi-implicit method, one can circumvent this problem. The resulting adjoint equation (D.2) with the semi-implicit method does not contain any velocities except the wall velocity gradients. Practical implementation of the control algorithm developed here may be possible with the restriction of only one iteration ($k = 1$) at each instant of time. The effectiveness of the control algorithm with one iteration was investigated: cases considered still showed a significant reduction of cost.

The result of the application of this semi-implicit scheme to the Navier-Stokes equations can not be predicted at this time even though the scheme was very successful for the Burgers equation. The mathematical analysis of this topic and the application of feedback control to the Navier-Stokes equations are in progress.

PART III

Direct Numerical Simulation of Turbulent Flow over Riblets

CHAPTER 1

INTRODUCTION

Organized structures have been observed in turbulent flows over the past three decades and are known to play an important role in turbulent transport (Cantwell 1981 and Robinson 1991). The awareness of the existence of deterministic structures has led to substantial research in turbulence control. Skin-friction reduction in turbulent flow has been investigated by several different passive means, such as riblets, large-eddy break-up devices, polymer additions, and compliant walls (see Bushnell & McGinley 1989 and Coustols & Savill 1992). Among those tested to date, surface-mounted longitudinal grooves have been most successful in reducing the net drag of turbulent boundary layers in spite of a substantial increase in the wetted surface area.

Walsh & Weinstein (1978) and Walsh (1980, 1982, 1983) showed that V-groove riblet surfaces can produce consistent net drag reductions (as large as 8 %) provided the height and spacing of the grooves are less than $25 \nu/u_\tau$, where ν and u_τ denote the kinematic viscosity and the wall-shear velocity, respectively. The effects of riblets on turbulent boundary layers have been investigated by several other researchers: Hooshmand *et al.* (1983), Gallagher & Thomas (1984), Bacher & Smith (1985), Sawyer & Winter (1987), Wallace & Balint (1987), Wilkinson & Lazos (1987), Bechert & Bartenwerfer (1989), Choi (1989), and Vukoslavčević *et al.* (1992), to name a few. Nitschke (1984), Liu *et al.* (1990), and Nakao (1991) studied the effects of riblets in turbulent pipe flows. Their results were in good agreement with previous investigations of turbulent boundary-layer flows over riblets.

The mechanisms by which riblets reduce drag, however, remain poorly understood. Two possible mechanisms have been proposed. The first is that the skin-friction reduction in the riblet valleys might be sufficient to overcome the skin-friction increase near riblet tips. The second is that riblet tips actually reduce momentum transport by impeding the cross-flow motion. Walsh & Weinstein (1978) and Walsh (1980) designed riblet surfaces to confine the turbulent "wall bursts" to their initial birth regions. Gallagher & Thomas (1984) suggested from a flow visualization study that the observed drag reductions result less from a direct interaction of riblets with the turbulence than from the low velocities in the bottoms

of the grooves. Bacher & Smith (1985) observed by a flow visualization that, below $y^+ = yu_\tau/\nu = 15$, the lateral movement of the streaks above a riblet surface is substantially less than the lateral movement observed above a flat surface. They suggested that the secondary vortices generated at the riblet peaks weaken the well known near-wall streamwise vortices and inhibit the spanwise concentration of low-speed fluid into streak formations. Wallace *et al.* (1987) reviewed the existing experimental data and proposed that riblets shield the surface from much of the turbulent momentum transport, resulting in smaller velocity gradients on the bounding surface. Robinson (1988) studied the effects of riblets on turbulence in a supersonic boundary layer. He hypothesized that riblets reduce skin friction by impeding the cross-stream flow necessary to replace the near-wall fluid that is ejected during turbulence production events. Bechert & Bartenwerfer (1989) introduced a so-called "protrusion height" for different types of riblets and related it to the ability of riblets to impede the cross-flow. Choi (1989) indicated that the restriction of spanwise movement of the longitudinal vortices is a prime mechanism for turbulent drag reduction.

Choi *et al.* (1991) studied the effect of riblets in fully developed laminar channel flows in order to investigate whether the skin-friction reduction in the riblet valley is sufficient to compensate for the skin-friction increase in the region of the tip. They showed that drag reduction is not obtained in the laminar channel flow even though the wall-shear rate on most of the riblet surface was smaller than that of the corresponding flat channel flow.

Effects of riblets on turbulence statistics have been reported by several authors. These include an upward shift in the log-law velocity profile due to an increase of viscous sublayer thickness, a displaced virtual origin of the wall, a reduction of turbulence intensities and Reynolds shear stress, a decrease of momentum thickness, an increase of the mean streak spacing, little change in the skewness and flatness factors of the streamwise fluctuating velocity, and limited changes of the mean velocity and turbulence quantities in the inner regions of the boundary layer.

The reported changes in turbulence statistics are not conclusive, however, and no clear picture of the drag reduction mechanism set up by riblets has emerged. The difficulty in measurement of velocity fields near riblets and the modest change in skin friction and turbulence statistics have hampered efforts to understand the mechanics of drag reduction.

In recent years, numerical simulations of turbulent flows have become an important tool for studying the basic physics of turbulence (Rogallo & Moin 1984). Kim *et al.* (1987) performed a direct numerical simulation of a turbulent channel flow. A large variety of turbulence statistics were computed and compared with the existing experimental data at comparable Reynolds numbers. Jiménez & Moin (1991) performed direct numerical simulations of unsteady channel flow at low to moderate Reynolds numbers on computational boxes chosen small enough so that the flow consists of a doubly periodic array of identical structures. The goal of their work was to isolate the basic flow unit, to study its morphology and dynamics, and to evaluate its contribution to turbulence in fully developed channels. They showed that the near-wall turbulence statistics and presumable flow mechanisms in the minimal channel are in good agreement with the "natural" channel.

The objective of this work is to perform direct numerical simulations of turbulent flows over riblets, to analyze the resulting flow database, and to educe the mechanism of drag reduction by riblets. Such an understanding can potentially lead to the design of riblet configurations that give even higher drag reduction. In PART III we describe the results of these simulations and our observations on the drag reduction mechanism. The computed results are compared extensively with available experimental data. The computational domain and grid spacing are described in chapter 2, followed in chapter 3 by the numerical method developed for complex geometries. Chapter 4 describes the drag variation due to riblets and the virtual origin of the wall. Turbulence statistics are reported in chapter 5. Modified turbulent structures and mechanisms of drag reduction by riblets are presented in chapter 6, followed by a brief summary in chapter 7.

CHAPTER 2

COMPUTATIONAL DOMAIN AND GRID SPACING

The flow geometry and coordinate system are shown in figure 1. The upper wall is a flat plate, whereas the lower wall is a plate with riblets. Fully developed turbulent flow over riblets is homogeneous in the streamwise (x_1) direction, and periodic boundary conditions are used in the streamwise (x_1) and spanwise (x_3) directions. The no-slip condition is applied at both walls. The simulation imposes a constant instantaneous volume flux in the streamwise direction,

$$Q = \int_{A_c} u_1 dA = \frac{2}{3} A_c U_l,$$

where $A_c = L_{x_2} L_{x_3}$ is the cross-sectional area, and U_l is the centerline velocity of a laminar parabolic profile with the same volume flux. The computation is carried out for a Reynolds number of 4200 based on the laminar centerline velocity U_l and the channel half-width $\delta (= L_{x_2}/2)$; i.e.

$$Re_l = \frac{3Q}{4\nu L_{x_3}} = \frac{U_l \delta}{\nu}.$$

This Reynolds number corresponds to a Reynolds number of about 180 based on the wall-shear velocity of the flat plate, u_{τ_f} . Unless otherwise stated, wall units of flow quantities are based on the wall-shear velocity of the flat plate. For the Reynolds number considered here, the computational box is chosen to be a *minimal flow unit* of Jiménez & Moin (1991) (see chapter 1); the streamwise and spanwise computational periods, L_{x_1} and L_{x_3} , are $\pi\delta$ and $0.289\pi\delta$, respectively (roughly 570 and 160 wall units).

A uniform mesh with spacing $\Delta x_1^+ \approx 35$ is used in the streamwise direction. This streamwise spacing is rather coarse, however, for comparison the calculations of flows over both riblets and flat surface will be carried out with the same resolution. A non-uniform mesh of 129 points with hyperbolic tangent distribution is used in the wall-normal direction. The first mesh point away from the flat wall is at $x_2^+ \approx$

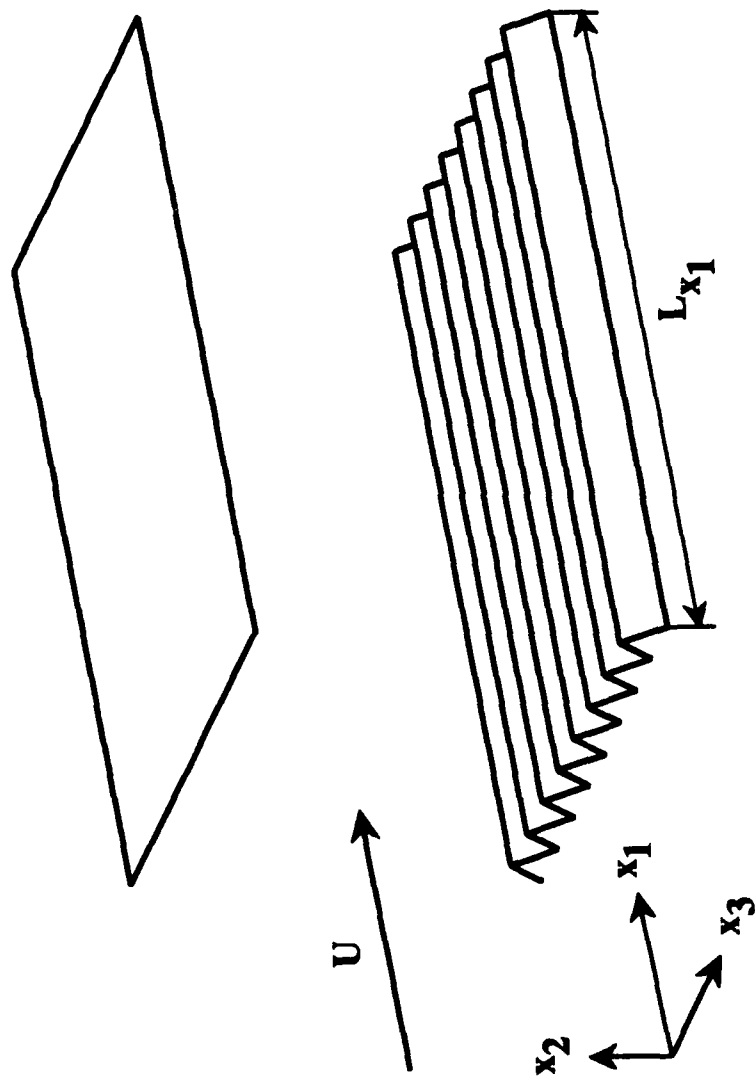
Case	s/δ	s^+	h^+	α	$N_{x_1} \times N_{x_2} \times N_{x_3}^\dagger$	Δx_3^+
A	0.2270	40	20.0	45°	$16 \times 129 \times 128$	1.28
B	0.2270	40	34.6	60°	$16 \times 129 \times 128$	1.28
C	0.1135	20	10.0	45°	$16 \times 129 \times 256$	0.64
D	0.1135	20	17.3	60°	$16 \times 129 \times 256$	0.64

$^\dagger N_{x_i}$ is the number of grid points in the x_i direction.

Table 1. Parameters for the simulations of turbulent flows over riblets.

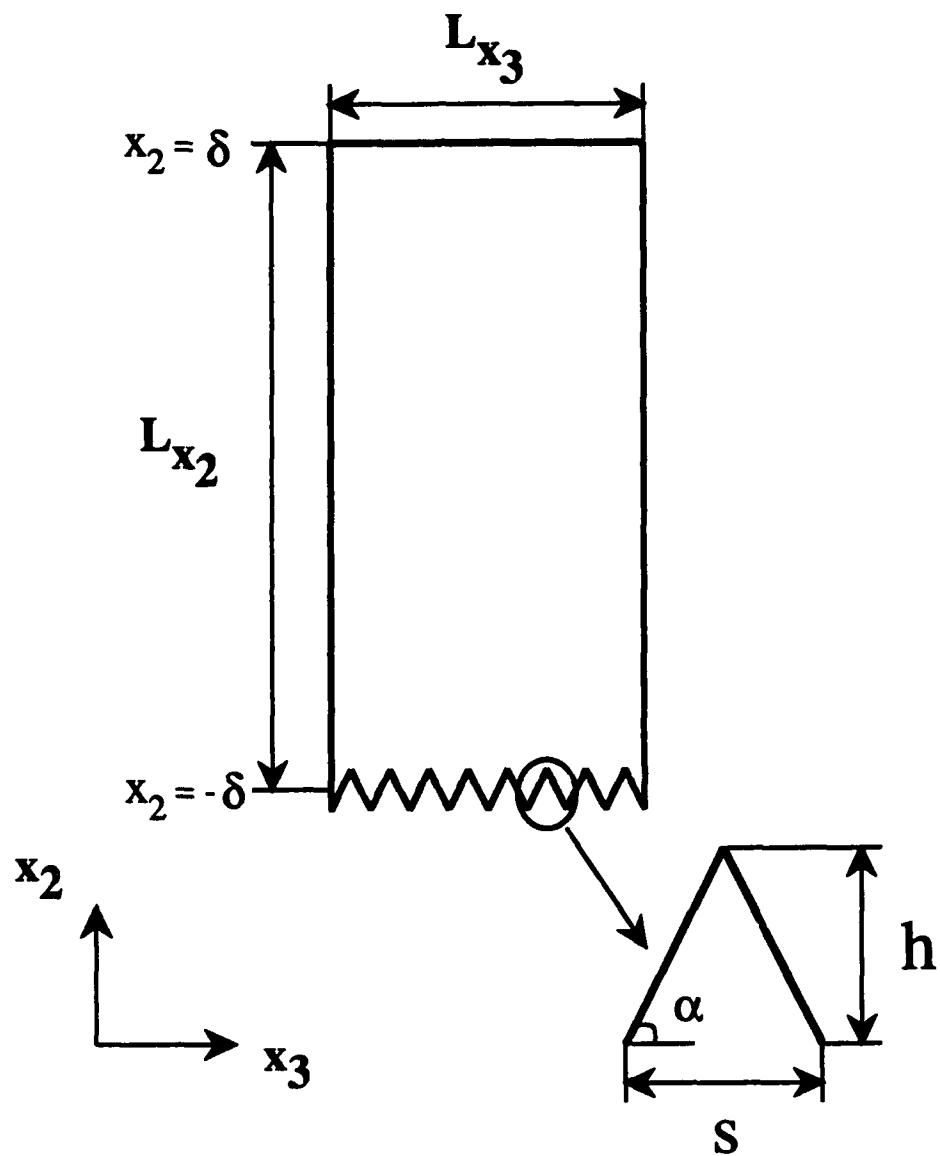
0.1, and the maximum spacing at the centerline of the channel is 8 wall units. A non-uniform orthogonal mesh developed by Bechert & Bartenwerfer (1989) is used in the wall-normal and spanwise directions; the non-uniform mesh is distributed using a conformal mapping such that the shear *force* of each numerical cell on the riblet is constant when the mean-flow distribution is a uniform Couette flow very near the riblet. An extensive grid refinement study was performed to insure adequate resolution. Thirty-two grid points on each riblet surface are necessary to resolve the high shear rates near the riblet tips. Doubling the number of mesh points in the spanwise direction changes the drag on the riblet surface by less than 1%. Insufficient grid resolution in the spanwise direction results in an underestimation of the skin friction as observed by Launder & Li (1989). The spacing between adjacent grid points far above the riblet surface, Δx_3^+ , is approximately 1 wall unit in the present calculation. An example of the computational mesh near riblets in a cross-flow plane is shown in figure 2.

We have tested four riblet configurations: riblet spacings of 20 and 40 wall units and ridge angles α of 45° and 60° . A detailed description of the parametric study is shown in table 1. The results from cases A - D near the riblets are compared to those near the flat wall.



(a)

FIGURE 1. For caption see the following page.



(b)

FIGURE 1. (a) Three-dimensional view of computational domain; (b) cross sectional view of riblet configuration.

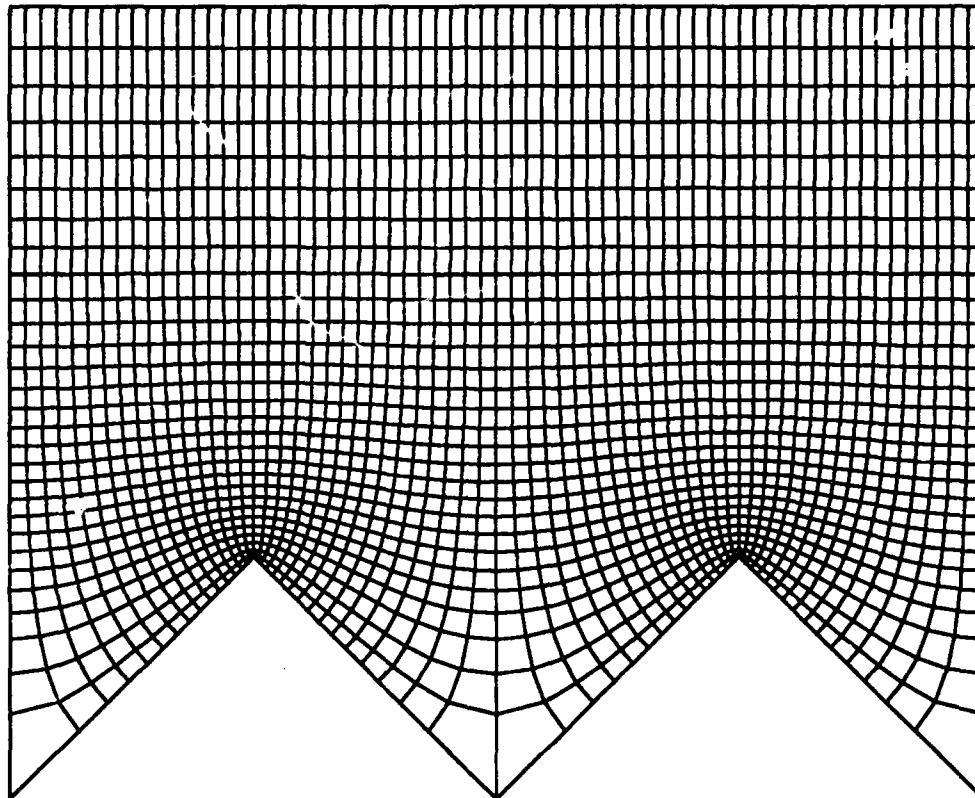


FIGURE 2. Computational mesh near riblets in the case of $s^+ \approx 20$ and $\alpha = 45^\circ$. A non-uniform mesh of 129 points with hyperbolic tangent distribution is used in the wall-normal direction, and thirty-two grid points are used on each riblet surface.

CHAPTER 3

NUMERICAL METHODS

The governing equations for an incompressible flow can be written in the following form

$$\frac{\partial u_i}{\partial t} + \frac{\partial}{\partial x_j} u_i u_j = -\frac{\partial p}{\partial x_i} + \frac{1}{Re_l} \frac{\partial}{\partial x_j} \frac{\partial}{\partial x_j} u_i, \quad (3.1)$$

$$\frac{\partial u_i}{\partial x_i} = 0, \quad (3.2)$$

where x_i are Cartesian coordinates, and u_i are the corresponding velocity components. All variables are non-dimensionalized by the channel half-width δ and the laminar centerline velocity U_l . In these units, the value of the laminar spanwise vorticity magnitude at the flat channel wall is $|\omega_z| = 2$. Re_l denotes the Reynolds number, defined as $Re_l = U_l \delta / \nu$.

Equations (3.1) and (3.2) are written in a conservative form in generalized coordinates as

$$\frac{\partial q^i}{\partial t} + N^i(\mathbf{q}) = -G^i(p) + L_1^i(\mathbf{q}) + L_2^i(\mathbf{q}), \quad (3.3)$$

$$D^i q^i = \frac{\partial q^1}{\partial \eta^1} + \frac{1}{J} \left(\frac{\partial q^2}{\partial \eta^2} + \frac{\partial q^3}{\partial \eta^3} \right) = 0, \quad (3.4)$$

where $\mathbf{q} = (q^1, q^2, q^3)$, N^i is the convection term, $G^i(p)$ is the pressure gradient term, L_1^i and L_2^i are the diffusion terms without and with cross derivatives, respectively, and D^i is the divergence operator. Here, we introduce generalized coordinates for the wall-normal and spanwise directions (i.e., $(x_2, x_3) \rightarrow (\eta^2, \eta^3)$), and use a Cartesian coordinate for the streamwise direction ($\eta^1 = x_1$). The q^i 's are volume fluxes across the faces of the cells, which are equivalent to using the contravariant velocity components on a staggered grid multiplied by the Jacobian

of the coordinate transformation, J (figure 3). Using this choice, the discretized mass conservation can be easily satisfied (Rosenfeld *et al.* 1991). The terms in equation (3.3) are (the summation convention applies),

for $i = 1$,

$$\begin{aligned} N^1 &= \frac{\partial}{\partial \eta^1} q^1 q^1 + \frac{1}{J} \frac{\partial}{\partial \eta^j} q^j q^1, \\ G^1(p) &= \frac{\partial p}{\partial \eta^1}, \\ L_1^1 &= \frac{1}{Re_l} \left(\frac{\partial}{\partial \eta^1} \frac{\partial}{\partial \eta^1} q^1 + \frac{1}{J} \frac{\partial}{\partial \eta^k} \alpha^{kj} \frac{\partial}{\partial \eta^j} q^1 \right); \quad j = k, \\ L_2^1 &= \frac{1}{Re_l} \frac{1}{J} \frac{\partial}{\partial \eta^k} \alpha^{kj} \frac{\partial}{\partial \eta^j} q^1; \quad j \neq k, \end{aligned} \tag{3.5}$$

for $i = 2, 3$,

$$\begin{aligned} N^i &= \frac{\partial}{\partial \eta^1} q^1 q^i + \frac{1}{J} \gamma_m^i \frac{\partial}{\partial \eta^j} \frac{1}{J} c_k^m q^k q^j, \\ G^i(p) &= \alpha^{ij} \frac{\partial p}{\partial \eta^j}, \\ L_1^i &= \frac{1}{Re_l} \left(\frac{\partial}{\partial \eta^1} \frac{\partial}{\partial \eta^1} q^i + \frac{1}{J} \gamma_m^i \frac{\partial}{\partial \eta^k} \alpha^{kj} \frac{\partial}{\partial \eta^j} \frac{1}{J} c_l^m q^l \right); \quad j = k, \\ L_2^i &= \frac{1}{Re_l} \frac{1}{J} \gamma_m^i \frac{\partial}{\partial \eta^k} \alpha^{kj} \frac{\partial}{\partial \eta^j} \frac{1}{J} c_l^m q^l; \quad j \neq k, \end{aligned} \tag{3.6}$$

where $q^1 = u_1$, $q^j = \gamma_k^j u_k$, $c_k^j = \partial x_j / \partial \eta^k$, $\gamma_k^j = J (c_j^k)^{-1}$, $\alpha^{jk} = J c_j^m c_k^m$,

$J = \sqrt{|c_j^m c_k^m|}$, and $j, k, l, m = 2, 3$.

The integration method used to solve equations (3.3) and (3.4) is based on a fully implicit, fractional step method (appendix E); all terms in equation (3.3) including cross-derivative diffusion terms are advanced with the Crank-Nicholson

method in time, and are resolved with the second-order central-difference scheme in space. A Newton method is used to solve the discretized nonlinear equations. The suitability of a second-order central-difference scheme for direct simulation of turbulent channel flow is discussed in appendix E.

Rapid variation of skin friction near the riblet tips requires dense grid clustering in their vicinity; this would restrict the computational time step for numerical stability if an explicit or (as in the usual practice in direct simulation) a semi-implicit method were used. In a separate study, we found the largest computational time step (in wall units) which accurately predicted turbulence statistics in a turbulent plane channel flow at $Re_l = 4200$ (appendix E). For cases A - D (table 1), we have used this same computational time step, $\Delta t U_l / \delta = 0.05$ ($\Delta t^+ \approx 0.4$). About 7 Newton iterations were needed to solve the discretized nonlinear momentum equations. The CPU time required for cases C and D was about 60 Cray-YMP seconds per time step. For all cases, the computations were carried out for 500 non-dimensional time units ($t U_l / \delta$), which corresponds to about 4000 viscous time units ($t u_{\tau}^2 / \nu$). Ten thousand time steps were required for each case. The conventional semi-implicit method would have required about a five fold increase in the required CPU time.

In PART III, x_1, x_2 , and x_3 denote the streamwise (x), wall-normal (y), and spanwise (z) directions, respectively. The velocity notations u_1, u_2 , and u_3 in the x, y , and z directions are used interchangeably with u, v , and w . The subscript w indicates the value at the wall, and the superscript $+$ indicates a non-dimensional quantity scaled by the wall variables; for example, $y^+ = y u_\tau / \nu$, where $u_\tau = (\tau_w / \rho)^{1/2}$ is the wall-shear velocity.

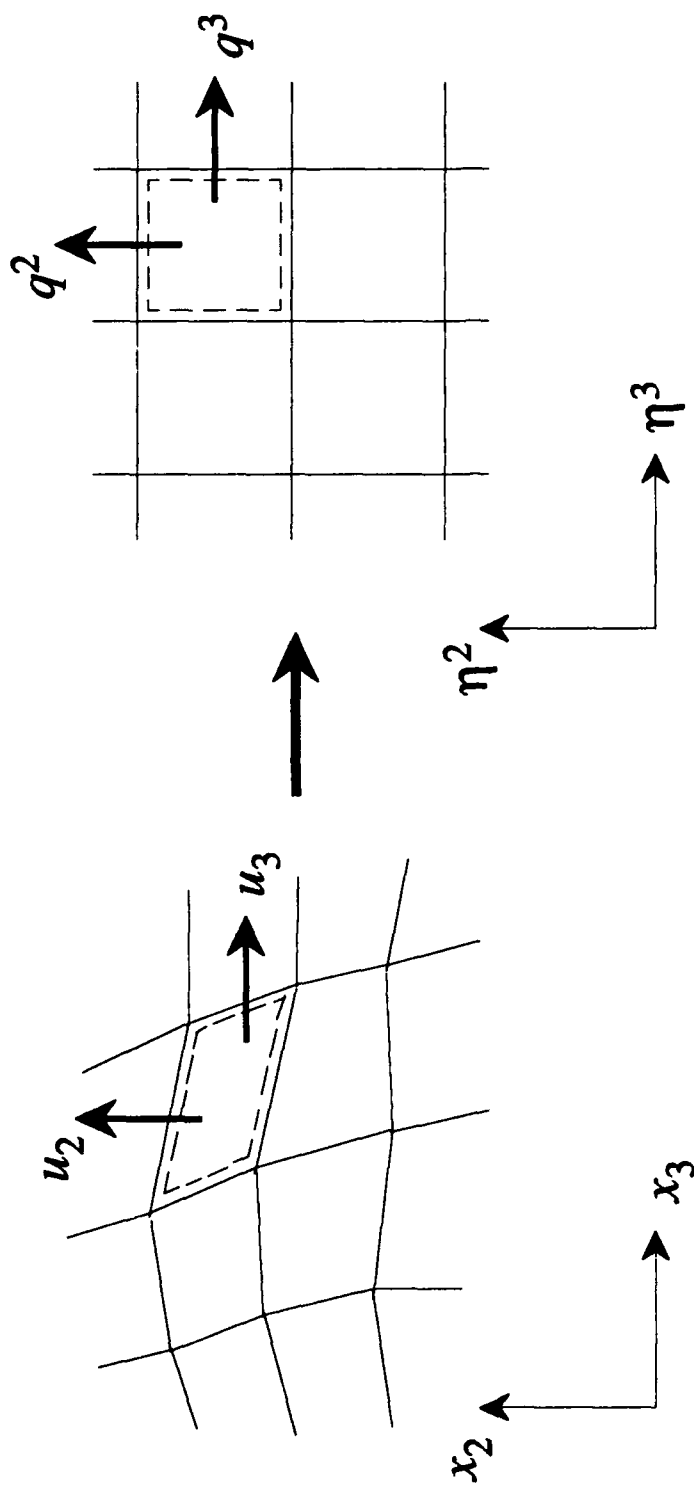


FIGURE 3. Coordinate transformation.

CHAPTER 4

DRAG MEASUREMENT, MEAN-VELOCITY PROFILE, AND THE VIRTUAL ORIGIN

For each case (A - D), random disturbances were initially imposed upon the laminar mean velocity profile. Starting from these initial velocity fields, the governing equations were integrated forward in time until the numerical solutions reached statistically steady states. These equilibrium states were identified by a quasi-periodic behavior of the wall-shear stresses. Once the velocity field reached the statistically steady state, the equations were integrated further in time to obtain the time average of the various statistical quantities. The total averaging time was $500 \delta/U_l$ ($\approx 4000\nu/u_{\tau_f}^2$) for all results reported here. In this chapter, an overbar indicates average over x , t , and the same spanwise locations over different riblets, and a prime indicates perturbation from this average.

4.1 Drag measurement

The average skin-friction drag is obtained as the integral of the product of the wall-shear stress and the differential wetted area. Note that the wetted area of a plate with riblets is $\sec(\alpha)$ times wider than that of a flat plate, where α is the ridge angle of the riblet (figure 1 (b)). The drag variation due to the presence of riblets is calculated by comparing the skin friction of the flat plate (upper wall) and the plate with riblets (lower wall). This comparison relies upon the observation that turbulent flow near one side of channel does not affect the skin friction at the other. It was shown in Jiménez & Moin (1991) that the correlation coefficient between the shear histories at the two walls of a symmetric channel is always small, $|corr| \leq 0.15$, indicating that the intermittent behavior acts independently at each wall.

The instantaneous plane-averaged drags of the flat surface, D_f , and of the riblet surface, D_r , are computed with

Case	s^+	h^+	α	Present study [†]	Walsh (1982) [†]
A	40	20.0	45°	+ 2%	+ 3%
B	40	34.6	60°	+12%	+11%*
C	20	10.0	45°	- 5%	- 2%
D	20	17.3	60°	- 6%	- 4%*

[†] + and - denote the drag increase and decrease, respectively.

* Data were obtained from the case $s^+ = h^+$.

Table 2. Drag variation for each riblet configuration.

$$D_f = \mu \int_{A_f} \frac{\partial u}{\partial n} dA_f = \mu \left(\frac{\partial u}{\partial y} \right)_f^* A_f, \quad (4.1)$$

$$D_r = \mu \int_{A_r} \frac{\partial u}{\partial n} dA_r = \mu \left(\frac{\partial u}{\partial y} \right)_r^* A_f,$$

where n is the coordinate normal to the surface, and A_r and A_f denote the wetted areas of the riblet and flat surfaces, respectively; $A_r = L_{x_1} \times N_r s \sec(\alpha)$ and $A_f = A_r \cos(\alpha) = L_{x_1} \times L_{x_3}$. Here, N_r is the number of riblets in the computational domain; $N_r = 4$ and 8 for the cases $s^+ = 40$ and 20, respectively.

Figure 4 shows the time history of the average wall-shear rates, $(\partial u / \partial y)_f^*$ and $(\partial u / \partial y)_r^*$, for the case $s^+ = 20$ and $\alpha = 60^\circ$. Stochastic and intermittent behaviors of the wall-shear rates are clearly discernible. This intermittency is due to the limited size of the computational box in the (x, z) plane and the correspondingly small statistical sample of near-wall events. Clearly further averaging in time is required. The histories of plane- and time-averaged wall-shear rates, i.e. $1/t \int_0^t (\partial u / \partial y)_f^*(\tau) d\tau$ and $1/t \int_0^t (\partial u / \partial y)_r^*(\tau) d\tau$, are also shown in figure 4. The drag reduction by the riblets is clearly evident.

Table 2 shows the drag increase or decrease for each riblet configuration studied. Also given are the experimental results of Walsh (1982) for similar riblet geometries. The error bounds in Walsh's drag measurements were reported to be about $\pm 1\%$. Error bounds for statistical sampling errors for the present drag measurements were obtained by comparing the wall-shear rates of the *two flat walls* in a plane

channel simulation; the values of averaged wall-shear rates should be identical with sufficient time averaging. After averaging over 500 non-dimensional time units (tU_l/δ), remaining fluctuation was about $\pm 2\%$. Thus, the data in table 2 show a reasonable agreement in the drag variation between the present study and the experimental data.

4.2 Mean-velocity profile and origin of the wall

Figure 5 shows the variation of the mean velocity in the transverse plane. No apparent spanwise variation of the mean velocity is found above $y/\delta \approx -0.9$ in the case $s^+ \approx 20$ or above $y/\delta \approx -0.8$ in the case $s^+ \approx 40$. Note that the midpoint of the riblet valley and tip corresponds to $y/\delta = -1$ (figure 1 (b)). The spanwise variation of the mean velocity occurs only very near the riblets where, at a given y , the mean velocity above the riblet valley is larger than that above the riblet tip. These observations have also been reported in experimental (Hooshmand *et al.* 1983, Benhalilou *et al.* 1991 and Vukoslavčević *et al.* 1992) and analytical (Bechert & Bartenwerfer 1989) studies.

The lack of spanwise variation of the mean velocity above a certain y -location suggests the use of a *virtual origin*. The virtual origin for riblets is defined as the location y_0 of an *imaginary flat surface* which has the *same drag* as the riblet mounted surface and matches the riblet velocity profile above the viscous sublayer. For the case of the smooth wall, the virtual origin is located at the surface.

Definitions of the virtual origin and the friction velocity at that position are useful for comparison of the results with the flat plate data. There have been four methods used to evaluate the virtual origin of the riblet wall: (1) using a modified Clauser's method (Hooshmand *et al.* 1983), (2) using a *measured* linear velocity profile inside the viscous sublayer (Hooshmand *et al.* 1983), (3) using a velocity defect profile above the inner region (Choi 1989), and (4) using a conformal mapping, assuming that a linear velocity region exists inside the viscous sublayer (Bechert & Bartenwerfer 1989 and Luchini *et al.* 1991).

Figure 6 shows the wall-shear rate and the contribution to the drag as a function of the spanwise position along the riblet for all configurations tested. The wall-shear rate at the riblet surface is defined as $\partial \bar{u} / \partial n(z) = \frac{1}{T} \frac{1}{L_x} \int_0^T \int_0^{L_x} \frac{\partial u}{\partial n}(x, z, t) dx dt$. The wall-shear rate over most of the riblet surface is smaller than that of the

corresponding plane turbulent channel flow. In cases with $\alpha = 45^\circ$, the wall-shear rates near the tip and valley regions are nearly identical regardless of riblet spacing (it has been shown by Moffatt & Duffy (1980) and Choi *et al.* (1991) that, when the convection terms of equation (3.1) are negligible, local similarity solutions and asymptotic behaviors exist near corners and the velocity distributions very near corners (tip or valley) are governed mostly by the angle of the corner). However, near the middle of riblets, the wall-shear rate of riblets with $s^+ \approx 40$ is noticeably higher than that with $s^+ \approx 20$. Riblets with $\alpha = 60^\circ$ show the same trend. This difference in the wall-shear rate near the middle of the riblet determines the net performance of riblets of a given spacing. Note that the integration of the curves in figure 6 (b) gives the drag on the riblets.

Time- and plane-averaged drag of the riblet surface, \bar{D}_r , is obtained by

$$\bar{D}_r = \frac{1}{T} \int_0^T D_r dt = \mu \left(\frac{\partial \bar{u}}{\partial y} \right)_r^* A_f, \quad (4.2)$$

where D_r is defined in equation (4.1). The wall-shear velocity $u_{\tau_r}^*$ at the virtual origin is defined by

$$u_{\tau_r}^* = \sqrt{\nu \left(\frac{\partial \bar{u}}{\partial y} \right)_r^*}. \quad (4.3)$$

The wall-shear velocities defined by equation (4.3) for each riblet configuration are shown in table 3. Before exploring the four different methods described previously for obtaining the virtual origin, consider plots of the mean-velocity profiles, normalized by the local wall-shear velocities $u_{\tau_r} = \sqrt{\nu \partial \bar{u} / \partial n}$, at various points along the perimeter of the riblet surface (figure 7). Significant downward shifts in the log-law are obtained near the riblet tip, whereas significant upward shifts are obtained near the riblet valley. Note that this plot is normalized by the *local* wall-shear velocity, not by $u_{\tau_r}^*$.

In most experimental studies, the location of the virtual origin is taken to be the riblet tip, valley, or the midpoint between the tip and valley. Figure 8 shows the variation of the mean-velocity profile with different choices of the virtual origin for cases with $\alpha = 60^\circ$. Here, the wall-shear velocity is chosen to be $u_{\tau_r}^*$ (equation

Case	$u_{\tau_f}^*/U_l^b$	β^\dagger	β^\ddagger	$y_{tip}^+{}^\natural$	$F^\#$	$F^{\#\#}$
A	0.0435	0.11	0.12 ± 0.02	5.4	-0.1	-0.5
B	0.0456	0.26	0.30 ± 0.02	5.8	-1.0	-1.0
C	0.0418	0.11	0.19 ± 0.05	1.2	+0.9	+1.0
D	0.0414	0.26	0.33 ± 0.05	2.0	+0.9	+1.0

^b For the flat plate, $u_{\tau_f}/U_l = 0.0430$ and $U_c/u_{\tau_f} = 18.1$, where U_c is the centerline velocity.

[†] From Bechert & Bartenwerfer (1989). $y_o/\delta = -1 + \beta s/\delta$.

[‡] From equation (4.4). $y_o/\delta = -1 + \beta s/\delta$. Error bounds for β are obtained noting a 10% variation of the location y_m^+ . Note that $y_o/\delta = -1$ corresponds to the midpoint between the riblet tip and valley.

[‡] $y_{tip}^+ = (y_{tip} - y_o)u_{\tau_f}^*/\nu$. y_o is obtained from equation (4.4).

[#] From Gaudet (1987). See equation (4.6).

^{##} From equation (4.6). y_o is obtained from equation (4.4).

Table 3. Wall-shear velocity and location of the virtual origin for each riblet configuration.

(4.3)). This plot does not contain the velocity inside the viscous sublayer because of the spanwise variation of the mean velocity there. The slope of the log-law above the riblets is little changed as compared with the flat plate profile. In the case $s^+ \approx 20$, the intercept of the log-law with $u^+ = y^+$ is farther away from the wall regardless of the location of the virtual origin (when the *local* wall-shear velocity was used, both upward and downward shifts in the log-law were obtained (figure 7)). This upward shift in the log-law has previously been observed in drag-reduced flows such as large-eddy breakup devices (Bandyopadhyay 1986 and Nguyen *et al.* 1987), riblets (Hooshmand *et al.* 1983 and Choi 1989), and polymers (Lumley 1973 and Virk 1975), and it may be considered the result of the increase of the viscous sublayer thickness. On the other hand, in the case $s^+ \approx 40$, the location of the intercept is decreased, indicating a decrease of the viscous sublayer thickness. Cases with $\alpha = 45^\circ$ show the same trend (figure F.2).

The four methods of evaluating the virtual origin of the wall discussed earlier are based on the existence of either a linear velocity region or a logarithmic region near the surface. The logarithmic region for the present calculation is quite narrow

(figure 8), so the application of methods (1) and (3) will not give an accurate estimation of the location of the virtual origin. Method (2) is also not useful since the location of the virtual origin depends on the baseline of the mean velocity (see figure 3 in Hooshmand *et al.* 1983). Bechert & Bartenwerfer (1989) determined the location of the virtual origin of the wall, y_o , using a conformal mapping, assuming that a linear velocity region exists inside the viscous sublayer; using their method, for $\alpha = 45^\circ$, $y_o/\delta = -1 + 0.11s/\delta$, and for $\alpha = 60^\circ$, $y_o/\delta = -1 + 0.26s/\delta$. The mean-velocity profile based on this virtual origin is shown in figure 8. Again, an upward shift in the log-law is evident in the case $s^+ \approx 20$. However, the weak point of the method of Bechert & Bartenwerfer (1989) is that it can not be used for flows for which the drag is increased because in such cases the riblet surface is not completely immersed in the viscous sublayer.

It should be mentioned that all the existing methods of evaluating the virtual origin are based on changes in the mean streamwise velocity rather than changes in turbulence structure. Since an upward shift in the log-law is closely related to the balance between turbulent energy production and viscous dissipation (Lumley 1973), measurement of changes of turbulent structure above the wall may be another criterion to determine the virtual origin. The maximum turbulent kinetic energy production on the flat plate side occurs at $y^+ \approx 13$, as does the maximum intensity of the streamwise velocity fluctuations. One may therefore define the virtual origin from

$$y_m^+ \approx 13 = \frac{(y_m - y_o)u_{\tau}^*}{\nu},$$

where y_m and y_o are the locations of the maximum turbulent kinetic energy production (or the maximum streamwise velocity fluctuation intensity) and the virtual origin, respectively. Therefore, the location of the virtual origin is

$$y_o = y_m - \frac{13\nu}{u_{\tau}^*}. \quad (4.4)$$

The location of the virtual origin y_o may be obtained from the profile of the streamwise velocity fluctuation intensity (figure 9) for each riblet configuration, and is tabulated in table 3, together with results by Bechert & Bartenwerfer (1989). There is a rough agreement between the two methods. It can be clearly seen that, as the

ridge angle increases, the virtual origin moves closer to the riblet tip. The location of the riblet tip, $y_{tip}^+ = (y_{tip} - y_o)u_{\tau_r}^*/\nu$, is tabulated in table 3, where y_o is obtained from equation (4.4). The riblet surfaces with $s^+ \approx 20$ are completely immersed in the viscous sublayer.

The mean-velocity profiles based on these virtual origins for cases with $\alpha = 60^\circ$ are shown in figure 8. The mean-velocity profiles by the method of Bechert & Bartenwerfer (1989) and equation (4.4) are nearly identical in the log-law region. The upward and downward shifts in the log-law are clearly seen for drag-decreasing and drag-increasing cases, respectively. Cases with $\alpha = 45^\circ$ show the same trend (figure F.2).

The velocity profile in the wall region of a turbulent boundary layer is described by

$$\frac{\bar{u}}{u_{\tau_f}} = \frac{1}{\kappa} \ln \frac{u_{\tau_f} y}{\nu} + B, \quad (4.5)$$

where $\kappa = 0.4$ and $B = 5.5$. For rough surfaces, the velocity profile has been described by equation (4.5) with the addition of a function F of the surface roughness parameter (Nikuradse 1933 and Schlichting 1936). This modified representation of the mean-velocity profile has been used to model the mean flow over riblets by Sawyer & Winter (1987), Gaudet (1987) and Tani (1988):

$$\frac{\bar{u}}{u_{\tau_r}^*} = \frac{1}{\kappa} \ln \frac{u_{\tau_r}^* (y - y_o)}{\nu} + B + F. \quad (4.6)$$

Since $u_{\tau_r}^*$ and y_o are given in table 3, the constant F for each riblet configuration may be obtained and is listed in table 3. It is clear from table 3 that F is positive for drag-reducing cases and is negative for drag-increasing cases. Values of F obtained in this study are compared with those by Gaudet (1987) in table 3; except for case A, good agreement is found between the two results.

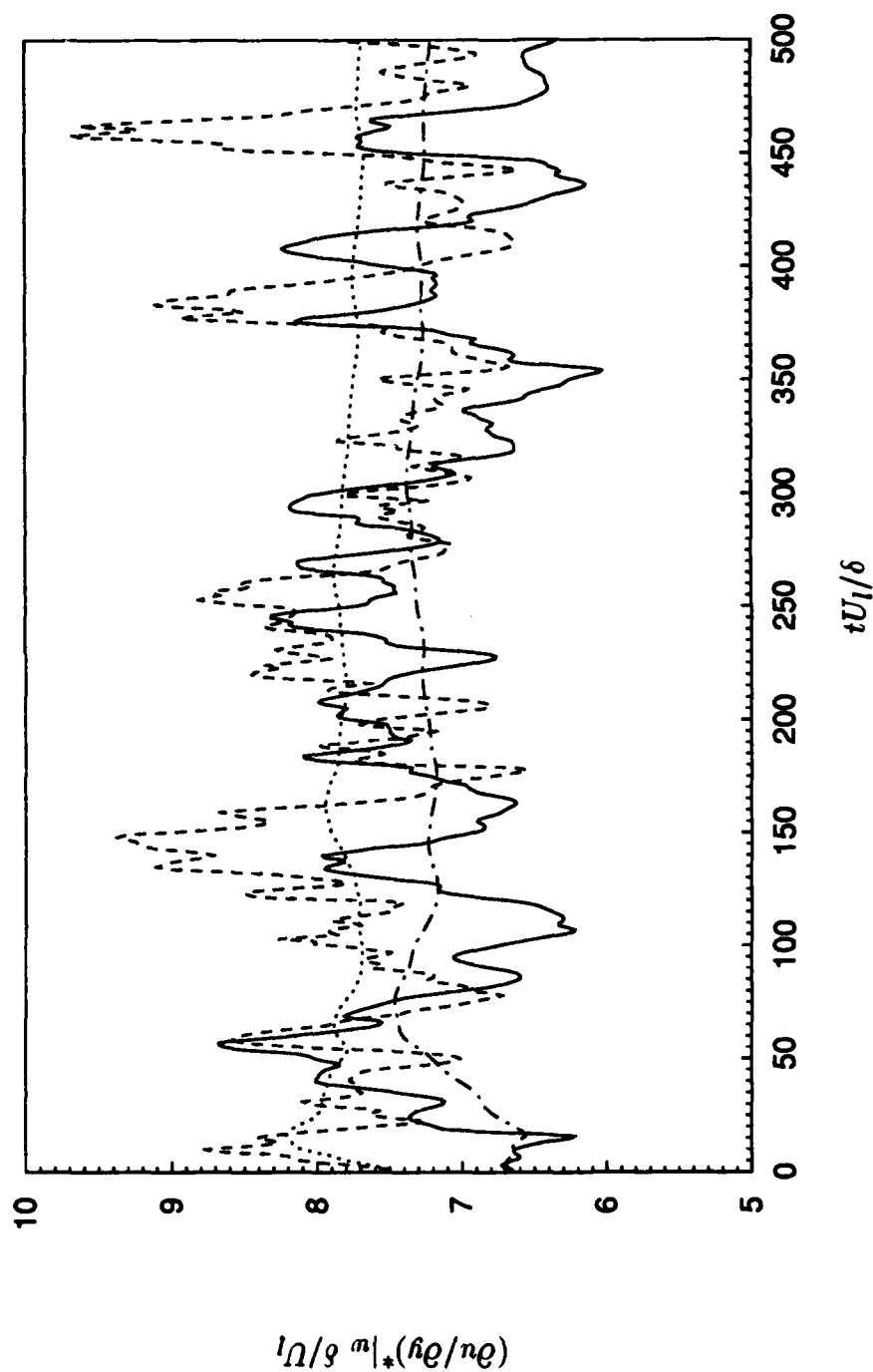


FIGURE 4. Time history of wall-shear rates at both flat and riblet walls in the case of $s^+ \approx 20$ and $\alpha = 60^\circ$: instantaneous plane-averaged wall-shear rate, —, at the flat plate, $(\partial u / \partial y)_f^*$; ----, at the riblet wall, $(\partial u / \partial y)_r^*$; - · - · -, at the riblet wall; · · · · ·, at the riblet wall; · · · · ·, at the riblet wall. $(\partial u / \partial y)|_w \delta / U_1 = 2$ corresponds to fully developed laminar plane channel flow.

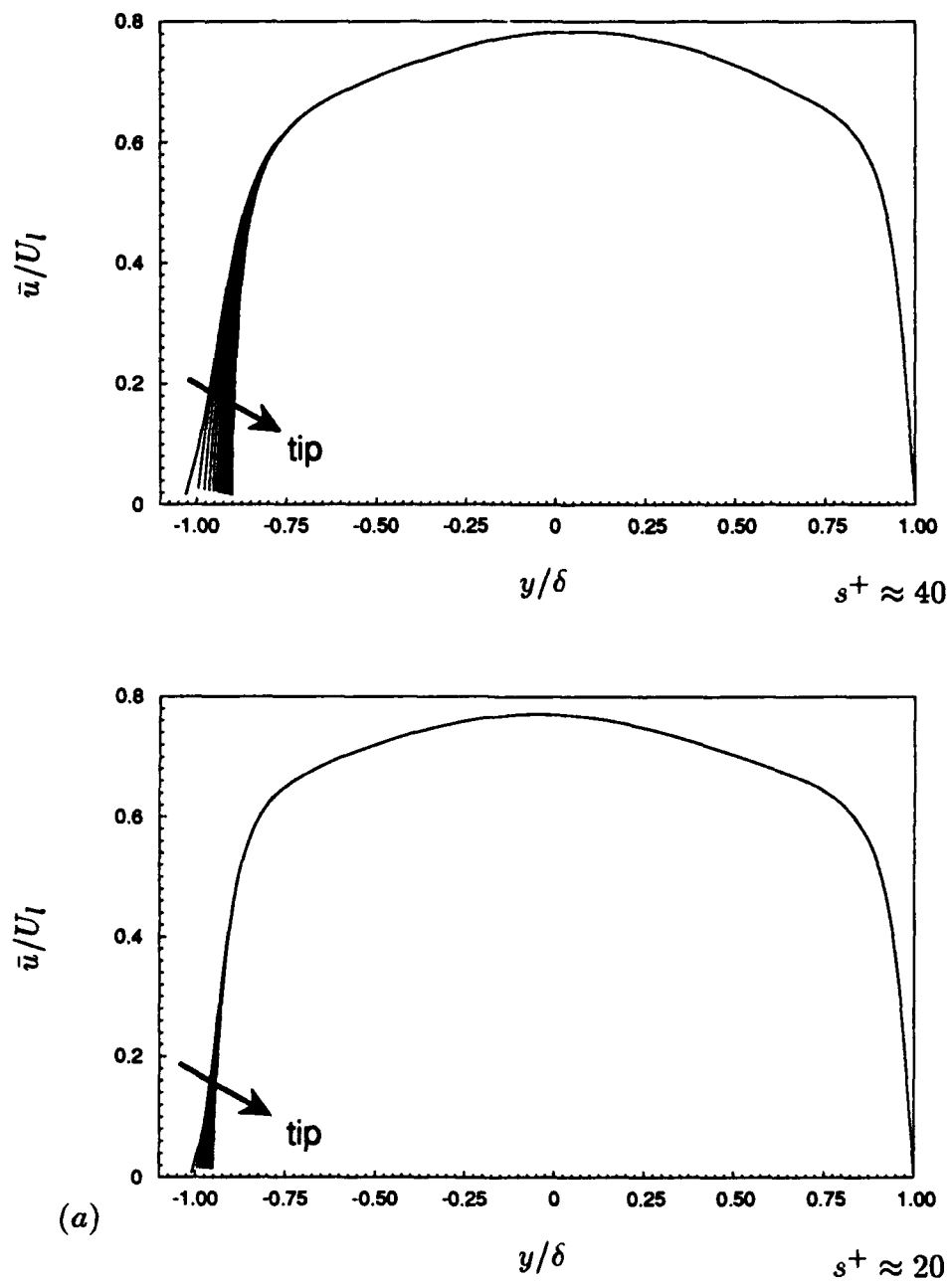
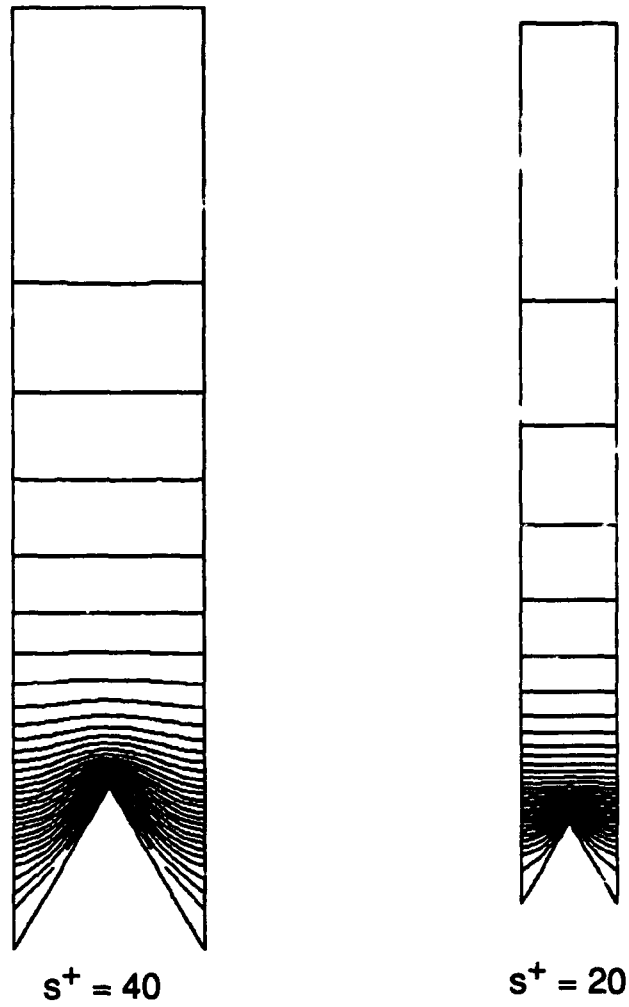


FIGURE 5. For caption see the following page.



(b)

FIGURE 5. Mean-velocity profiles for cases with $\alpha = 60^\circ$. (a) One-dimensional view with different spanwise locations; (b) contours of the mean velocity in the (y, z) plane. The contour levels normalized by U_l range from 0 to 0.75 by increments of 0.025. The plot domain extends from the riblet surface to the centerline of the channel.

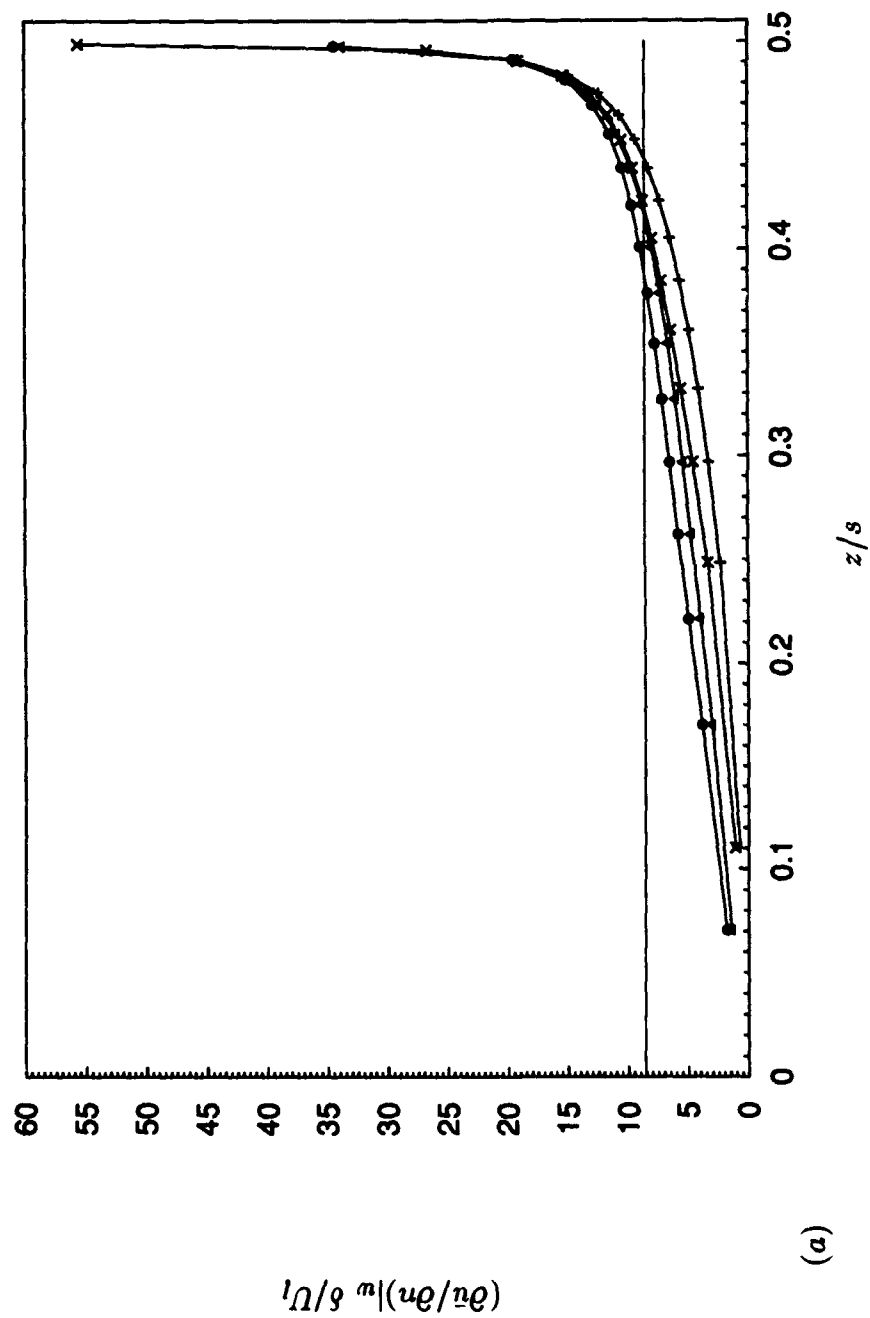


FIGURE 6. For caption see the following page.

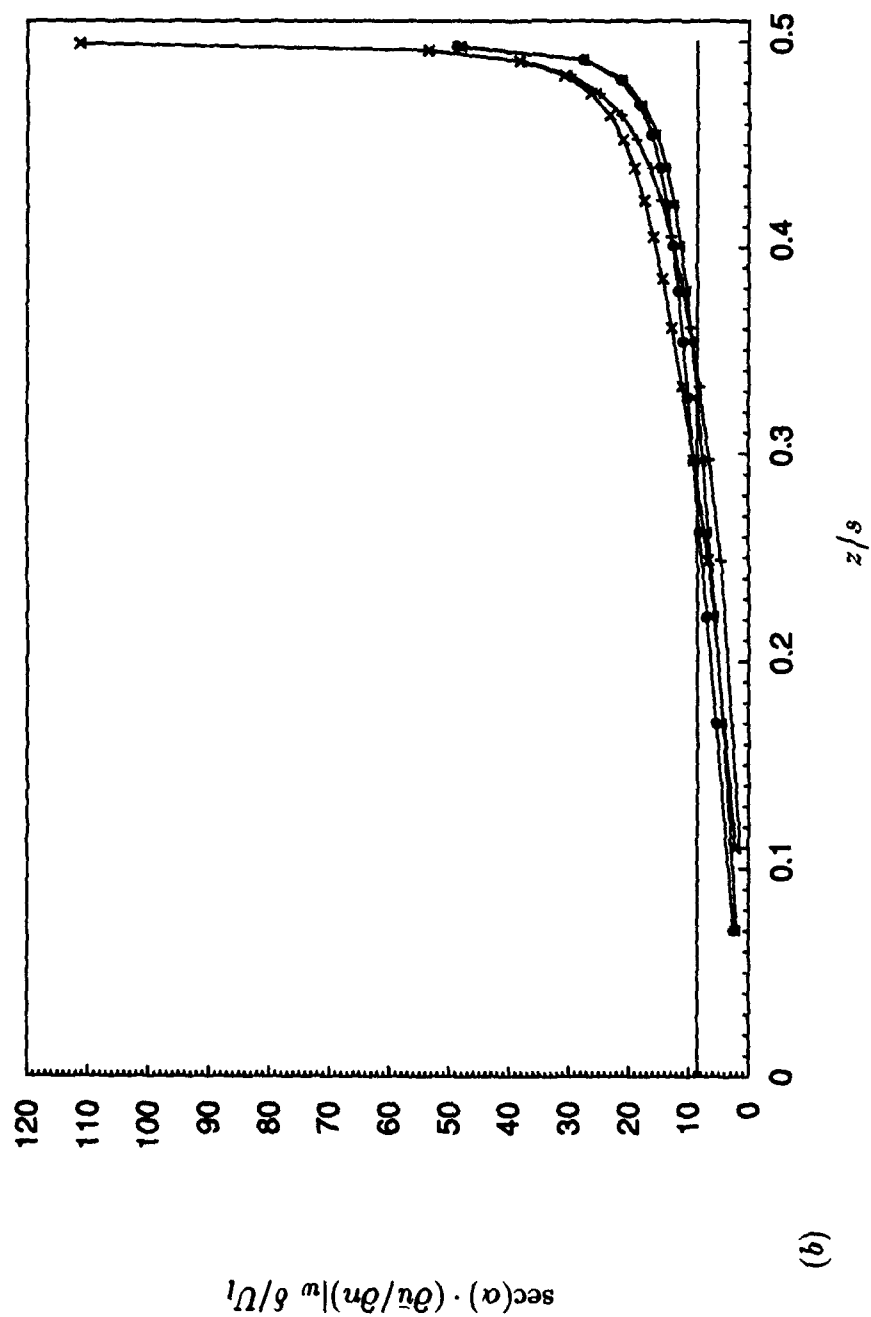


Figure 6. (a) Wall-shear rates and (b) contribution to the drag at several spanwise positions on riblet surfaces: ●, $s^+ \approx 40$ and $\alpha = 45^\circ$; ▲, $s^+ \approx 20$ and $\alpha = 45^\circ$; ×, $s^+ \approx 40$ and $\alpha = 60^\circ$; +, $s^+ \approx 20$ and $\alpha = 60^\circ$. $z/s = 0$ and 0.5 correspond to the valley and tip of the riblet, respectively. Solid line denotes the value of the wall-shear rate on the flat plate side. $(\partial \bar{u} / \partial n)|_w \delta / U_l = 2$ corresponds to fully developed laminar plane channel flow.

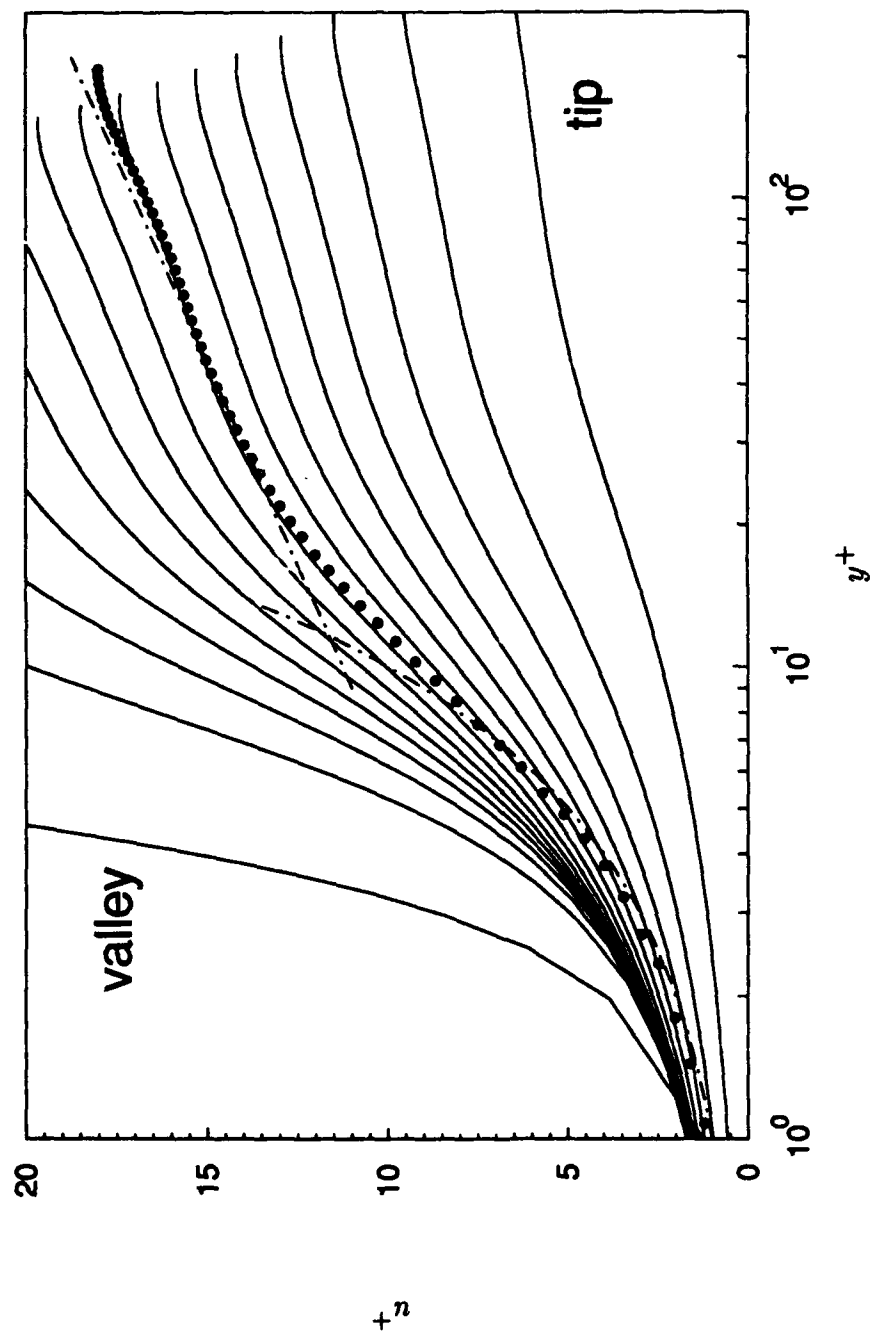


FIGURE 7. Mean-velocity profiles normalized by the local wall-shear velocity $u_\tau(z)$ in the case of $s^+ \approx 20$ and $\alpha = 60^\circ$: —, mean velocity over the riblet at different spanwise locations; •, mean velocity over the flat plate; ----, laws of the wall ($u^+ = y^+$ and $u^+ = 2.5 \ln y^+ + 5.5$). $u_\tau(z) = \sqrt{\nu (\partial \bar{u} / \partial n)|_w}$. The wall-shear rates are shown in figure 6.

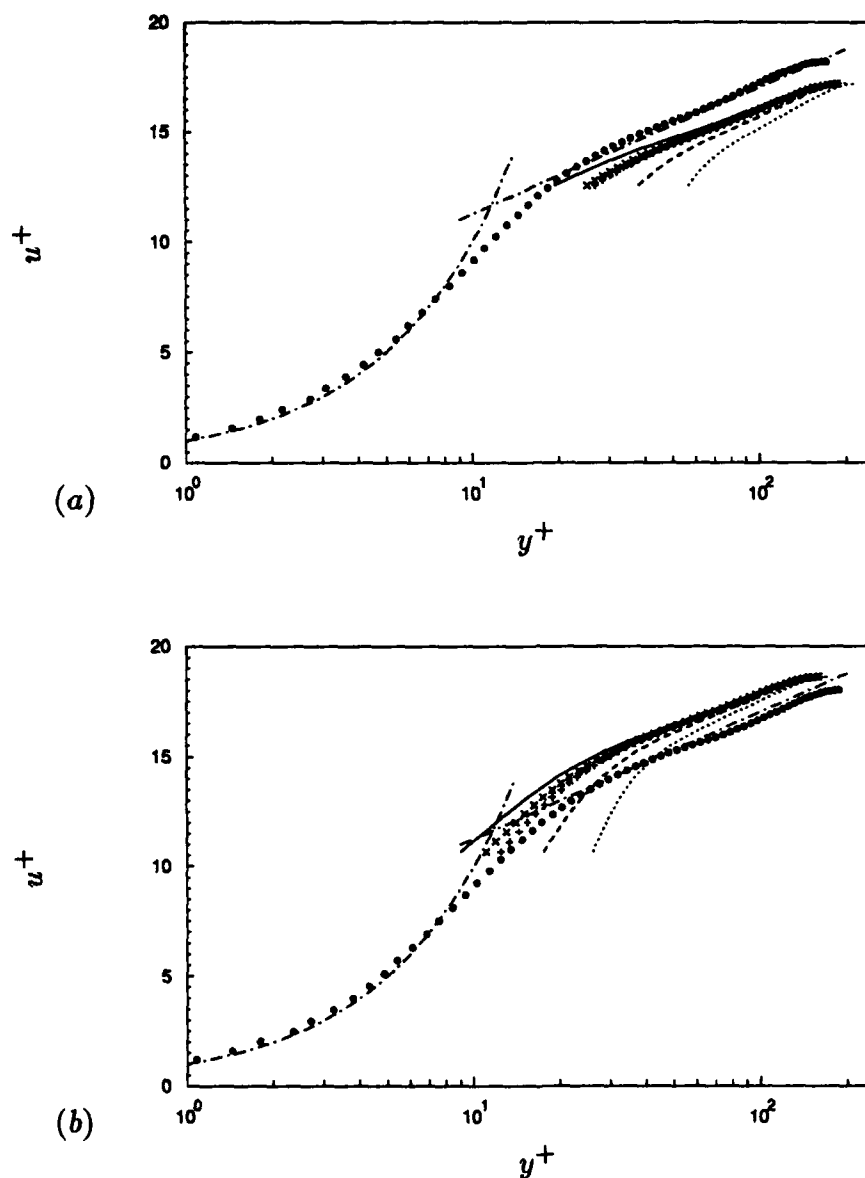


FIGURE 8. Variation of mean-velocity profiles, normalized by the wall-shear rates $u_{\tau_r}^*$ (equation (4.3)), with the location of the virtual origin for cases with $\alpha = 60^\circ$: (a) $s^+ \approx 40$; (b) $s^+ \approx 20$. The virtual origin is located: — at the riblet tip; ----, at the midpoint between tip and valley; , at the riblet valley; +, at the location from Bechert & Bartenwerfer (1989); x, at the location from equation (4.4). —·—, Laws of the wall; •, mean velocity over the flat wall.

CHAPTER 5

TURBULENCE STATISTICS

In this chapter turbulence statistics from the calculations of turbulent flow over the riblets are presented. Flow variables on the side of the channel with the riblets (lower wall) are averaged only in x , t , and the same spanwise locations over different riblets, while those on the side of the flat plate (upper wall) are averaged in x , z and t . Results in both global and wall coordinates are presented. In global coordinates, velocities are normalized by the centerline velocity U_c , and lengths are normalized by the channel half-width δ . When flow variables are plotted in wall coordinates, velocities are normalized by either $u_{\tau,f}$ (for the flat plate) or $u_{\tau,r}^*$ (for the plate with riblets), and $y_f^+ = u_{\tau,f}y/\nu$ and $y_r^+ = u_{\tau,r}^*(y - y_o)/\nu$. The virtual origin, y_o , and the wall-shear velocity at that location, $u_{\tau,r}^*$, are obtained from equations (4.4) and (4.3), respectively. The changes in the absolute magnitudes of flow statistics are more evident in global coordinates, whereas wall coordinates are better suited for the structural changes of flow variables. In this chapter, we present the results of cases with $\alpha = 60^\circ$ ($s^+ \approx 20$ and 40). Riblets with $\alpha = 45^\circ$ showed nearly the same trend (appendix F).

5.1 Turbulence intensities

Turbulence-intensity profiles at various spanwise locations are shown in figure 9 and contours of turbulence intensities in the cross-flow plane are shown in figure 10. Significant variations of the turbulence intensities occur only very near the riblets in the case $s^+ \approx 20$, while, in the case $s^+ \approx 40$, effects of the riblets penetrate further into the channel (figure 10) and spanwise variations of the normal and spanwise components of the turbulence intensity extend even into the region where there is no noticeable spanwise variation of the mean velocity (figure 5) or the streamwise velocity fluctuations (figure 10 (a)). This indicates that the cross flow is more sensitive to the presence of riblets than is the flow in the streamwise direction.

Reduction of all three components of turbulent intensity by the riblets is evident in a drag-reducing configuration ($s^+ \approx 20$) (figure 9). Note that the maximum wall-normal and spanwise root-mean-square velocity fluctuations are reduced by 10%,

while only a 5% reduction is obtained in the maximum streamwise root-mean-square velocity fluctuations. Turbulence intensities increase near the riblets in the case $s^+ \approx 40$ (a drag-increasing configuration). The streamwise component of the turbulence intensity is reduced by 15% above the riblet valley and increased by 5% above the riblet tip as compared to the flat plate case. However, the maximum values of the other two components are increased by 5% across the entire span.

Reductions of the streamwise velocity fluctuations by riblets have been observed in several experiments (Walsh 1980, Hooshmand *et al.* 1983, Nitschke 1984, Johansen & Smith 1986, Choi 1989, Benhalilou *et al.* 1991, Wilkinson & Lazos 1991 and Vukoslavčević *et al.* 1992). Bacher & Smith (1985) reported an increase of the streamwise velocity fluctuations, which is clearly contradictory to the present results and other experimental results. There is limited data available for the normal and spanwise velocity fluctuations. Walsh (1980) found a small reduction in the normal velocity fluctuations. Benhalilou *et al.* (1991) used riblets with $s^+ = 2h^+ \approx 30$ and observed a large reduction of the streamwise and spanwise velocity fluctuations in the vicinity of the riblet valley and a significant increase close to the riblet tip. The behavior of the streamwise velocity fluctuations in their work is quite similar to the present results for drag-increasing configurations with $s^+ = 2h^+ \approx 40$ (figure F.3 (a)) and $s^+ = 1.155h^+ \approx 40$ (figure 9 (a)). As drag was not measured in their study, the increase of the streamwise velocity fluctuations probably resulted from having a drag-increasing configuration. Reduction of the spanwise velocity fluctuations above the riblet valley, as seen in the results of Benhalilou *et al.* (1991), was not obtained in the present study for drag-increasing configurations, however. The spanwise distributions of the mean velocity and turbulence intensities obtained by Benhalilou *et al.* (1991) also indicate considerable asymmetry with respect to the riblet valley. Vukoslavčević *et al.* (1992) measured streamwise velocity fluctuations above riblets with $s^+ = 2h^+ \approx 35$ and found a decrease in magnitude across the entire span. The present study shows that the turbulence intensity above riblets is modified differently depending upon whether the configuration is drag-reducing or drag-increasing. Hence, measurements of turbulence intensities should be accompanied by drag measurements in order to properly correlate these quantities.

Turbulence intensities normalized by either u_{τ_f} (for the flat plate) or $u_{\tau_r}^*$ (for the plate with riblets) are shown in figure 11. The y^+ locations of the peak streamwise velocity fluctuations above both the flat plate and the riblets are nearly identical

due to the particular choice of the virtual-origin location (equation (4.4)). Profiles of v_{rms} and w_{rms} are also nearly identical. The viscous sublayer is significantly modified by the riblets in all configurations.

5.2 Reynolds shear stress

The Reynolds shear stress $-\overline{u'v'}$, normalized by the mean centerline velocity, is shown in figure 12 (a). In the case $s^+ \approx 20$, the maximum Reynolds shear stress above the riblets is reduced by 12% as compared with that above the flat plate, and there is negligible spanwise variation of the Reynolds shear stress near the riblets. Walsh (1980) reported a maximum reduction of 16% in the Reynolds shear stress above riblets. Pulles *et al.* (1989) showed that the Reynolds shear stress is noticeably reduced through the log-law region for a riblet mounted surface. In the case $s^+ \approx 40$, however, the maximum Reynolds shear stress above the riblets is significantly increased above the riblet tip and is nearly unaffected above the riblet valley as compared to the flat plate side. There is also substantial spanwise variation of $-\overline{u'v'}$ near the riblets in this case.

The Reynolds shear stress above the riblets, normalized by the wall-shear velocity u_{τ}^* , is shown in figure 12 (b). Also shown is the Reynolds shear stress above the flat plate. In the case $s^+ \approx 40$, peak locations and magnitudes of the Reynolds shear stress above the riblet tip and valley differ greatly from the flat plate profile. However, in the case $s^+ \approx 20$, there is a good agreement.

The total shear stress, $-\overline{uv} + \nu \partial \bar{u} / \partial y$, above the riblets is shown in figure 13. Taking the average of the streamwise momentum equation over time and space (x) gives

$$\frac{\partial}{\partial y}(-\overline{uv} + \nu \frac{\partial \bar{u}}{\partial y}) + \frac{\partial}{\partial z}(-\overline{uw} + \nu \frac{\partial \bar{u}}{\partial z}) = \frac{1}{\rho} \frac{\partial \bar{p}}{\partial x} = \text{constant}. \quad (5.1)$$

When the spanwise variations of the mean velocity and shear stresses are negligible compared with their normal variations, the total shear stress becomes linear across the channel. The computed result away from the riblets clearly indicates that this is indeed the case. However, a linear profile is not obtained very near the riblets since the spanwise variations of $-\overline{uw}$ and $\partial \bar{u} / \partial z$ are not negligible (figures 5 (b) and 10). This deviation from linearity illustrates the zone of influence of the riblets

in the channel. As expected, the effects of the riblets penetrate further into the channel in the case $s^+ \approx 40$.

5.3 Vorticity

There is no known experimental data on vorticity fluctuations above riblets. Root-mean-square vorticity fluctuations normalized by the mean centerline velocity and the channel half-width are shown in figure 14. All three vorticity fluctuation components show maximum values at the riblet tip. Significant spanwise variations of the vorticity fluctuations occur only very near the riblets in the case $s^+ \approx 20$, while, in the case $s^+ \approx 40$, there is further penetration into the channel.

Reductions of all three components of the vorticity fluctuations by the riblets occur in the drag-reducing configuration ($s^+ \approx 20$). The local maximum streamwise vorticity fluctuation above the riblets is reduced by 12% as compared with that above the flat plate. The local maximum of the normal vorticity fluctuation is reduced only marginally. In the case $s^+ \approx 40$, vorticity fluctuations are increased above the riblets. It is interesting to note that, near the local maximum ($y/\delta \approx -0.8$), ω_x above the riblet valley is larger than that above the riblet tip, but the converse is true for ω_y and ω_z .

Root-mean-square vorticity fluctuations normalized by the wall-shear velocity u_τ are shown in figure 15. As described in sections 5.1 and 5.2, use of the virtual origin y_0 and the wall-shear velocity u_τ^* collapses the peak locations as well as the magnitudes of the vorticity fluctuations for the case $s^+ \approx 20$ but not for the case $s^+ \approx 40$. The local maximum ω_x occurs at $y^+ \approx 20$ regardless of the presence of the riblets, which suggests that the center of the streamwise vortex is located on the average at $y^+ \approx 20$ (Kim *et al.* 1987). It is clear from figure 14 (a) that, in the case $s^+ \approx 20$, the streamwise vortices above the riblets are weakened.

5.4 Quadrant analysis

Quadrant analysis of the Reynolds shear stress provides detailed information on the contributions to the total turbulent energy production from various combinations of positive and negative u' and v' (Willmarth & Lu 1972 and Kim *et al.* 1987).

The total turbulent energy production P_k is

$$\begin{aligned}
 P_k &= -\overline{u'_i u'_j} S_{ij} \\
 &= -\overline{u'^2} \frac{\partial \bar{u}}{\partial x} - \overline{v'^2} \frac{\partial \bar{v}}{\partial y} - \overline{w'^2} \frac{\partial \bar{w}}{\partial z} \\
 &\quad - \overline{u'v'} \left(\frac{\partial \bar{u}}{\partial y} + \frac{\partial \bar{v}}{\partial x} \right) - \overline{u'w'} \left(\frac{\partial \bar{u}}{\partial z} + \frac{\partial \bar{w}}{\partial x} \right) - \overline{v'w'} \left(\frac{\partial \bar{v}}{\partial z} + \frac{\partial \bar{w}}{\partial y} \right),
 \end{aligned} \tag{5.2}$$

where S_{ij} is the mean strain rate tensor. For the present study, $\partial \bar{u}/\partial x = \partial \bar{v}/\partial x = \partial \bar{w}/\partial x = 0$ due to flow homogeneity in the streamwise direction.

Turbulent kinetic energy k and turbulent energy production P_k are shown in figures 16 and 17. Maximum turbulent kinetic energy is reduced by 10% in the case $s^+ \approx 20$, but, in the case $s^+ \approx 40$, it is increased above the riblet tip and is decreased above the riblet valley. The turbulent energy production exhibits the same behavior as the turbulent kinetic energy. In the case $s^+ \approx 20$, the peak of the turbulent energy production occurs at $y^+ \approx 13$, as mentioned in section 4.2. However, in the case $s^+ \approx 40$, the peak location varies slightly. All terms except $-\overline{u'v'} \partial \bar{u}/\partial y$ in the right hand side of equation (5.2) are negligible away from the riblets. Very near the riblets these terms are not negligible, but are still an order of magnitude smaller than $-\overline{u'v'} \partial \bar{u}/\partial y$.

Since most of the turbulent energy production comes from $-\overline{u'v'} \partial \bar{u}/\partial y$, we restrict our quadrant analysis to the Reynolds shear stress $-\overline{u'v'}$. The analysis divides the Reynolds shear stresses into four categories according to the signs of u' and v' . The second- ($u' < 0$ and $v' > 0$; ejection) and fourth- ($u' > 0$ and $v' < 0$; sweep) quadrant events contribute to positive production, and the first- ($u' > 0$ and $v' > 0$) and third- ($u' < 0$ and $v' < 0$) quadrant events contribute to negative production.

The contributions to the Reynolds shear stress from each quadrant, normalized by the mean centerline velocity, are shown in figure 18. The sum of the values at a position y from all four quadrants is the mean Reynolds shear stress at y . For all cases considered, the ejection event is dominant away from the wall, and the sweep event is dominant in the wall region. Regardless of the riblet spacing and lateral position about the riblet, the Reynolds shear stresses from the first

and third quadrant events are nearly unchanged except for a small outward shift of the data. The maximum values from the first and third quadrant events are $-\overline{u'v'}/U_c^2 \approx -0.0005$ for all cases considered here (figure 18 (a) and (b)). However, the Reynolds shear stresses from the second and fourth quadrant events are changed by the riblets. In the case $s^+ \approx 40$, the maximum value of the Reynolds shear stress from the ejection (second quadrant) event is reduced above the riblet valley but is substantially increased above the riblet tip. The Reynolds shear stress from the sweep (fourth quadrant) event is also significantly reduced very near the riblet valley but increased very near the riblet tip. However, there is no noticeable difference in the fourth quadrant event above $y/\delta \approx -0.7$ (figure 18 (a)).

In the case $s^+ \approx 20$, there is no spanwise variation of the Reynolds shear stress except very near the riblets. Hence, the profiles above the three different spanwise locations show essentially the same result except very near the riblets. The maximum values of the Reynolds shear stress from the second and fourth quadrant events are reduced, while those from the first and third quadrant events are almost unchanged (figure 18 (b)), indicating that only the positive Reynolds-shear-stress producing events are changed by the riblets. Accordingly, as expected the riblets intensify the positive Reynolds-shear-stress producing events in a drag-increasing configuration, while they mitigate the positive Reynolds-shear-stress producing events in a drag-reducing configuration.

The contribution to the Reynolds shear stress from each quadrant, normalized by the local mean Reynolds shear stress, is shown in figure 19. This plot shows the fractional contribution from each quadrant event to the local mean Reynolds shear stress. Above the flat plate, the contributions from the ejection and sweep events are about the same at $y^+ \approx 10$. In the case $s^+ \approx 40$, the location at which the contributions from the ejection and sweep events are equal varies significantly. However, in the case $s^+ \approx 20$, this location is fixed at $y^+ \approx 10$, which once again indicates the proper choice of the virtual origin y_0 as well as the wall-shear velocity u_{τ}^* at y_0 . The fractional contribution from each quadrant is nearly the same as that for the flat plate above $y^+ \approx 20$. The sharp increases in the normalized Reynolds shear stress from each quadrant near the riblet tip and the centerline in figure 19 simply reflect the small mean Reynolds shear stress at those locations.

Pulles *et al.* (1989) found from a quadrant analysis at $y^+ = 38$ that there was a lower fractional contribution from the second quadrant and a higher contribution

from the fourth quadrant above the riblets compared to those above the flat plate, and they concluded that ejections were weaker above the riblet and sweeps were much stronger. However, a higher fractional contribution from fourth-quadrant events does not imply stronger sweep motions above the riblets because the absolute magnitude of the Reynolds shear stress from the fourth quadrant events above the riblets may still be lower than that above the flat plate. Our results show that this is indeed the case (figures 18 and 19).

5.5 Higher-order statistics

The skewness and flatness factors of the velocity fluctuations are shown in figures 20 and 21. The skewness of w' should be zero away from the riblets because of the reflectional symmetry of the flow statistics. The skewness and flatness factors are nearly unchanged above $y^+ \approx 30$, but are significantly changed near the riblets. The skewness of u' is decreased near the riblet valley, while it is increased near the riblet tip. For $10 < y^+ < 15$, in the case $s^+ \approx 40$, the skewness of u' is increased across the entire span. The skewness of v' reaches large negative values near the riblet valley and large positive ones near the riblet tip.

The flatness of u' is decreased very near the riblet valley and increased near the riblet tip. However, the flatness of v' is significantly reduced above both riblet tip and valley, indicating that the normal velocity above the riblets is less intermittent than in the flat plate case. The flatness of w' is nearly unchanged in the case $s^+ \approx 20$, while it is slightly reduced in the case $s^+ \approx 40$.

Hooshmand *et al.* (1983) found that riblets have no effect on the skewness of the velocity fluctuations. Coustols & Cousteix (1989) reported that the skewness and flatness of the streamwise velocity fluctuations were reduced near $y^+ = 5$, while there were no modifications for $y^+ > 20$ ($y^+ = 0$ corresponded to the riblet tip in their data). On the other hand, Tardu & Truong (1991) found that the skewness and flatness of u' were increased for $y^+ < 15$. As shown in figures 20 (b) and 21 (b), in the presence of riblets there is a significant spanwise variation of the skewness and flatness of u' below $y^+ \approx 10$. Hence, the spanwise locations of their measurements should have been indicated to clarify this issue. Vukoslavčević *et al.* (1992) reported that the skewness and flatness of u' near the riblets significantly increase above the riblet valley and decrease above the riblet tip, which apparently

contradicts the present results. However, this discrepancy is due to the fact that each of their profiles was vertically shifted to match the origin of the flat wall. When replotted with the same coordinates used here, the same conclusion is drawn: i.e., at a given y^+ (< 10), the skewness and flatness of u' are increased above the riblet tip and decreased above the riblet valley.

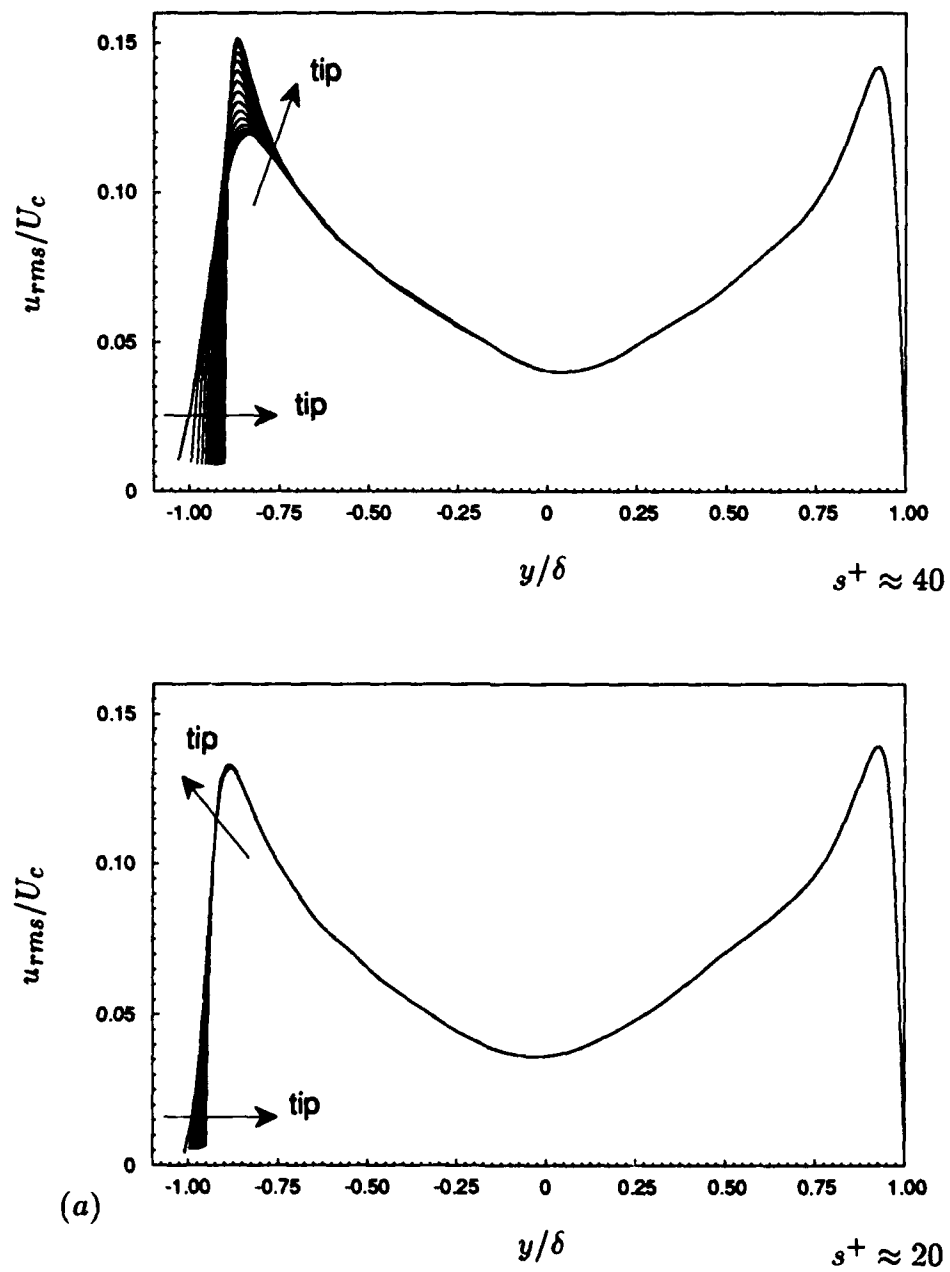


FIGURE 9. For caption see the following page.

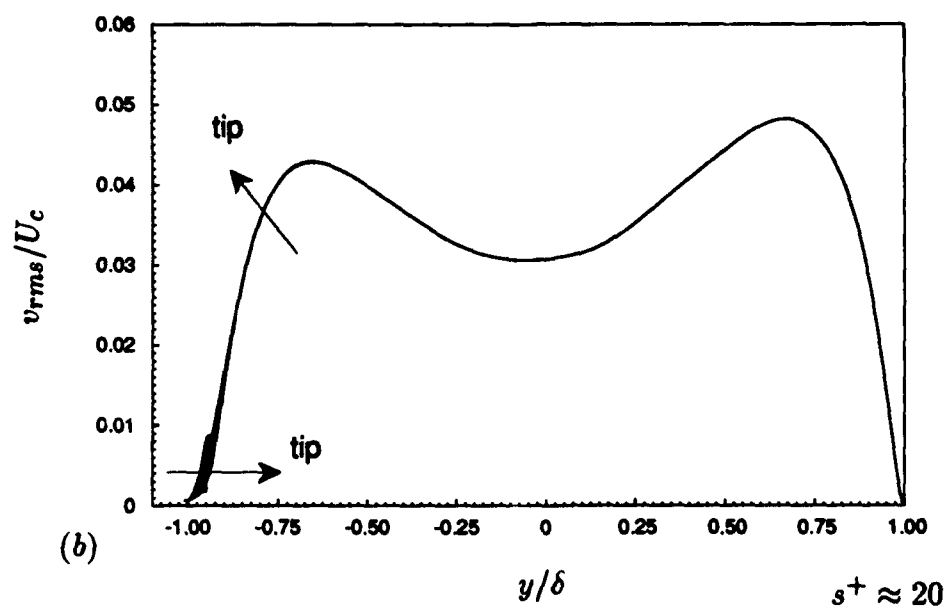
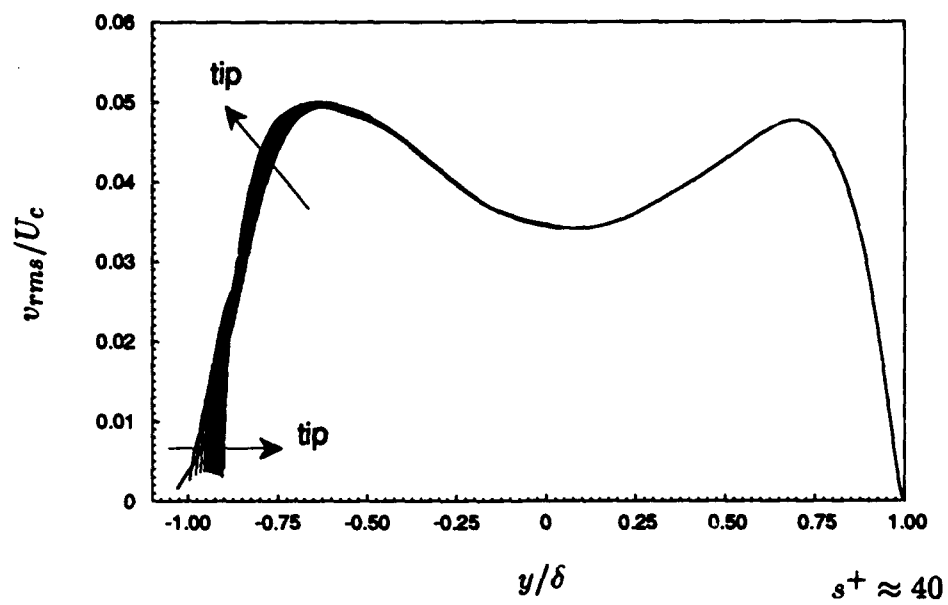


FIGURE 9. For caption see the following page.

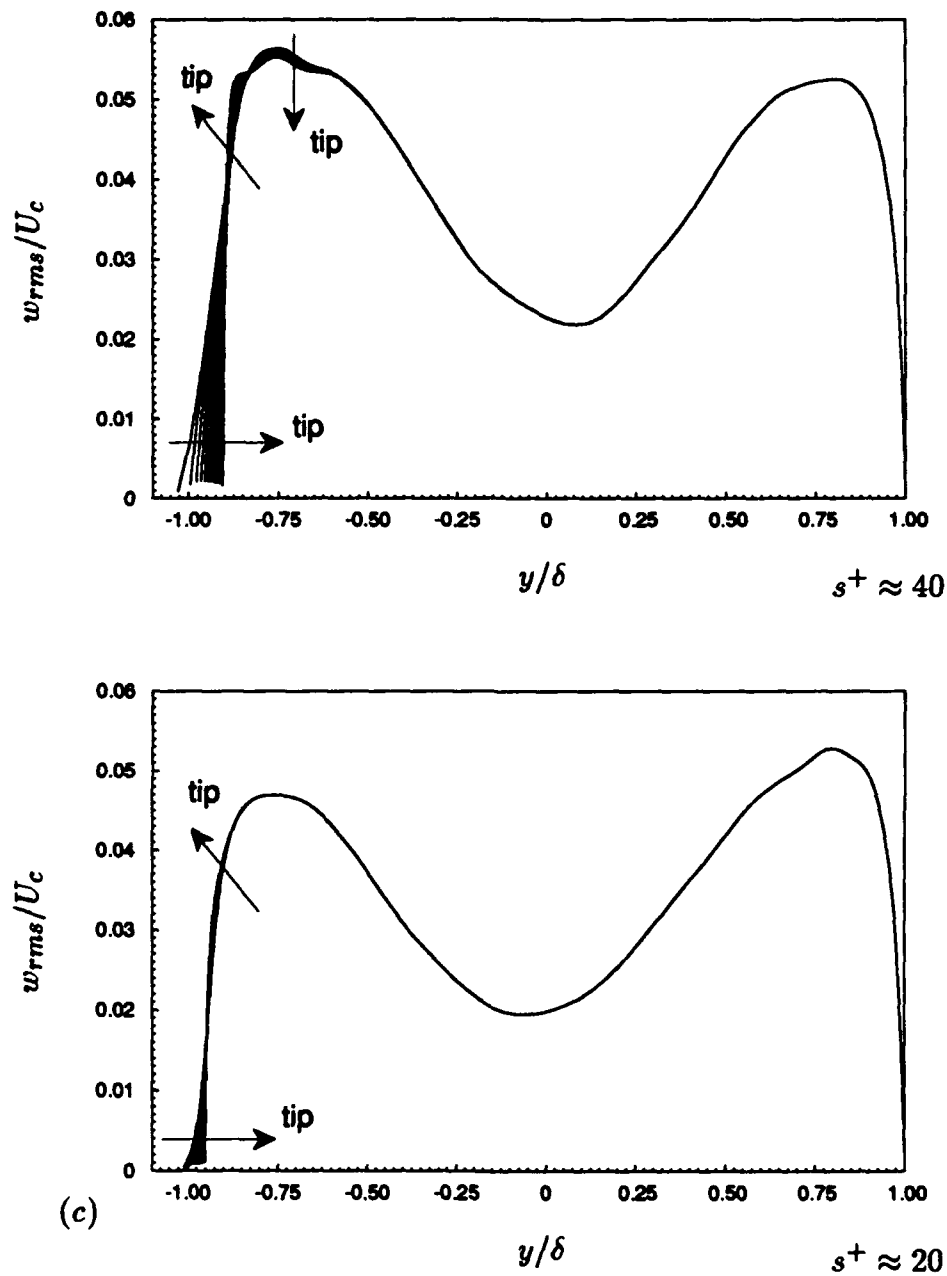
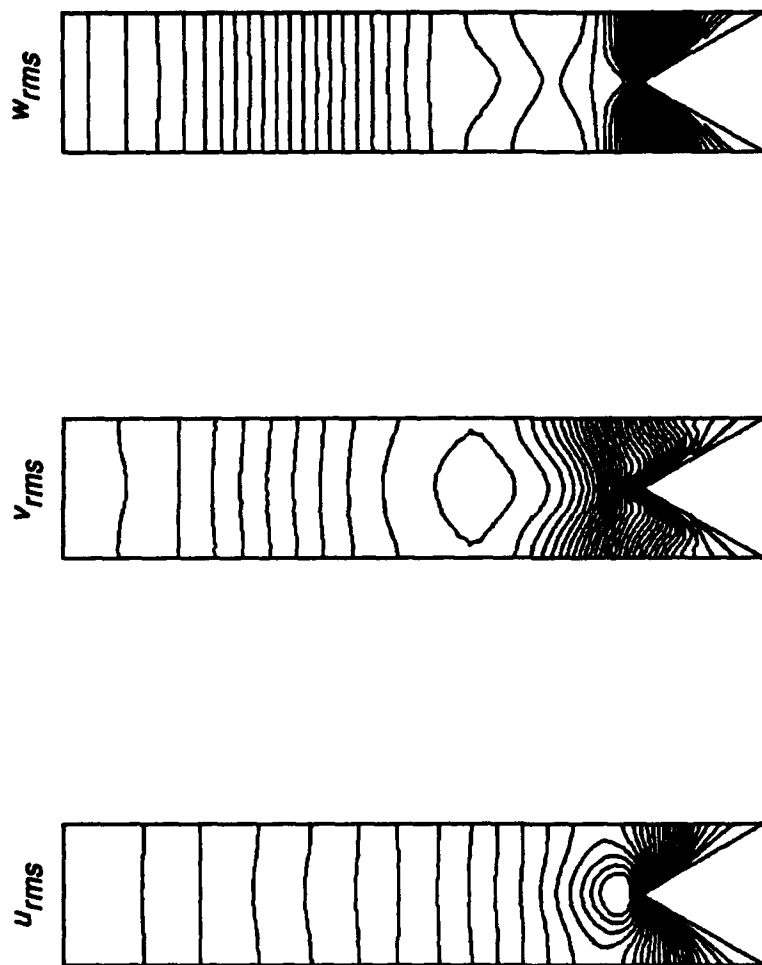
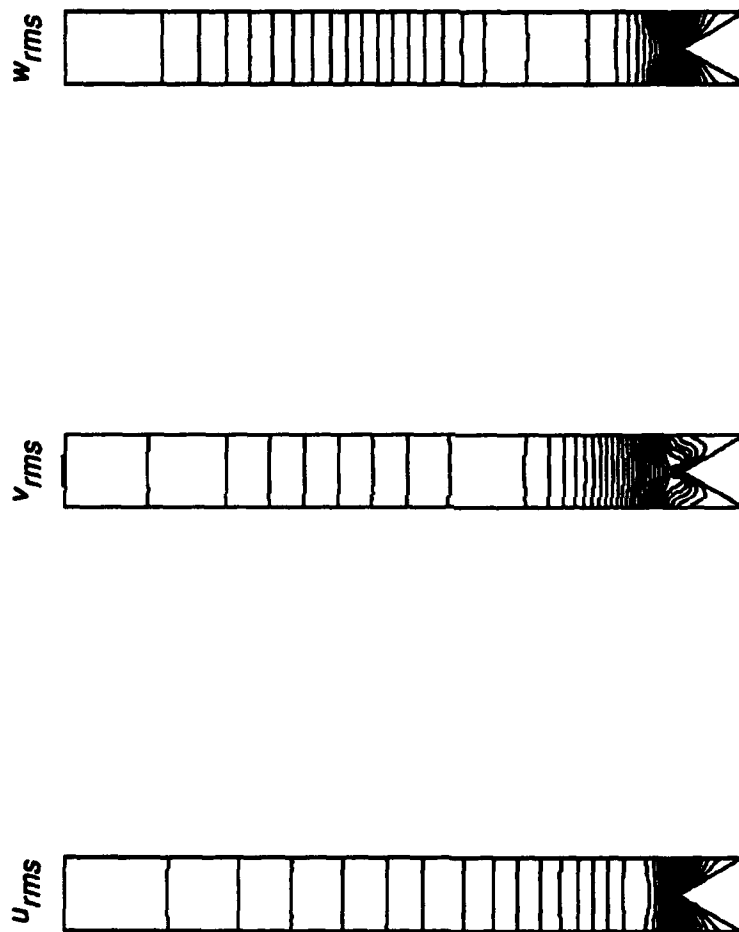


FIGURE 9. Root-mean-square velocity fluctuations normalized by the mean centerline velocity U_c in global coordinates for cases with $\alpha = 60^\circ$. (a) Streamwise; (b) normal; (c) spanwise velocity fluctuations.



(a)

FIGURE 10. For caption see the following page.



(b)

FIGURE 10. Contours of root-mean-square velocity fluctuations in the (y, z) plane for cases with $\alpha = 60^\circ$: (a) $s^+ \approx 40$; (b) $s^+ \approx 20$. The increments of contour levels for u_{rms} , v_{rms} and w_{rms} normalized by U_c are 0.0064, 0.0016 and 0.0016, respectively. The plot domain extends from the riblet surface to the centerline of the channel.

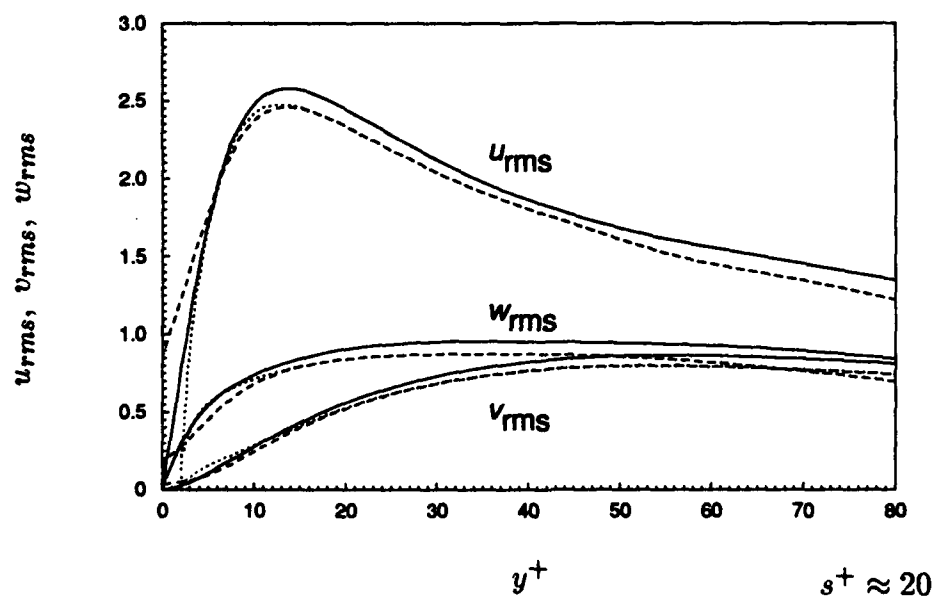
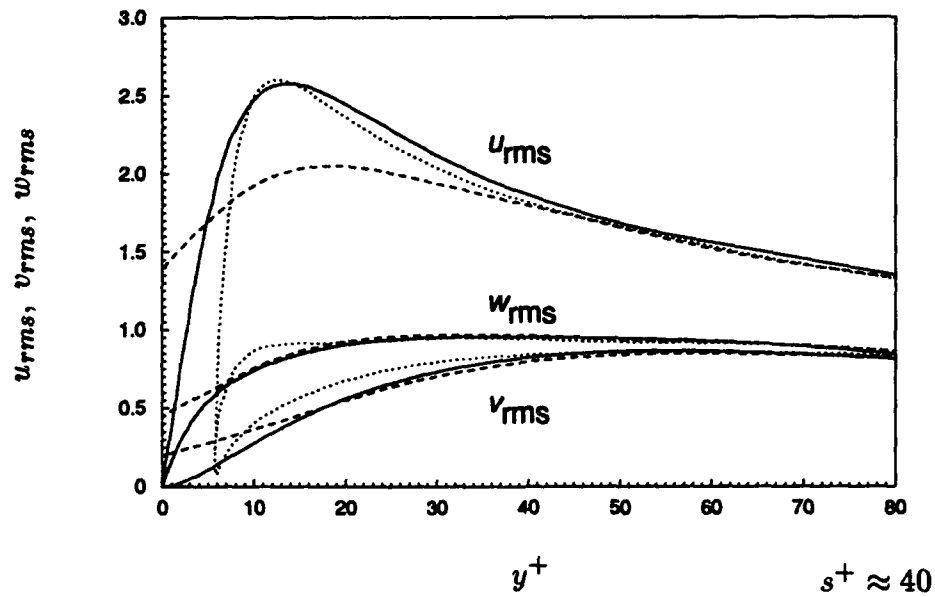


FIGURE 11. Root-mean-square velocity fluctuations normalized by the wall-shear velocity u_τ in wall coordinates for cases with $\alpha = 60^\circ$: ----, above the riblet valley; , above the riblet tip; —, above the flat plate.

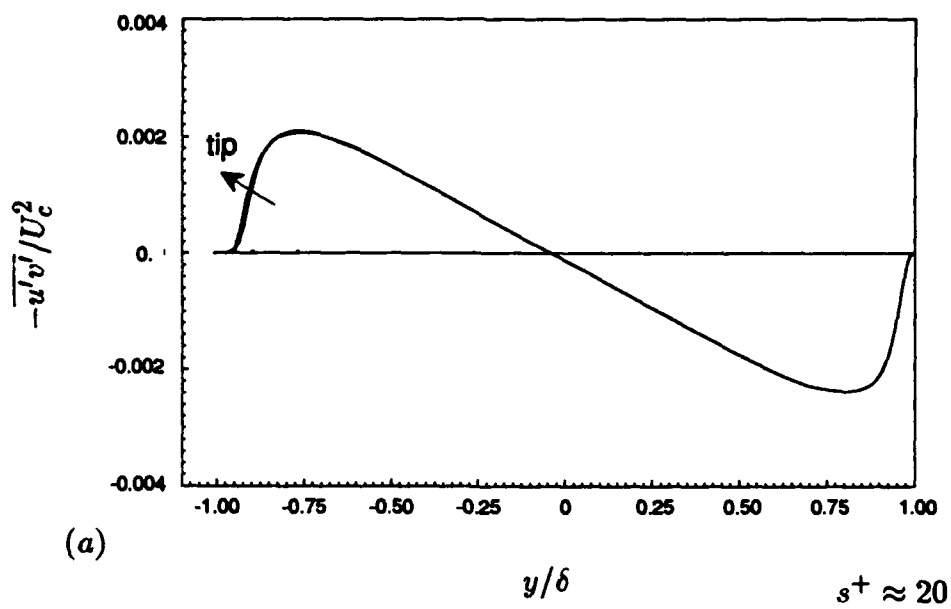
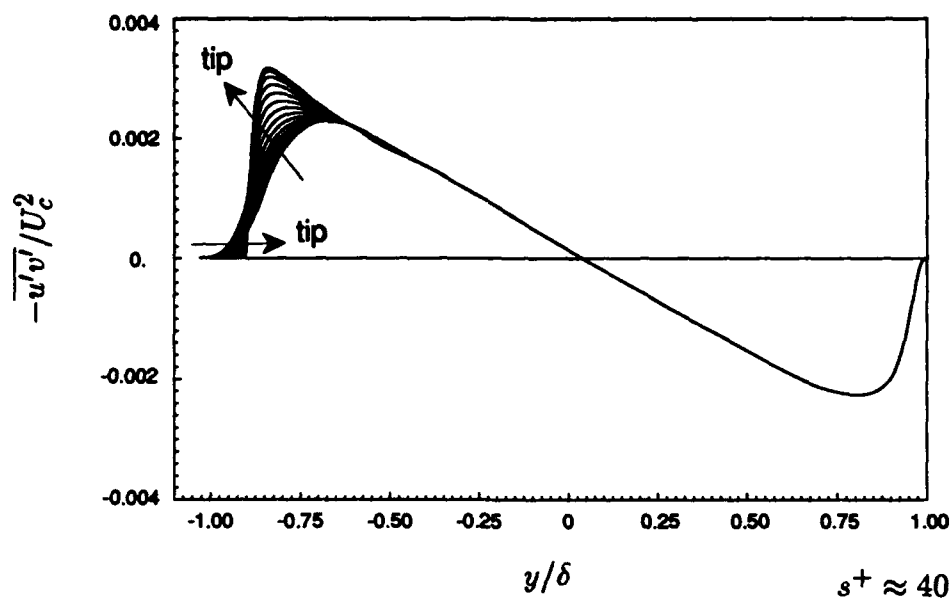


FIGURE 12. For caption see the following page.

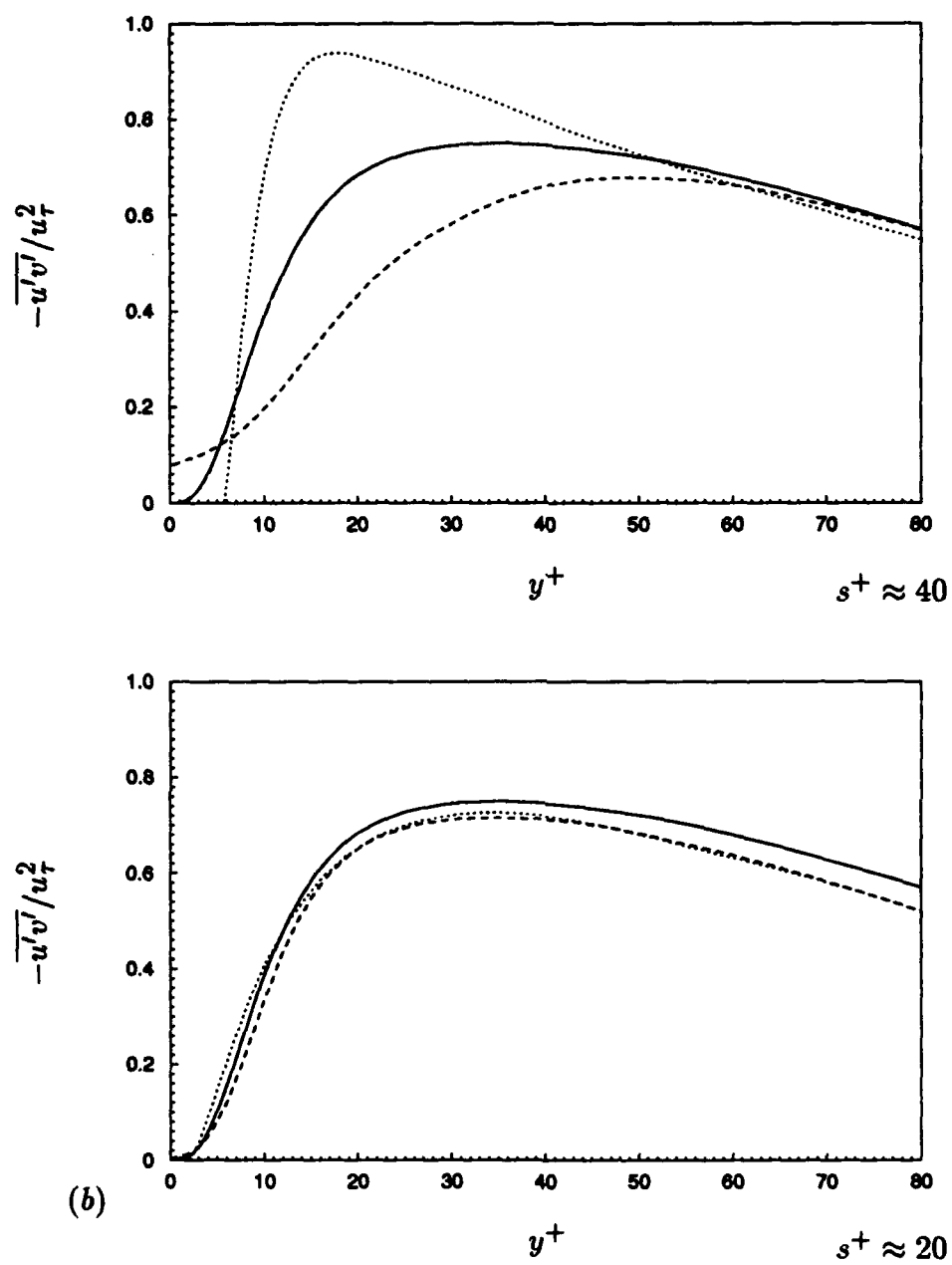


FIGURE 12. Reynolds shear stress for cases with $\alpha = 60^\circ$: (a) in global coordinates; (b) in wall coordinates. ----, Above the riblet valley; , above the riblet tip; —, above the flat plate.

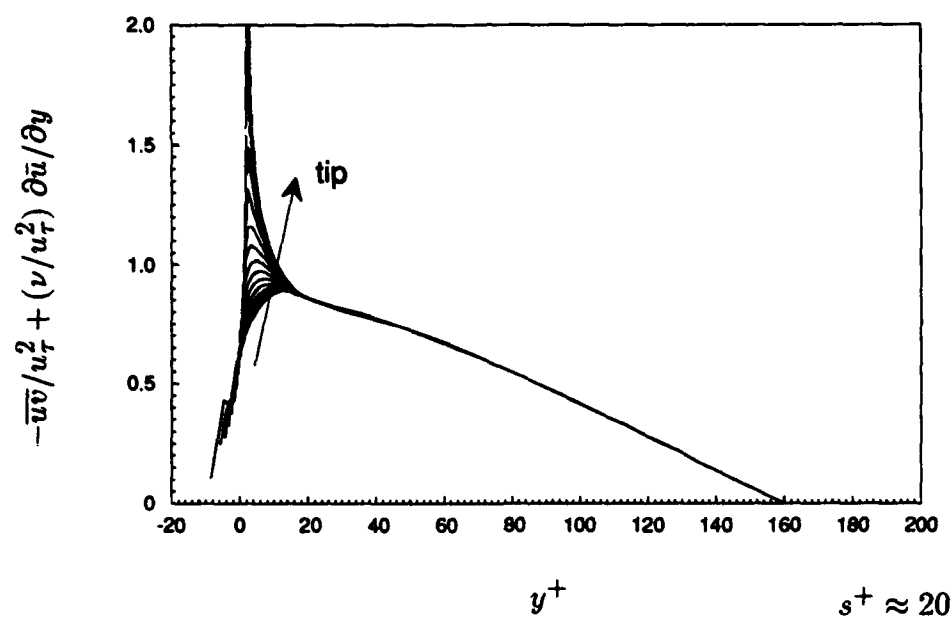
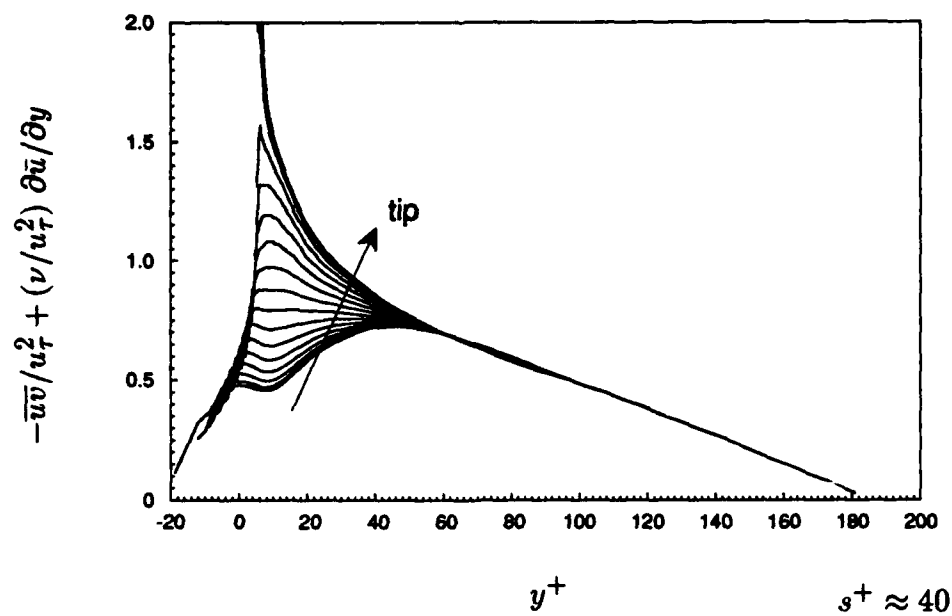


FIGURE 13. Total shear stress normalized by the wall-shear velocity u_τ^* in wall coordinates for cases with $\alpha = 60^\circ$.

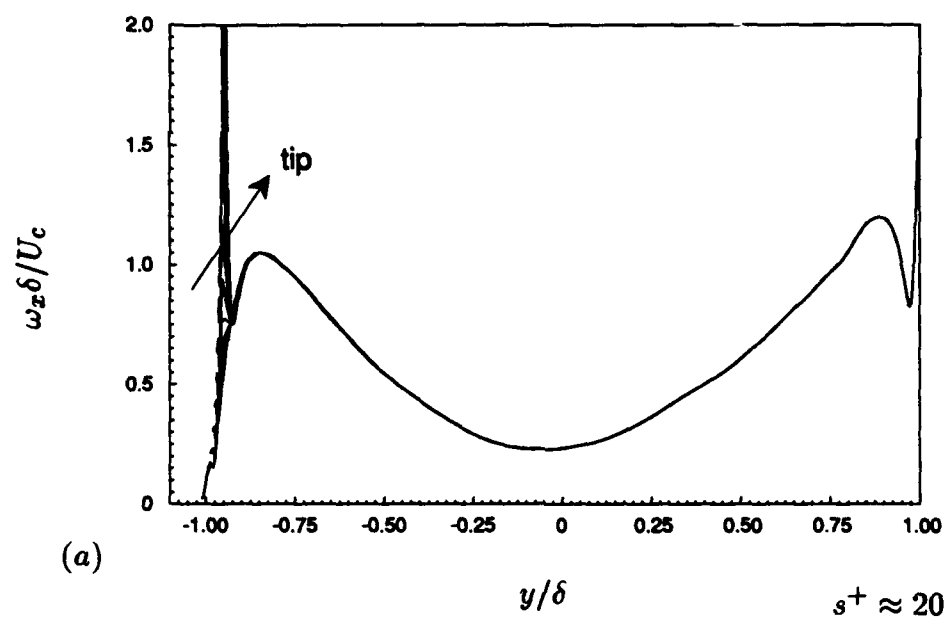
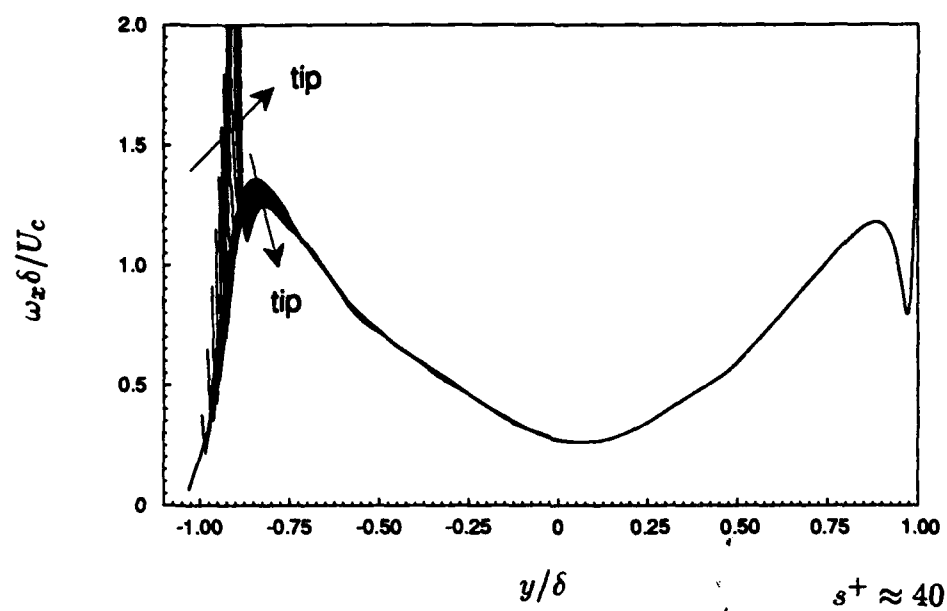


FIGURE 14. For caption see the following page.

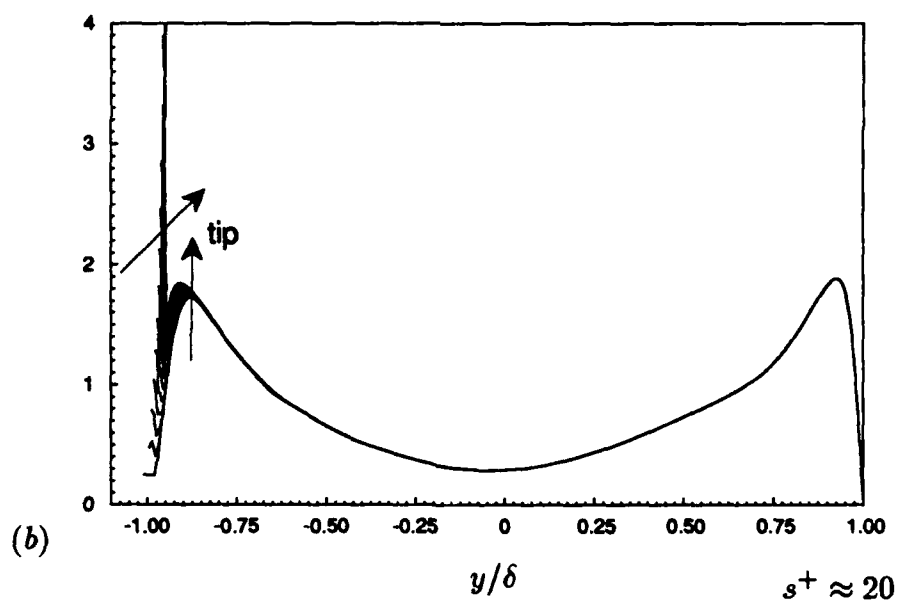
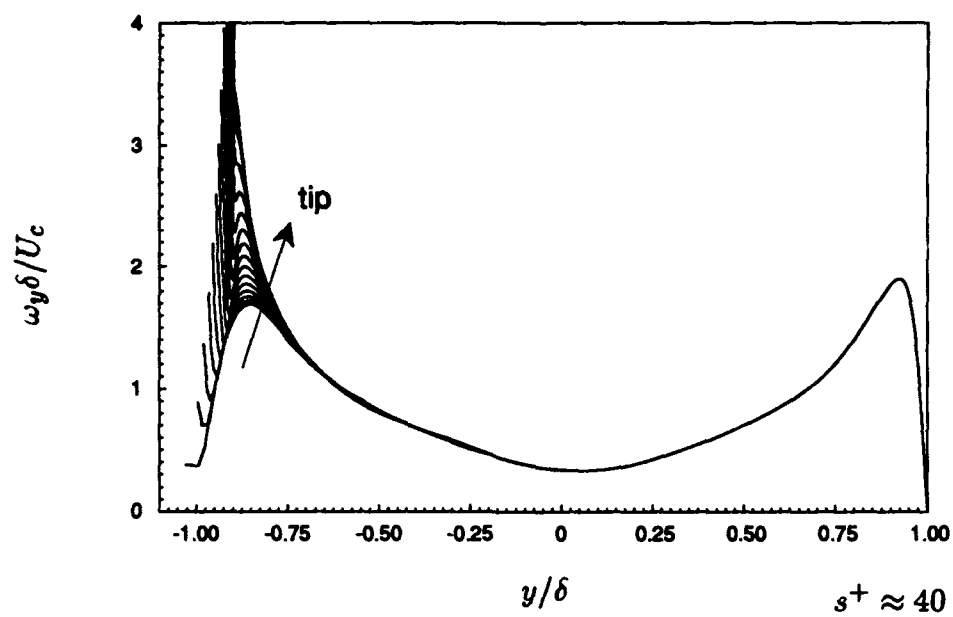


FIGURE 14. For caption see the following page.

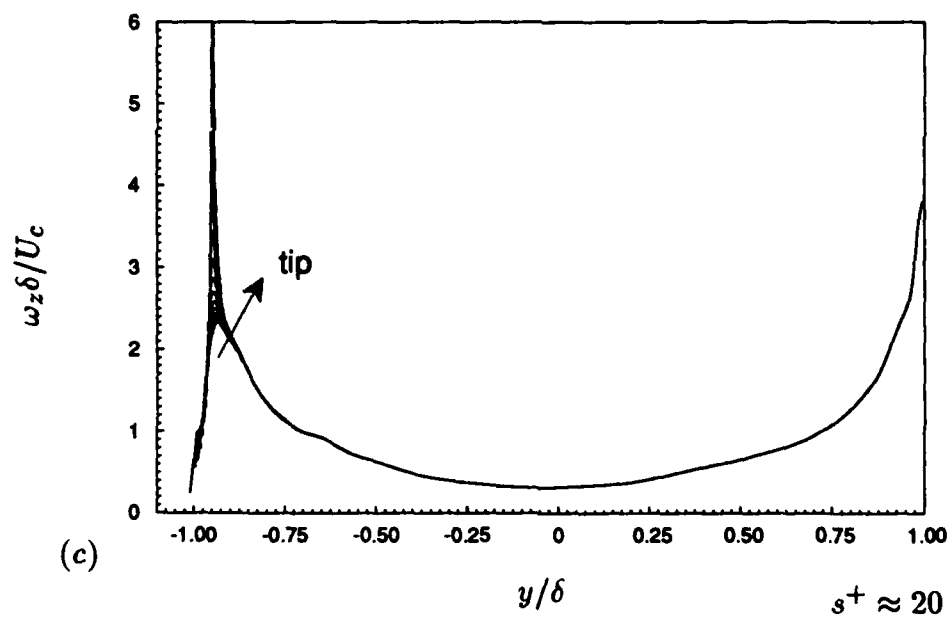
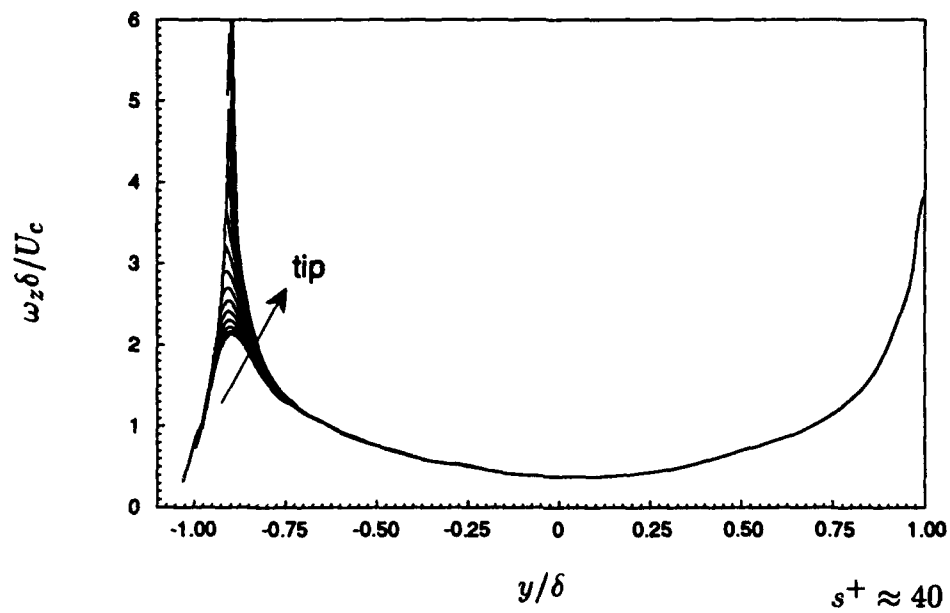


FIGURE 14. Root-mean-square vorticity fluctuations normalized by the mean centerline velocity U_c and channel half-width δ in global coordinates for cases with $\alpha = 60^\circ$. (a) Streamwise; (b) normal; (c) spanwise vorticity fluctuations.

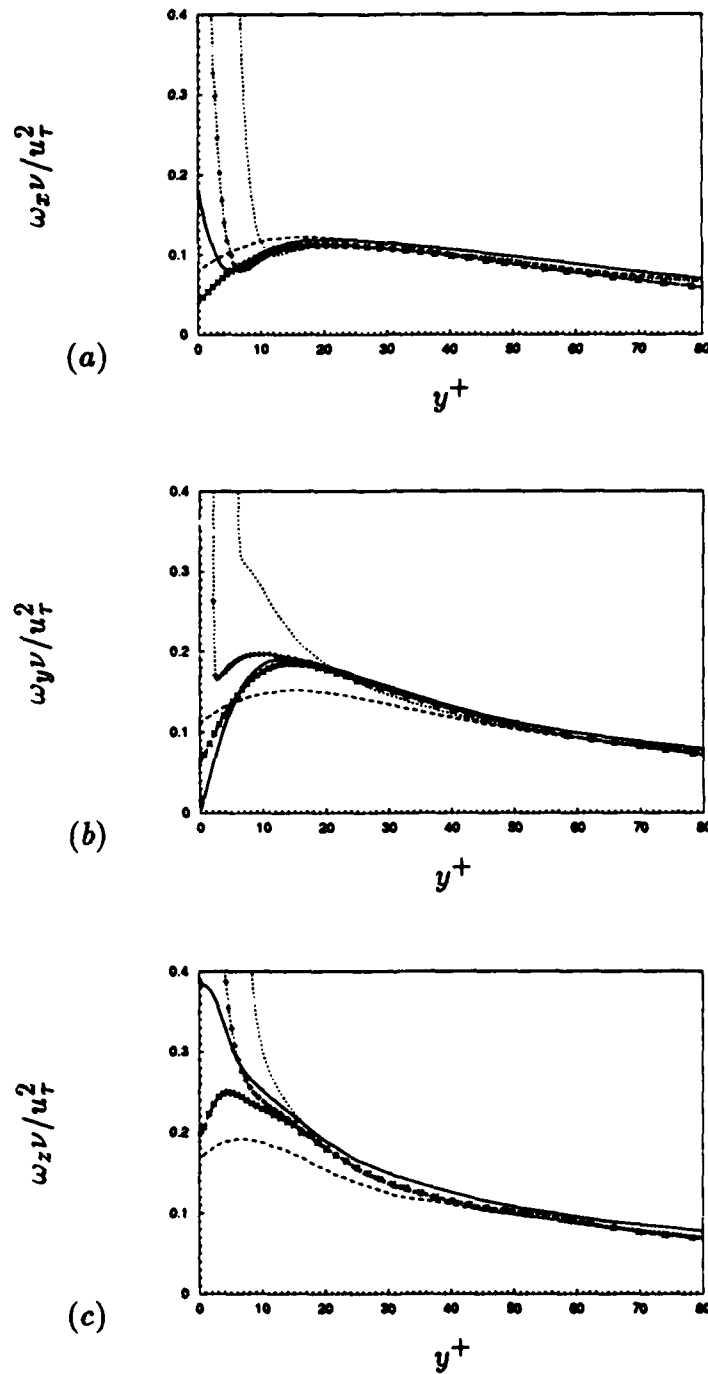


FIGURE 15. Root-mean-square vorticity fluctuations normalized by the wall-shear velocity u_τ in wall coordinates for cases with $\alpha = 60^\circ$. (a) Streamwise; (b) normal; (c) spanwise vorticity fluctuations: —, above the flat plate; above the riblet valley, ----, $s^+ \approx 40$; x, $s^+ \approx 20$; above the riblet tip, , $s^+ \approx 40$; +, $s^+ \approx 20$.

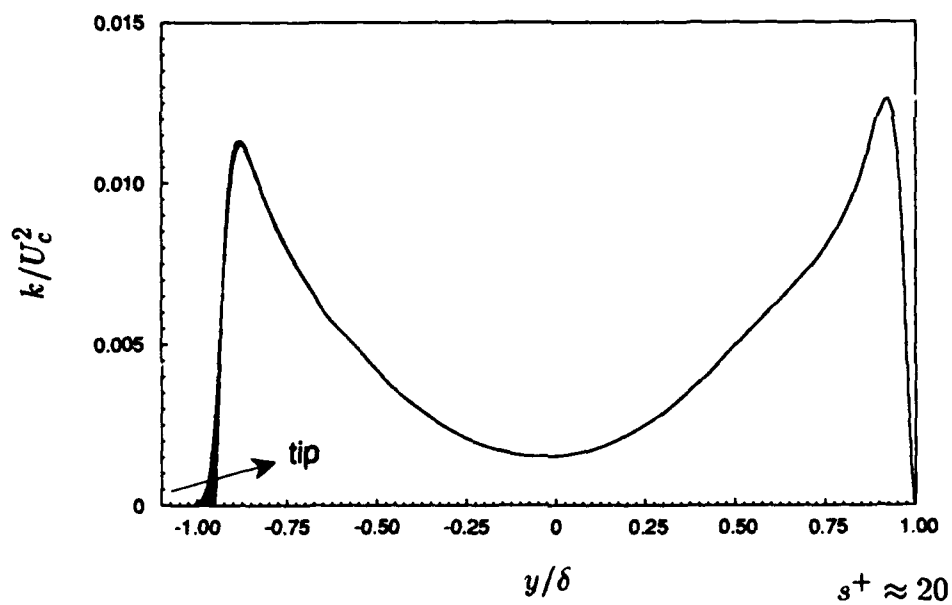
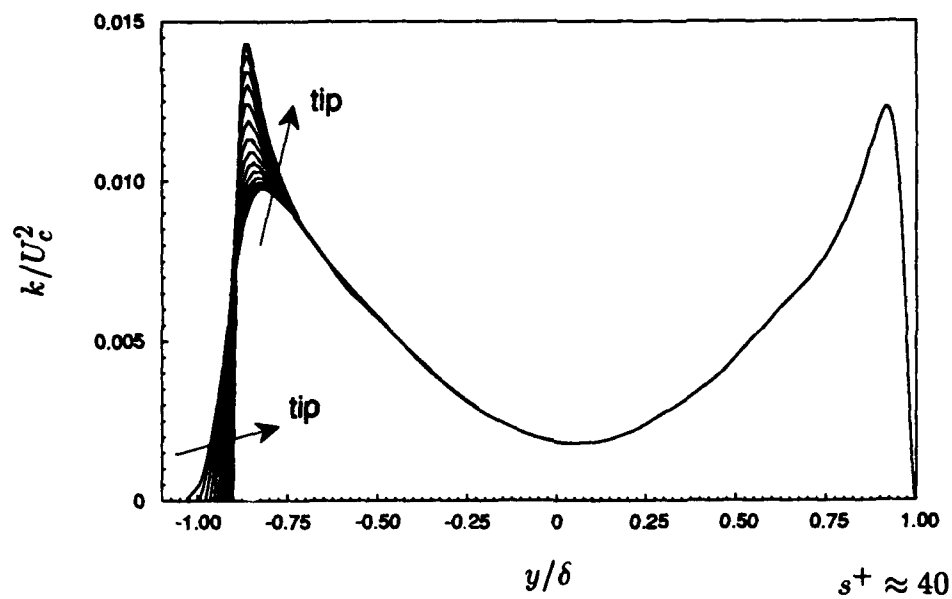


FIGURE 16. Turbulent kinetic energy normalized by the mean centerline velocity U_c for cases with $\alpha = 60^\circ$. $k = \frac{1}{2}(\overline{u'^2} + \overline{v'^2} + \overline{w'^2})$.

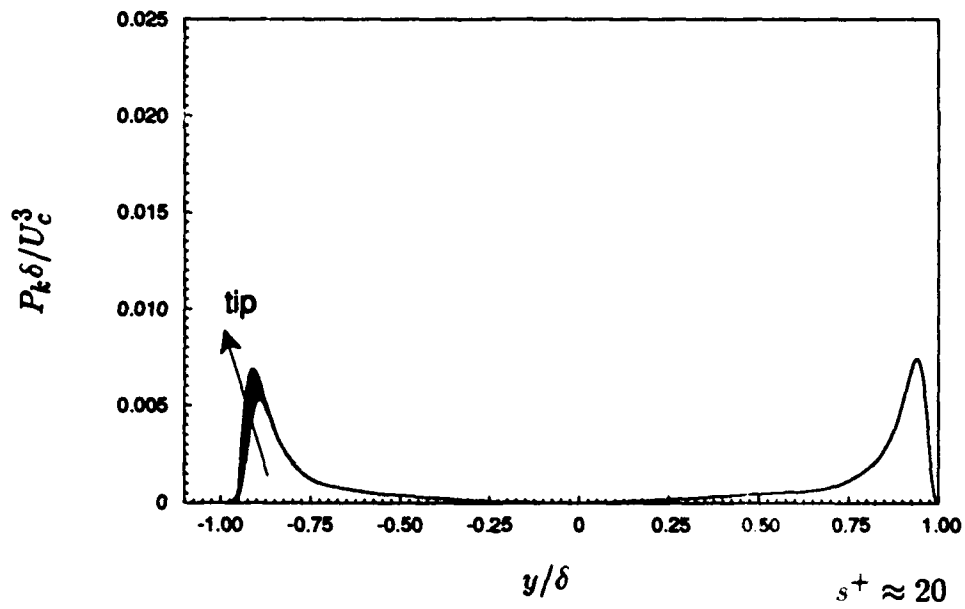
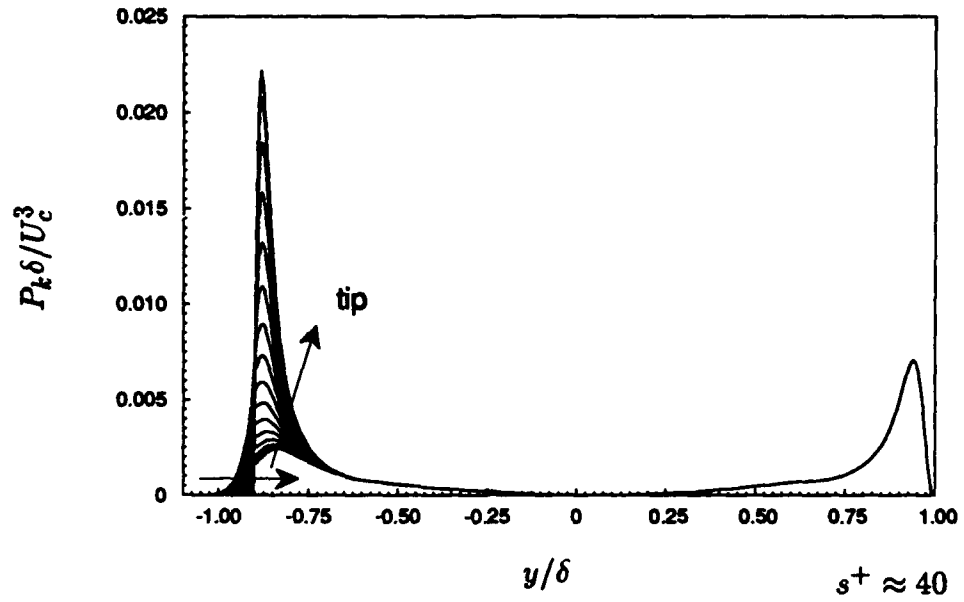


FIGURE 17. Turbulent energy production normalized by the mean centerline velocity U_c and the channel half-width δ for cases with $\alpha = 60^\circ$.

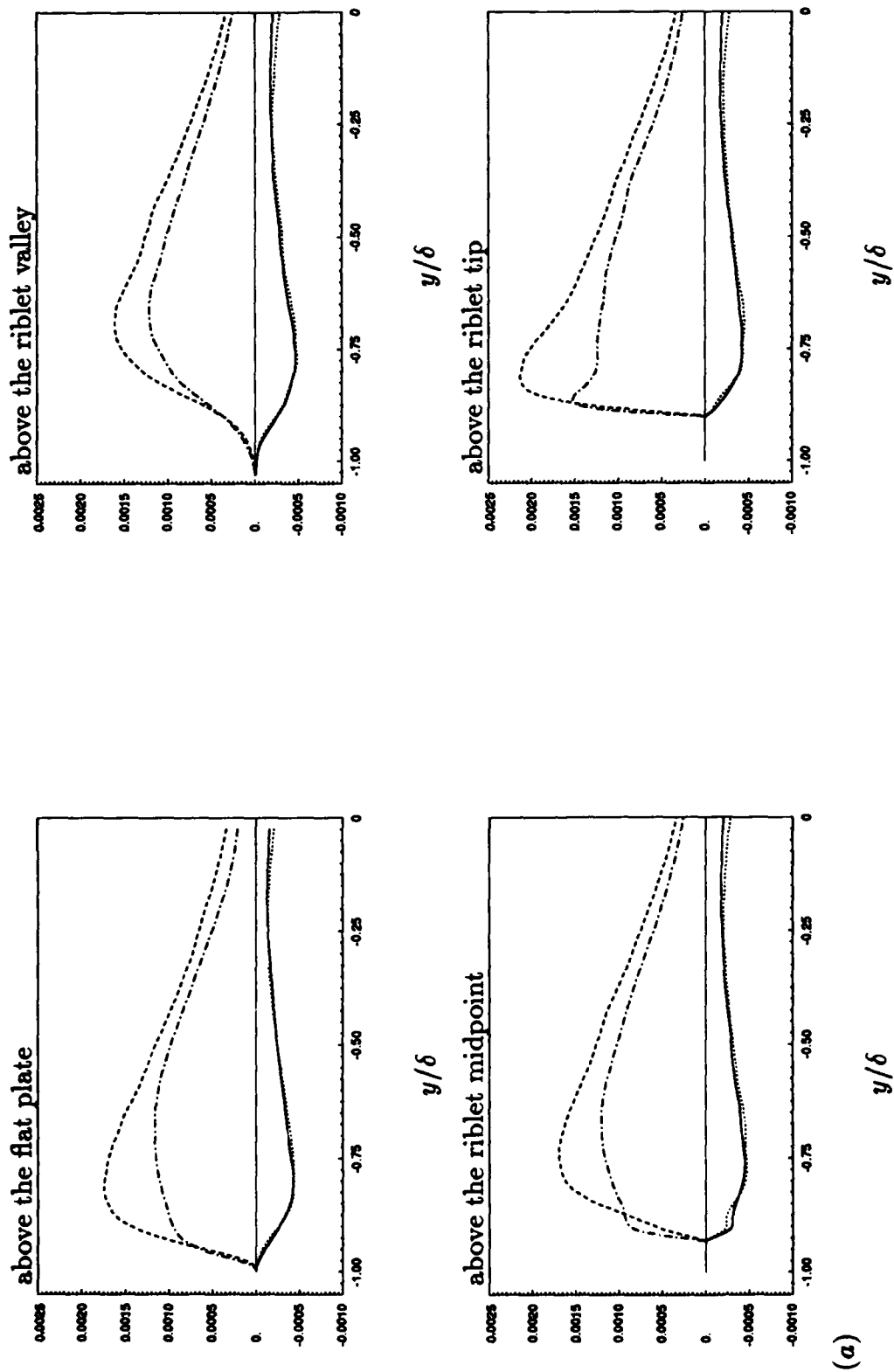


FIGURE 18. For caption see the following page.

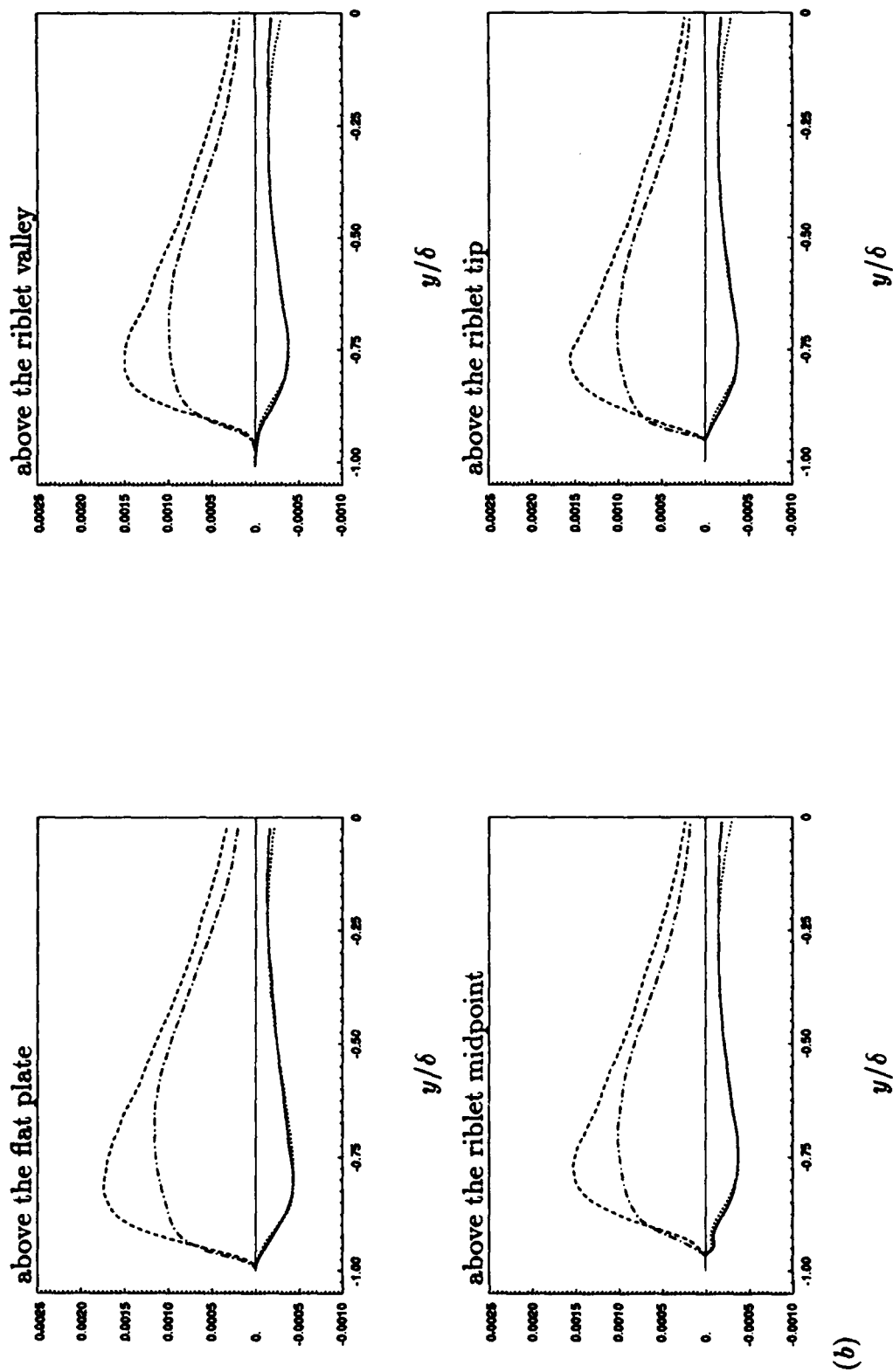


FIGURE 18. Reynolds shear stress $-\overline{u'v'}$ from each quadrant normalized by the mean centerline velocity U_c for cases with $\alpha = 60^\circ$: —, first; ----, second; , third; -.-.-, fourth quadrant. (a) $s^+ \approx 40$; (b) $s^+ \approx 20$.

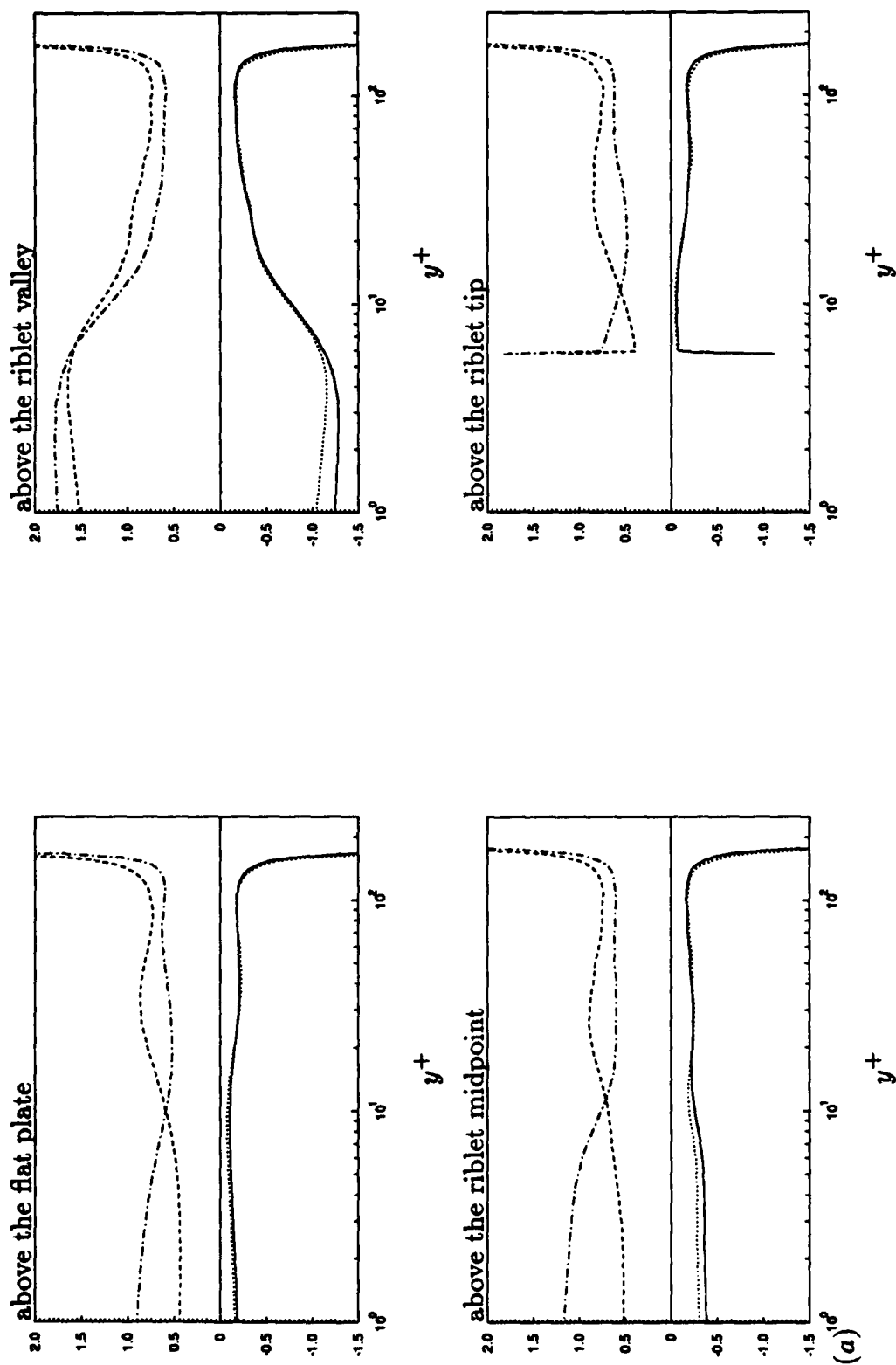


FIGURE 19. For caption see the following page.

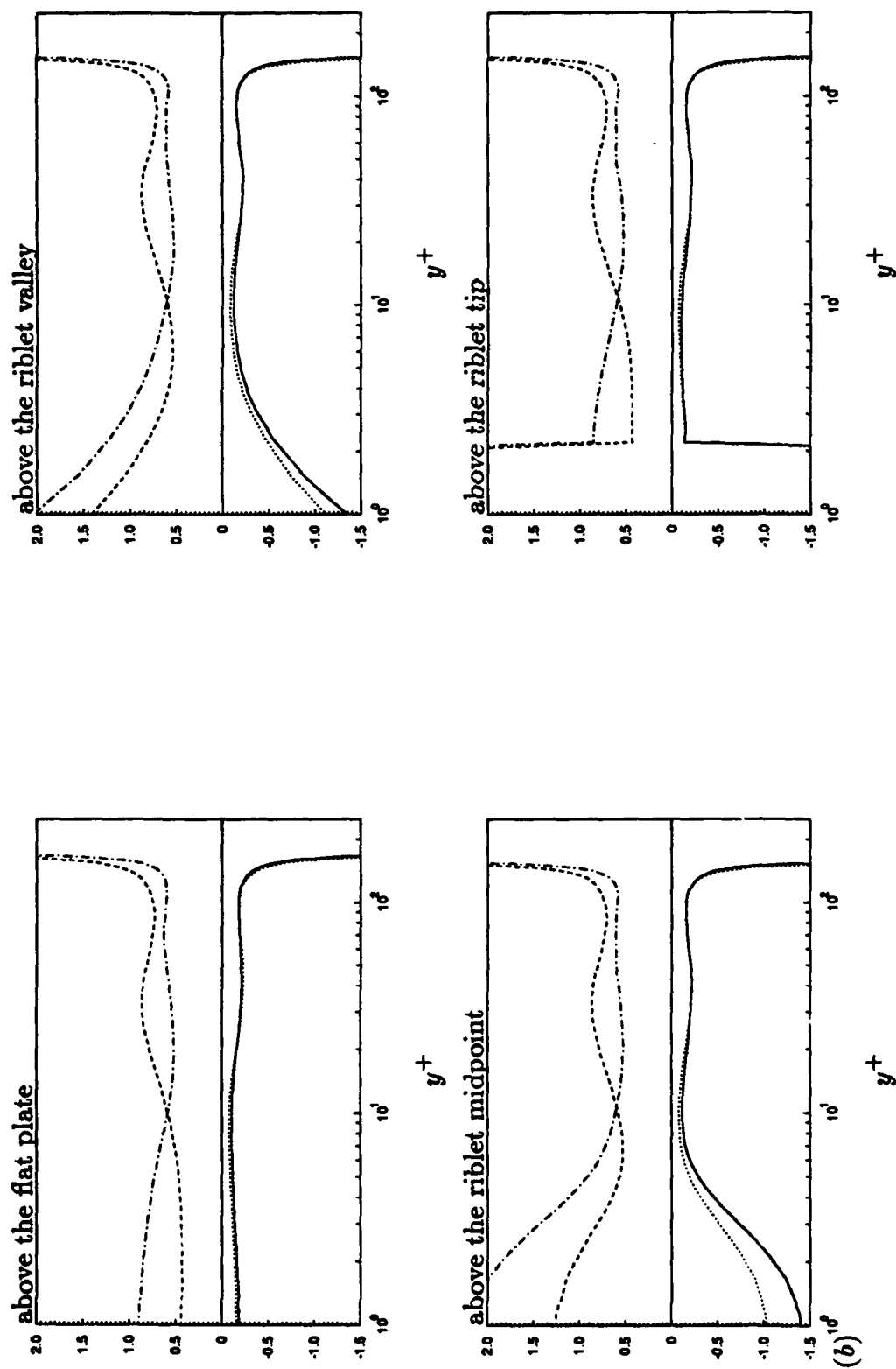


FIGURE 19. Reynolds shear stress $-\overline{u'v'}$ from each quadrant normalized by the absolute value of the local mean Reynolds shear stress $|\overline{u'v'}|$ for cases with $\alpha \approx 60^\circ$: —, first; ----, second; , third; -.-.-, fourth quadrant. (a) $s^+ \approx 40$; (b) $s^+ \approx 20$.

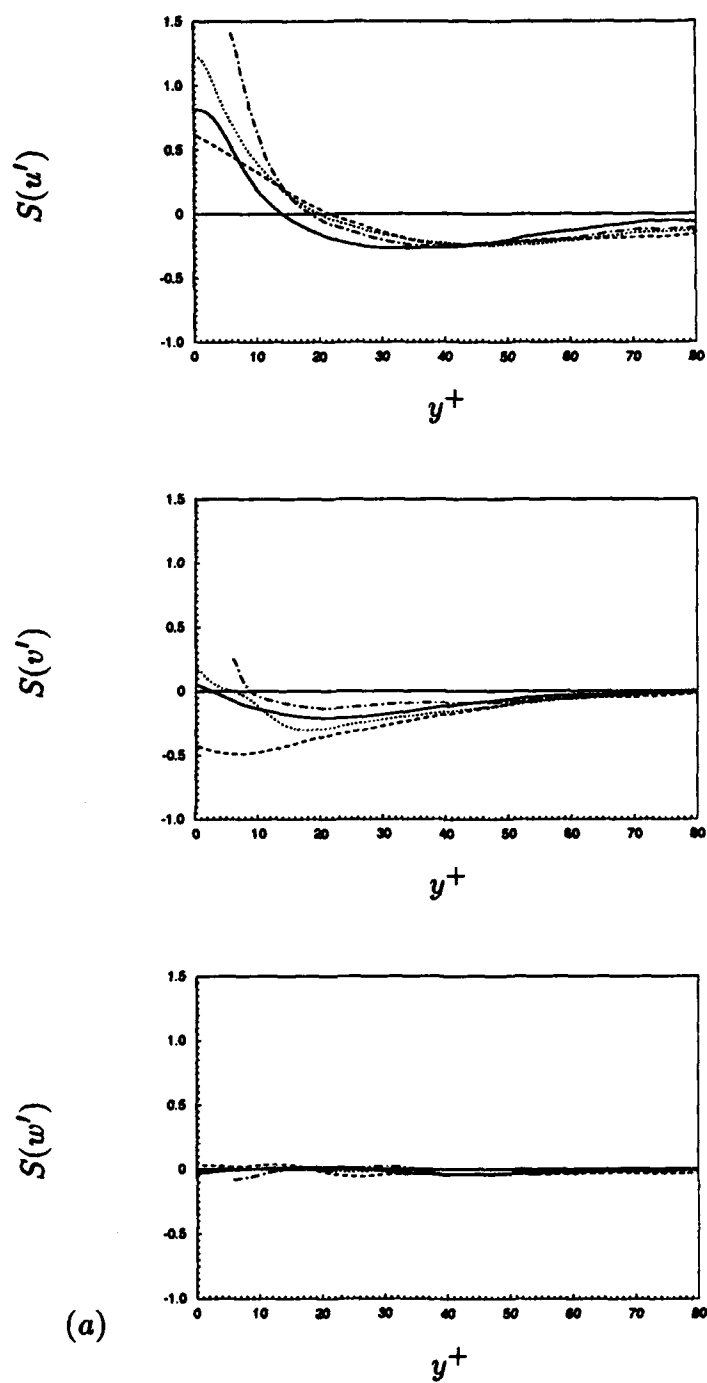


FIGURE 20. For caption see the following page.

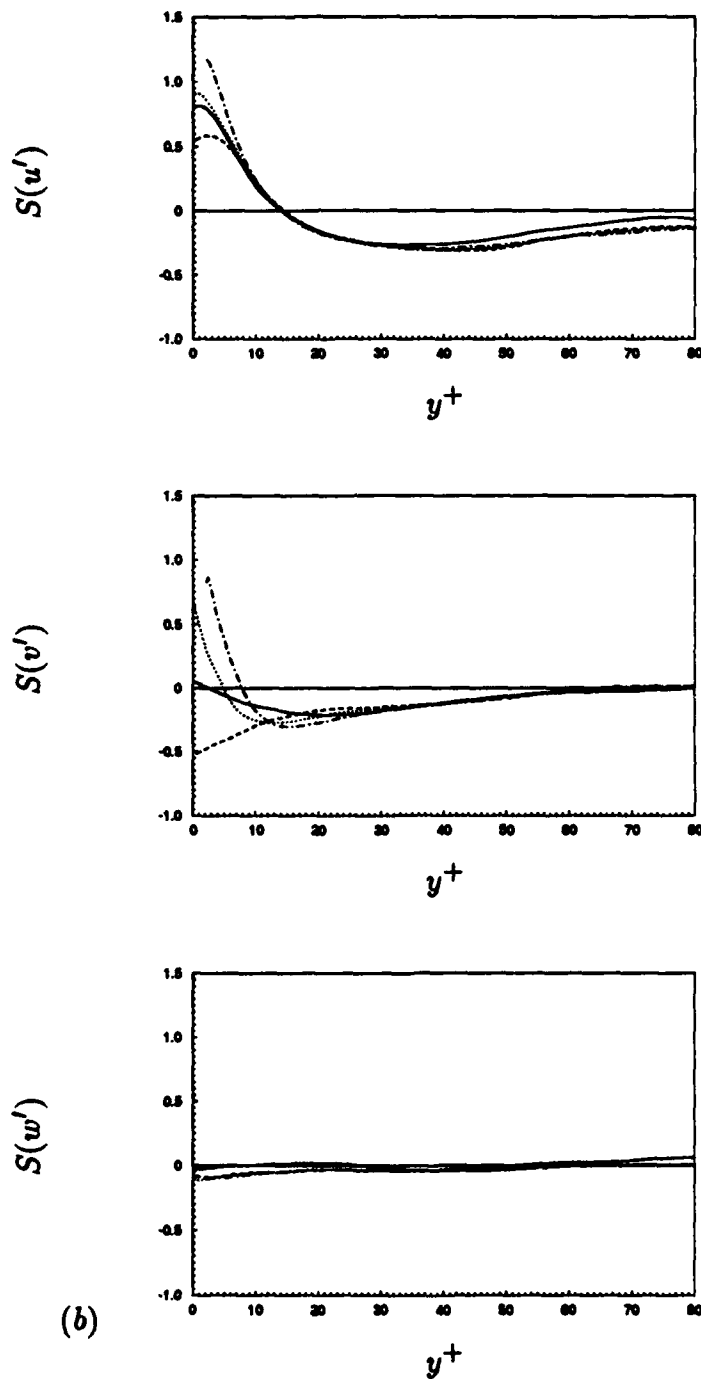


FIGURE 20. Skewness factors in wall coordinates: — , above the flat plate; ---- , above the riblet valley; , above the riblet midpoint; -.- , above the riblet tip. (a) $s^+ \approx 40$; (b) $s^+ \approx 20$. $y^+ = (y - y_0)u_{\tau}^*/\nu$.

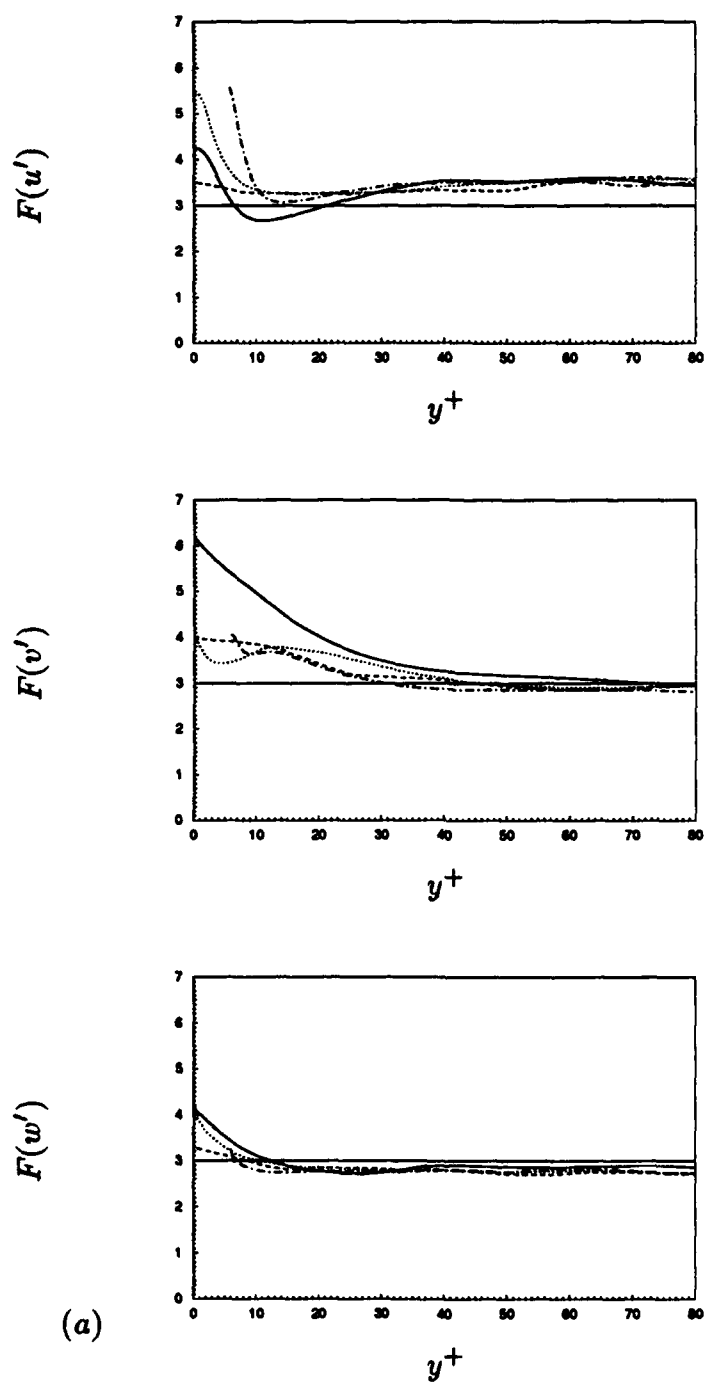


FIGURE 21. For caption see the following page.

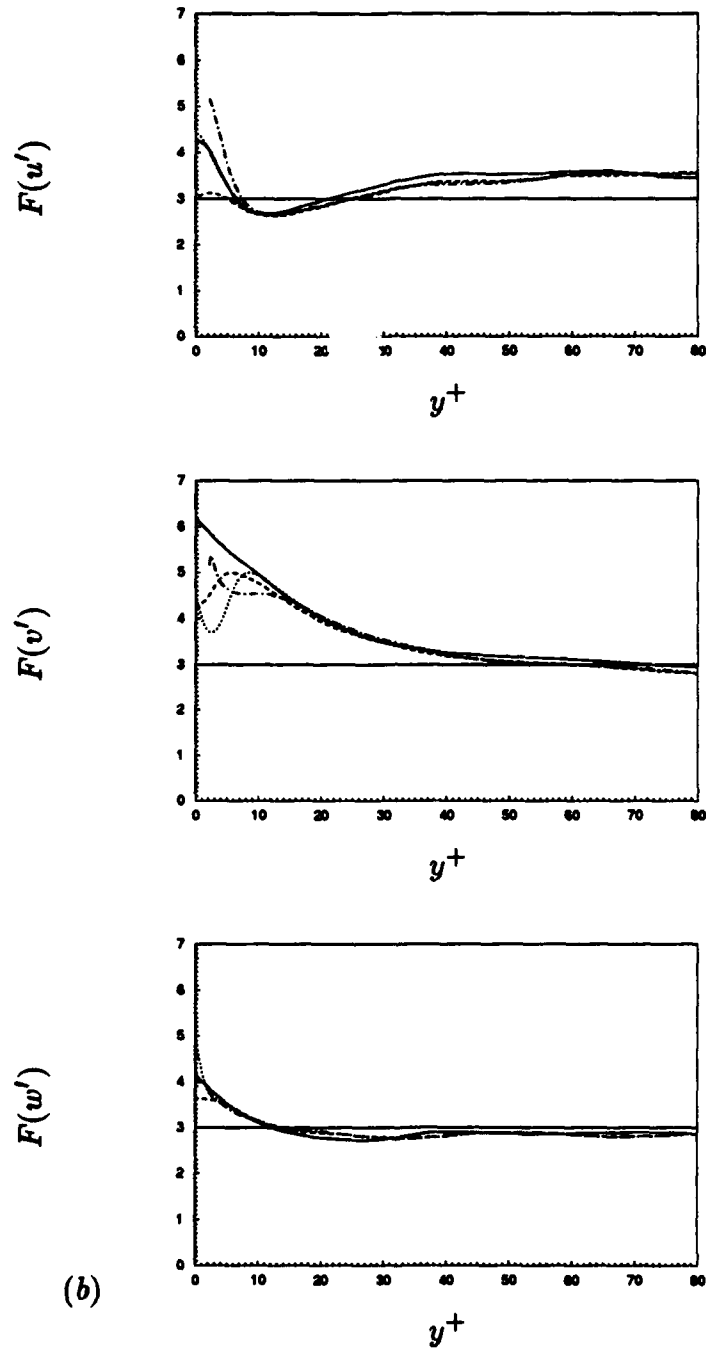


FIGURE 21. Flatness factors in wall coordinates: — , above the flat plate; ---- , above the riblet valley; , above the riblet midpoint; -.- , above the riblet tip. (a) $s^+ \approx 40$; (b) $s^+ \approx 20$. $y^+ = (y - y_0)u_{\tau}^*/\nu$.

CHAPTER 6

DRAG REDUCTION MECHANISM

As mentioned in chapter 5, in the case $s^+ \approx 20$, the turbulence intensities as well as the Reynolds shear stress near the riblets are decreased. The strength of the streamwise vortex above the riblets is also reduced (figure 14 (a)), indicating that the downwash and ejection motions due to the streamwise vortices are weakened. In this chapter, we focus on the turbulence structures above riblets by examining instantaneous flow fields. Our objective is to elucidate the physical mechanism by which riblets reduce drag.

Figure 22 (a) shows contours of the instantaneous wall-shear rate $\partial u / \partial n$ normalized by U_l and δ on the riblet surfaces for cases with $\alpha = 60^\circ$. The non-dimensionalized plane- and time-averaged wall-shear rate on the flat plate is 7.8, and the wetted area of the plate with riblets is $\sec(\alpha)$ times greater than that of the flat plate. Hence, a wall-shear rate on the riblet surface that is larger than $7.8 \cos(\alpha)$ results in an increased drag on the riblet surface over that of the flat plate, whereas a value smaller than $7.8 \cos(\alpha)$ results in a decrease. The contour line with value $7.8 \cos(\alpha)$ is drawn with black lines in figure 22 (a). Regions of high wall-shear rate (red contours) can be seen not only near the riblet tips but also in the middle of the riblets in the case $s^+ \approx 40$, whereas, in the case $s^+ \approx 20$, the regions of high wall-shear rates are restricted to the tips.

It has been shown in PART I that, in plane channel flow, local regions of high skin friction are associated with streamwise vortices just above the wall. The sweep motion due to these strong streamwise vortices creates regions of high skin friction on the wall. The transverse-flow structures leading to high skin friction can be seen in the cross-sectional views at the locations (marked with arrows in figure 22 (a)) at which the highest wall-shear rates occur. Figure 22 (b) shows cross-flow velocity vectors (v, w) and contours of the streamwise vorticity component in the transverse plane. Strong streamwise vortices near the riblets are present in both cases. It was estimated in Kim *et al.* (1987) from the profile of root-mean-square streamwise vorticity in plane channel flow that the centers of streamwise vortices are located on the average at $y^+ \approx 20$, and that their average diameter is $d^+ \approx 30$. Since

the average diameter of the streamwise vortices above the wall is smaller than the spacing of the riblets in the case $s^+ \approx 40$, the streamwise vortices can move freely and can be found inside the riblet valleys. This exposes a larger surface area of the riblets to the sweep motion that they induce. On the other hand, in the case $s^+ \approx 20$, most streamwise vortices stay above the riblets, because their average diameter is larger than the spacing of the riblets, and only a limited area of the riblet tips is exposed to their induced sweep. A schematic diagram of this drag modification mechanism is shown in figure 23. Note that even in the case of riblets with $s^+ \approx 40$ the skin friction per unit of surface area is reduced due to the less but still significant inhibition of streamwise vortices approaching the wetted area. In the case $s^+ \approx 20$, only a small part of the wetted surface is exposed, resulting in a net drag reduction despite a significant increase in the wetted area.

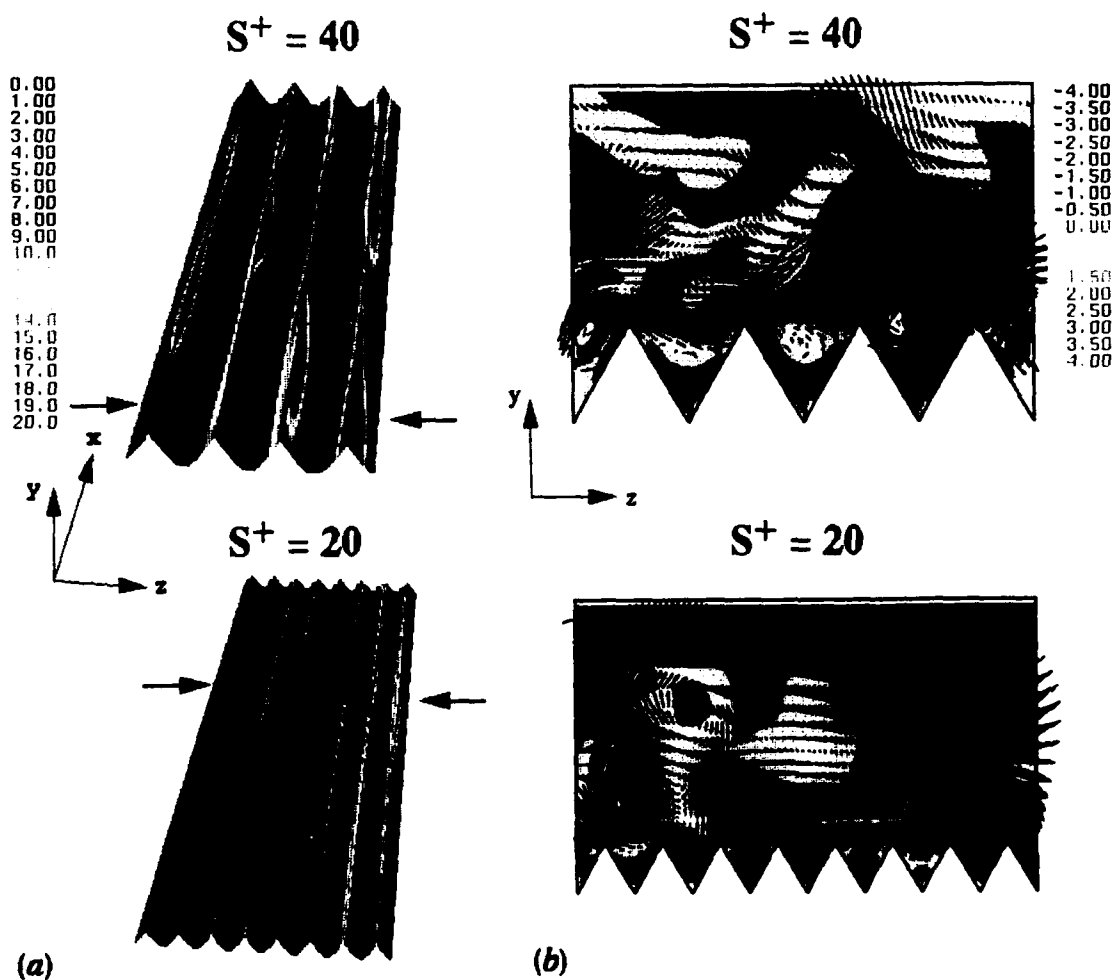


FIGURE 22. Instantaneous flows over the riblets with $\alpha = 60^\circ$: (a) contours of the wall-shear rate on the riblet surfaces; (b) cross-flow velocity vectors (v, w) and contours of the streamwise vorticity in (y, z) planes.

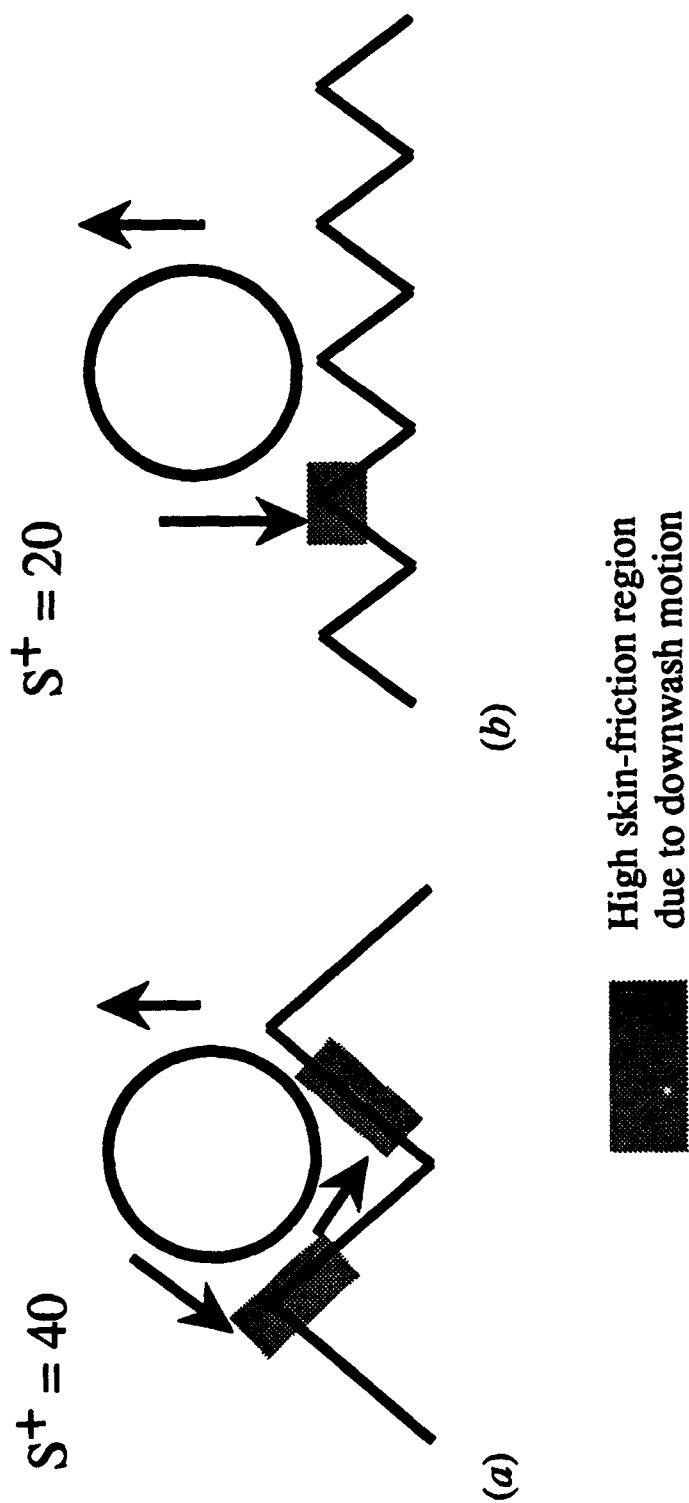


FIGURE 23. Schematic diagram of drag increase and reduction mechanisms by riblets: (a) $s^+ \approx 40$ - drag increase (extensive area affected by downwash motion); (b) $s^+ \approx 20$ - drag reduction (limited area affected by downwash motion).

CHAPTER 7

SUMMARY

Direct numerical simulations of turbulent flows over riblets were carried out at a Reynolds number of 4200 based on the centerline velocity of a laminar parabolic profile (with the same volume flux) and the channel half-width. A fully implicit (Crank-Nicholson), fractional step method was used for the time-advancement, and a second-order central finite-difference method was used for the spatial derivatives.

The drags computed for each riblet configuration were in good agreement with the experimental results of Walsh (1982). Cases with $s^+ \approx 20$ showed a 5 – 6% drag reduction, and cases with $s^+ \approx 40$ showed a drag increase.

The virtual origin of the wall was defined such that the maximum turbulent kinetic energy production occurred at $y^+ \approx 13$. As the ridge angle of the riblets increased, the virtual origin moved closer to the riblet tip. The mean-velocity profiles based on these virtual origins showed upward and downward shifts in the log-law for drag-decreasing and drag-increasing cases, respectively.

Flow statistics above the riblets were compared to those above the flat plate. Differences between the mean-velocity profiles and turbulence quantities were limited to the inner region of the boundary layer. Velocity and vorticity fluctuations as well as the Reynolds shear stress above the riblets were reduced in drag-reducing configurations. Reduction of the normal and spanwise velocity fluctuations above the riblets indicated that the transverse flow near the wall was impeded by the riblets, one of the drag reduction mechanisms suggested by Bechert & Bartenwerfer (1989) and Choi (1989). Quadrant analysis indicated that the riblets intensified the positive Reynolds-shear-stress producing events in drag-increasing configurations, while they mitigated these (second and fourth quadrant) events in drag-reducing configurations. The Reynolds shear stresses from the first and third quadrant events were nearly unchanged by the riblets.

From examination of the instantaneous flow field, a drag reduction mechanism was proposed: a certain spacing of riblets reduces viscous drag by restricting the location of streamwise vortices above the wetted surface such that only a limited area of the riblets is exposed to their induced downwash of high speed fluid. Only

the tip region is exposed to high wall-shear rates in drag-reducing configurations, whereas, in drag-increasing configurations, both the middle and tip regions are exposed to them.

APPENDICES

APPENDIX A

OPTIMAL CONTROL OF WALL-BOUNDED TURBULENT FLOWS

Abergel and Temam (1990) addressed the problem of minimizing turbulence fluctuations from the point of view of optimal control theory. We investigate the possibility of controlling turbulent boundary layers by placing sensors at the wall using optimal control theory. The optimal control problem for turbulent channel flow is formulated as follows:

- Find ϕ minimizing the functional (cost function)

$$J(\phi) = \int_0^T \int_{\partial\Omega} \frac{1}{4} \left[\left(\frac{\partial u}{\partial y} \right)_w^2 + \left(\frac{\partial w}{\partial y} \right)_w^2 \right] d\sigma dt + \frac{\alpha}{2} \int_0^T \int_{\partial\Omega} \phi^2 d\sigma dt, \quad (A.1)$$

where the quantity inside the bracket is the square magnitude of the shear rate at the wall ($\partial\Omega$), and u_i is the solution of the state equations (the Navier-Stokes equations)

$$\begin{aligned} \frac{\partial u_i}{\partial t} + u_j \frac{\partial u_i}{\partial x_j} &= -\frac{\partial p}{\partial x_i} + \frac{1}{Re} \frac{\partial}{\partial x_j} \frac{\partial u_i}{\partial x_j} \\ \frac{\partial u_i}{\partial x_i} &= 0, \end{aligned} \quad (A.2)$$

subject to the wall boundary conditions

$$\begin{aligned} u(x, y = \pm\delta, z, t) &= w(x, y = \pm\delta, z, t) = 0 \\ v(x, y = \pm\delta, z, t) &= \phi, \end{aligned} \quad (A.3)$$

the initial condition $u_i(x, y, z, t = 0) = u_{i0}(x, y, z)$, periodic boundary conditions

$$\begin{aligned} u_i(x = 0, y, z, t) &= u_i(x = L_x, y, z, t) \\ u_i(x, y, z = 0, t) &= u_i(x, y, z = L_z, t) \\ p(x = 0, y, z, t) &= p(x = L_x, y, z, t) + C(t) \\ p(x, y, z = 0, t) &= p(x, y, z = L_z, t) \end{aligned} \quad (A.4)$$

$$C(t) = -\frac{dP}{dx}(t) L_x,$$

and the constant mass flow rate constraint

$$\int_{\partial\Omega} \phi \, d\sigma = 0. \quad (A.5)$$

Here ϕ is the input normal velocity at the wall, T is a fixed (but arbitrary) control time, and α is an arbitrary constant related to the expense associated with the control. u_{i0} is an instantaneous velocity field from fully developed channel flow. $C(t)$ is affected by the action of the control. That is, the mean pressure gradient (or drag) can change, but the mass flow rate is kept constant. L_x and L_z denote the streamwise and spanwise computational periods, respectively. The subscript w indicates the value at the wall. \square

Let $(\bar{u}_i, \bar{\phi})$ be an optimal pair; then, the Fréchet differential¹ of J in the direction of $\hat{\phi}$ is given by

$$\begin{aligned} \frac{\mathcal{D}J}{\mathcal{D}\phi} \hat{\phi} &= \int_0^T \int_{\partial\Omega} \left[\frac{1}{2} \frac{\partial \bar{u}}{\partial y} \frac{\partial q_1}{\partial y} + \frac{1}{2} \frac{\partial \bar{w}}{\partial y} \frac{\partial q_3}{\partial y} \right] d\sigma dt + \alpha \int_0^T \int_{\partial\Omega} \bar{\phi} \hat{\phi} \, d\sigma dt \\ &= 0, \end{aligned} \quad (A.6)$$

¹ When it exists, the Fréchet differential of J in the direction of $\hat{\phi}$ is defined by (Finlayson 1972)

$$\frac{\mathcal{D}J}{\mathcal{D}\phi} \hat{\phi} = \lim_{\epsilon \rightarrow 0} \frac{J(\phi + \epsilon \hat{\phi}) - J(\phi)}{\epsilon}$$

where q_i is the solution of the linearized state equations with respect to ϕ , i.e., $q_i = (\mathcal{D}u_i/\mathcal{D}\phi) \hat{\phi}$ and

$$\begin{aligned} \frac{\partial q_i}{\partial t} + \bar{u}_j \frac{\partial q_i}{\partial x_j} + q_j \frac{\partial \bar{u}_i}{\partial x_j} &= -\frac{\partial p_l}{\partial x_i} + \frac{1}{Re} \frac{\partial}{\partial x_j} \frac{\partial q_i}{\partial x_j} \\ \frac{\partial q_i}{\partial x_i} &= 0. \end{aligned} \quad (A.7)$$

Equation (A.7) is subject to wall boundary conditions

$$\begin{aligned} q_1(x, y = \pm\delta, z) &= q_3(x, y = \pm\delta, z) = 0 \\ q_2(x, y = \pm\delta, z) &= \hat{\phi}, \end{aligned} \quad (A.8)$$

the initial condition $q_i(x, y, z, t = 0) = 0$, periodic boundary conditions

$$\begin{aligned} q_i(x = 0, y, z, t) &= q_i(x = L_x, y, z, t) \\ q_i(x, y, z = 0, t) &= q_i(x, y, z = L_z, t) \\ p_l(x = 0, y, z, t) &= p_l(x = L_x, y, z, t) + C_l(t) \\ p_l(x, y, z = 0, t) &= p_l(x, y, z = L_z, t), \end{aligned} \quad (A.9)$$

and the constant mass flow rate constraint

$$\int_{\partial\Omega} \hat{\phi} d\sigma = 0,$$

where $p_l = (\mathcal{D}p/\mathcal{D}\phi) \hat{\phi}$, and $C_l = \mathcal{D}C/\mathcal{D}\phi \hat{\phi}$.

In order to determine the Fréchet derivative of J , we introduce the adjoint state \tilde{q}_i which is the solution of linearized adjoint state equations

$$\begin{aligned} -\frac{\partial \tilde{q}_i}{\partial t} - u_j \frac{\partial \tilde{q}_i}{\partial x_j} + \tilde{q}_j \frac{\partial u_j}{\partial x_i} &= -\frac{\partial \tilde{p}_l}{\partial x_i} + \frac{1}{Re} \frac{\partial}{\partial x_j} \frac{\partial \tilde{q}_i}{\partial x_j} \\ \frac{\partial \tilde{q}_i}{\partial x_i} &= 0, \end{aligned} \quad (A.10)$$

subject to wall boundary conditions

$$\begin{aligned}\tilde{q}_1(x, y = \pm\delta, z) &= \frac{1}{2} \frac{\partial u}{\partial y} |_w \\ \tilde{q}_2(x, y = \pm\delta, z) &= 0 \\ \tilde{q}_3(x, y = \pm\delta, z) &= \frac{1}{2} \frac{\partial w}{\partial y} |_w,\end{aligned}\tag{A.11}$$

the initial condition $\tilde{q}_i(x, y, z, t = T) = 0$, and periodic boundary conditions

$$\begin{aligned}\tilde{q}_i(x = 0, y, z, t) &= \tilde{q}_i(x = L_x, y, z, t) \\ \tilde{q}_i(x, y, z = 0, t) &= \tilde{q}_i(x, y, z = L_z, t) \\ \tilde{p}_l(x = 0, y, z, t) &= \tilde{p}_l(x = L_x, y, z, t) + \tilde{C}_l(t) \\ \tilde{p}_l(x, y, z = 0, t) &= \tilde{p}_l(x, y, z = L_z, t).\end{aligned}\tag{A.12}$$

We obtain the following expression for the Fréchet differential of J by substituting equation (A.11) into equation (A.6)

$$\frac{\mathcal{D}J}{\mathcal{D}\phi} \hat{\phi} = \int_0^T \int_{\partial\Omega} \left[\tilde{q}_1 \frac{\partial q_1}{\partial y} + \tilde{q}_3 \frac{\partial q_3}{\partial y} \right] d\sigma dt + \alpha \int_0^T \int_{\partial\Omega} \phi \hat{\phi} d\sigma dt.\tag{A.13}$$

On the other hand, the definition of adjoint operator for \tilde{q}_i is

$$\langle \tilde{q}_i, LS(q_i) \rangle = \langle q_i, LS^*(\tilde{q}_i) \rangle + B(q_i, \tilde{q}_i),$$

$$B(q_i, \tilde{q}_i) = \int_{\partial\Omega} (q_i \tilde{S}_i + \tilde{q}_i S_i) d\sigma,\tag{A.14}$$

$$\tilde{S}_i = -\tilde{p}'_l n_i + \frac{1}{Re} \frac{\partial \tilde{q}_i}{\partial x_j} n_j,$$

$$S_i = q_i u_j n_j + p'_l n_i - \frac{1}{Re} \frac{\partial q_i}{\partial x_j} n_j,$$

where LS is the differential operator of the linearized state equations, LS^* is the corresponding adjoint operator, n_j is the unit vector normal to boundary, and p'_l and \tilde{p}'_l are the fluctuating parts of the linearized and linearized adjoint pressures, respectively. The boundary terms $B(q_i, \tilde{q}_i)$ should be zero by the definition of the adjoint operator.

For the present problem (blowing/suction at the wall),

$$B = \int_{\partial\Omega} [q_2 \tilde{S}_2 + \tilde{q}_1 S_1 + \tilde{q}_3 S_3] d\sigma = 0, \quad (A.15)$$

where

$$\tilde{S}_2 = -\tilde{p}'_l + \frac{1}{Re} \frac{\partial \tilde{q}_2}{\partial y}, \quad S_1 = -\frac{1}{Re} \frac{\partial q_1}{\partial y}, \quad S_3 = -\frac{1}{Re} \frac{\partial q_3}{\partial y}.$$

Using the above relations, we get

$$\begin{aligned} \frac{\mathcal{D}J}{\mathcal{D}\phi} \hat{\phi} &= \int_0^T \int_{\partial\Omega} [(-Re \tilde{q}_1 S_1 - Re \tilde{q}_3 S_3) + \alpha \phi \hat{\phi}] d\sigma dt \\ &= \int_0^T \int_{\partial\Omega} \hat{\phi} [-Re \tilde{p}'_l + \frac{\partial \tilde{q}_2}{\partial y} + \alpha \phi] d\sigma dt. \end{aligned} \quad (A.16)$$

If J attains its minimum at $\bar{\phi}$, then we necessarily have $(\mathcal{D}J/\mathcal{D}\phi) \hat{\phi} = 0$ for every $\hat{\phi}$ in $L^2(0, T; H)$, that is to say

$$\bar{\phi} = -\frac{1}{\alpha} \frac{\partial \tilde{q}_2}{\partial y}|_w + \frac{Re}{\alpha} \tilde{p}'_l|_w. \quad (A.17)$$

Using the continuity equation, $\frac{\partial \tilde{q}_2}{\partial y} = -\frac{\partial \tilde{q}_1}{\partial x} - \frac{\partial \tilde{q}_3}{\partial z}$, we get

$$\bar{\phi} = \frac{1}{\alpha} \left(\frac{\partial \tilde{q}_1}{\partial x}|_w + \frac{\partial \tilde{q}_3}{\partial z}|_w + Re \tilde{p}'_l|_w \right).$$

Substituting the boundary conditions (A.11) of the linearized adjoint state equations into the above equation, we finally get

$$\bar{\phi} = \frac{1}{2\alpha} \left[\frac{\partial}{\partial x} \frac{\partial \bar{u}}{\partial y} \Big|_w + \frac{\partial}{\partial z} \frac{\partial \bar{w}}{\partial y} \Big|_w \right] + \frac{Re}{\alpha} \bar{p}'_l \Big|_w. \quad (A.18)$$

Note that the initial condition of the linearized adjoint state is given at $t = T$ rather than at $t = 0$, i.e. $\tilde{q}_i(x, y, z, t = T) = 0$. This condition is obtained from the definition of the adjoint operator, i.e.,

$$\begin{aligned} \int_0^T \frac{\partial q_i}{\partial t} \tilde{q}_i dt &= \int_0^T \frac{\partial}{\partial t} q_i \tilde{q}_i - q_i \frac{\partial \tilde{q}_i}{\partial t} dt \\ &= \int_0^T - q_i \frac{\partial \tilde{q}_i}{\partial t} dt + [q_i \tilde{q}_i]_0^T \\ &= \int_0^T - q_i \frac{\partial \tilde{q}_i}{\partial t} dt + q_i(t = T) \tilde{q}_i(t = T) - q_i(t = 0) \tilde{q}_i(t = 0). \end{aligned}$$

The boundary terms at $t = 0$ and T , i.e. $q_i(t = T) \tilde{q}_i(t = T) - q_i(t = 0) \tilde{q}_i(t = 0)$, should disappear with a proper choice of the boundary condition of the linearized adjoint state \tilde{q}_i . Since $q_i(t = 0) = 0$, we must set $\tilde{q}_i(t = T) = 0$ in order for the boundary terms to disappear. Hence the time marching of the linearized adjoint state can only be done backward in time from $\tilde{q}_i(t = T) = 0$. Due to this restriction, one has to *store* all the velocity and linearized adjoint velocity fields in the time interval $[0, T]$ to solve both the Navier-Stokes equations and the linearized adjoint Navier-Stokes equations *iteratively*. This is impractical with current computer resources.

We also have tested other cost functions

$$J_1(\phi) = \int_0^T \int_{\partial\Omega} \frac{1}{4} \left[\left(\frac{\partial u}{\partial y} \right)_w^2 \right] d\sigma dt + \frac{\alpha}{2} \int_0^T \int_{\partial\Omega} \phi^2 d\sigma dt, \quad (A.19)$$

$$J_2(\phi) = \int_0^T \int_{\partial\Omega} \frac{1}{4} \left[\left(\frac{\partial w}{\partial y} \right)_w^2 \right] d\sigma dt + \frac{\alpha}{2} \int_0^T \int_{\partial\Omega} \phi^2 d\sigma dt, \quad (A.20)$$

$$J_3(\phi) = \int_0^T \int_{\partial\Omega} \frac{1}{4} \left[\left(\frac{\partial U}{\partial y} \right)_w^2 \right] d\sigma dt + \frac{\alpha}{2} \int_0^T \int_{\partial\Omega} \phi^2 d\sigma dt, \quad (\text{A.21})$$

where U is the mean streamwise velocity. The cost functions in equations (A.19) - (A.21) represent the square magnitude of the instantaneous streamwise shear rate, the fluctuating spanwise shear rate, and the mean streamwise shear rate at the wall, respectively. Following the same procedure described in this appendix, we get the following relations derived from the first-order optimality condition for minimizing above the cost functions

for $J_1(\bar{\phi}_1)$,

$$\bar{\phi}_1 = \frac{1}{2\alpha} \left[\frac{\partial}{\partial x} \frac{\partial \bar{u}}{\partial y} \Big|_w \right] + \frac{Re}{\alpha} \bar{p}'_l \Big|_w \quad (\text{A.22})$$

with the adjoint boundary conditions

$$\tilde{q}_1(x, y = \pm\delta, z) = \frac{1}{2} \frac{\partial u}{\partial y} \Big|_w \quad (\text{A.23})$$

$$\tilde{q}_2(x, y = \pm\delta, z) = \tilde{q}_3(x, y = \pm\delta, z) = 0,$$

for $J_2(\bar{\phi}_2)$,

$$\bar{\phi}_2 = \frac{1}{2\alpha} \left[\frac{\partial}{\partial z} \frac{\partial \bar{w}}{\partial y} \Big|_w \right] + \frac{Re}{\alpha} \bar{p}'_l \Big|_w \quad (\text{A.24})$$

with the adjoint boundary conditions

$$\begin{aligned} \tilde{q}_1(x, y = \pm\delta, z) &= \tilde{q}_2(x, y = \pm\delta, z) = 0 \\ \tilde{q}_3(x, y = \pm\delta, z) &= \frac{1}{2} \frac{\partial w}{\partial y} \Big|_w, \end{aligned} \quad (\text{A.25})$$

and for $J_3(\bar{\phi}_3)$,

$$\bar{\phi}_3 = \frac{Re}{\alpha} \tilde{p}'_l|_w \quad (A.26)$$

with the adjoint boundary conditions

$$\tilde{q}_1(x, y = \pm\delta, z) = \frac{1}{2} \frac{\partial U}{\partial y}|_w \quad (A.27)$$

$$\tilde{q}_2(x, y = \pm\delta, z) = \tilde{q}_3(x, y = \pm\delta, z) = 0.$$

It is interesting to note that the optimal input velocity for minimizing the square magnitude of the *mean* shear rate at the wall (drag) only contains the linearized adjoint pressure fluctuations (equation (A.26)). It should be noted that the linearized adjoint pressure fluctuations \tilde{p}'_l , appearing in equations (A.18), (A.22), (A.24) and (A.26), do not necessarily have the same magnitude. It is not clear at this stage which cost function produces the maximum drag reduction. The cost function J_3 is directly related to the skin friction at the wall. However, skin friction may also be minimized indirectly through modification of turbulence structures with other cost functions such as J_2 .

APPENDIX B

DISTRIBUTED CONTROL OF THE BURGERS EQUATION

The Burgers equation with distributed control is given by equation (4.4) in PART II. Crank-Nicholson in time and second-order centered difference in space are used to discretize equation (4.4) in PART II. Analog of equation (3.18) in PART II, then, reads

$$\mathcal{A} u + \mathcal{R}^n(u, f) = 0, \quad (B.1)$$

with $u = u^n$, $f = f^n$, and

$$\begin{aligned} \mathcal{A} u &= u_i^n - \frac{1}{2} \frac{1}{Re} \frac{\Delta t}{\Delta x^2} (u_{i+1}^n - 2u_i^n + u_{i-1}^n), \\ \mathcal{R}^n(u, f) &= \frac{1}{8} \frac{\Delta t}{\Delta x} (u_{i+1}^{n2} - u_{i-1}^{n2}) - \frac{1}{2} \Delta t f_i^n \\ &\quad - u_i^{n-1} + \frac{1}{8} \frac{\Delta t}{\Delta x} (u_{i+1}^{n-12} - u_{i-1}^{n-12}) - \frac{1}{2} \Delta t f_i^{n-1} \\ &\quad - \frac{1}{2} \frac{1}{Re} \frac{\Delta t}{\Delta x^2} (u_{i+1}^{n-1} - 2u_i^{n-1} + u_{i-1}^{n-1}) - \frac{1}{2} \Delta t (\chi_i^n + \chi_i^{n-1}), \end{aligned}$$

where $f_i^n = \alpha_{0,i}^n + \alpha_{1,i}^n \theta_{1,i}^n$, and $i = 2, \dots, I-1$. From equation (4.6) in PART II, the cost function becomes

$$J(e^n) = \frac{l_d}{2} \sum_{i=2}^{I-1} (\alpha_{0,i}^{n2} + \alpha_{1,i}^{n2}) + \frac{m_d}{2} \sum_{i=1}^{I-1} \frac{(u_{i+1}^n - u_i^n)^2}{\Delta x}. \quad (B.2)$$

From equations (B.1) and (B.2), we find

$$\frac{\mathcal{DR}}{\mathcal{D}u} \eta^n = \frac{1}{4} \frac{\Delta t}{\Delta x} (u_{i+1}^n \eta_{i+1}^n - u_{i-1}^n \eta_{i-1}^n),$$

$$\frac{\mathcal{DR}}{\mathcal{D}f} \alpha_1^n \frac{\mathcal{D}\theta_1}{\mathcal{D}u} \eta^n = -\frac{1}{2} \Delta t \alpha_{1,i}^n \kappa_{1,i}^n \eta_i^n,$$

$$\frac{\mathcal{DR}}{\mathcal{D}f} (\hat{\alpha}_0^n + \hat{\alpha}_1^n \theta_1^n) = -\frac{1}{2} \Delta t (\hat{\alpha}_{0,i}^n + \hat{\alpha}_{1,i}^n \theta_{1,i}^n),$$

$$\|Cu^n - \gamma_d\|^2 = \sum_{i=1}^{I-1} \frac{(u_{i+1}^n - u_i^n)^2}{\Delta x},$$

$$< C^*(Cu^n - \gamma_d), \eta^n > = \sum_{i=2}^{I-1} \frac{1}{\Delta x} (-u_{i+1}^n + 2u_i^n - u_{i-1}^n) \eta_i^n,$$

where $\kappa_1 = \frac{\mathcal{D}\theta_1}{\mathcal{D}u}$, and $i = 2, \dots, I-1$. For distributed control, θ_1 is usually taken to be u . In that case, $\kappa_1 = 1$. The analog of equation (3.13) in PART II, then, reads

$$\begin{aligned} & \left(-\frac{1}{4} \frac{\Delta t}{\Delta x} u_{i-1}^n - \frac{1}{2} \frac{1}{Re} \frac{\Delta t}{\Delta x^2} \right) \eta_{i-1}^n + \left(1 + \frac{1}{Re} \frac{\Delta t}{\Delta x^2} - \frac{1}{2} \Delta t \alpha_{1,i}^n \kappa_{1,i}^n \right) \eta_i^n \\ & + \left(\frac{1}{4} \frac{\Delta t}{\Delta x} u_{i+1}^n - \frac{1}{2} \frac{1}{Re} \frac{\Delta t}{\Delta x^2} \right) \eta_{i+1}^n = \frac{1}{2} \Delta t (\hat{\alpha}_{0,i}^n + \hat{\alpha}_{1,i}^n \theta_{1,i}^n), \\ & \eta_1^n = \eta^n(x=0) = 0, \quad \eta_I^n = \eta^n(x=1) = 0, \end{aligned} \quad (B.3)$$

where $i = 2, \dots, I-1$.

Using the property of the discrete adjoint operator (e.g. $\mathcal{A}_{ij}^* = \mathcal{A}_{ji}$) the analog of equation (3.14) in PART II is

$$\begin{aligned} & \left(\frac{1}{4} \frac{\Delta t}{\Delta x} u_i^n - \frac{1}{2} \frac{1}{Re} \frac{\Delta t}{\Delta x^2} \right) \zeta_{i-1}^n + \left(1 + \frac{1}{Re} \frac{\Delta t}{\Delta x^2} - \frac{1}{2} \Delta t \alpha_{1,i}^n \kappa_{1,i}^n \right) \zeta_i^n \\ & + \left(-\frac{1}{4} \frac{\Delta t}{\Delta x} u_i^n - \frac{1}{2} \frac{1}{Re} \frac{\Delta t}{\Delta x^2} \right) \zeta_{i+1}^n = \frac{1}{\Delta x} (-u_{i+1}^n + 2u_i^n - u_{i-1}^n), \\ & \zeta_1^n = \zeta^n(x=0) = 0, \quad \zeta_I^n = \zeta^n(x=1) = 0. \end{aligned} \quad (B.4)$$

where $i = 2, \dots, I - 1$.

The directional derivative of J (equation (3.15) in PART II) is

$$\frac{\mathcal{D}J}{\mathcal{D}e}\hat{e} = \sum_{i=2}^{I-1} (l_d \alpha_{0,i}^n + \frac{1}{2} m_d \Delta t \zeta_i^n) \hat{\alpha}_{0,i}^n + \sum_{i=2}^{I-1} (l_d \alpha_{1,i}^n + \frac{1}{2} m_d \Delta t \theta_{1,i}^n \zeta_i^n) \hat{\alpha}_{1,i}^n. \quad (B.5)$$

The analog of the gradient algorithm equation (3.11) in PART II consists of constructing two sequences $\alpha_0^{n,k}, \alpha_1^{n,k}$, recursively defined by

$$\begin{aligned} \alpha_{0,i}^{n,k+1} &= \alpha_{0,i}^{n,k} - \rho_0 (l_d \alpha_{0,i}^{n,k} + \frac{1}{2} m_d \Delta t \zeta_i^{n,k}), \\ \alpha_{1,i}^{n,k+1} &= \alpha_{1,i}^{n,k} - \rho_1 (l_d \alpha_{1,i}^{n,k} + \frac{1}{2} m_d \Delta t \theta_{1,i}^{n,k} \zeta_i^{n,k}), \end{aligned} \quad (B.6)$$

where k is the iteration index, $\rho_0, \rho_1 > 0$, and $i = 2, \dots, I - 1$.

The sensitivity of the cost function with respect to the control variables can be described by

$$\begin{aligned} \frac{\mathcal{D}J}{\mathcal{D}\alpha_{0,i}}(\alpha_{0,i}^{n,k}, \alpha_{1,i}^{n,k}) &= l_d \alpha_{0,i}^{n,k} + \frac{1}{2} m_d \Delta t \zeta_i^{n,k}, \\ \frac{\mathcal{D}J}{\mathcal{D}\alpha_{1,i}}(\alpha_{0,i}^{n,k}, \alpha_{1,i}^{n,k}) &= l_d \alpha_{1,i}^{n,k} + \frac{1}{2} m_d \Delta t \theta_{1,i}^{n,k} \zeta_i^{n,k}, \end{aligned} \quad (B.7)$$

where $i = 2, \dots, I - 1$.

APPENDIX C

BOUNDARY CONTROL OF THE BURGERS EQUATION

The Burgers equation with boundary control is given by equation (4.7) in PART II. Crank-Nicholson in time and second-order centered difference in space are used to discretize equation (4.7) in PART II. Analog of equation (3.18) in PART II, then, reads

$$\mathcal{A} u + \mathcal{R}^n(u, \psi) = 0, \quad (C.1)$$

with $u = u^n$, $\psi = \psi^n$, and

$$\mathcal{A} u = \begin{cases} u_i^n - \frac{1}{2} \frac{1}{Re} \frac{\Delta t}{\Delta x^2} (u_{i+1}^n - 2u_i^n + u_{i-1}^n), & \text{for } i = 2, \dots, I-1; \\ u_1^n, & \text{for } i = 1; \\ u_I^n, & \text{for } i = I, \end{cases}$$

$$\mathcal{R}^n(u, \psi) = \begin{cases} \frac{1}{8} \frac{\Delta t}{\Delta x} (u_{i+1}^{n-2} - u_{i-1}^{n-2}) \\ \quad - u_i^{n-1} + \frac{1}{8} \frac{\Delta t}{\Delta x} (u_{i+1}^{n-1} - u_{i-1}^{n-1}) \\ \quad - \frac{1}{2} \frac{1}{Re} \frac{\Delta t}{\Delta x^2} (u_{i+1}^{n-1} - 2u_i^{n-1} + u_{i-1}^{n-1}) \\ \quad - \frac{1}{2} \Delta t (\chi_i^n + \chi_i^{n-1}), & \text{for } i = 2, \dots, I-1; \\ -\psi_0^n, & \text{for } i = 1; \\ -\psi_1^n, & \text{for } i = I, \end{cases}$$

where $\psi_j^n = \alpha_{0,j}^n + \alpha_{1,j}^n \theta_{1,j}^n$, and $j = 0, 1$. From equation (4.9) in PART II, the cost function becomes

$$J(e^n) = \frac{l_b}{2} (\alpha_{0,0}^{n-2} + \alpha_{0,1}^{n-2} + \alpha_{1,0}^{n-2} + \alpha_{1,1}^{n-2}) + \frac{m_b}{2} [(\frac{u_2^n - u_1^n}{\Delta x})^2 + (\frac{u_I^n - u_{I-1}^n}{\Delta x})^2]. \quad (C.2)$$

From equations (C.1) and (C.2), we find

$$\frac{\mathcal{DR}}{\mathcal{D}u}(u^n, \psi^n) \eta^n = \begin{cases} \frac{1}{4} \frac{\Delta t}{\Delta x} (u_{i+1}^n \eta_{i+1}^n - u_{i-1}^n \eta_{i-1}^n), & \text{for } i = 2, \dots, I-1; \\ 0, & \text{for } i = 1, I, \end{cases}$$

$$\frac{\mathcal{DR}}{\mathcal{D}\psi} \alpha_1^n \frac{\mathcal{D}\theta_1}{\mathcal{D}u} \eta^n = \begin{cases} 0, & \text{for } i = 2, \dots, I-1; \\ -\alpha_{1,0}^n \kappa_{1,0}^n \frac{\partial \eta^n}{\partial x}(x=0), & \text{for } i = 1; \\ -\alpha_{1,1}^n \kappa_{1,1}^n \frac{\partial \eta^n}{\partial x}(x=1), & \text{for } i = I, \end{cases}$$

$$\frac{\mathcal{DR}}{\mathcal{D}\psi} (\hat{\alpha}_0^n + \hat{\alpha}_1^n \theta_1^n) = \begin{cases} 0 & \text{for } i = 2, \dots, I-1; \\ -(\hat{\alpha}_{0,0}^n + \hat{\alpha}_{1,0}^n \theta_{1,0}^n), & \text{for } i = 1; \\ -(\hat{\alpha}_{0,1}^n + \hat{\alpha}_{1,1}^n \theta_{1,1}^n), & \text{for } i = I, \end{cases}$$

$$\|Cu^n - \gamma_d\|^2 = \left(\frac{u_2^n - u_1^n}{\Delta x}\right)^2 + \left(\frac{u_I^n - u_{I-1}^n}{\Delta x}\right)^2,$$

$$< C^*(Cu^n - \gamma_d), \eta > = < Cu^n - \gamma_d, C\eta >$$

$$= \frac{1}{\Delta x^2} [(u_2^n - u_1^n)(\eta_2^n - \eta_1^n) + (u_I^n - u_{I-1}^n)(\eta_I^n - \eta_{I-1}^n)].$$

Here we assumed that $\theta_1 = \theta_1(\partial u / \partial x)$. Hence $\frac{\mathcal{D}\theta_1}{\mathcal{D}u} \eta = \frac{\mathcal{D}\theta_1}{\mathcal{D}(\partial u / \partial x)} \frac{\mathcal{D}(\partial u / \partial x)}{\mathcal{D}u} \eta = \kappa_1 \frac{\partial \eta}{\partial x}$,

where $\kappa_1 = \frac{\mathcal{D}\theta_1}{\mathcal{D}(\partial u / \partial x)}$. The analog of equation (3.13) in PART II, then, reads

$$\begin{aligned} & \left(-\frac{1}{4} \frac{\Delta t}{\Delta x} u_{i-1}^n - \frac{1}{2} \frac{1}{Re} \frac{\Delta t}{\Delta x^2}\right) \eta_{i-1}^n + \left(1 + \frac{1}{Re} \frac{\Delta t}{\Delta x^2}\right) \eta_i^n \\ & + \left(\frac{1}{4} \frac{\Delta t}{\Delta x} u_{i+1}^n - \frac{1}{2} \frac{1}{Re} \frac{\Delta t}{\Delta x^2}\right) \eta_{i+1}^n = 0, \end{aligned} \tag{C.3}$$

$$\eta_1^n = \eta^n(x=0) = \hat{\alpha}_{0,0}^n + \hat{\alpha}_{1,0}^n \theta_{1,0}^n + \alpha_{1,0}^n \kappa_{1,0}^n \frac{\partial \eta^n}{\partial x}(x=0),$$

$$\eta_I^n = \eta^n(x=1) = \hat{\alpha}_{0,1}^n + \hat{\alpha}_{1,1}^n \theta_{1,1}^n + \alpha_{1,1}^n \kappa_{1,1}^n \frac{\partial \eta^n}{\partial x}(x=1),$$

where $i = 2, \dots, I-1$.

Using the property of the discrete adjoint operator (e.g. $\mathcal{A}_{ij}^* = \mathcal{A}_{ji}$), the analog of equation (3.14) in PART II is

for $i = 3, \dots, I - 2$:

$$\left(\frac{1}{4} \frac{\Delta t}{\Delta x} u_i^n - \frac{1}{2} \frac{1}{Re} \frac{\Delta t}{\Delta x^2}\right) \zeta_{i-1}^n + \left(1 + \frac{1}{Re} \frac{\Delta t}{\Delta x^2}\right) \zeta_i^n + \left(-\frac{1}{4} \frac{\Delta t}{\Delta x} u_i^n - \frac{1}{2} \frac{1}{Re} \frac{\Delta t}{\Delta x^2}\right) \zeta_{i+1}^n = 0,$$

for $i = 1$:

$$\left(1 + \frac{1}{\Delta x} \alpha_{1,0}^n \kappa_{1,0}^n\right) \zeta_1^n + \left(-\frac{1}{4} \frac{\Delta t}{\Delta x} u_1^n - \frac{1}{2} \frac{1}{Re} \frac{\Delta t}{\Delta x^2}\right) \zeta_2^n = \frac{1}{\Delta x^2} (-u_2^n + u_1^n),$$

for $i = 2$:

$$\left(-\frac{1}{\Delta x} \alpha_{1,0}^n \kappa_{1,0}^n\right) \zeta_1^n + \left(1 + \frac{1}{Re} \frac{\Delta t}{\Delta x^2}\right) \zeta_2^n + \left(-\frac{1}{4} \frac{\Delta t}{\Delta x} u_2^n - \frac{1}{2} \frac{1}{Re} \frac{\Delta t}{\Delta x^2}\right) \zeta_3^n = -\frac{1}{\Delta x^2} (-u_2^n + u_1^n),$$

for $i = I - 1$:

$$\left(\frac{1}{4} \frac{\Delta t}{\Delta x} u_{I-1}^n - \frac{1}{2} \frac{1}{Re} \frac{\Delta t}{\Delta x^2}\right) \zeta_{I-2}^n + \left(1 + \frac{1}{Re} \frac{\Delta t}{\Delta x^2}\right) \zeta_{I-1}^n + \left(\frac{1}{\Delta x} \alpha_{1,1}^n \kappa_{1,1}^n\right) \zeta_I^n = \frac{1}{\Delta x^2} (-u_I^n + u_{I-1}^n),$$

for $i = I$:

$$\left(\frac{1}{4} \frac{\Delta t}{\Delta x} u_I^n - \frac{1}{2} \frac{1}{Re} \frac{\Delta t}{\Delta x^2}\right) \zeta_{I-1}^n + \left(1 - \frac{1}{\Delta x} \alpha_{1,1}^n \kappa_{1,1}^n\right) \zeta_I^n = -\frac{1}{\Delta x^2} (-u_I^n + u_{I-1}^n).$$

(C.4)

The directional derivative of J (equation (3.15) in PART II) is

$$\begin{aligned} \frac{\mathcal{D}J}{\mathcal{D}\epsilon} \hat{\epsilon} = & (l_b \alpha_{0,0}^n + m_b \zeta_1^n) \hat{\alpha}_{0,0}^n + (l_b \alpha_{0,1}^n + m_b \zeta_I^n) \hat{\alpha}_{0,1}^n \\ & + (l_b \alpha_{1,0}^n + m_b \zeta_1^n \theta_{1,0}^n) \hat{\alpha}_{1,0}^n + (l_b \alpha_{1,1}^n + m_b \zeta_I^n \theta_{1,1}^n) \hat{\alpha}_{1,1}^n. \end{aligned} \quad (C.5)$$

The analog of the gradient algorithm equation (3.11) in PART II consists of constructing two sequences $\alpha_0^{n,k}, \alpha_1^{n,k}$, recursively defined by

$$\begin{aligned}
\alpha_{0,0}^{n,k+1} &= \alpha_{0,0}^{n,k} - \rho_0(l_b \alpha_{0,0}^{n,k} + m_b \zeta_1^{n,k}), \\
\alpha_{0,1}^{n,k+1} &= \alpha_{0,1}^{n,k} - \rho_0(l_b \alpha_{0,1}^{n,k} + m_b \zeta_I^{n,k}), \\
\alpha_{1,0}^{n,k+1} &= \alpha_{1,0}^{n,k} - \rho_1(l_b \alpha_{1,0}^{n,k} + m_b \zeta_1^{n,k} \theta_{1,0}^{n,k}), \\
\alpha_{1,1}^{n,k+1} &= \alpha_{1,1}^{n,k} - \rho_1(l_b \alpha_{1,1}^{n,k} + m_b \zeta_I^{n,k} \theta_{1,1}^{n,k}),
\end{aligned} \tag{C.6}$$

where k is the iteration index, and $\rho_0, \rho_1 > 0$.

The sensitivity of the cost function with respect to the control variables can be described by

$$\begin{aligned}
\frac{\mathcal{D}J}{\mathcal{D}\alpha_{0,0}}(\alpha_{0,j}^{n,k}, \alpha_{1,j}^{n,k}) &= l_b \alpha_{0,0}^{n,k} + m_b \zeta_1^{n,k}, \\
\frac{\mathcal{D}J}{\mathcal{D}\alpha_{0,1}}(\alpha_{0,j}^{n,k}, \alpha_{1,j}^{n,k}) &= l_b \alpha_{0,1}^{n,k} + m_b \zeta_I^{n,k}, \\
\frac{\mathcal{D}J}{\mathcal{D}\alpha_{1,0}}(\alpha_{0,j}^{n,k}, \alpha_{1,j}^{n,k}) &= l_b \alpha_{1,0}^{n,k} + m_b \zeta_1^{n,k} \theta_{1,0}^{n,k}, \\
\frac{\mathcal{D}J}{\mathcal{D}\alpha_{1,1}}(\alpha_{0,j}^{n,k}, \alpha_{1,j}^{n,k}) &= l_b \alpha_{1,1}^{n,k} + m_b \zeta_I^{n,k} \theta_{1,1}^{n,k},
\end{aligned} \tag{C.7}$$

where $j = 0, 1$.

APPENDIX D

DEPENDENCE OF THE CONTROL ALGORITHM ON THE TIME-DISCRETIZATION METHOD

In this appendix, a semi-implicit method is used to discretize the Burgers equation with boundary control (equation (4.7) in PART II): Adams-Bashforth scheme for the nonlinear term and Crank-Nicholson scheme for the viscous term. The equations corresponding to equations (C.3) and (C.4) become

$$\left(-\frac{1}{2} \frac{1}{Re} \frac{\Delta t}{\Delta x^2}\right) \eta_{i-1}^n + \left(1 + \frac{1}{Re} \frac{\Delta t}{\Delta x^2}\right) \eta_i^n + \left(-\frac{1}{2} \frac{1}{Re} \frac{\Delta t}{\Delta x^2}\right) \eta_{i+1}^n = 0,$$

$$\eta_1^n = \eta^n(x=0) = \hat{\alpha}_{0,0}^n + \hat{\alpha}_{1,0}^n \theta_{1,0}^n + \alpha_{1,0}^n \kappa_{1,0}^n \frac{\partial \eta^n}{\partial x}(x=0), \quad (D.1)$$

$$\eta_I^n = \eta^n(x=1) = \hat{\alpha}_{0,1}^n + \hat{\alpha}_{1,1}^n \theta_{1,1}^n + \alpha_{1,1}^n \kappa_{1,1}^n \frac{\partial \eta^n}{\partial x}(x=1),$$

where $i = 2, \dots, I-1$.

For $i = 3, \dots, I-2$:

$$\left(-\frac{1}{2} \frac{1}{Re} \frac{\Delta t}{\Delta x^2}\right) \zeta_{i-1}^n + \left(1 + \frac{1}{Re} \frac{\Delta t}{\Delta x^2}\right) \zeta_i^n + \left(-\frac{1}{2} \frac{1}{Re} \frac{\Delta t}{\Delta x^2}\right) \zeta_{i+1}^n = 0,$$

for $i = 1$:

$$\left(1 + \frac{1}{\Delta x} \alpha_{1,0}^n \kappa_{1,0}^n\right) \zeta_1^n + \left(-\frac{1}{2} \frac{1}{Re} \frac{\Delta t}{\Delta x^2}\right) \zeta_2^n = \frac{1}{\Delta x^2} (-u_2^n + u_1^n),$$

for $i = 2$:

$$\left(-\frac{1}{\Delta x} \alpha_{1,0}^n \kappa_{1,0}^n\right) \zeta_1^n + \left(1 + \frac{1}{Re} \frac{\Delta t}{\Delta x^2}\right) \zeta_2^n + \left(-\frac{1}{2} \frac{1}{Re} \frac{\Delta t}{\Delta x^2}\right) \zeta_3^n = -\frac{1}{\Delta x^2} (-u_2^n + u_1^n),$$

for $i = I-1$:

$$\left(-\frac{1}{2} \frac{1}{Re} \frac{\Delta t}{\Delta x^2}\right) \zeta_{I-2}^n + \left(1 + \frac{1}{Re} \frac{\Delta t}{\Delta x^2}\right) \zeta_{I-1}^n + \left(\frac{1}{\Delta x} \alpha_{1,1}^n \kappa_{1,1}^n\right) \zeta_I^n = \frac{1}{\Delta x^2} (-u_I^n + u_{I-1}^n),$$

for $i = I$:

$$\left(-\frac{1}{2} \frac{1}{Re} \frac{\Delta t}{\Delta x^2}\right) \zeta_{I-1}^n + \left(1 - \frac{1}{\Delta x} \alpha_{1,1}^n \kappa_{1,1}^n\right) \zeta_I^n = -\frac{1}{\Delta x^2} (-u_I^n + u_{I-1}^n).$$

(D.2)

Note that only the wall velocity gradients are needed to solve the adjoint equation (D.2). This fact is, of course, of crucial importance for the physical implementation of the control algorithm.

APPENDIX E

A FULLY IMPLICIT METHOD FOR THE UNSTEADY INCOMPRESSIBLE NAVIER-STOKES EQUATIONS IN GENERALIZED COORDINATE SYSTEMS

In this appendix, we present a new time-accurate, fully implicit method for the unsteady incompressible Navier-Stokes equations in generalized coordinate systems. Fully implicit methods have been used in solving the unsteady compressible Navier-Stokes equations (Beam & Warming 1978). On the other hand, semi-implicit methods have been used widely for the unsteady incompressible Navier-Stokes equations (Kim & Moin 1985 and Rosenfeld *et al.* 1991). Recently, fully implicit methods have been used for incompressible flows: Soh & Goodrich (1988) time-advanced the Navier-Stokes equations in Cartesian coordinates with a Crank-Nicholson method where a pseudo time was introduced with artificial compressibility in order to satisfy the continuity equation at the advanced time level. Mansour & Hamed (1990) and Sotiropoulos & Abdallah (1990) used an implicit Euler method and showed numerical results mostly for steady state problems. Explicit and semi-implicit methods have been successfully applied to a variety of incompressible flow problems. An implicit method is preferred when the time-step limit imposed by an explicit or semi-implicit stability bound must be significantly less than the time-step limit imposed by the accuracy requirements (i.e. the smallest physical flow time scale).

The small grid size necessary to resolve the smallest spatial scale in turbulent flows significantly restricts the computational time step for numerical stability when an explicit or a semi-implicit method is used. This computational time step may be considerably smaller than any other physical time scales of turbulent flows. For example, the three-dimensional frequency/wave-number power spectrum of wall-pressure fluctuations in turbulent channel flow shows that negligible power resides in the frequency corresponding to two times the computational time step (see figure 9 in Choi & Moin 1990). Furthermore, if the flow geometry contains sharp corners (e.g. riblet tips), rapid variation of flow variables in their vicinity requires dense grid clustering which would restrict the computational time step. A fully implicit method may overcome this restriction with a trade-off of higher operation counts per time step.

The fully implicit method developed herein is based on a fractional-step method (Kim & Moin 1985) in conjunction with a Newton-iterative method to solve the nonlinear momentum equations. The flow field is represented on a staggered grid, and a Poisson equation for the pressure correction is solved to satisfy the continuity equation at every time step. The numerical method is described in section E.1. Section E.2 provides numerical results for turbulent plane channel flow with different *CFL* (Courant-Friedrichs-Lewy) numbers. Also the suitability of a second-order central-difference scheme for direct simulation of turbulent plane channel flow is discussed in section E.2. The convergence of the Newton-iterative method for turbulent flow over riblets is presented in section E.3.

E.1 Numerical method

The governing equations for an incompressible flow are

$$\frac{\partial u_i}{\partial t} + \frac{\partial}{\partial x_j} u_i u_j = -\frac{\partial p}{\partial x_i} + \frac{1}{Re} \frac{\partial}{\partial x_j} \frac{\partial}{\partial x_j} u_i, \quad (E.1)$$

$$\frac{\partial u_i}{\partial x_i} = 0, \quad (E.2)$$

where x_i 's are the Cartesian coordinates, and u_i 's are the corresponding velocity components. All variables are non-dimensionalized by a characteristic velocity and length scale, and Re is the Reynolds number.

Equations (E.1) and (E.2) are written in the conservative form in generalized coordinates as

$$\frac{\partial q^i}{\partial t} + N^i(\mathbf{q}) = -G^i(p) + L_1^i(\mathbf{q}) + L_2^i(\mathbf{q}), \quad (E.3)$$

$$D^i q^i = \frac{\partial q^1}{\partial \eta^1} + \frac{1}{J} \left(\frac{\partial q^2}{\partial \eta^2} + \frac{\partial q^3}{\partial \eta^3} \right) = 0, \quad (E.4)$$

where $\mathbf{q} = (q^1, q^2, q^3)$, N^i is the convection term, $G^i(p)$ is the pressure gradient term, L_1^i and L_2^i are the diffusion terms without and with cross derivatives,

respectively, and D^i is the divergence operator. Here, we introduce generalized coordinates for the wall-normal and spanwise directions (i.e., $(x_2, x_3) \rightarrow (\eta^2, \eta^3)$), and use a Cartesian coordinate for the streamwise direction ($\eta^1 = x_1$). The q^i 's are volume fluxes across the faces of the cells, which are equivalent to using the contravariant velocity components on a staggered grid multiplied by the Jacobian of the coordinate transformation, J (see figure 3 in PART III). Using this choice, the discretized mass conservation can be easily satisfied (Rosenfeld *et al.* 1991). The terms in equation (E.3) are (the summation convention applies),

for $i = 1$,

$$\begin{aligned} N^1 &= \frac{\partial}{\partial \eta^1} q^1 q^1 + \frac{1}{J} \frac{\partial}{\partial \eta^j} q^j q^1, \\ G^1(p) &= \frac{\partial p}{\partial \eta^1}, \\ L_1^1 &= \frac{1}{Re} \left(\frac{\partial}{\partial \eta^1} \frac{\partial}{\partial \eta^1} q^1 + \frac{1}{J} \frac{\partial}{\partial \eta^k} \alpha^{kj} \frac{\partial}{\partial \eta^j} q^1 \right); \quad j = k, \\ L_2^1 &= \frac{1}{Re} \frac{1}{J} \frac{\partial}{\partial \eta^k} \alpha^{kj} \frac{\partial}{\partial \eta^j} q^1; \quad j \neq k, \end{aligned} \tag{E.5}$$

for $i = 2, 3$,

$$\begin{aligned} N^i &= \frac{\partial}{\partial \eta^1} q^1 q^i + \frac{1}{J} \gamma_m^i \frac{\partial}{\partial \eta^j} \frac{1}{J} c_k^m q^k q^j, \\ G^i(p) &= \alpha^{ij} \frac{\partial p}{\partial \eta^j}, \\ L_1^i &= \frac{1}{Re} \left(\frac{\partial}{\partial \eta^1} \frac{\partial}{\partial \eta^1} q^i + \frac{1}{J} \gamma_m^i \frac{\partial}{\partial \eta^k} \alpha^{kj} \frac{\partial}{\partial \eta^j} \frac{1}{J} c_l^m q^l \right); \quad j = k, \\ L_2^i &= \frac{1}{Re} \frac{1}{J} \gamma_m^i \frac{\partial}{\partial \eta^k} \alpha^{kj} \frac{\partial}{\partial \eta^j} \frac{1}{J} c_l^m q^l; \quad j \neq k, \end{aligned} \tag{E.6}$$

where $q^1 = u_1$, $q^j = \gamma_k^j u_k$, $c_k^j = \partial x_j / \partial \eta^k$, $\gamma_k^j = J (c_k^j)^{-1}$, $\alpha^{jk} = J c_j^m c_k^m$,

$J = \sqrt{||c_j^m c_k^m||}$, and $j, k, l, m = 2, 3$.

Rewriting equation (E.3) gives

$$\frac{\partial q^i}{\partial t} = L^i(\mathbf{q}) - N^i(\mathbf{q}) - G^i(p), \quad (E.7)$$

where $L^i = L_1^i + L_2^i$. The integration method used to solve equations (E.7) and (E.4) is based on a fully implicit, fractional step method; all terms in equation (E.7) including cross-derivative diffusion terms are advanced with the Crank-Nicholson method in time, and are resolved with the second-order central-difference scheme in space using a staggered mesh system.

The fully implicit, fractional step method is given by

$$\frac{\hat{q}^i - q^{in}}{\Delta t} = \frac{1}{2} \left(L^i(\hat{\mathbf{q}}) + L^i(\mathbf{q}^n) \right) - \frac{1}{2} \left(N^i(\hat{\mathbf{q}}) + N^i(\mathbf{q}^n) \right), \quad (E.8)$$

$$\frac{q^{in+1} - \hat{q}^i}{\Delta t} = -G^i(\phi^{n+1}), \quad (E.9)$$

with

$$D^i q^{in+1} = 0, \quad (E.10)$$

where ϕ is a scalar to be determined and D^i is the divergence operator defined in equation (E.4). Implicit treatment of all the terms eliminates the numerical stability restriction. Equation (E.8) is a second-order-accurate approximation of equation (E.7) with $G^i(p)$ excluded. By substituting equation (E.9) into equation (E.8), one can show that the overall accuracy of this splitting method is still second order. Note that ϕ is different from the original pressure: in fact,

$$G^i(p^{n+1}) = G^i(\phi^{n+1}) + \frac{\Delta t}{2} \left[-L^i(G(\phi^{n+1})) + N^i(G(\phi^{n+1})) \right], \quad (E.11)$$

where $\mathbf{G} = (G^1, G^2, G^3)$.

An appropriate boundary condition for the intermediate velocity fields (\hat{q}^i) is needed to solve equation (E.8). Using the method suggested by Kim & Moin (1985), the resulting boundary condition for intermediate velocity is

$$\hat{q}^i = q^{i^{n+1}} + \Delta t G^i(\phi^n) + O(\Delta t^2). \quad (E.12)$$

Equations (E.9) and (E.10) can be combined to eliminate $q^{i^{n+1}}$ and thus obtain a Poisson equation for ϕ^{n+1} :

$$D^i G^i(\phi^{n+1}) = \frac{1}{\Delta t} D^i \hat{q}^i. \quad (E.13)$$

This Poisson equation is solved using a multigrid method (Hackbusch 1985). The final velocity field $q^{i^{n+1}}$ is then obtained from equation (E.9).

The discretized nonlinear equation (E.8) can be solved using a Newton-iterative method. [†] From equation (E.8), one gets

$$\begin{aligned} \hat{q}^i + \frac{1}{2} \Delta t (N^i(\hat{\mathbf{q}}) - L^i(\hat{\mathbf{q}})) &= q^{i^n} - \frac{1}{2} \Delta t (N^i(\mathbf{q}^n) - L^i(\mathbf{q}^n)) \\ &\equiv R^{i^n}. \end{aligned} \quad (E.14)$$

Equation (E.14) is rewritten as follows

$$F^i(\hat{\mathbf{q}}) \equiv \hat{q}^i + \frac{1}{2} \Delta t (N^i(\hat{\mathbf{q}}) - L^i(\hat{\mathbf{q}})) - R^{i^n} = 0. \quad (E.15)$$

[†] One may consider using an approximate factorization technique after linearization of the nonlinear momentum equations in order to avoid iterative methods. However, this is feasible only when non-staggered grid systems are used for incompressible Navier-Stokes equations. Also, in the case of generalized coordinates, the cross-derivative diffusion terms must be treated explicitly to avoid an iterative solution technique at each step. Such a method may not be accurate when the time rate of change of the solution is large or when Δt is large because some of the desirable properties of the nonlinear equations may be lost upon linearization. However, the Newton-iterative method described in this appendix retains the nonlinearity of the equations and the factorization error goes to zero when converged. It also has a quadratic convergence when the initial condition is near the solution. The disadvantage of using this Newton-iterative method is the added computational effort at each time step.

Applying the Newton-iterative method to equation (E.15) gives

$$\left\{ \frac{\partial F^i(\hat{\mathbf{q}})}{\partial \hat{q}^j} \right\}^r \delta \hat{q}^{j,r+1} = -F^i(\hat{\mathbf{q}}^r), \quad (\text{E.16})$$

where

$$\frac{\partial F^i(\hat{\mathbf{q}})}{\partial \hat{q}^j} = \delta_{ij} + \frac{1}{2} \Delta t \frac{\partial}{\partial \hat{q}^j} (N^i(\hat{\mathbf{q}}) - L^i(\hat{\mathbf{q}})),$$

and

$$\delta \hat{q}^{j,r+1} = \hat{q}^{j,r+1} - \hat{q}^{j,r},$$

$$F^i(\hat{\mathbf{q}}^r) = \hat{q}^{i,r} + \frac{1}{2} \Delta t (N^i(\hat{\mathbf{q}}^r) - L^i(\hat{\mathbf{q}}^r)) - R^{i,r},$$

and r is the iteration index, and $j = 1, 2, 3$.[†]

Equation (E.16) becomes

$$\left\{ \delta_{ij} + \frac{1}{2} \Delta t \frac{\partial}{\partial \hat{q}^j} (N^i(\hat{\mathbf{q}}) - L_1^i(\hat{\mathbf{q}}) - L_2^i(\hat{\mathbf{q}})) \right\}^r \delta \hat{q}^{j,r+1} = -F^i(\hat{\mathbf{q}}^r). \quad (\text{E.17})$$

Here, we introduce two variables, M_{ij} and Q_{ij} , such that

$$(M_{ij})^r \delta \hat{q}^{j,r+1} = \left\{ \frac{\partial}{\partial \hat{q}^j} (N^i(\hat{\mathbf{q}}) - L_1^i(\hat{\mathbf{q}})) \right\}^r \delta \hat{q}^{j,r+1},$$

$$(Q_{ij})^r \delta \hat{q}^{j,r+1} = \left\{ \frac{\partial}{\partial \hat{q}^j} (-L_2^i(\hat{\mathbf{q}})) \right\}^r \delta \hat{q}^{j,r+1}.$$

The equations for M_{ij} and Q_{ij} are obtained from equations (E.5) and (E.6):

[†] Upon convergence, i.e. when $\hat{\mathbf{q}} = \hat{\mathbf{q}}^{r+1} = \hat{\mathbf{q}}^r$, $F(\hat{\mathbf{q}}) = 0$ and equation (E.15) is satisfied.

For $i = 1$,

$$(M_{1j})^r \delta q^j{}^{r+1} = \frac{\partial}{\partial \eta^1} 2q^{1r} \delta q^1{}^{r+1} + \frac{1}{J} \frac{\partial}{\partial \eta^l} q^{1r} \delta q^l{}^{r+1} + \frac{1}{J} \frac{\partial}{\partial \eta^l} q^{lr} \delta q^1{}^{r+1} \\ - \frac{1}{Re} \left(\frac{\partial}{\partial \eta^1} \frac{\partial}{\partial \eta^1} \delta q^1{}^{r+1} + \frac{1}{J} \frac{\partial}{\partial \eta^k} \alpha^{kn} \frac{\partial}{\partial \eta^n} \delta q^1{}^{r+1} \right); \quad n = k, \quad (E.18)$$

$$(Q_{1j})^r \delta q^j{}^{r+1} = -\frac{1}{Re} \frac{1}{J} \frac{\partial}{\partial \eta^k} \alpha^{kn} \frac{\partial}{\partial \eta^n} \delta q^1{}^{r+1}; \quad n \neq k,$$

for $i = 2, 3$,

$$(M_{ij})^r \delta q^j{}^{r+1} = \frac{\partial}{\partial \eta^1} q^{1r} \delta q^i{}^{r+1} + \frac{\partial}{\partial \eta^1} q^{ir} \delta q^1{}^{r+1} \\ + \frac{1}{J} \gamma_m^i \frac{\partial}{\partial \eta^l} \frac{1}{J} c_k^m q^{kr} \delta q^l{}^{r+1} + \frac{1}{J} \gamma_m^i \frac{\partial}{\partial \eta^l} \frac{1}{J} c_k^m q^{lr} \delta q^k{}^{r+1} \\ - \frac{1}{Re} \left(\frac{\partial}{\partial \eta^1} \frac{\partial}{\partial \eta^1} \delta q^i{}^{r+1} + \frac{1}{J} \gamma_m^i \frac{\partial}{\partial \eta^k} \alpha^{kn} \frac{\partial}{\partial \eta^n} \frac{1}{J} c_l^m \delta q^l{}^{r+1} \right); \quad n = k,$$

$$(Q_{ij})^r \delta q^j{}^{r+1} = -\frac{1}{Re} \frac{1}{J} \gamma_m^i \frac{\partial}{\partial \eta^k} \alpha^{kn} \frac{\partial}{\partial \eta^n} \frac{1}{J} c_l^m \delta q^l{}^{r+1}; \quad n \neq k,$$

(E.19)

where $k, l, m, n = 2, 3$.

Rewriting equation (E.17) gives

$$\left\{ \delta_{ij} + \frac{1}{2} \Delta t \left(M_{ij}^1 + M_{ij}^2 + M_{ij}^3 \right) + \frac{1}{2} \Delta t Q_{ij} \right\}^r \delta q^j{}^{r+1} = -F^i(\hat{q}^r). \quad (E.20)$$

Note that $M_{ij} (= M_{ij}^1 + M_{ij}^2 + M_{ij}^3)$ is split into three parts such that M_{ij}^1 , M_{ij}^2 , and M_{ij}^3 contain the η^1 -, η^2 -, and η^3 - derivatives, respectively, and Q_{ij} contains the cross derivatives.

When equation (E.20) is spatially discretized with the second-order central-difference scheme using a staggered mesh system, Q_{ij} and some terms of M_{ij} lead

to a sparse matrix instead of a tridiagonal matrix. Therefore, terms with Q_{ij} and $M_{\alpha j}(\alpha \neq j)$ are lagged in the iteration process. Using an approximate factorization technique (Beam & Warming 1976), the left hand side of equation (E.20) becomes (no summation on α ; $\alpha = 1, 2$, or 3):

$$\begin{aligned} & \left(1 + \frac{1}{2}\Delta t M_{\alpha\alpha}^1\right)^r \left(1 + \frac{1}{2}\Delta t M_{\alpha\alpha}^2\right)^r \left(1 + \frac{1}{2}\Delta t M_{\alpha\alpha}^3\right)^r \delta q^{\alpha r+1} \\ & = -F^\alpha(\hat{q}^r) - \frac{1}{2}\Delta t \kappa \sum_{l=1}^3 \left(M_{\alpha j}^l\right)^r \delta q^{j*} - \frac{1}{2}\Delta t (Q_{\alpha j})^r \delta q^{j*}, \end{aligned} \quad (E.21)$$

where $\kappa = 1$ for $j \neq \alpha$ and $\kappa = 0$ for $j = \alpha$, and $j = 1, 2, 3$. The δq^{j*} is partially updated during the iteration step (see Step 2 below). Equation (E.21) is an $O(\Delta t^3)$ approximation to equation (E.20). However, it requires inversions of tridiagonal matrices rather than inversion of a large sparse matrix as in the case of equation (E.20). This results in a significant reduction in computing cost and memory.

The CFL (Courant-Friedrichs-Lewy) number can be defined in generalized coordinates

$$CFL = \left[\frac{|q^1|}{\Delta \eta^1} + \frac{1}{J} \left(\frac{|q^2|}{\Delta \eta^2} + \frac{|q^3|}{\Delta \eta^3} \right) \right] \Delta t. \quad (E.22)$$

The steps taken to advance the flow from time step n to $n+1$ are summarized below

Step 1: Start with an initial condition q_0 or the solution of the previous time step q^n .

Step 2: Solve the discretized nonlinear momentum equations using the Newton-iterative method (equation (E.21)) to obtain \hat{q}^{n+1} .

Step 2.1: Start with $\hat{q}^r = \hat{q}^n$ and $\delta \hat{q}^r = \delta \hat{q}^n$.

Step 2.2: Solve equation (E.21) for $\alpha = 1$ with $\delta q^{2*} = \delta q^{2r}$ and $\delta q^{3*} = \delta q^{3r}$ to obtain δq^{1r+1} .

Step 2.3: Solve equation (E.21) for $\alpha = 2$ with $\delta q^{\hat{1}*} = \delta q^{\hat{1}^{r+1}}$ and $\delta q^{\hat{3}*} = \delta q^{\hat{3}^r}$ to obtain $\delta q^{\hat{2}^{r+1}}$.

Step 2.4: Solve equation (E.21) for $\alpha = 3$ with $\delta q^{\hat{1}*} = \delta q^{\hat{1}^{r+1}}$ and $\delta q^{\hat{2}*} = \delta q^{\hat{2}^{r+1}}$ to obtain $\delta q^{\hat{3}^{r+1}}$.

Step 2.5: Update \hat{q}^{r+1} .

Step 2.6: Repeat Steps 2.2 - 2.5 until \hat{q}^{r+1} converges.

Step 2.7: When converged, $\hat{q}^{n+1} = \hat{q}^{r+1}$.

Step 3: Solve the Poisson equation (E.13) with \hat{q}^{n+1} to obtain ϕ^{n+1} .

Step 4: Obtain q^{n+1} using ϕ^{n+1} from equation (E.9).

E.2 Application to turbulent plane channel flow

To assess its accuracy the present fully implicit method was applied to a turbulent plane channel flow. The computation was carried out for a Reynolds number of 4200 based on the laminar centerline velocity U_l and the channel half-width δ . This Reynolds number corresponds to a Reynolds number of about 180 based on the turbulent wall-shear velocity u_τ and the channel half-width δ . For the Reynolds number considered here, the computational box is chosen to be the *minimal flow unit* of Jiménez & Moin (1991); the streamwise and spanwise computational periods are $\pi\delta$ and $0.289\pi\delta$, respectively (roughly 570 and 160 wall units). The grid points used are $16 \times 129 \times 32$ in the x, y and z directions, respectively. Uniform meshes with spacing $\Delta x^+ \approx 35$ and $\Delta z^+ \approx 5$ are used in the streamwise and spanwise directions. A non-uniform mesh of 129 points with hyperbolic tangent distribution is used in the wall-normal direction. The first mesh point away from the wall is at $y^+ \approx 0.1$, and the maximum spacing (at the centerline of the channel) is 8 wall units.

The initial flow field is an instantaneous solution of the Navier-Stokes equations using a semi-implicit method. Starting from this initial velocity field, the governing equations were integrated forward in time until the numerical solutions reached statistically steady states. These equilibrium states were identified by a quasi-periodic behavior of the wall-shear stresses. Once the velocity field reached the statistically steady state, the equations were integrated further in time to obtain

the time average of the various statistical quantities. The total averaging time was about $500\delta/U_l$. We also performed a direct numerical simulation of turbulent plane channel flow using a spectral method at the same Reynolds number, the same computational box, and the same number of grid points as used in the present study. The spectral method used in this study is identical to that of Kim *et al.* (1987). However, in this study, we used a third-order Runge-Kutta time advancement for the convective terms instead of the original Adams-Bashforth method. Therefore, the *CFL* limit of the present spectral method is $\sqrt{3}/\pi (= 0.551)$. The results of the computation with the fully implicit method are compared with those of the spectral computation.

The objectives of the numerical study presented in this section are two-fold: The first is to find the largest computational time step (in wall units) which accurately predicts turbulence statistics in turbulent plane channel flow at a given Reynolds number. The second is to investigate the suitability of the second-order central-difference scheme for direct numerical simulation of turbulent channel flow.

E.2.1 Effect of the *CFL* number on turbulence statistics

In this section, the effect of the *CFL* number

$$CFL = \left(\frac{|u|}{\Delta x} + \frac{|v|}{\Delta y} + \frac{|w|}{\Delta z} \right) \Delta t$$

on turbulence statistics is investigated. Six different *CFL* numbers, $CFL = 0.5, 1, 2, 3, 4$, and 5 , have been investigated. These *CFL* numbers correspond to the computational time steps in wall units, $\Delta t^+ \approx 0.2, 0.4, 0.8, 1.2, 1.6, 2$, for the specific Reynolds number investigated here. The computational time step for the spectral method is $\Delta t^+ \approx 0.24$ ($CFL = \sqrt{3}/\pi$). Note that the viscous time scale in the sublayer (the Kolmogorov time scale) is $O(1)$ in wall units (Tennekes & Lumley 1972 and Jiménez & Moin 1991).

Figure E.1 shows the convergence of the Newton-iterative method for different *CFL* numbers. It can be seen that lower convergence rates are obtained for larger *CFL* numbers. The relative L_2 norm of $\delta \hat{\mathbf{u}}$, $L_2(\delta \hat{\mathbf{u}}^r)/L_2(\delta \hat{\mathbf{u}}^1)$, for the convergence criterion, is taken to be 10^{-4} ; the value of 10^{-7} gives essentially the same solution.

Figure E.2 shows the turbulence intensities normalized by the wall shear velocity along with the spectral result. The results using the present fully implicit method are shown only for $CFL = 0.5, 1, 2$ and 3 . The calculations with $CFL = 4$ and 5 resulted in laminar flow solutions. The calculations with large CFL numbers overpredict the streamwise fluctuations (u_{rms}) and underpredict the normal and spanwise fluctuations (v_{rms}, w_{rms}) when compared with the spectral result. The u_{rms} and v_{rms} profiles with $CFL = 0.5$ and 1 are in good agreement with the spectral result, but the w_{rms} profile is underpredicted near $y^+ = 40$. This underprediction of w_{rms} near $y^+ = 40$ is also obtained when the number of grid points are doubled in all three directions (figure E.5).

The Reynolds shear stress profile is shown in figure E.3. The result with $CFL = 0.5$ is almost identical with the spectral result. The Reynolds shear stress with $CFL = 1$ shows some underestimation near the peak (5%). The computations with larger CFL numbers underpredict the peak Reynolds shear stress when compared with the spectral result.

Root-mean-square vorticity fluctuations normalized by the mean shear at the wall ($\omega_i \nu / u_\tau^2$) are shown in figure E.4 along with the spectral result. For all CFL numbers the calculations underpredict the streamwise and normal vorticity fluctuations and overpredict the spanwise vorticity fluctuations when near-wall values are compared with the spectral solution. Local maxima of the streamwise and normal vorticity fluctuations are lower than those of the spectral result, which is also obtained even when the number of grid points are doubled (figure E.7) or when a higher-order-accurate finite-difference scheme is used (Rai & Moin 1991).

The turbulence statistics with $CFL = 1$ are nearly identical with those with $CFL = 0.5$ and are in overall agreement with the spectral result. The computational time step for $CFL = 1$ is about $0.05\delta/U_l$ ($0.4\nu/u_\tau^2$). This non-dimensional computational time step is therefore used in the computation of turbulent flow over riblets (see section E.3).

E.2.2 Suitability of a second-order central-difference scheme for a direct numerical simulation of turbulent channel flow

In this section, the accuracy of the second-order central-difference scheme for direct numerical simulation of turbulent channel flow is investigated. The finite-difference results are compared with the spectral results. Advantages of finite-difference schemes over spectral methods are that finite-difference methods can be applied to complex geometries easily and also can readily employ a fully implicit time advancement. Rai & Moin (1991) showed that a high-order-accurate upwind biased finite-difference scheme was a good candidate for direct simulation of turbulent flows. In this study, we investigate the changes of turbulence statistics by doubling the number of grid points in each direction using a second-order central-difference scheme.

The basic simulation uses $16 \times 129 \times 32$ grid points in the x , y and z directions, respectively. The *CFL* number for these finite-differenced computations is fixed at 1. Two additional computations have been carried out: one by doubling N_x and N_z , and one by doubling N_x , N_y and N_z , where N_x , N_y and N_z are the number of grid points in the streamwise, wall-normal and spanwise directions, respectively. Note that, for the spectral method used for comparison, the time accuracy for the advancement of the convective terms is third order and the *CFL* number limit is about 0.55. Hence, some differences in turbulence statistics between the results by the finite-difference and spectral methods may exist due to the different computational time steps and the different orders of time accuracy for the convective terms.

The turbulence intensities normalized by the wall shear velocity are shown in figure E.5 along with the spectral result. There is no clear trend in the turbulence intensity profiles by doubling the number of grid points. This is probably due to the dominance of the time advancement errors over spatial discretization errors. A similar lack of correlation is observed in the Reynolds shear stress profiles (figure E.6). Again, as can be seen from a comparison of figures E.3 and E.6, the disagreement in the peak values of the spectral and fine-mesh finite-difference calculations is due to the time-advancement errors rather than inadequacy of the finite-difference simulations. However, the vorticity fluctuations shown in figure E.7 show a clear trend: as the number of grid points increase, the vorticity fluctuation

profiles approach the spectral result. The vorticity fluctuation profiles with double the number of grid points in all three directions are in good agreement with the spectral result even though there is still a slight underprediction near the peaks of the streamwise and normal vorticity fluctuations. One may suggest, then, that, when a second-order-accurate finite-difference scheme is used, the same number of grid points as the spectral scheme is sufficient to have a spectral resolution of the velocity fluctuations, but the about twice number of grid points in each direction is necessary to have a spectral resolution of the vorticity fluctuations. The same conclusion was reached by Herring *et al.* (1974) in direct numerical simulation of two-dimensional homogeneous turbulence.

E.3 Computational details for turbulent flow over riblets

In this section we present the convergence of the Newton-iterative method in a turbulent flow over riblets. Figure E.8 shows the convergence behavior of the Newton-iterative method for several CFL numbers in the case of the riblet spacing $s^+ \approx 20$ and the ridge angle $\alpha = 60^\circ$ (for more details, see table 1 in PART III). It can be seen that lower convergence rates are obtained for larger CFL numbers.

In section E.2 we found the largest computational time step in wall units which accurately predicted turbulence statistics in plane channel flow at $Re_l = 4200$. We have used this same computational time step, $\Delta t U_l / \delta = 0.05$ ($\Delta t^+ \approx 0.4$), which corresponds to $CFL \approx 3$ in the channel with riblets (equation (E.22)). About 7 Newton iterations are needed to solve the nonlinear momentum equations. The relative L_2 norm of $\delta \hat{q}$, $L_2(\delta \hat{q}^r) / L_2(\delta \hat{q}^1)$, for the convergence criterion is taken to be 10^{-4} . The value of 10^{-6} gives essentially the same solution.

The present fully implicit method allows a larger computational time step with a trade-off of a higher operational count per time step to solve the nonlinear momentum equations. However, it should also be noted that with a conventional semi-implicit method about 70% of total computational time is consumed in solving the Poisson equation (E.13) at each time step. Therefore, fully implicit methods save a significant portion of the CPU time in solving the Poisson equation by allowing larger time steps. The conventional semi-implicit method would have required about a five fold increase in the required CPU time for the present problem.

Turbulence statistics obtained using the present fully implicit methods are presented in PART III and appendix F.

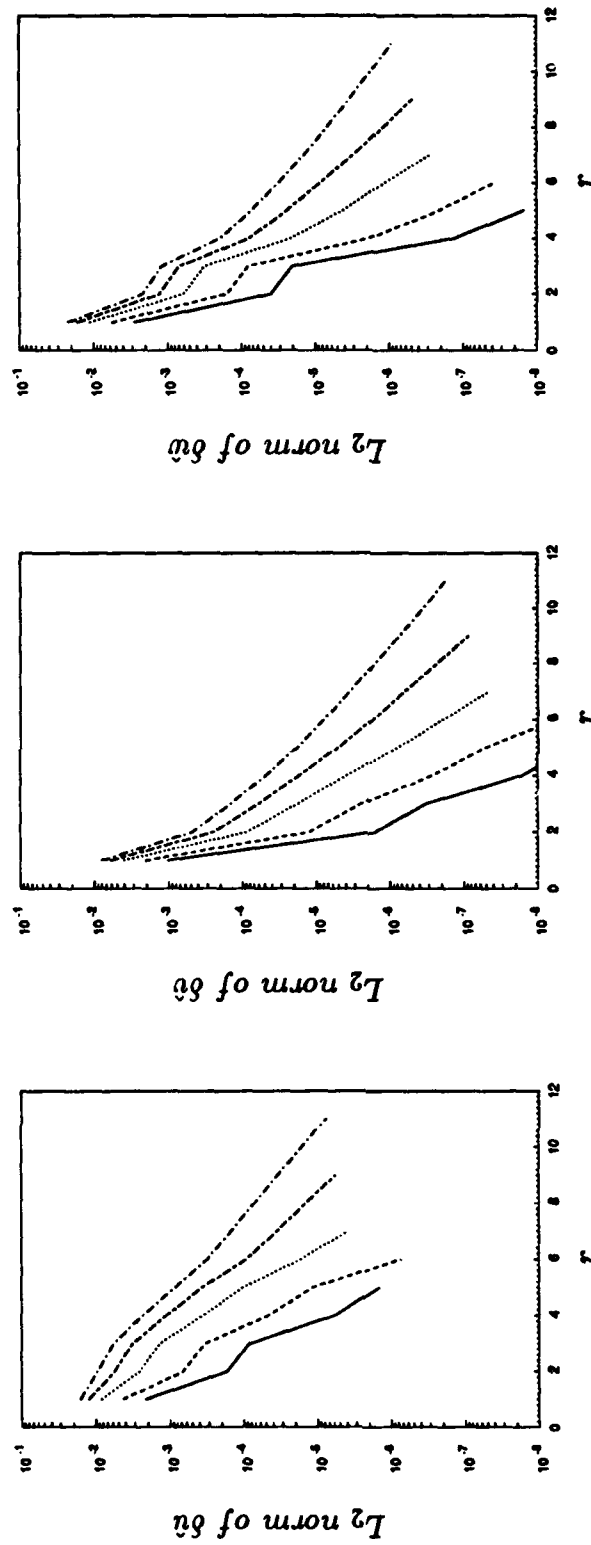


FIGURE E.1. Convergence behavior of the Newton-iterative method for different CFL numbers in turbulent plane channel flow: —, $CFL = 0.5$; ---, $CFL = 1$; , $CFL = 2$; -.-.-, $CFL = 3$; — — —, $CFL = 4$. r denotes the number of Newton iterations.

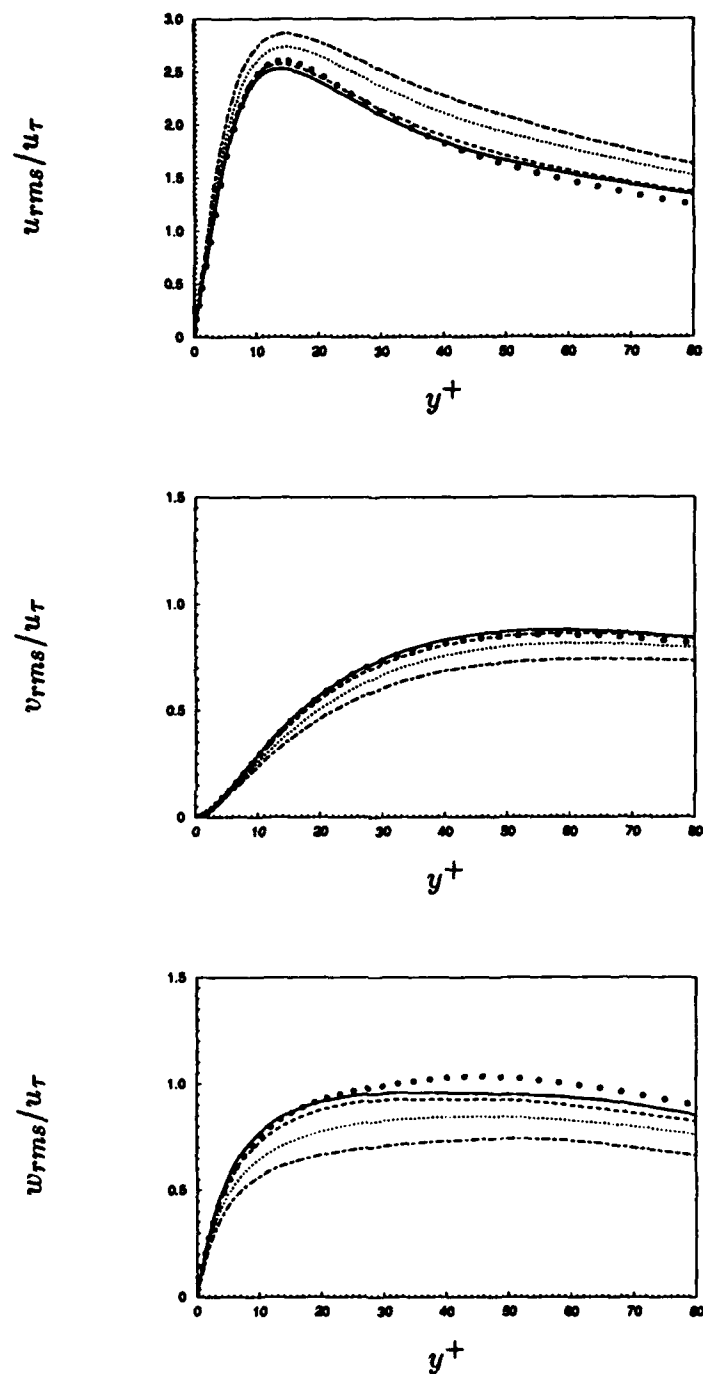


FIGURE E.2. Variation of root-mean-square velocity fluctuations with respect to the *CFL* number: —, *CFL* = 0.5; ----, *CFL* = 1; , *CFL* = 2; -.-.-, *CFL* = 3. Symbol \bullet represents the spectral result.

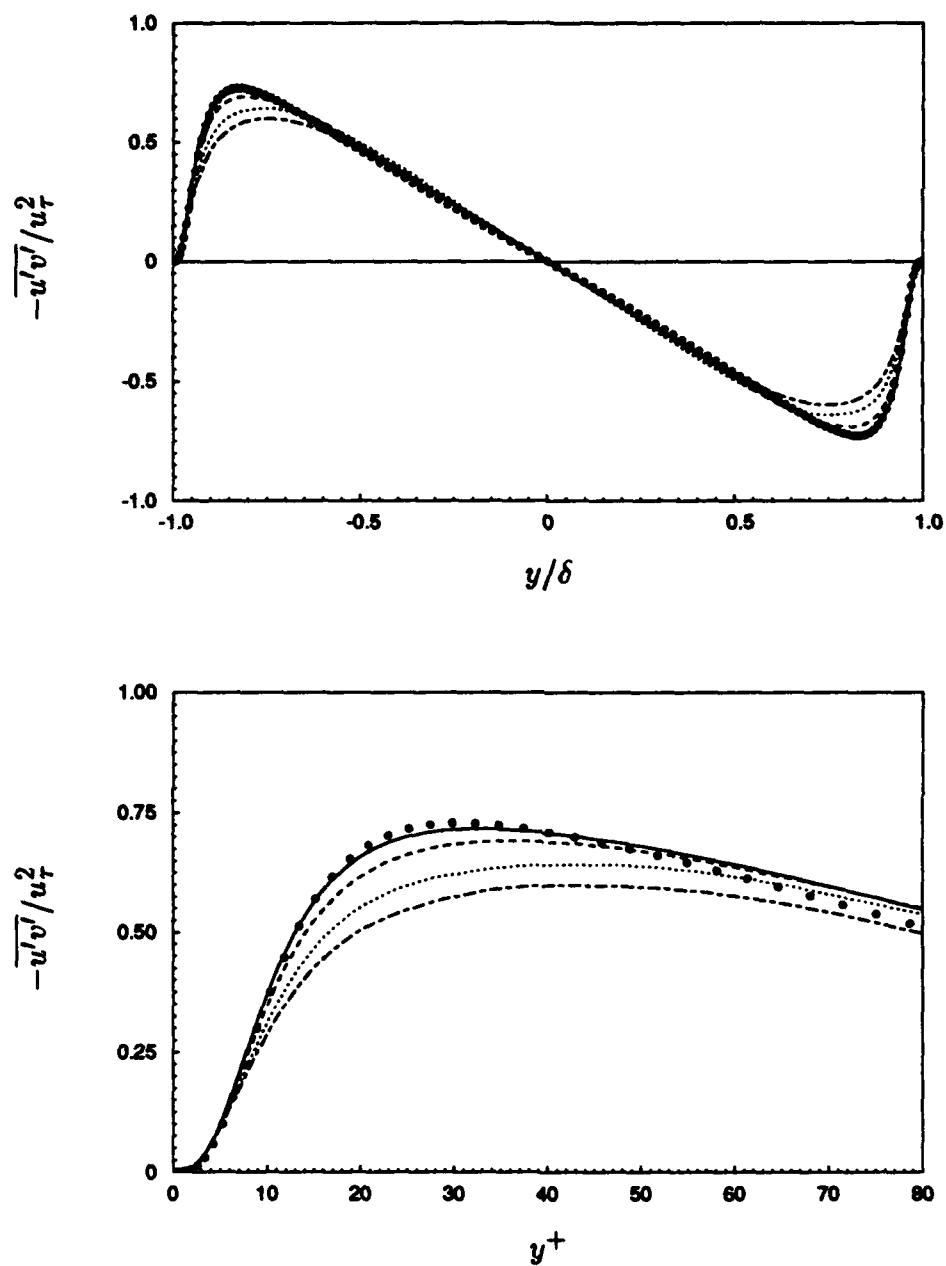


FIGURE E.3. Variation of the Reynolds shear stress with respect to the *CFL* number: —, *CFL* = 0.5; ----, *CFL* = 1; ·····, *CFL* = 2; ---, *CFL* = 3. Symbol • represents the spectral result.

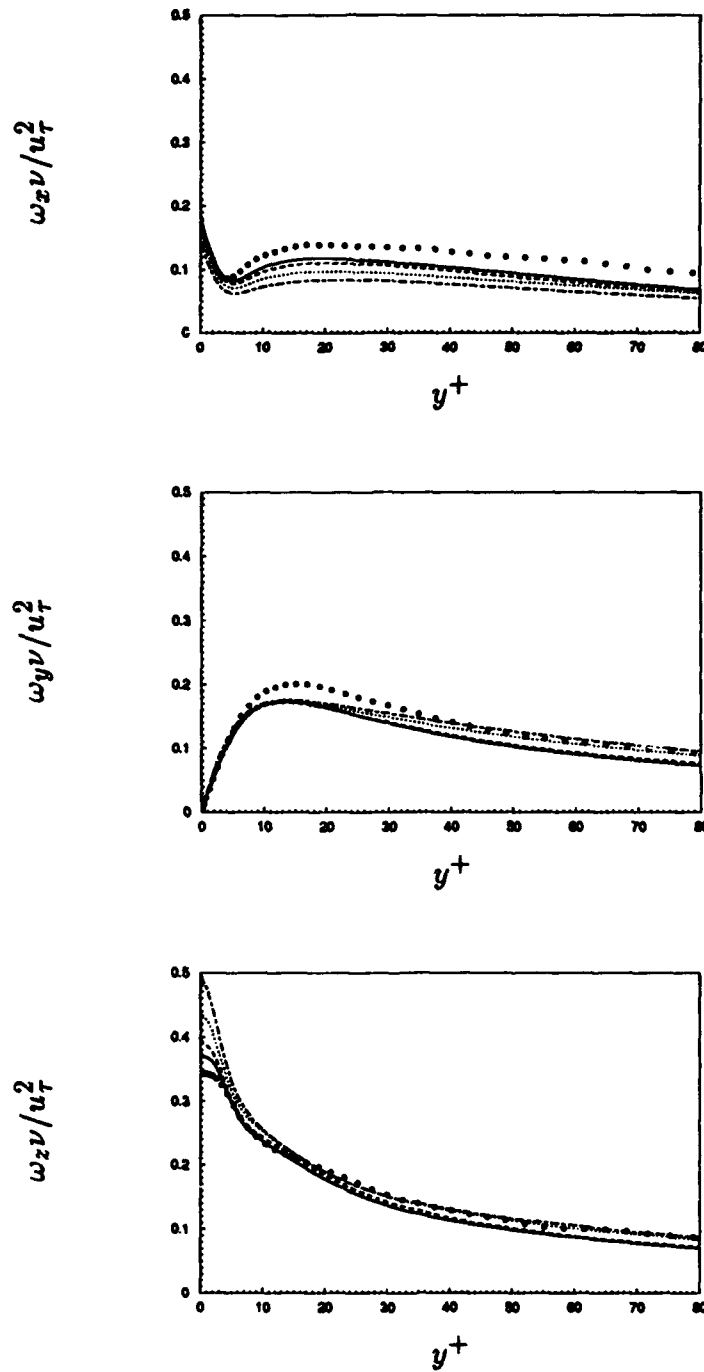


FIGURE E.4. Variation of root-mean-square vorticity fluctuations with respect to the *CFL* number: —, *CFL* = 0.5; ----, *CFL* = 1; ·····, *CFL* = 2; ---, *CFL* = 3. Symbol • represents the spectral result.

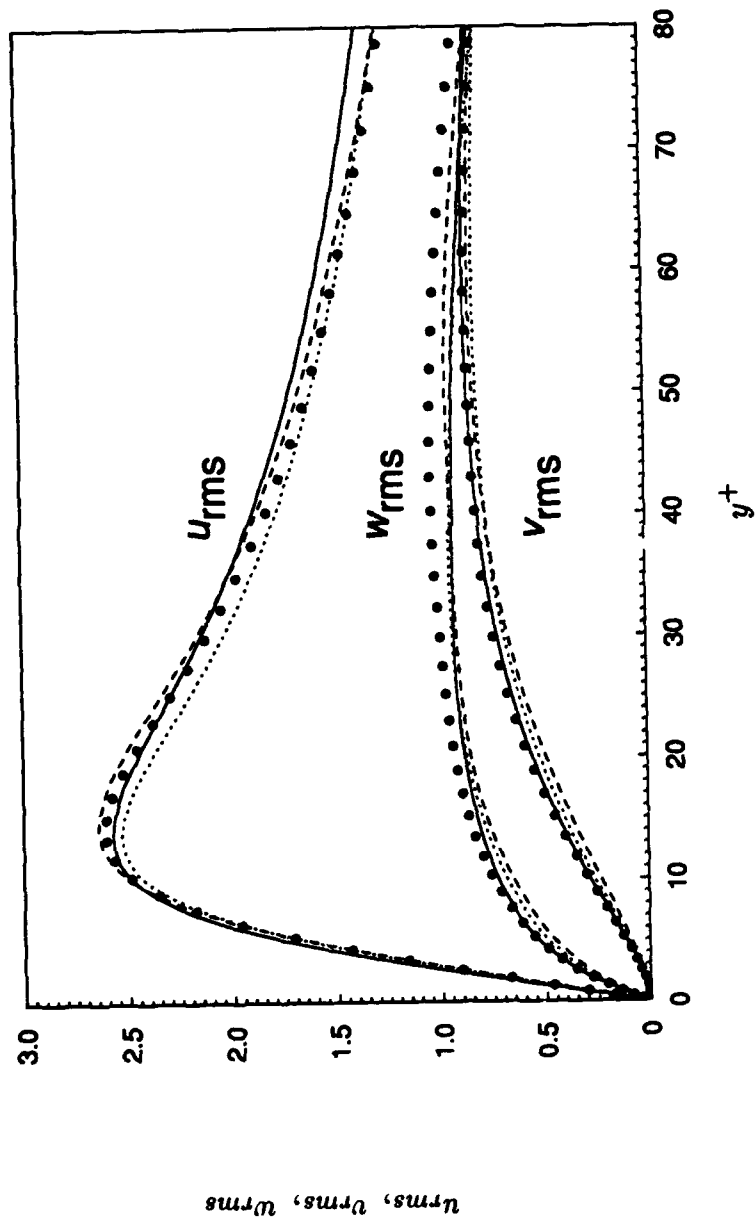


FIGURE E.5. Variation of root-mean-square velocity fluctuations by doubling the number of grid points ($N_x \times N_y \times N_z$): —, $16 \times 129 \times 32$; ---, $32 \times 129 \times 64$; , $32 \times 257 \times 64$. Symbol • represents the spectral result with $16 \times 129 \times 32$.

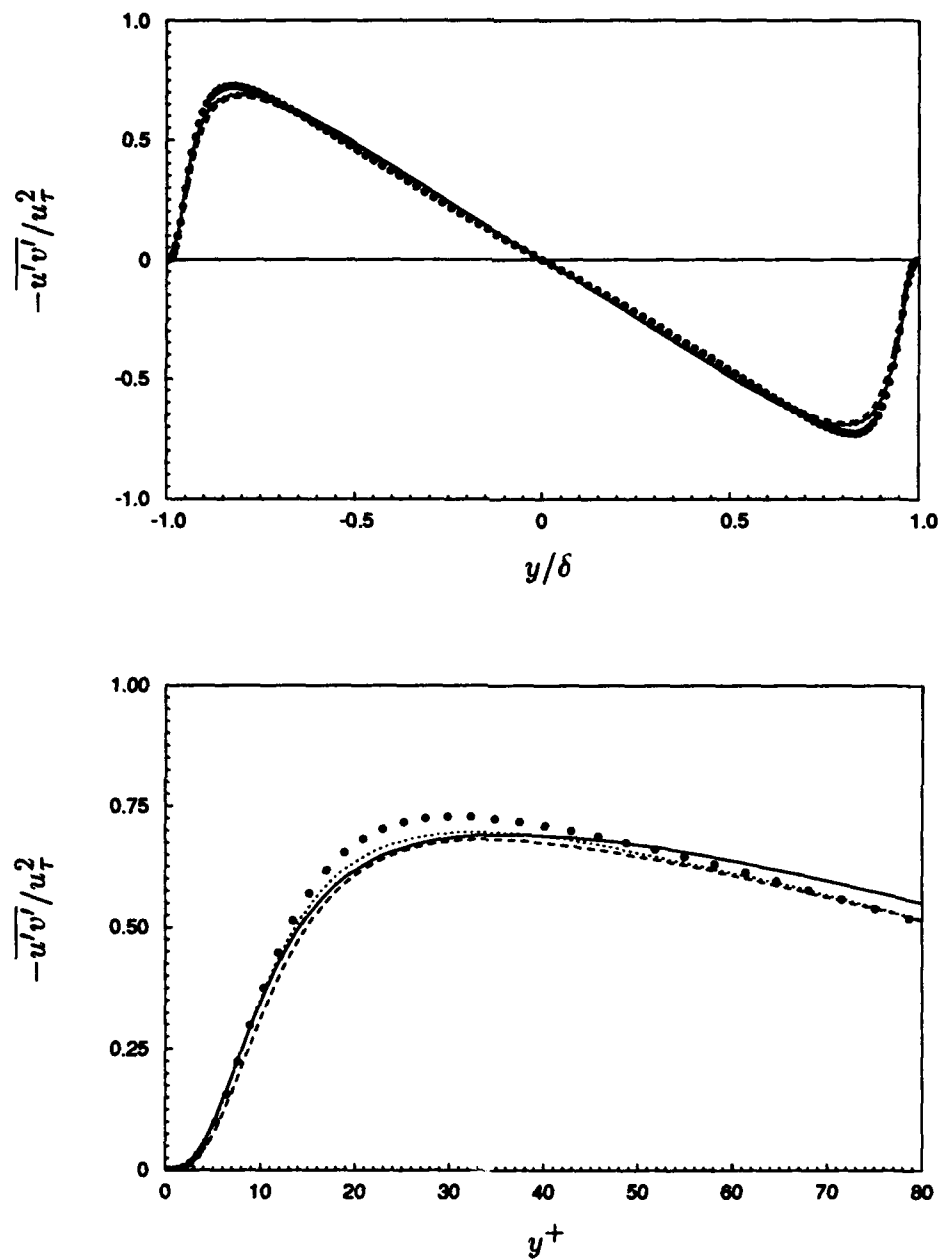


FIGURE E.6. Variation of the Reynolds shear stress by doubling the number of grid points ($N_x \times N_y \times N_z$): —, $16 \times 129 \times 32$; ----, $32 \times 129 \times 64$; ·····, $32 \times 257 \times 64$. Symbol • represents the spectral result with $16 \times 129 \times 32$.

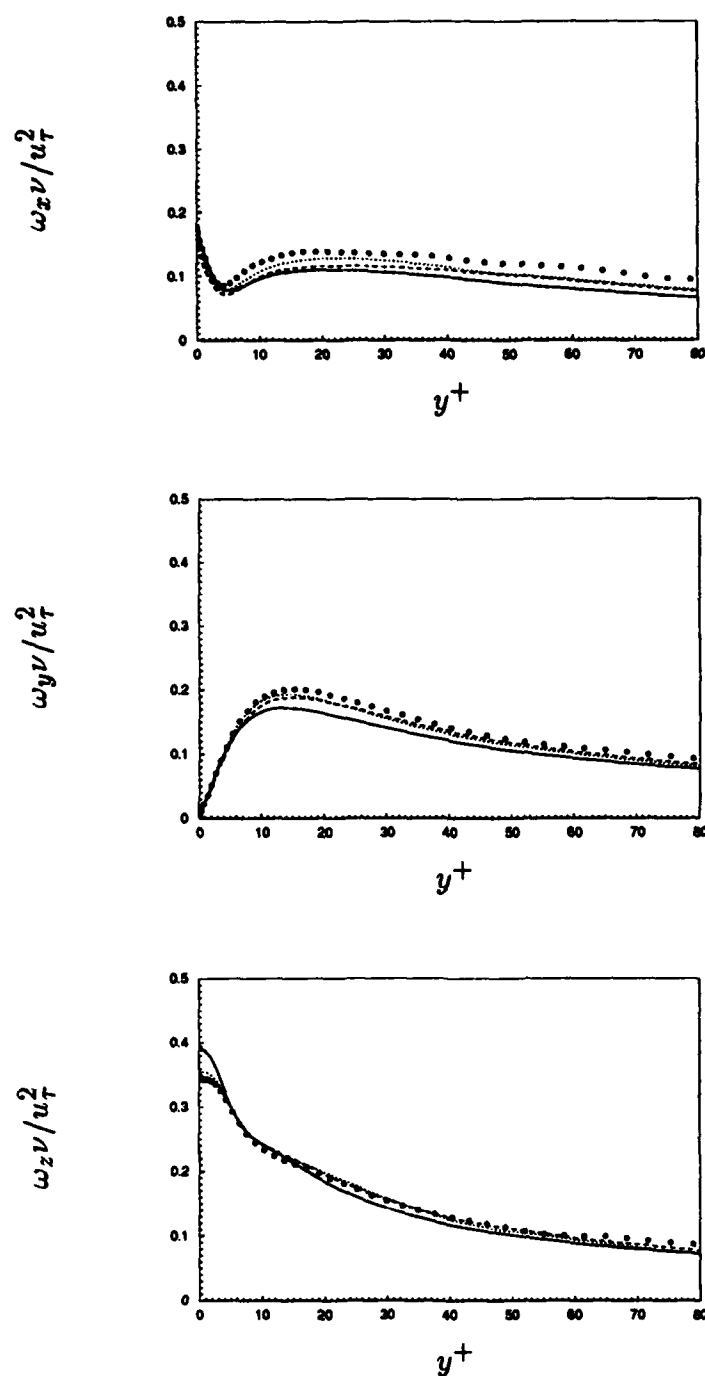


FIGURE E.7. Variation of root-mean-square vorticity fluctuations by doubling the number of grid points ($N_x \times N_y \times N_z$): —, $16 \times 129 \times 32$; ----, $32 \times 129 \times 64$; , $32 \times 257 \times 64$. Symbol • represents the spectral result with $16 \times 129 \times 32$.

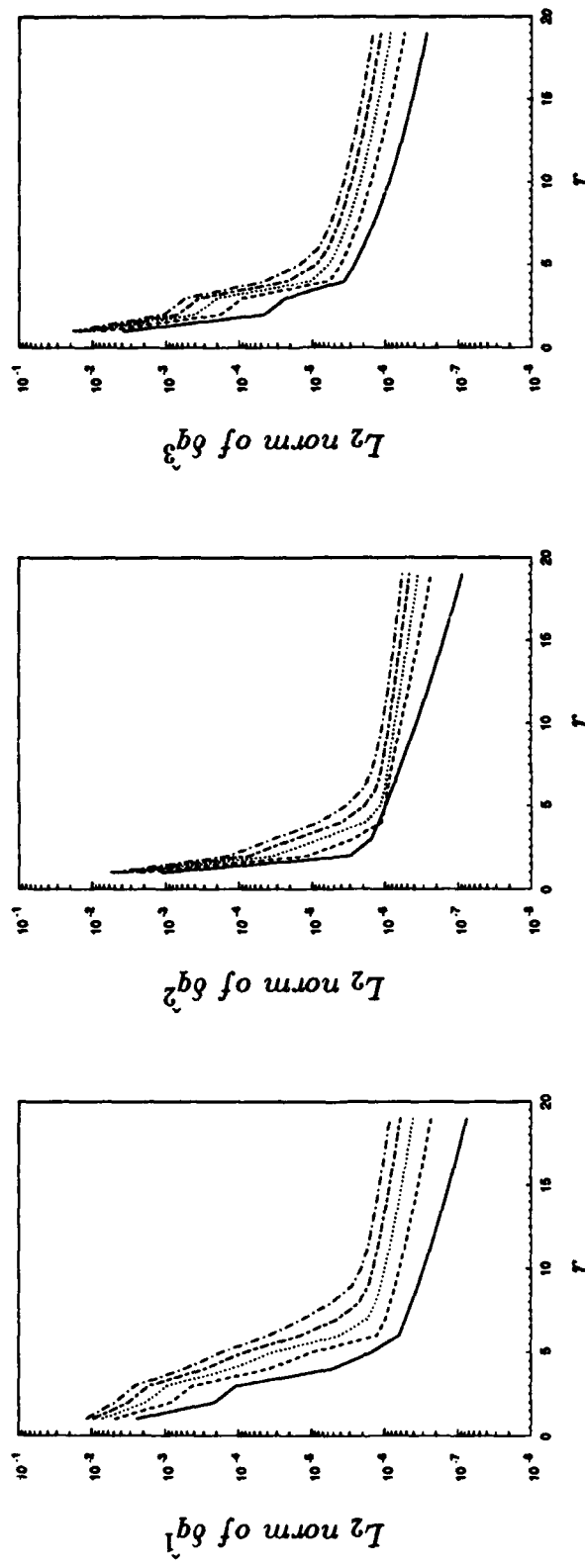


FIGURE E.8. Convergence behavior of the Newton-iterative method for different CFL numbers in turbulent flow over riblets: —, $CFL = 1$; ----, $CFL = 2$; , $CFL = 3$; - - - - , $CFL = 4$; — — — — , $CFL = 5$. The r denotes the number of Newton iterations.

APPENDIX F

TURBULENCE STATISTICS ABOVE THE RIBLETS WITH $\alpha = 45^\circ$ FOR CASES $s^+ \approx 40$ AND $s^+ \approx 20$

In this appendix, we present turbulence statistics above the riblets with $\alpha = 45^\circ$ for cases $s^+ \approx 40$ and $s^+ \approx 20$. These statistical results show nearly the same trend as those above the riblet with $\alpha = 60^\circ$. However, the changes in the magnitude of the turbulence statistics above the riblets with $\alpha = 45^\circ$ are less significant than those above the riblets with $\alpha = 60^\circ$.

Figure F.1 shows the variation of the mean velocity in the transverse plane. As also seen for cases with $\alpha = 60^\circ$, no apparent spanwise variation of the mean velocity is found above $y/\delta \approx -0.9$ in the case $s^+ \approx 20$ or above $y/\delta \approx -0.8$ in the case $s^+ \approx 40$. The spanwise variation of the mean velocity occurs only very near the riblets where, at a given y , the mean velocity above the riblet valley is larger than that above the riblet tip. The wall-shear velocity and the location of the virtual origin for each riblet configuration are listed in table 3 in PART III.

The mean-velocity profiles based on these virtual origins for cases with $\alpha = 45^\circ$ are obtained and compared with those based on other choices of the virtual origins in figure F.2. The mean-velocity profiles by the method of Bechert & Bartenwerfer (1989) and equation (4.4) in PART III are nearly identical in the log-law region. The upward and downward shifts in the log-law are clearly seen for drag-decreasing and drag-increasing cases, respectively.

Turbulence intensity profiles at various spanwise locations are shown in figure F.3. Significant variations of the turbulence intensities occur only very near the riblets in the case $s^+ \approx 20$, while, in the case $s^+ \approx 40$, effects of the riblets penetrate further into the channel. Reduction of all three components of turbulent intensity by the riblets is found in the drag-reducing configuration ($s^+ \approx 20$). Turbulence intensities increase near the riblets in the case $s^+ \approx 40$ (the drag-increasing configuration).

Turbulence intensities normalized by either u_{τ_f} (for the flat plate) or $u_{\tau_r}^*$ (for the plate with riblets) are shown in figure F.4. The y^+ locations of the peak streamwise velocity fluctuations above both the flat plate and the riblets are nearly identical

due to the particular choice of the virtual-origin location (equation (4.4) in PART III). Profiles of v_{rms} and w_{rms} are also nearly identical. The viscous sublayer is significantly modified by the riblets in all configurations.

The Reynolds shear stress $-\overline{u'v'}$, normalized by the mean centerline velocity, is shown in figure F.5. In the case $s^+ \approx 20$, the maximum Reynolds shear stress above the riblets is reduced as compared with that above the flat plate, and there is negligible spanwise variation of the Reynolds shear stress near the riblets. In the case $s^+ \approx 40$, however, the maximum Reynolds shear stress above the riblets is increased above the riblet tip and is nearly unaffected above the riblet valley as compared to the flat plate side. There is also substantial spanwise variation of $-\overline{u'v'}$ near the riblets in this case.

Root-mean-square vorticity fluctuations normalized by the mean centerline velocity and the channel half-width are shown in figure F.6. All three vorticity fluctuation components reach their maximum values at the riblet tip. Significant spanwise variations of the vorticity fluctuations occur only very near the riblets in the case $s^+ \approx 20$, while in the case $s^+ \approx 40$, there is further penetration into the channel.

Reductions of all three components of the vorticity fluctuations by the riblets occur in the drag-reducing configuration ($s^+ \approx 20$). The local maximum of the streamwise vorticity fluctuations above the riblets is reduced as compared with that above the flat plate. The local maximum of the normal vorticity fluctuation is reduced only marginally. In the case $s^+ \approx 40$, vorticity fluctuations are increased above the riblets.

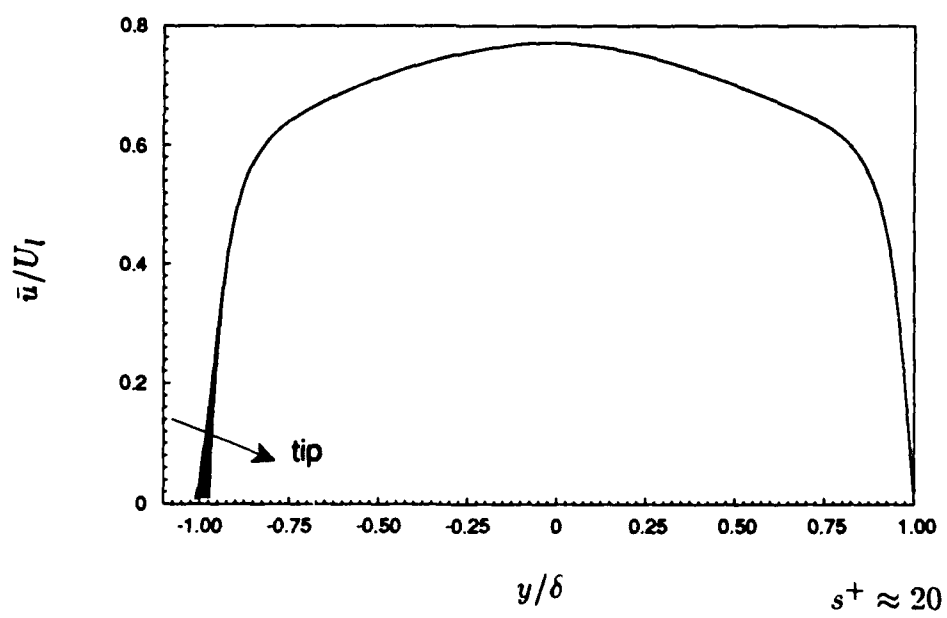
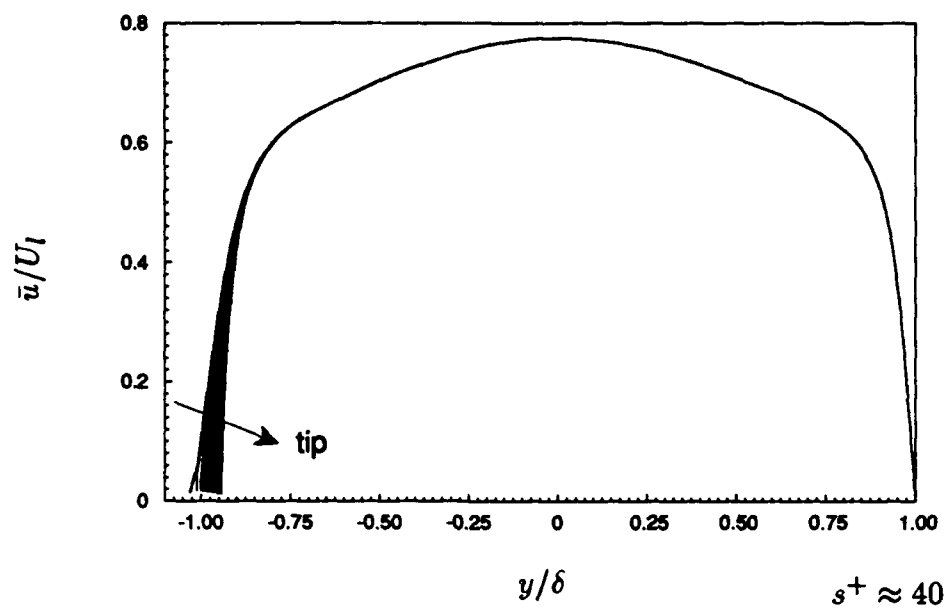


FIGURE F.1. Mean-velocity profiles for cases with $\alpha = 45^\circ$.

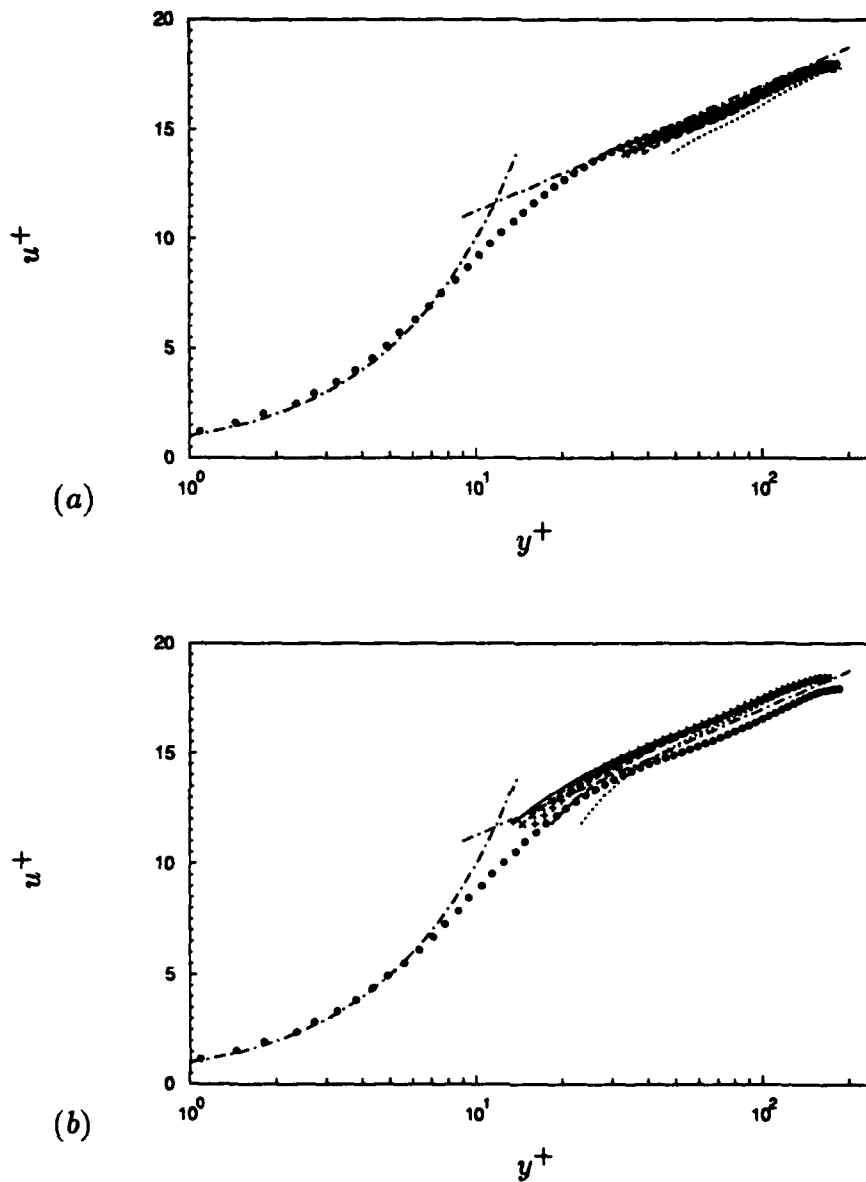


FIGURE F.2. Variation of mean-velocity profiles, normalized by the wall-shear rates u_{τ}^* (equation (4.3) in PART III), with the location of the virtual origin for cases with $\alpha = 45^\circ$: (a) $s^+ \approx 40$; (b) $s^+ \approx 20$. The virtual origin is located: — at the riblet tip; ----, at the midpoint between tip and valley; , at the riblet valley; +, at the location from Bechert & Bartenwerfer (1989); x, at the location from equation (4.4) in PART III. —, Laws of the wall; •, mean velocity over the flat wall.

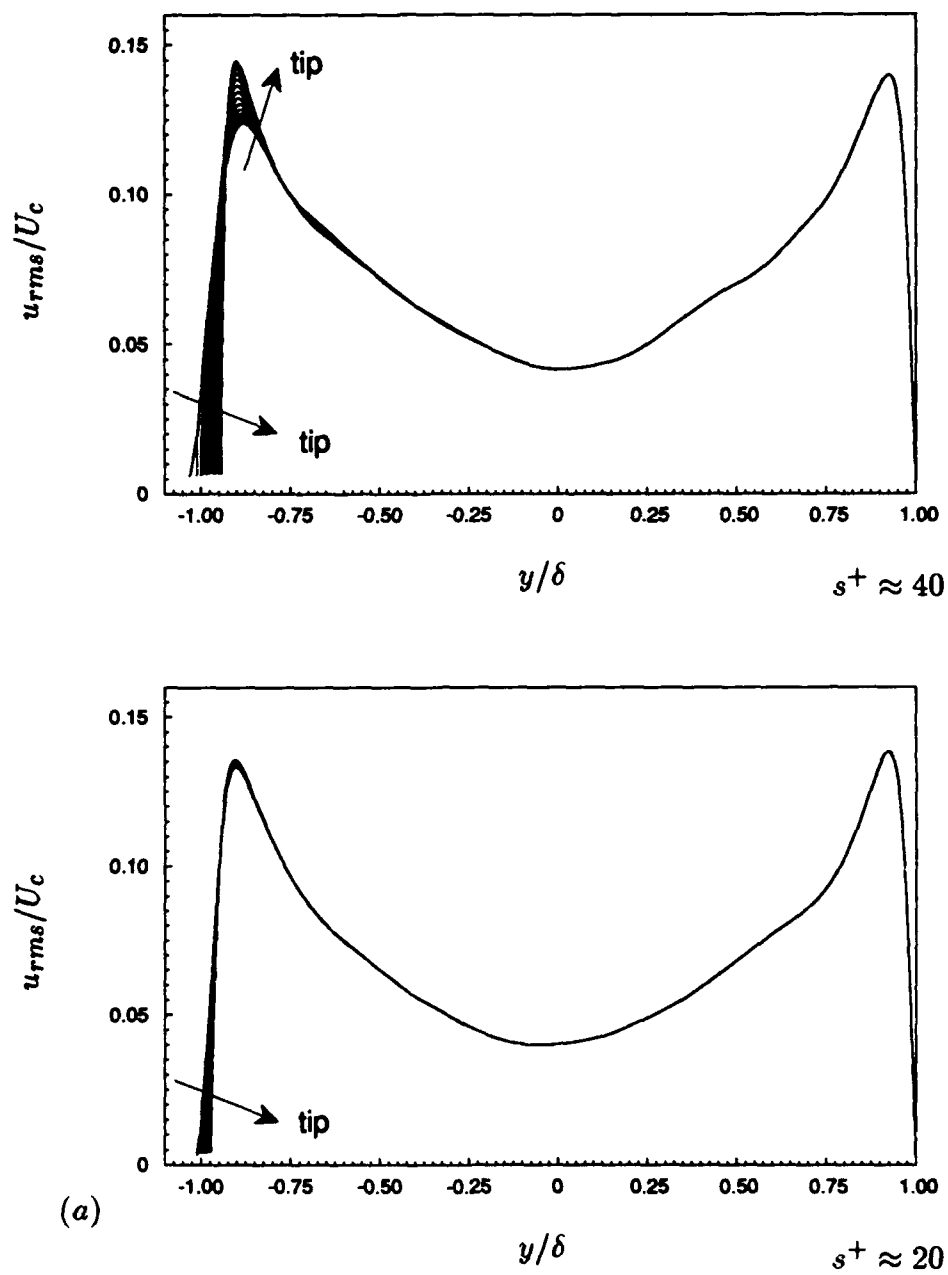


FIGURE F.3. For caption see the following page.

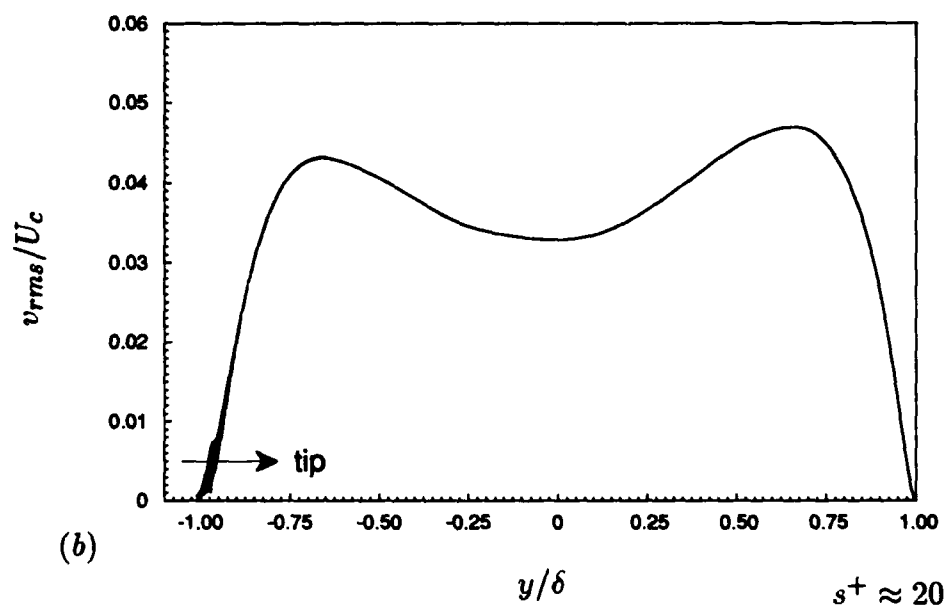
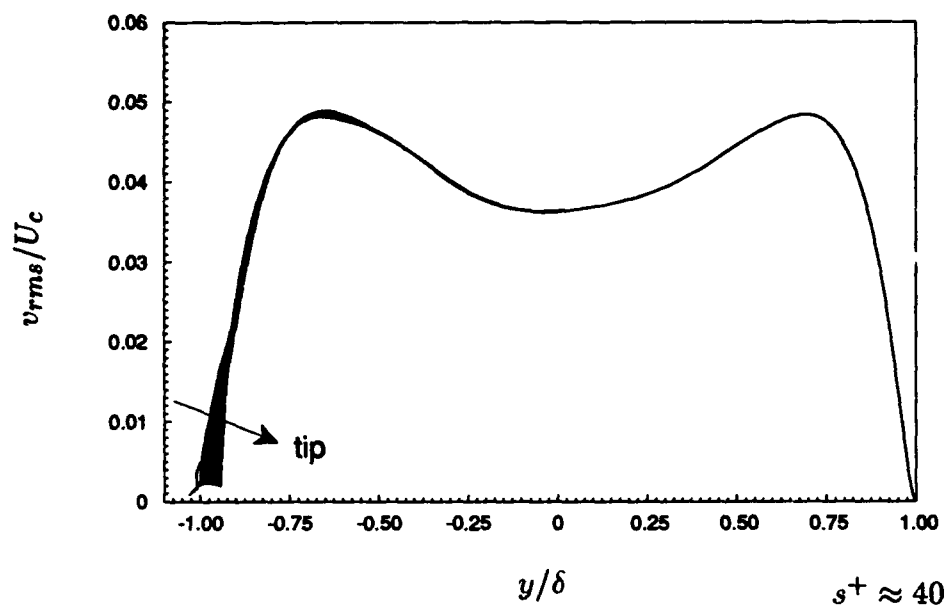


FIGURE F.3. For caption see the following page.

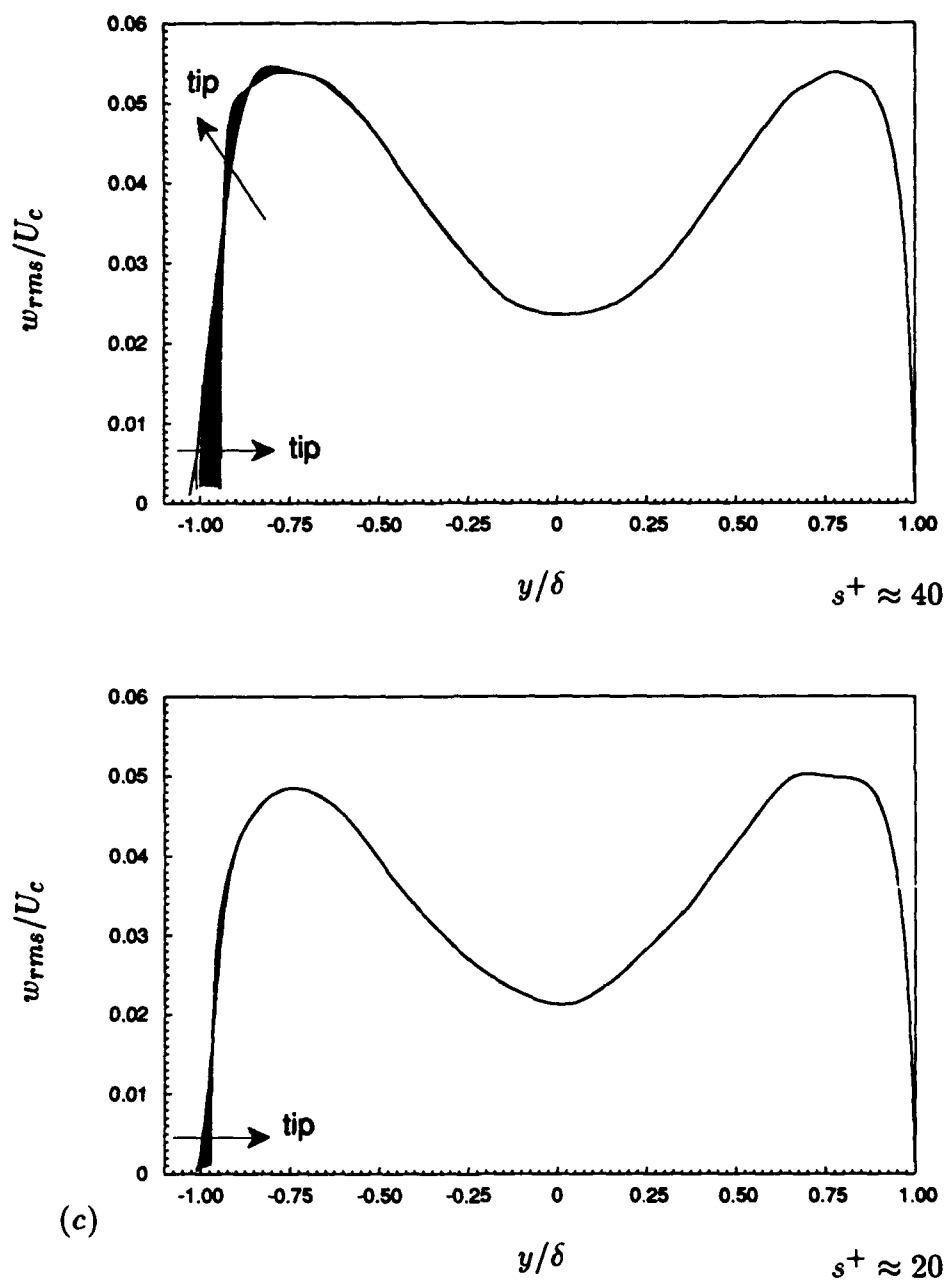


FIGURE F.3. Root-mean-square velocity fluctuations normalized by the mean centerline velocity U_c in global coordinates for cases with $\alpha = 45^\circ$. (a) Streamwise; (b) normal; (c) spanwise velocity fluctuations.

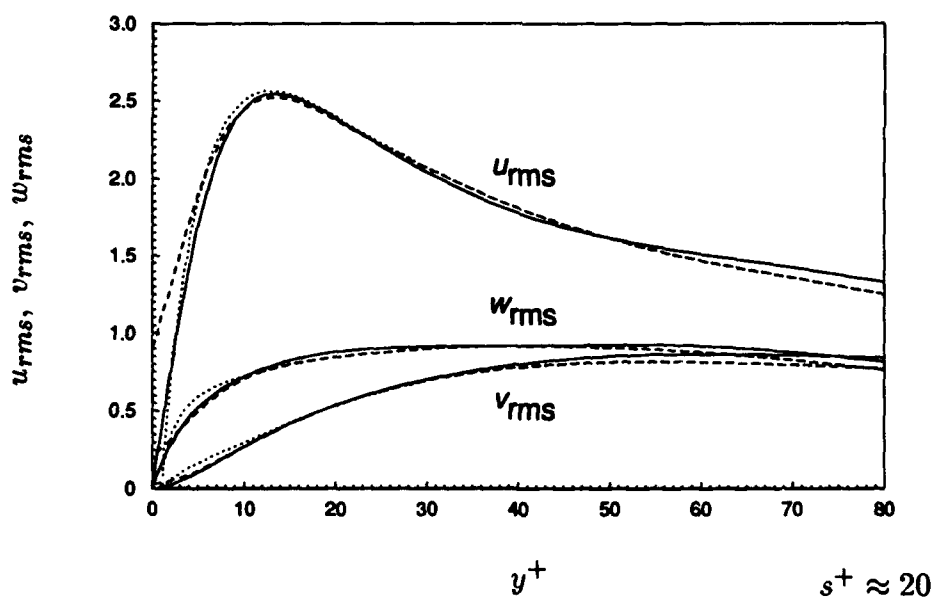
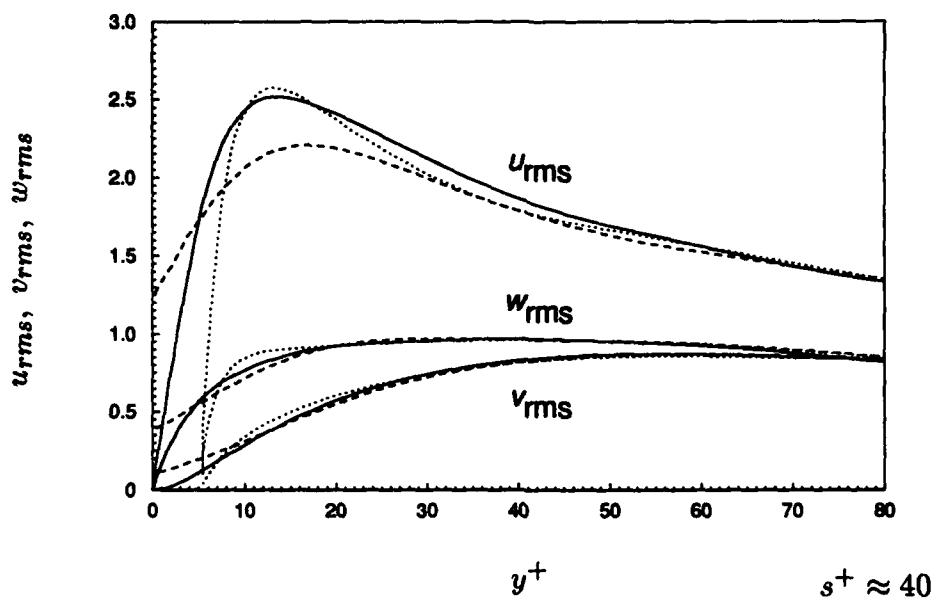


FIGURE F.4. Root-mean-square velocity fluctuations normalized by the wall-shear velocity u_τ in wall coordinates for cases with $\alpha = 45^\circ$: ----, above the riblet valley;, above the riblet tip; —, above the flat plate.

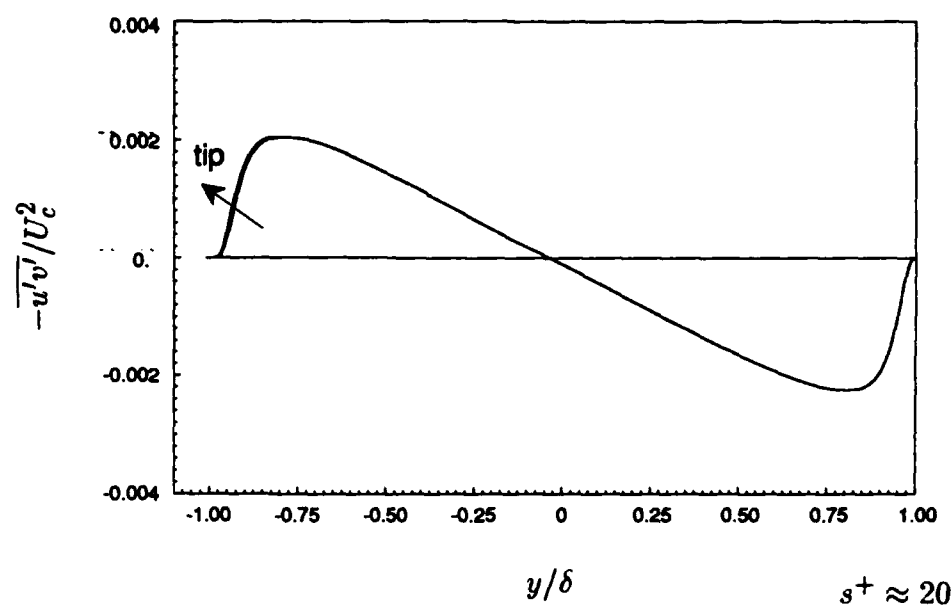
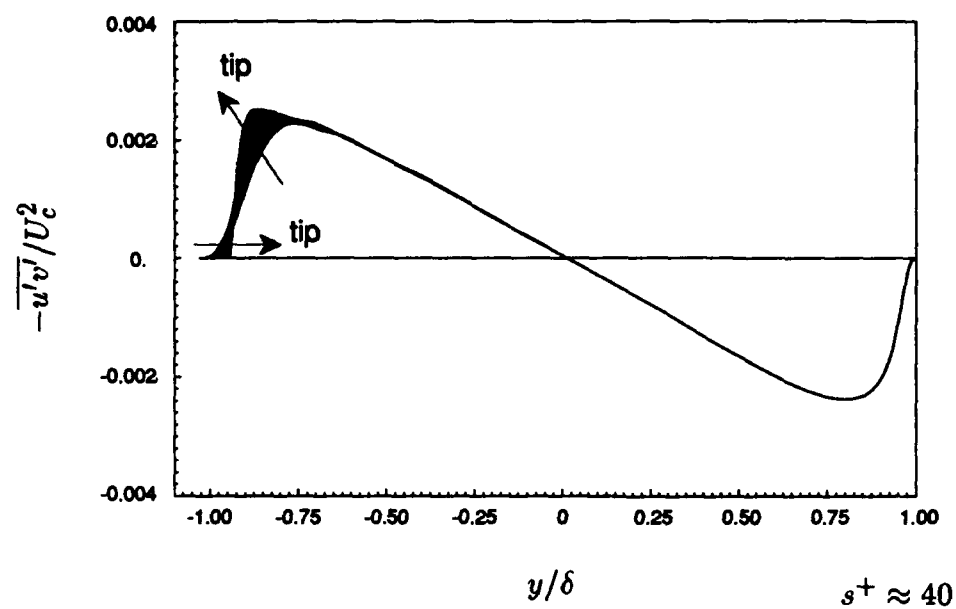


FIGURE F.5. Reynolds shear stress in global coordinates for cases with $\alpha = 45^\circ$.

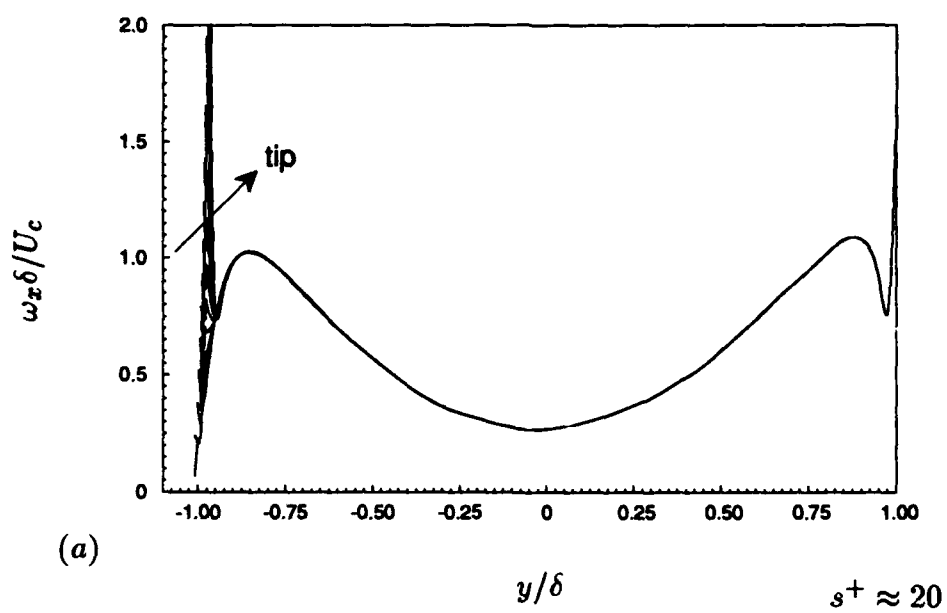
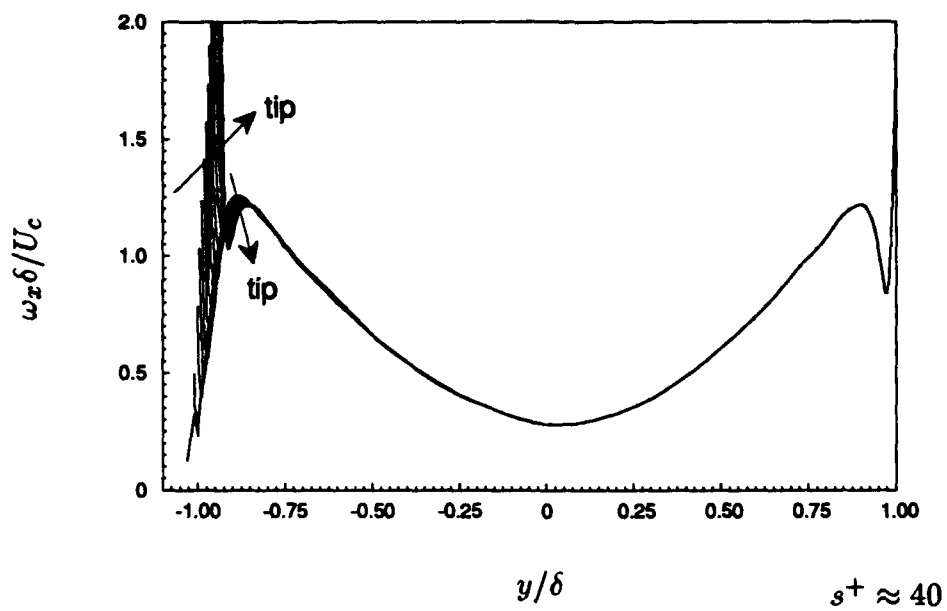


FIGURE F.6. For caption see the following page.

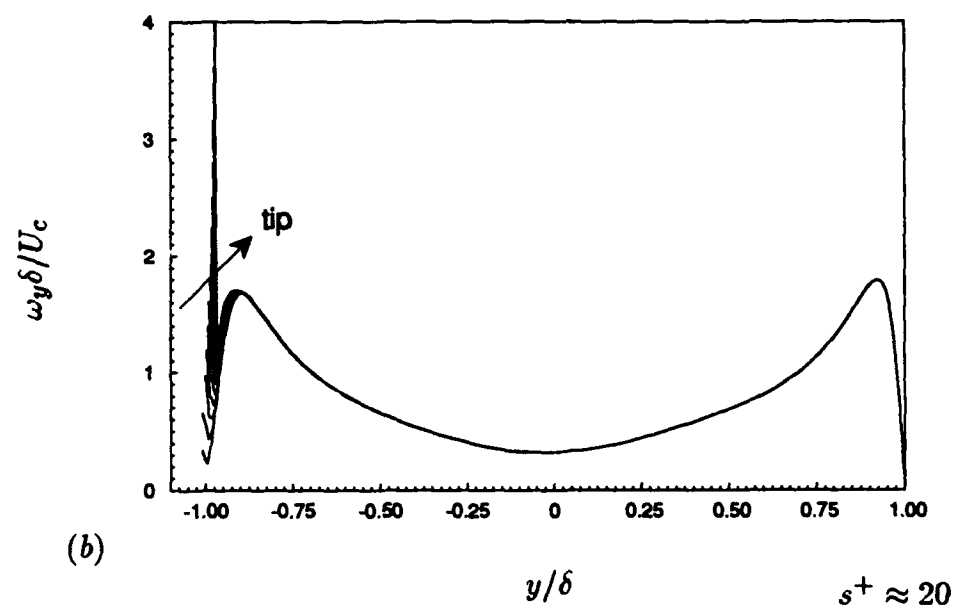
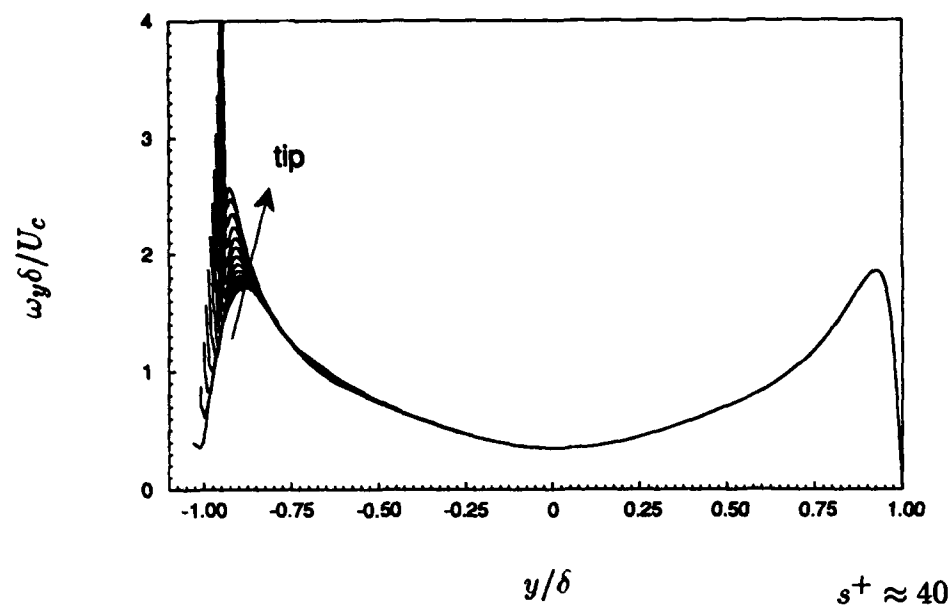


FIGURE F.6. For caption see the following page.

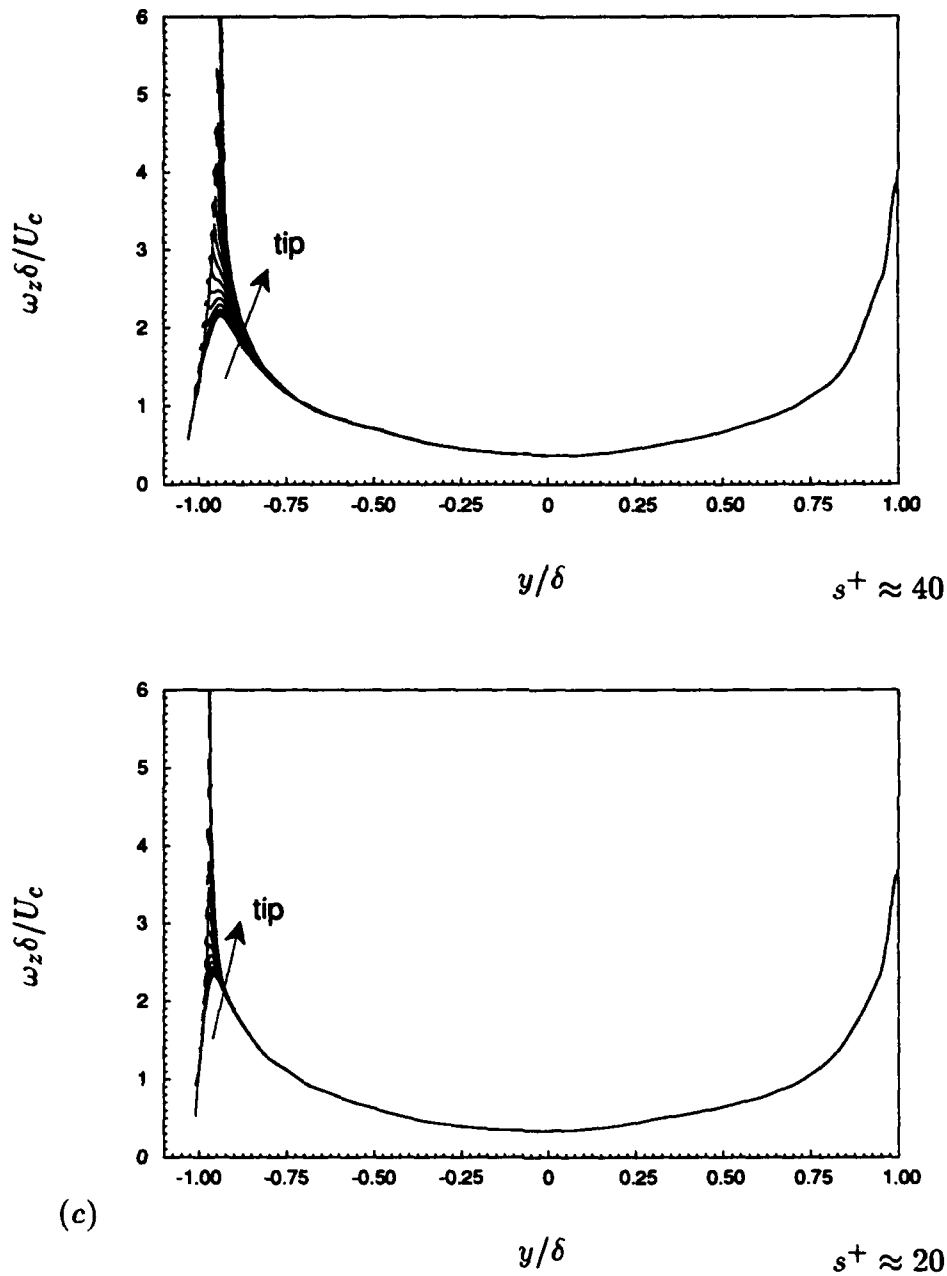


FIGURE F.6. Root-mean-square vorticity fluctuations normalized by the mean centerline velocity U_c and channel half-width δ in global coordinates for cases with $\alpha = 45^\circ$. (a) Streamwise; (b) normal; (c) spanwise vorticity fluctuations.

REFERENCES

- ABERGEL, F. & TEMAM, R. 1990 On some control problems in fluid mechanics. *Theoret. Comput. Fluid Dynamics* **1**, 303.
- ABERGEL, F. & TEMAM, R. 1992 Optimal control of turbulent flows. To appear in the *Optimal Control of Viscous Flows* (ed. S. Sritharan). Frontiers in Applied Mathematics Series, SIAM, Philadelphia.
- ALFREDSSON, P. H., JOHANSSON, A. V. & KIM, J. 1988 Turbulence production near walls: the role of flow structures with spanwise asymmetry. In *Studying Turbulence Using Numerical Simulation Databases*, Proc. 1988 Summer Program of the Center for Turbulence Research, NASA-Ames & Stanford University. pp. 131 - 141.
- BACHER, E. V. & SMITH, C. R. 1985 A combined visualization-anemometry study of the turbulent drag reducing mechanisms of triangular micro-groove surface modifications. *AIAA paper* 85-0548.
- BANACH, A. S. & BAUMANN, W. T. 1990 Gain-scheduled control of nonlinear partial differential equations. *Proc. 29th Conf. on Decision and Control*. pp. 387 - 392.
- BANDYOPADHYAY, P. R. 1986 Review - Mean flow in turbulent boundary layers disturbed to alter skin friction. *J. Fluid Eng.* **108**, 127.
- BARBU, V. 1992 H_∞ boundary control with state feedback; the hyperbolic case. Preprint.
- BEAM, R. M. & WARMING, R. F. 1976 An implicit finite-difference algorithm for hyperbolic systems in conservation law form. *J. Comput. Phys.* **22**, 87.
- BEAM, R. M. & WARMING, R. F. 1978 An implicit factored scheme for the compressible Navier-Stokes equations. *AIAA J.* **16**, 393.
- BECHERT, D. W. & BARTENWERFER, M. 1989 The viscous flow on surfaces with longitudinal ribs. *J. Fluid Mech.* **206**, 105.
- BENHALILOU, M., ANSELMET, F., LIANDRAT, J. & FULACHIER, L. 1991 Experimental and numerical investigation of a turbulent boundary layer over riblets. *Proc. 8th Symp. on Turbulent Shear Flows*. Technical University of Munich. pp. 18.5.1 - 18.5.6.

- BENSOUSSAN, A. & TEMAM, R. 1972 Equations aux dérivées partielles stochastiques non linéaires (I). *Israel J. of Math.* **11**, 95.
- BENSOUSSAN, A. & TEMAM, R. 1973 Equations stochastiques du type Navier-Stokes. *J. Funct. Anal.* **13**, 195.
- BUSHNELL, D. M. & MCGINLEY, C. B. 1989 Turbulence control in wall flows. *Ann. Rev. Fluid Mech.* **21**, 1.
- BYRNES, C. I. & GILLIAM, D. S. 1991 Boundary feedback design for nonlinear distributed parameter systems. *Proc. 30th Conf. on Decision and Control.* pp. 2340 - 2342.
- CANTWELL, B. J. 1981 Organized motion in turbulent flow. *Ann. Rev. Fluid Mech.* **13**, 457.
- CHAMBERS, D. H., ADRIAN, R. J., MOIN, P., STEWART, D. S. & SUNG, H. J. 1988 Karhunen-Loève expansion of Burgers' model of turbulence. *Phys. Fluids* **31**, 2573.
- CHOI, H. & MOIN, P. 1990 On the space-time characteristics of wall-pressure fluctuations. *Phys. Fluids A* **2**, 1450.
- CHOI, H., MOIN, P. & KIM, J. 1991 On the effect of riblets in fully developed laminar channel flows. *Phys. Fluids A* **3**, 1892.
- CHOI, K.-S. 1989 Near-wall structure of a turbulent boundary layer with riblets. *J. Fluid Mech.* **208**, 417.
- CORINO, E. R. & BRODKEY, R. S. 1969 A visual investigation of the wall region in turbulent flow. *J. Fluid Mech.* **37**, 1.
- COUSTOLS, E. & COUSTEIX, J. 1989 Experimental manipulation of turbulent boundary layers in zero pressure gradient flows through external and internal devices. *Proc. 7th Symp. on Turbulent Shear Flows.* Stanford University. pp. 25.3.1 - 25.3.6.
- COUSTOLS, E. & SAVILL, A. M. 1992 Turbulent skin-friction drag reduction by active and passive means. In *Special course on skin friction drag reduction* (ed. J. Cousteix), AGARD Report 786.
- FINLAYSON, B. A. 1972 *The Method of Weighted Residuals and Variational Principles.* Academic Press.

- FOIAS, C. & TANNENBAUM, A. 1989 Weighted optimization theory for nonlinear systems. *SIAM J. on Control and Opt.* **27**, 842.
- GALLAGHER, J. A. & THOMAS, A. S. W. 1984 Turbulent boundary layer characteristics over streamwise grooves. *AIAA Paper* 84-2185.
- GAUDET, L. 1987 An assessment of the drag reduction properties of riblets and the penalties of off-design conditions. *RAE TM* 2113.
- GUNZBURGER, M. D. 1992 *Proceedings of the Conference on Control of Flows*. Inst. for Math. and Its Appl., Univ. of Minnesota.
- GUNZBURGER, M. D., HOU, L. & SVOBODNY, T. P. 1991 Analysis and finite element approximations of optimal control problems for the stationary Navier-Stokes equations with Dirichlet controls. *Math. Model. Numer. Anal.* **25**, 711.
- GUNZBURGER, M. D., HOU, L. & SVOBODNY, T. P. 1992 Boundary velocity control of incompressible flow with an application to viscous drag reduction. *SIAM J. Control Optim.* **30**, 167.
- HACKBUSCH, W. 1985 *Multi-Grid Methods and Applications*. Springer-Verlag.
- HERRING, J. R., ORSZAG, S. A., KRAICHNAN, R. H. & FOX, D. G. 1974 Decay of two-dimensional homogeneous turbulence. *J. Fluid Mech.* **66**, 417.
- HINZE, J. O. 1975 *Turbulence*. 2nd edition. McGraw-Hill.
- HO, C. M. & HUANG, L. S. 1982 Subharmonics and vortex merging in mixing layers. *J. Fluid Mech.* **119**, 443.
- HOOSHMAND, A., YOUNGS, R. A., WALLACE, J. M. & BALINT, J.-L. 1983 An experimental study of changes in the structure of a turbulent boundary layer due to surface geometry changes. *AIAA Paper* 83-0230.
- JIMÉNEZ, J. 1987 Bifurcations and bursting in two-dimensional Poiseuille flow. *Phys. Fluids* **30**, 3644.
- JIMÉNEZ, J. & MOIN, P. 1991 The minimal flow unit in near-wall turbulence. *J. Fluid Mech.* **225**, 213.
- JIMÉNEZ, J., MOIN, P., MOSER, R. & KEEFE, L. 1988 Ejection mechanisms in the sublayer of a turbulent channel. *Phys. Fluids* **31**, 1311.
- JOHANSEN, J. B. & SMITH, C. R. 1986 The effects of cylindrical surface modifications on turbulent boundary layers. *AIAA J.* **24**, 1081.

- JOHANSSON, A. V., ALFREDSSON, P. H. & KIM, J. 1987 Shear layer structures in near-wall turbulence. In *Studying Turbulence Using Numerical Simulation Databases*, Proc. 1987 Summer Program of the Center for Turbulence Research, NASA-Ames & Stanford University. pp. 237 - 251.
- JOHANSSON, A. V., HER, A. V. & HARITONODIS, J. H. 1987 On the generation of high amplitude pressure peaks in turbulent boundary layers and spots. *Fluid Mech.* **175**, 119.
- KANG, S., ITO, K. & BURNS, J. A. 1991 Unbounded observation and boundary control problems for Burgers equation. *Proc. 30th Conf. on Decision and Control*. pp. 2687 - 2692.
- KIM, J. 1989 On the structure of pressure fluctuations in simulated turbulent channel flow. *J. Fluid Mech.* **205**, 421.
- KIM, J. & MOIN, P. 1985 Application of a fractional-step method to incompressible Navier-Stokes equations. *J. Comput. Phys.* **59**, 308.
- KIM, J. & MOIN, P. 1986 Flow structures responsible for the bursting process. *Bull. Amer. Phys. Soc.* **31**, no. 10, 1716.
- KIM, J., MOIN, P. & MOSER, R. 1987 Turbulence statistics in fully developed channel flow at low Reynolds number. *J. Fluid Mech.* **177**, 133.
- KLINE, S. J., REYNOLDS, W. C., SCHRAUB, F. A. & RUNSTADLER, P. W. 1967 The structure of turbulent boundary layers. *J. Fluid Mech.* **30**, 741.
- KUHN, G. D., MOIN, P., KIM, J. & FERZIGER, J. H. 1984 Turbulent flow in a channel with a wall with progressive waves. *Proc. ASME Symposium on Laminar Turbulent Boundary Layers: Control, Modification and Marine Applications*. New Orleans.
- LADYZHENSKAYA, O. A. 1963 *The Mathematical Theory of Viscous Incompressible Flow*. Gordon and Breach.
- LAUNDER, B. E. & LI, S. 1989 A numerical study of riblet effects on laminar flow through a plane channel. *Appl. Sci. Res.* **46**, 271.
- LIONS, J. L. 1971 *Optimal Control of Systems Governed by Partial Differential Equations*. Springer-Verlag.
- LIU, K. N., CHRISTODOULOU, C., RICCIUS, O. & JOSEPH, D. D. 1990 Drag reduction in pipes lined with riblets. *AIAA J.* **28**, 1697.

- LUCHINI, P., MANZO, F. & POZZI, A. 1991 Resistance of a grooved surface to parallel flow and cross-flow. *J. Fluid Mech.* **228**, 87.
- LUENBERGER, D. 1973 *Introduction to linear and nonlinear programming*. Addison-Welsey.
- LUMLEY, J. L. 1973 Drag reduction in turbulent flow by polymer additives. *J. Polymer Sci. D: Macromol. Rev.* **7**, 263.
- MANSOUR, M. L. & HAMED, A. 1990 Implicit solution of the incompressible Navier-Stokes equations on a non-staggered grid. *J. Comput. Phys.* **86**, 147.
- METCALFE, R. W., RUTLAND, C. J., DUNCAN, J. H. & RILEY, J. J. 1986 Numerical simulation of active stabilization of laminar boundary layers. *AIAA J.* **24**, 1494.
- MOFFATT, H. K. & DUFFY, B. R. 1980 Local similarity solutions and their limitations. *J. Fluid Mech.* **96**, 299.
- MOIN, P. 1987 Analysis of turbulence data generated by numerical simulations. *AIAA paper* 87-0194.
- MOIN, P. & KIM, J. 1982 Numerical investigation of turbulent channel flow. *J. Fluid Mech.* **118**, 341.
- MOIN, P., KIM, J. & CHOI, H. 1989 On the active control of wall-bounded turbulent flows. *AIAA paper* 89-0960.
- NAKAO, S.-I. 1991 Application of V shape riblets to pipe flows. *J. Fluids Eng.* **113**, 587.
- NGUYEN, V. D., SAVILL, A. M. & WESTPHAL, R. V. 1987 Skin friction measurements following manipulation of a turbulent boundary layer. *AIAA J.* **25**, 498.
- NIKURADSE, J. 1933 Stromungsgesetze in rauher rohen. *VDI-Forschungsheft* 361. (Also, Laws of flow in rough pipes, *NACA TM* 1292).
- NITSCHKE, P. 1984 Experimental investigation of the turbulent flow in smooth and longitudinal grooved tubes. *NASA TM* 77480.
- ORLANDI, P. 1990 Vortex dipole rebound from a wall. *Phys. Fluids A* **2**, 1429.
- PULLES, C. J. A., PRASAD, K. K. & NIEUWSTADT, F. T. M. 1989 Turbulence measurements over longitudinal micro-grooved surfaces. *Appl. Sci. Res.* **46**, 197.

- RAI, M. M. & MOIN, P. 1991 Direct simulations of turbulent flow using finite-difference schemes. *J. Comput. Phys.* **96**, 15.
- ROBINSON, S. K. 1988 Effects of riblets on turbulence in a supersonic boundary layer. *AIAA Paper* 88-2526.
- ROBINSON, S. K. 1991 Coherent motions in the turbulent boundary layer. *Ann. Rev. Fluid Mech.* **23**, 601.
- ROGALLO, R. S. & MOIN, P. 1984 Numerical simulation of turbulent flows. *Ann. Rev. Fluid Mech.* **16**, 99.
- ROSENFELD, M., KWAK, D. & VINOKUR, M. 1991 A fractional step solution method for the unsteady incompressible Navier-Stokes equations in generalized coordinate systems. *J. Comput. Phys.* **94**, 102.
- SAWYER, W. G. & WINTER, K. G. 1987 An investigation of the effect on turbulent skin friction of surfaces with streamwise grooves. *RAE TM* 2112.
- SCHLICHTING, H. 1936 Experimentelle untersuchungen zum rauhgkeits problem. *Ingenieur-Archiv VII* 1, 1. (Also, Experimental investigation of the problem of surface roughness, *NACA TM* 823).
- SOH, W. Y. & GOODRICH, J. W. 1988 Unsteady solution of incompressible Navier-Stokes equations. *J. Comput. Phys.* **79**, 113.
- SOTIROPOULOS, F. & ABDALLAH, S. 1990 Coupled fully implicit solution procedure for the steady incompressible Navier-Stokes equations. *J. Comput. Phys.* **87**, 328.
- SRITHARAN, S. S. 1992 *Optimal Control of Viscous Flows*. Frontiers in Applied Mathematics Series, SIAM.
- SRITHARAN, S. S., OU, Y.-R., BURNS, J. A., LADD, D., HENDRICKS, E. & NOSSIER, N. 1991 Active control of viscous flow past a cylinder: theory, computation and experiment. Preprint. Also in *Bull. of the Amer. Phys. Soc.* **36**, 2626.
- TANI, I. 1988 Drag reduction by riblet viewed as roughness problem. *Proc. Japan Acad.* **64**, Ser. B, 21.
- TARDU, S. & TRUONG, T. V. 1991 *Proc. 6th European Drag Reduction Meeting*. Eindhoven.
- TEMAM, R. 1984 *Navier-Stokes Equations*. 3rd revised ed. North-Holland.

- TEMAM, R. 1991 Navier-Stokes Equations: Theory and Approximation, Chapter I. *Preprint n° = 91 - 16, Institute for Scientific Computing and Applied Mathematics, Bloomington, Indiana*. To appear in the *Handbook of Numerical Analysis* (eds. P.G. Ciarlet & J.L. Lions). North-Holland.
- TENNEKES, H. & LUMLEY, J. L. 1972 *A First Course in Turbulence*. The MIT Press.
- VIRK, P. S. 1975 Drag reduction fundamentals. *AIChE J.* **21**, 625.
- VUKOSLAVČEVIĆ, P., WALLACE, J. M. & BALINT, J.-L. 1992 Viscous drag reduction using streamwise-aligned riblets. *AIAA J.* **30**, 1119.
- WALLACE, J. M. & BALINT, J.-L. 1987 Viscous drag reduction using streamwise aligned riblets: survey and new results. In *Turbulence Management and Relaminarisation* (eds. H. W. Liepman & R. Narasimha). Springer-Verlag.
- WALSH, M. J. 1980 Drag characteristics of V-groove and transverse curvature riblets. In *Viscous Drag Reduction* (ed. G. R. Hough). American Institute of Aeronautics and Astronautics.
- WALSH, M. J. 1982 Turbulent boundary layer drag reduction using riblets. *AIAA Paper* 82-0169.
- WALSH, M. J. 1983 Riblets as a viscous drag reduction technique. *AIAA J.* **21**, 485.
- WALSH, M. J. & WEINSTEIN, L. M. 1978 Drag and heat transfer on surfaces with small longitudinal fins. *AIAA Paper* 78-1161.
- WHITE, F. M. 1974 *Viscous Fluid Flow*. McGraw-Hill.
- WILKINSON, S. P. & LAZOS, B. S. 1987 Direct drag and hot-wire measurements on thin-element riblet arrays. In *Turbulence Management and Relaminarisation* (eds. H. W. Liepman & R. Narasimha). Springer-Verlag.
- WILLMARTH, W. W. & LU, S. S. 1972 Structure of the Reynolds stress near the wall. *J. Fluid Mech.* **55**, 65.